Development of High Performance Cutting Tools for Machining of Gamma-Titanium Aluminide Intermetallic Alloys, Ti6Al4V and Inconel 718 in Aerospace Applications

Γ-Titanyum Alüminyum İntermetalik Alaşımlarının, Ti6Al4V Ve İnkonel 718 Malzemelerinin Havacılık Uygulamaları Için Frezelenmesinde Kullanılmak Üzere Yüksek Performanslı Takım Ucu Geliştirilmesi

by

Mohammad Akmal

A Thesis Submitted to the
Graduate School of Engineering
in Partial Fulfillment of the Requirements for
the Degree of

Doctor of Philosophy
in
Mechanical Engineering

Koç University
October 2017

Koç University

Graduate School of Sciences and Engineering

This is to certify that I have examined this copy of a doctoral thesis by

Mohammad Akmal

and have found that it is complete and satisfactory in all respects,
and that any and all revisions required by the final
examining committee have been made.

Committee Members:

İsmail Lazoğlu, Ph. D. (Advisor)

Alphan Sennaroğlu, Ph.D.

Arif Karabeyoğlu, Ph. D.

Mustafa Bakkal, Ph. D.

Umut Karagüzel, Ph. D.

Date: 17/10/2017

To My

Teachers

Parents

Wife

Daughter

Sons

&

friends

ABSTRACT

Aerospace industry use advance engineering materials such Titanium and Nickel super alloys due to their superior mechanical and thermal properties. Ti6Al4V, Inconel 718 and Gamma-Titanium Aluminide are critical materials, especially for the aircraft engines and rockets. In this research, milling tools are designed and investigated for the machining of the famous aerospace alloys, namely, the intermetallic compound gamma titanium aluminide, the nickel alloy Inconel 718, the titanium alloy Ti6Al4V and the aircraft structural material Aluminum alloy Al7050. Besides the milling process, the drilling of Ti6Al4V and Al7050 workpiece was also investigated. Solid carbide end-mills are designed for milling the intermetallic alloy gamma titanium aluminide and Ti6Al4V. Besides the geometry of the end-mill, the effect of the surface finishing techniques and the coating material is investigated on the performance of the solid carbide end-mill. The designed tools are produced using three surface finish techniques; the magnetic powder finish, drag finish and wet sandblast finish. Whereas, the two types of surface coating materials investigated for the study are the aluminum chromium nitride AlCrN and the aluminum titanium nitride AlTiN. The performance of the designed end-mills is evaluated using the cutting forces magnitudes, specific cutting forces, tool wear and friction coefficient. A new method is proposed to establish the friction coefficients for the coating material and workpiece pairs directly from the mechanics of the milling process and machining force data. The method was applied to find the friction coefficient for the AlCrN and AlTiN coatings on Ti6Al4V and Al7050. Furthermore, the thermal analysis of the drilling process is provided through a semi-analytical approach for predicting the temperature distribution on the drill tool when drilling Ti6Al4V. The simulation results were confirmed through a novel rotary tool temperature measuring device. The simulation of machining of the Inconel 718 alloy is achieved by providing the constitutive model to establish the necessary mechanical properties for

simulating the cutting process in the milling process. The constitutive model was then used to estimating the cutting coefficients and for predicting the cutting forces for the milling process. Subsequently, the validated simulation model is used for the parametric analysis to establish the ideal end-mill design for high-performance milling of the Inconel 718 alloy. A new monolithic ceramic end-mill is designed, manufactured and validated for the high-performance milling of the Inconel 718 alloy. The experimental results confirmed the improvement in productivity in the milling of Inconel 718.

ÖZET

Havacılık ve uzay endüstrisi, yüksek mekanik ve termal özelliklerinden dolayı titanyum ve nikel süper alaşımlarını kullanmaktadır. Ti6Al4V, Inconel 718 ve Gamma Titanyum Alüminid özellikle uçak motoru ve roketler için kritik önemdeki malzemelerdir. Bu araştırmada, Gamma Titanyum Alüminid, Inconel 718, Ti6Al4V ve uçak yapımında kullanılan Al7050 gibi iyi bilinen havacılık ve uzay alaşımlarının işlenmesi için parmak frezeler tasarlanmış ve araştırılmıştır. Frezelemenin yanı sıra, Ti6Al4V ve Al7050 malzemelerin delinmesi de araştırılmıştır. Gamma Titanyum Alüminid ve Ti6Al4V malzemelerin frezelenmesi için katı karbür parmak frezeler tasarlanmıştır. Kesici takım geometrisinin yanı sıra, yüzey finiş tekniklerinin ve kaplama malzemelerinin karbür takımın performansına etkileri araştırılmıştır. Tasarlanan takımlar; manyetik toz kaplama, sürtünme kaplaması ve ıslak zımpara kaplaması olmak üzere üç farklı teknikle finişlenmiştir? Ayrıca alüminyum krom nitrür ve alüminyum titanyum nitrür omak üzere iki ayrı kaplama malzemesi de incelenmiştir. Tasarlanan parmak frezelerin performansı kesme kuvvetlerinin şiddeti, spesifik kesme kuvvetleri, takım aşınması ve sürtünme katsayıları kullanılarak değerlendirilmiştir. Kaplama malzemesi-parça arasındaki sürtünme katsayılarının belirlenmesi için direk olarak freze kuvvet verileri ve proses mekaniğini kullanan yeni bir metod sunulmuştur. Bu metod AlCrN ve AlTiN kaplamaların, Ti6Al4V ve Al7050 malzemelerin arasındaki sürtünme katsayılarının bulunmasında uygulanmıştır. Ayrıca, yarı-analitik bir yaklaşımla çalışılan delme işleminin termal analizi, Ti6Al4V malzemenin delinmesi esnasında oluşan ısı dağılımı ile gösterilmiştir. Simülasyon sonuçları özgün bir dönen takım ısı ölçüm cihazıyla doğrulanmıştır. Inconel 718 malzemenin işlenmesinin simülasyonu, kesme prosesini simüle etmek için gereken mekanik özelliklerin kurucu bir modelle sağlanmasıyla gerçekleştirilmiştir. Kurucu model, freze prosesindeki

kesme katsayılarının tahmini ve bu sayede kesme kuvvetlerinin bulunması için kullanılmıştır. Sonuç olarak, doğrulanan simülsayon modeli, Inconel 718 alaşımının yüksek performansla frezelenmesi için ideal parmak freze tasarımının parametrik analizi için kullanılmıştır. Yekpare seramik bir parmak freze tasarlanmış, üretilmiş ve Inconel 718 alaşımının yüksek performansla frezelenmesi için doğrulanmıştır. Deneysel sonuçlar tasarlanan takımın, Inconel 718 alaşımının işlenmesinde üretkenliği artırdığını göstermiştir.

ACKNOWLEDGEMENTS

I would like to express my utmost and sincere gratitude and appreciation to my thesis supervisor Professor, Ismail Lazoglu, first of all, for the opportunity and then the continued guidance, support and patience throughout the research period at the advance world-class facilities of the Manufacturing and Automation Research Center. I would also like to thank the respected thesis review committee members, Professor Alphan Sennaroglu and Professor Arif Karabeyoglu for their valuable time and input during the periodic committee meetings. I would also like to thank the respected thesis committee members for the review and input.

On behalf of the MARC, I also would like to acknowledge The Scientific and Technological Research Council of Turkey (TUBITAK), MANUNET: walking towards a European Regionally-based Research Area on New Processes and Flexible Manufacturing Systems, Karcan Cutting Tool Company, EU Machine Tool Technologies Research Foundation (MTTRF), Alp Aviation, Surface Science and Technology Center (KUYTAM), Koç university for their support.

I would like to thank the Higher Education Commission of Pakistan and the University of Engineering and Technology Peshawar Pakistan for funding my PhD studies abroad. I would like to thank Koç University for their efficient administration and high-quality support.

I am indebted to the expert opinions and support by Seyed Ehsan Layegh Khavidaki, Muzaffer Butun and Baris Yagci and the wonderful companionship and ever helping environment provided by friends at the MARC.

I would like to express my deep gratitude to the great nation of Turkey in general, for giving me such a beautiful experience, pleasant memories and amazing friends that will be forever cherished.

Finally, I would like to acknowledge the encouragement, deep and continuous support and prayers of my parents. My brothers and family members, who took care of matters I was responsible for. It would not have been possible without their assistance and patience. And, I am most thankful to my wife for making my studies abroad possible. It was with her strength and determination that I could continue my studies. She had to persevere and show tremendous courage in taking care of the 5 children, in an environment full of strife, terror and epidemics, while I was abroad. I am most thankful to my daughter Aiysha, my sons Ayub and Usman for helping their mother and the little ones Yahya and Fateh for giving me 4 years of their toddler years. It was only because of the unflinching love, encouragement, sacrifice and belief of the whole family and I dedicate this work to them.

TABLE OF CONTENTS

LIST OF TABLES

LIST OF FIGURES

NOMENCLATURE

ε	Strain
$\dot{\varepsilon}$	Strain-rate
$\dot{Q}$	Heating rate
T_m	Melting temperature of material
T_O	Room temperature
T	Selected temperature
σ	Axial stress
τ	Shear stress
τ_s	Shear flow stress
σ_ε	Flow stress corrected for strain hardening
σ_s	Saturation stress
σ_0	Material yield stress
N	Strain hardening index
R	Softening index
$\sigma_{\dot{\varepsilon}}$	Johnson-Cook model term for the strain rate hardening
σ_T	Johnson-Cook model term for the thermal softening
γ	Shear strain
$\dot{\gamma}$	Shear strain rate
α_r	Nominal rake angle
α_n	Normal rake angle
h	Uncut chip thickness
h_c	Cut chip thickness

r_c	Chip ration
ϕ_c	Shear angle
ϕ_n	Normal shear angle
β_a	Friction angle
β_n	Normal friction angle
μ	Friction coefficient
η	The chip flow angle
β	Helix angle
ϕ	Immersion angle
V	Cutting velocity
V_s	Shear flow velocity
Δd	Shear deformation zone thickness
l_t	Shear plane length
F_s	Shear force
b	Width of cut
db	Discrete disk width of cut
h_{ave}	Average chip thickness
P_s	Power consumed in shearing of the material in machining
i	The obliquity angle
ρ	Material density
C	The material specific heat
k	Material thermal conductivity
K_{tc}	Tangential cutting coefficient
K_{rc}	Feed cutting coefficient
K_{ac}	Axial cutting coefficient
K_{te}	Tangential edge coefficient

K_{re}	Feed edge coefficient
K_{ae}	Axial edge coefficient
F_{tc}	The tangential cutting force
F_{fc}	The feed cutting force
F_{te}	The tangential edge force
F_{fe}	The feed edge force
F_u	The friction force along the tool rake face.
F_v	The normal force on the tool rake face
dz	The disk thickness for the discretized end-mill
$dF_{t,j}$	The instantaneous tangential force for the select disk and immersion angle
$dF_{r,j}$	The instantaneous feed force for the select disk and immersion angle
$dF_{a,j}$	The instantaneous axial force for the select disk and immersion angle
dF_x	The instantaneous x direction force for the select disk and immersion angle
dF_y	The instantaneous y direction force for the select disk and immersion angle
dF_z	The instantaneous z direction force for the select disk and immersion angle
F_x	The x direction cutting force for the give depth of cut at the immersion angle
F_y	The y direction cutting force for the give depth of cut at the immersion angle
F_z	The z direction cutting force for the give depth of cut at the immersion angle
$\bar{F}_x$	The average force in the x direction for the full rotation of the spindle
$\bar{F}_y$	The average force in the y direction for the full rotation of the spindle
$\bar{F}_z$	The average force in the z direction for the full rotation of the spindle
F_{PR}	The planar resultant of the cutting forces for given immersion angle ϕ
N	Number of flutes
n	Spindle speed
f	Feedrate

f_z	The maximum chip thickness per flute
MRR	Material removal rate
V_B	Flank side wear+
D	Tool diameter
a_p	Depth of cut
a_e	Width of cut
E	Modulus of elasticity
L	Beam length
I	Moment of inertia
k_{st}	Beam stiffness
R_z, R_x, R_y	Rotation matrices
$2\kappa_t$	Drill tip angle
ψ	Drill chisel angle
ω	Drill chisel width
Δz	Drill discretized disk thickness
l_c	Chip contact length along the rake face
V_c	Chip flow velocity
P_u	The power lost to friction in machining
λ	The heat partition coefficient
θ	Instantaneous drill cutting lip position
T	Torque

Chapter 1
Introduction

1.1 Overview

The aerospace industry is the most stringent in safety regulation for parts integrity and reliability. The capability to simulate and control the manufacture process of intended parts is a keenly sought objective. The machining operations, specially milling and drilling, are the common tasks in the manufacture of aerospace parts. Besides every part requiring to be given their final shape and size through machining, such as milling or turning, 17000 holes are drilled in each 747-8 fuselage production line for sheet metal joining and assembly (Boeing, 2015) as an example.

1.2 Aerospace Materials

The nickel, titanium and aluminum alloys are from the main materials utilized in engine and structural components of an aircraft, shown in Figure 1-1 and Figure 1-2. Furthermore, the gas turbine engine has sections, where the passing gas temperature could be above the melting point temperature of almost any engineering material as shown in the Figure 1-3. The Figure 1-3 is for a general electric jet engine, working on the axial flow design and used for a variety of fighter and bomber aircrafts in the 1950s. It is also used in supersonic cruise missiles. By looking at the two figures, Figure 1-2 and Figure 1-3, together, then the working temperatures of different sections of the jet engine and primary material used for components in that section is recognized. The jet engine intake compressor section components see temperatures in the range of 500°C. The combustion chambers are the harshest with temperatures up to 1000°C. Then the high-pressure turbine is receiving the hot flu gases

directly from the combustion chamber and the blades at the entrance have the highest operating temperatures. Then comes the low-pressure turbine.

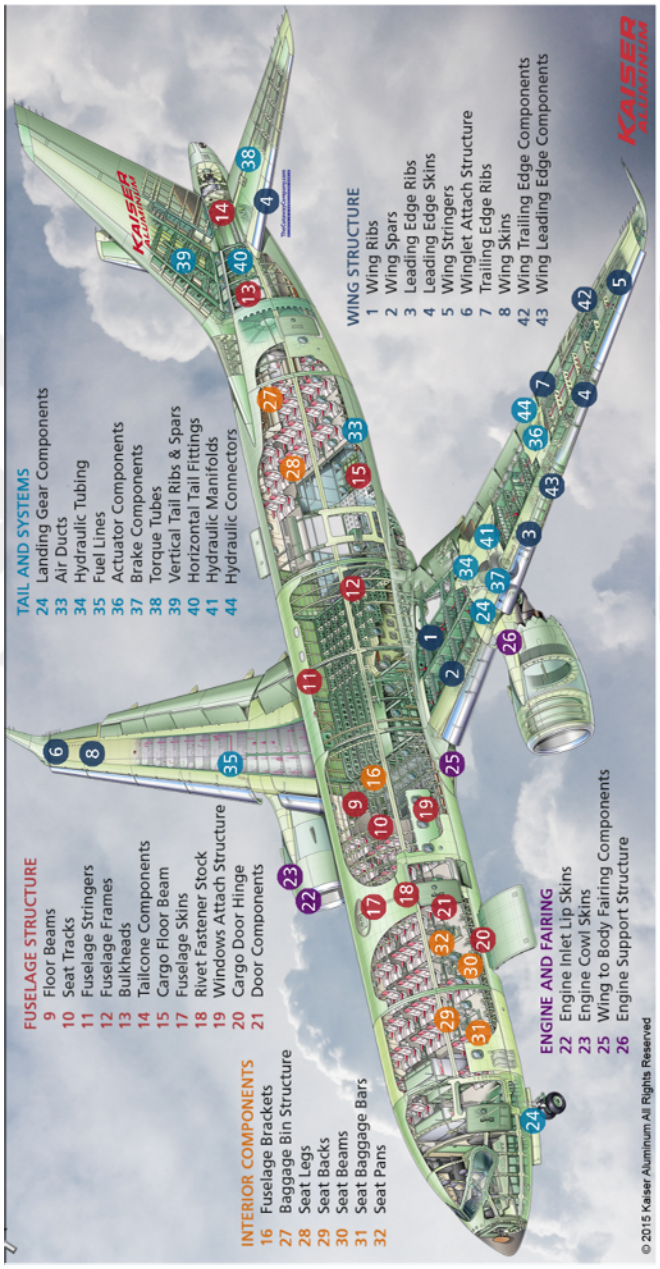

Figure 1-1: The aluminum alloy utilization in an airplane (Kaiser Aluminum, 2017).

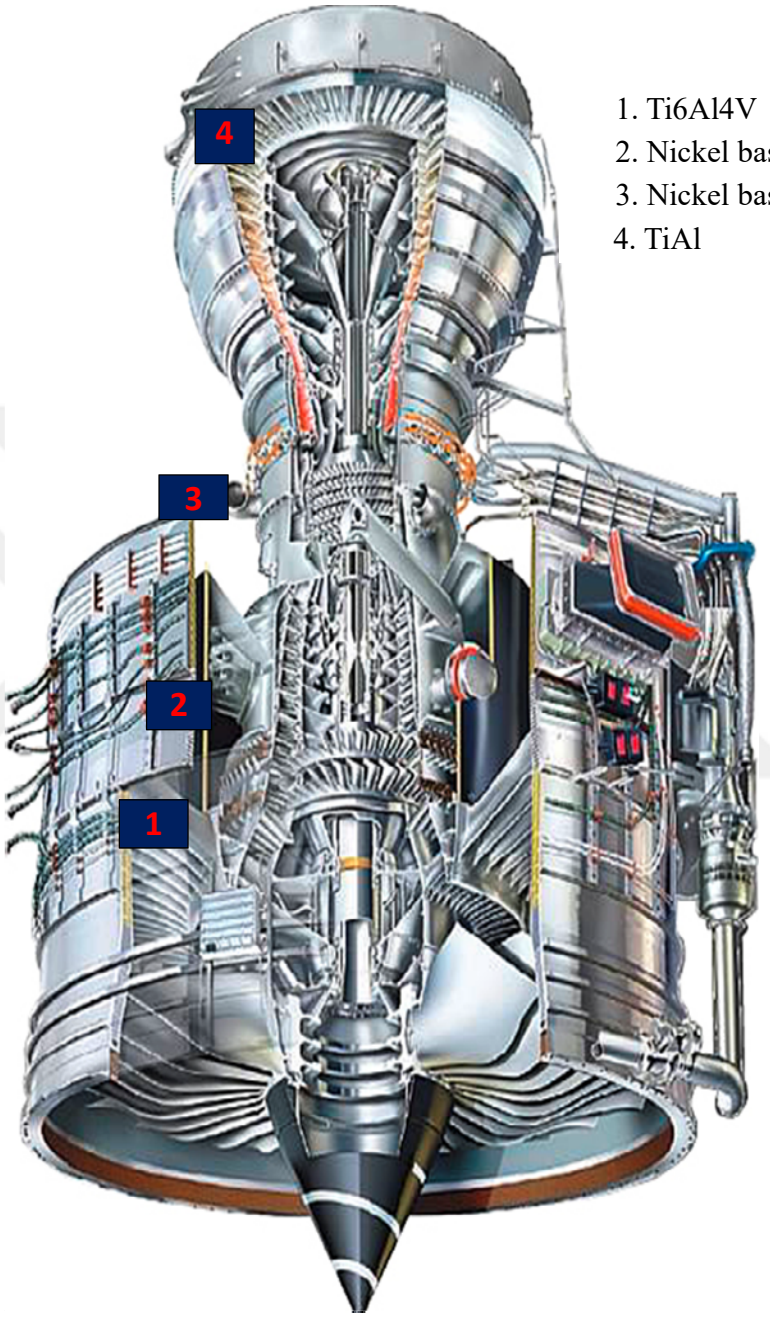

Figure 1-2: The nickel and titanium alloy components in a jet engine (AMG GfE, 2013).

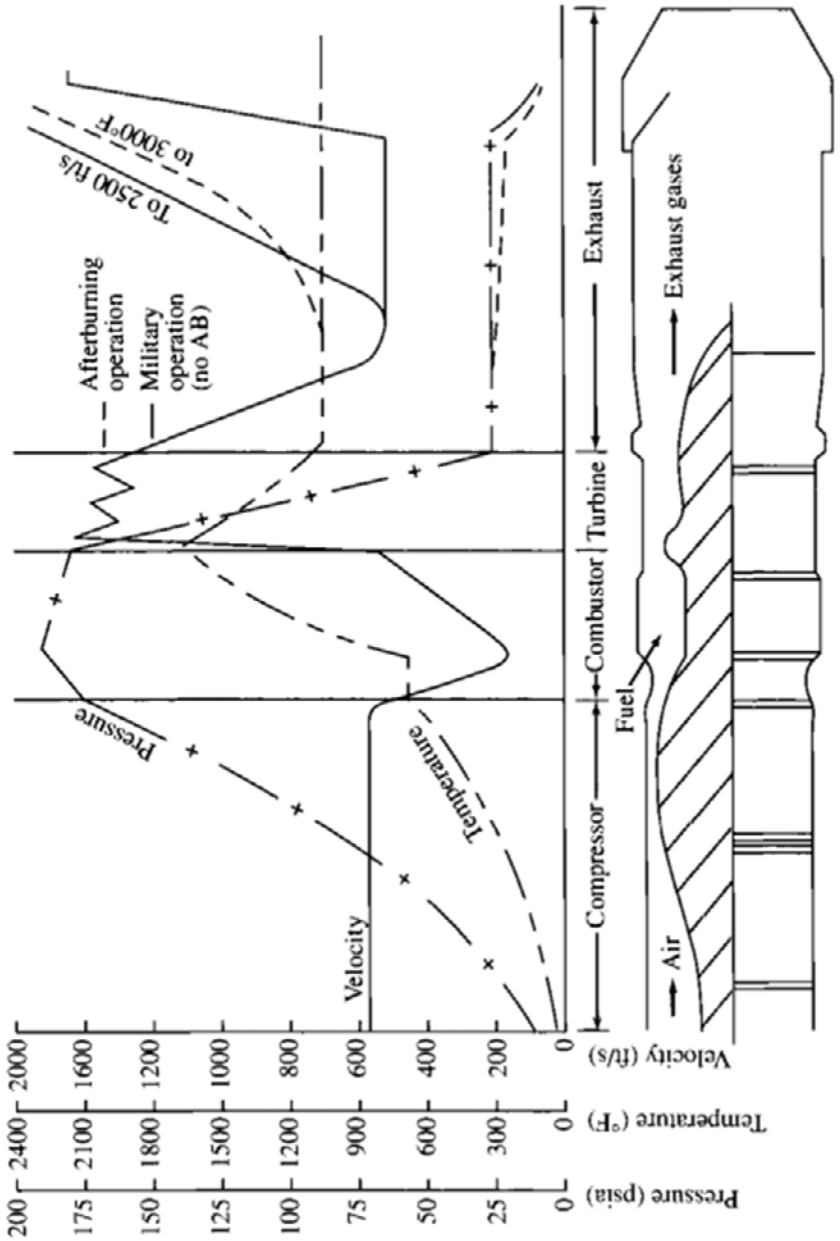

Figure 1-3: The property variation through the general electric J79 afterburning turbojet (Mattingly, 2006).

The first of the materials investigated for this thesis was nickel alloy Inconel 718. A typical aircraft engine will have 40% to 50% nickel based alloy components (Thellaputta et al., 2017). Nickel alloys possess superior corrosion and wear resistance combined with high mechanical strength at elevated temperatures. The high-pressure compressor and high-pressure turbine sections of the gas turbine engines, where the operating temperature is around 1600°C, utilize parts made from the nickel based superalloys. These alloys are the toughest materials to machine. Besides power generation, the oil and gas exploration, chemical processing, nuclear reactors, to name a few, are some of the harshest application environments that benefit from nickel alloy parts.

Nimonics, a nickel and chromium alloy, were the first family of nickel alloys, developed in 1940 England, for jet engine applications. Later with the development of Inconel, a nickel, chromium and iron alloy series, further improvements in the thermo-mechanical properties of the alloying series were reported.

Historically the development of structural materials has remained one of main topics for performance improvement in automotive, power generation (Williams and Starke, 2003) and aerospace applications (Yamaguchi et al., 2000). The advancement in structural materials has allowed continuous improvements in the performance of energy conversion systems by introducing new materials and improving existing materials that demonstrate superior specific mechanical properties at elevated temperatures. The intermetallic alloy gamma titanium aluminide is one such material to have emerged relatively recently.

The intermetallics have attracted great interest since the first Materials Research Society symposium 1984 (Liu, 1995). One of the factors for such interest is the growing demand by the advance heat engines for light weight, corrosion resistant and high temperature strength materials. Ordered intermetallics constitute a unique and an emerging class of metallic materials that form a long range ordered crystal structures below the critical ordering temperature (Liu and Kumar, 1993).

The titanium aluminides have demonstrated attractive properties for operations in hostile environment at elevated temperatures with lower densities. The employment of these can lead to substantial payoffs in the automotive industry, power plant turbines and aircraft engines. It took more than 20 years of very intensive research to obtain maturity level of TiAl-based alloys that is sufficient to consider this class of materials for critical rotating components in commercial jet engines (Lapin, 2009).

The γ-TiAl with the addition of other alloying elements have been more intensively studied. That is for couple of reasons. Firstly, their low density high temperature strength and modulus, tolerable tensile ductility at room temperature and reasonably good oxidation resistance. Secondly, and importantly, the manufacturability of TiAl-based alloys is possible through conventional equipment and familiar processes such as casting, forging and machining on almost all conventional equipment (Yamaguchi et al., 2000). The gamma titanium aluminide was the second material investigated for the thesis.

The third material investigated for this material is from the titanium alloys series, namely, Ti6Al4V. The titanium alloy Ti6Al4V is an established engineering material for use in the aerospace, medical, automotive, oil and gas, power generation and sports related industries. They are known for their medium range high temperature application. The outstanding corrosion resistance and strength efficiency besides the in general best all-round performance has made Ti6Al4V the most widely used titanium alloy.

The Ti6Al4V alloy is a hard-to-machine material. This titanium alloy exhibits high mechanical strength for elevated temperatures, low stiffness, low thermal conductivity and high chemical reactivity. Notably, the last two properties are responsible for the threat of potentially catastrophic, titanium fires.

Starting from the late 1920s, aluminum alloys have been used as main airframe materials instead of wood. Aluminum provides low cost, lightweight solution for the manufacturer and is easily fabricated compared to the other high-performance materials. Al7050 was

developed during the 1970s to meet the need for high strength in thick-section products, good resistance to stress corrosion cracking and good fracture toughness and fatigue characteristics (Prasad and Wanhill, 2017). Aluminum alloy Al7050 is the fourth and final material investigated for this thesis.

The bulk of published research for the machining is regarding turning operations, a continuous machining process. In contrast, the milling process is inherently an interrupted machining process. The drastic changes in force and temperature magnitudes create the hostile cutting conditions when machining the titanium alloys.

This work reports the end-milling of titanium alloy Ti6Al4V for coated tungsten carbide end-mills. How the coating and surface finish technique effect the tool workpiece pair is investigated for the solid carbide end-mills.

Drilling is one of the common machining operations and is always necessary for parts requiring non-permanent or semi-permanent assembly. The forces in the drilling process are predicted and using them the temperature distribution for a drilling end-mill is simulated.

This work modeled the cutting forces during the drilling operation of the titanium alloy Ti6Al4V with solid carbide drills and simulated the temperature distribution for the drill.

Chapter 2
Literature Review

2.1 Inconel 718:

Certain materials have the remarkable ability to retain their properties at elevated temperatures. Nickel alloys are from the family of such high strength materials called superalloys. The term superalloy was coined shortly after world war II to describe a class of alloys produced to be used in turbochargers and turbine engines. Since then their application has further expanded in to other areas demanding high strength and corrosion resistance at elevated temperatures. The full utilization of these alloys is dependent on their ability to be fabricated, namely, sufficient low temperature ductility.

The machining of Inconel parts remains a problem, even though many different tool materials, coatings and strategies have been developed, nevertheless, an effective approach is still not available.

One of the studied techniques is the ductile mode machining. The cutting speeds in this machining strategy produces enough localized heating for the thermal softening phenomena to take effect and help reduce the material strengths for cutting.

2.1.1 Constitutive models

Constitutive models from conventional material tests for Inconel 718 have been reported in literature, but they are for much smaller strains and strain rates than what are present in machining operations (Si et al., 2015). Flow stress magnitudes for varying strain, strain-rate and temperatures are established using material testing apparatus such as the split Hopkinson pressure bar test, the high speed tensile test or compression tests. (Song and Huh, 2007) applied the high speed tensile test for strain rates of up to 400 s^{-1} and the split Hopkinson pressure bar test for strain rates up to 400 s^{-1}. (Lin et al., 2015) investigated a wide range of

deformation temperatures and strain rate and proposed a constitutive model to account for the deformation temperature and strain rate.

A considerable effort exists in the researcher community to establish the material characteristics for high temperature high strain rate deformation of Inconel 718. (Wang et al., 2008) used hot compression tests to evaluate the flow behavior of Inconel 718 for strain rates 10^{-3} to 1 s^{-1}. (Iturbe et al., 2017) used the Gleeble 3500 testing machine to establish the flow stress for strain rates in the range of 10 – 102 s^{-1} at testing temperatures between 21°C and 1050°C. The high speed machining strain rates are much higher to the tune of 10^6 to 10^7 s^{-1}. (Wang et al., 2013) performed the split Hopkinson pressure bar test at 500 – 800°C for strain rates of 5000 – 11000 s^{-1}.

Few published articles have incorporated other physical phenomena, like hardness, recrystallization, activation energy, etc. to correct the flow stress values arriving from traditional tests. (Del Prete et al., 2013) introduced a new flow stress model to account for the hardness of the material because of different heat treatment recipes. (Lurdos et al., 2008) proposed an empirical formulation built on the discontinuous dynamic recrystallization mechanism. (Jafarian et al., 2014) accounted for the microstructure changes and modeled the recrystallization of the alloy and there influence on the mechanical properties of the nickel alloy Inconel 718 when machining in finite element analysis. (E Uhlmann et al., 2007) used the finite element simulation of segregated chip formation by incorporating the ductile damage besides the strain, strain-rate and thermal softening of the material.

2.1.2 Machining Simulations

Recognizing the difficulty in capturing the exact conditions present in machining operations, (Bäker, 2015) utilized the inverse technique, where the machining data itself was used to estimate the material properties. (Arrazola et al., 2004) discusses the difficulty in applying the inverse formulation when constituting the material characteristics. (Denkena et

al., 2015) used the particle swarm optimization algorithm to identify material properties to predict the machining forces.

(Wright and Chow, 1982) took the traditional route and used the orthogonal machining test for many nickel alloys to establish their material database. Material characteristics established from an orthogonal test are the necessary input for predicting cutting forces for any machining operation. Many of the reported works are for low cutting speeds, but (Pawade and Joshi, 2011) reported machined chip thickness for cutting speeds of 425 m/min.

2.1.3 Wear

Besides the prediction of cutting forces, the tool life is equally important. The aggressive cutting strategies mandate to establish if they would be feasible or not. (Richards and Aspinwall, 1989) conducted evaluation of a wide range of available ceramics for machining the Inconel alloys for speeds up to 750 m/min. (Wayne and Buljan, 1990) reported ceramic inserts to primarily fail due to fracture and nose wear in turning tests for speeds of 300 m/min. (Narutaki et al., 1993) reported accelerated wear of ceramic tools when cutting speeds were increased from 300m/min to 400m/min by the diffusion mechanism. (Brandt et al., 1990) reported the main wear mechanisms at cutting speeds higher than 300 m/min to be edge breakage.

2.2 Ti6Al4V

2.2.1 Machining of titanium alloy

Titanium alloys are widely accepted engineering materials for application in many diverse industries. Titanium alloys, owing to their excellent corrosion resistance and strength efficiency, are primarily utilized in the aerospace and power generation industry. Besides that, it is also used in surgical implants of various kinds such as heart implants, dentures, joint and bone implants, etc., chemical industry, oil and gas and food processing industries.

The same properties that made this alloy attractive for the mentioned industries has various sports craving the titanium advantage (Christoph Leyens and Peters, 2003). The titanium alloys provide excellent mechanical strength, corrosion resistance and fracture toughness for elevated temperature applications besides low density and high strength efficiency. There are many alloying compositions presently used in wide range of industries. Nevertheless, the Ti6Al4V has emerged as having the most versatile thermo-mechanical properties (Donachie, 2000) of the lot. (Davim, 2014) reports that in the last 50 years of titanium alloy production, Ti6Al4V has accounted for 50% of all titanium alloys produced.

The titanium alloys are ill-famed for their low thermal conductivity, high strength at elevated temperatures, low modulus of elasticity and chemical reactivity. Hence, (Zitoune et al., 2013) (Froes, 2015) placed the Ti6Al4V alloy in the category of hard-to-machine materials.

Despite in excess of 50 years of modern industrial practice and design experience, the machining of titanium alloys remains a major concern. There exists a significant room for progress in terms of tool life, productivity and workpiece integrity. The research community has addressed the titanium alloys challenge by refining and developing 1) the cutting tool materials, 2) the cutting tool geometry and the most heavily addressed is 3) the cutting environment and parameters.

Bulk of published research for machining of titanium alloys is concerning turning operations. The turning process is a continuous machining process whereas milling process is inherently an interrupted machining process. The intermittent nature of tool material engagement is in addition to the difficulties associated with machining titanium alloys, namely; the superior mechanical properties, low thermal conductivity and high chemical reactivity. (Pervaiz et al., 2014) declared the cutting conditions for this alloy as harsh for the drastic changes in force and temperature magnitudes are, in fact, mechanical impacts and thermal shocks.

(Islam et al., 2015) showed that the cutting tool receives up to 90% of the heat generated during machining of titanium alloys because of the poor thermal conductivity of the titanium alloys. This lopsided accumulation of generated heat in cutting tool results in quick rise in cutting tool temperature. The rise in temperature coupled with strong chemical affinity of titanium alloys with cutting tool materials, leads to rapid degradation of cutting tool integrity.

It is to be noted, all factors that cause increase in cutting temperatures from the nominal magnitudes, result in reduced tool life and consequently the productivity. Number of research have focused at estimating the heat generation, temperature distribution for cutting tools (Lazoglu and Bugdayci, 2014a) (Islam et al., 2012) and the factors affecting them. The coating materials are one of the factors as they exhibit different magnitudes of coefficient of friction and thermal properties (Grzesik, 2000). A coating material with higher coefficient of friction or poorer thermal properties will result in reduced tool life. Similarly the tool geometry parameters and cutting edge radius dimensions (Wyen and Wegener, 2010) are factors that directly effecting the cutting forces and in turn increase the magnitude of heat generated and its accumulation (Rech et al., 2013). One way to mitigate tool wear is to coat a material that would not only provide harder tool surface but inhibit chemical affinity between the workpiece and tool materials. Plasma boronized tools have been reported to improve productivity for machining Ti6Al4V (Basturk et al., 2010). Equally important are the cutting parameters. The cutting speed, axial and radial depth of cut and feedrate dictate tool life (Ghani et al., 2013). The five axis machining has been shown to minimize cutting forces for same cutting parameters (Layegh K. et al., 2015).

2.2.2 Friction coefficient

The friction coefficient at the tool-chip interface for any tool-workpiece pair is a fundamental input for the thermo-mechanical analysis of tool performance, workpiece geometric conformity and surface integrity. The pioneers built, fully analytical models to predict the friction coefficient (Merchant, 1945) followed by semi-analytical techniques

employing inputs from machining tests. (Budak et al., 1996) used force data from orthogonal machining experiments to calculate the friction coefficient for the titanium alloy Ti6Al4V. (Akmal et al., 2017) used force data from milling calibration tests to calculate the friction coefficient for differently coated solid carbide end-mills. (Ulutan and Özel, 2013) combined FEM techniques to strengthen the understanding of friction in machining of difficult to machine materials. Then other studies utilized friction measurement setups, (Valiorgue et al., 2008) and (Egaña et al., 2012) applied pin on disk apparatus to measure friction coefficients.

(Karpat, 2011) The thermo-mechanical simulation of the cutting process requires the heat generated between chip-tool interface and the tool-workpiece interface as an input. The magnitude of the heat generated between the chip-tool interface is a function of cutting speed, the friction coefficient between the chip-tool interface and the normal force component of the cutting forces on the tool rake face. (Lazoglu et al., 2017) used the friction coefficient and machining condition to simulate and experimentally confirm the temperatures produced on a drilling tool tip when drilling titanium alloy Ti6Al4V. Similarly, (Mamedov and Lazoglu, 2016) used the same definition of power lost to friction at the chip-tool interface to simulate the temperature distribution for the micro milling end-mill cutting edge and its diffusion into the workpiece machined surface during the micro-milling process. Number of research have used this power lost to friction as the heat source input for the thermal analysis of tool-workpiece interfaces (Ulutan et al., 2009). While investigating and successfully simulating the transient heat partition coefficient for the milling process (Islam et al., 2015) noted the fact that the cutting tools receive up to 90% of the heat generated at the chip-tool interface during machining processes because of the poor thermal conductivity of the titanium alloys. The lopsided accumulation of generated heat in cutting tool results in the quick rise in cutting tool temperature.

surface treatment solutions are one way to mitigate tool wear. They provide a harder tool surface and inhibit chemical affinity between the workpiece and tool materials. There are

many industry wide recognized coating materials available for different materials, processes and conditions. These coatings, besides the recognized improvement in wear resistance, change the friction behavior for the tool-workpiece pair. (Rech, 2006) evaluated the thermal performance of different coating materials for the chip-tool interaction. A coating material with a higher coefficient of friction or poorer thermal properties will result in reduced tool life.

(Çelebi et al., 2013) reported the effect of variation in the tool cutting edge geometry parameters on the cutting forces. This paper will further expand the effect of the cutting edge on the friction coefficient by including the effect of a surface finish technique.

This study introduces a direct approach to establish the friction coefficient for side cutting edge of the solid carbide milling tools for two coating materials and three finishing techniques when machining the titanium alloy Ti6Al4V. The two coating materials investigated in the study are aluminum titanium nitride, AlTiN and aluminum chromium nitride, AlCrN. The three surface finishing techniques investigated are namely, finishing with magnetic powder (FMP), drag finishing (DF) and wet sandblast finishing (WSB) techniques. The evaluation is performed by milling operation on Ti6Al4V for two depths of cut. The force data are then used to establish the friction coefficient for the respective tool.

2.3 Gamma titanium aluminide

2.3.1 Intermetallic alloys

The objective of the following report is to review chemical composition, microstructure and some properties of generic TiAl-based alloys, the factors governing alloy selection and current methods of manufacturing of components for automotive, turbine gas industry and aerospace applications.

Historically the development of structural materials has remained one of main topics for performance improvement in automotive, power generation (Williams and Starke, 2003) and

aerospace applications (Yamaguchi et al., 2000). The advancement in structural materials has allowed continuous Improvements in the performance of energy conversion systems by introducing new materials and improving existing materials that demonstrate superior specific mechanical properties at elevated temperatures.

Titanium-base alloys have been instrumental towards the performance improvements for gas turbine engines. These alloys allowed significant reduction in airframe weights owing to their superior specific properties, consequently resulting in higher thrust/weight ratio of gas turbine engines. Nevertheless, oxidation and strength considerations limit the current-state-of-the-art Titanium-base alloy applications to the temperatures of around 600°C (Kim, 1989). Furthermore Titanium-based alloys have also demonstrated high temperature limitation for damage tolerance, creep strength and fire resistance.

The effort towards development of new materials has been following two paths one to reduce weight and other is to push elevated temperature limits higher. Every °C increase in operating temperature in various sections of turbine have a direct impact on turbine efficiency and reduction in weight increases the thrust to weight ratio, resulting in overall improvement in fuel efficiency.

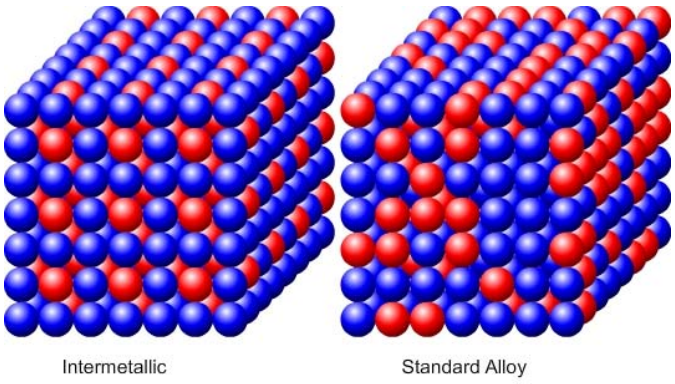

Figure 2-1: Comparison between a disordered crystal structure of a conventional alloy and a long-ranged ordered crystal structure of an ordered intermetallic compound. ("Intermetallic Alloys," 2017)

The intermetallics have attracted great interest since the first Materials Research Society symposium 1984 (Liu, 1995). When two or more metallic elements come together to form metal bonds, they are called intermetallic compounds. They demonstrate long range order meaning the regular order of the atom placement patterns are observable for long distances. The intermetallic compounds One of the factors for such interest is the growing demand by the advance heat engines for light weight, corrosion resistant and high temperature strength materials. Ordered intermetallics constitute a unique and an emerging class of metallic materials that form a long range ordered crystal structures below the critical ordering temperature (Liu and Kumar, 1993).

Some intermetallics of interest are the silicides, aluminides, beryllides and the chromides. From amongst these Titanium aluminides have demonstrated attractive properties for operations in hostile environment at elevated temperatures with lower densities. The employment of these can lead to substantial payoffs in the automotive industry, power plant turbines and aircraft engines. It took more than 20 years of very intensive research to obtain maturity level of TiAl-based alloys that is sufficient to consider this class of materials for critical rotating components in commercial jet engines(Lapin, 2009).

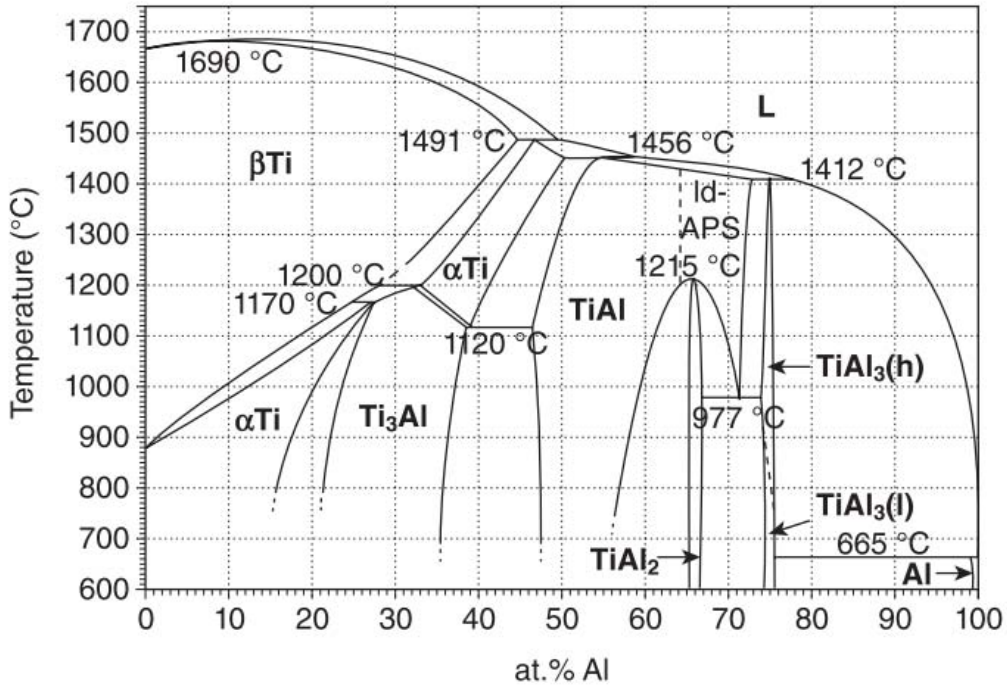

Figure 2-2: Ti-Al phase diagram (Appel et al., 2011)

Although Ti_3Al (α_2), TiAl (γ), Al_2Ti and Al_3Ti are the Ti-Al intermetallic compounds that are found to be stable at room temperature and their thermo-mechanical properties have been investigated for single phase test specimens. The γ -TiAl some other alloying elements and the two phase counterparts have been more intensively studied (Lapin, 2009). That is for couple of reasons. Firstly, their high temperature strength and modulus with low density, tolerable tensile ductility at room temperature, and reasonably good oxidation resistance. Secondly, the manufacturability of TiAl-based alloys is possible through conventional equipment and familiar processes such as casting, forging and machining on almost conventional equipment (Yamaguchi et al., 2000).

Table 2-1: Properties of Titanium Alloys, titanium Aluminides and Superalloys (Kim, 1994)

Property	Ti-Base	Ti_3Al (α_2)-Base	TiAl (γ)-Base	Superalloys
Structure	Hcp/bcc	$D0_{19}$	$L1_0$	FCC/$L1_2$
Density (g/cm3)	4.5	4.1-4.7	3.7-3.9	7.9-8.5
Modulus (GPa)	95-115	110-145	160-180	206
Yield strength (MPa)	380-1,150	700-990	350-600	800-1,200
Tensile Strength (MPa)	480-1,200	800-1,140	44-700	1,250-1,450
Room Temperature Ductility (%)	10-25	2-10	1-4	3-25
High Temperature Ductility (%/°C)	12-50	10-20/660	10-600/870	20-80/870
Room-Temp Fracture Toughness (MPa$\sqrt{m}$)	12-50	13-30	12-35	30-100
Creep Limit (°C)	600	750	750*-950[t]	800-1,090
Oxidation (°C)	600	650	800[t]-950[§]	870[t]-1,090[§]

*Duplex microstructures. [t] Fully-lamellar microstructure. [t] Uncoated. [§]Coated/Actively cooled.

The two phase TiAl alloy allows combining the favorable attributes of the two crystal structures. The γ-TiAl have a lamellar crystal structure exhibiting low ductility and little plasticity but excellent in fracture toughness, creep strength and high temperature fatigue strength. When combined with α2-TiAl the binary phase alloys exhibit good room temperature tensile ductility 1% - 3% (Naka, 1996). The improved ductility results in better machinability. The study of Titanium Aluminides has been focused on finding the right combination and manufacture of Titanium and Aluminum, and alloying additions, to allow for such a microstructure that would combine the advantageous part of phases and improve manufacturability.

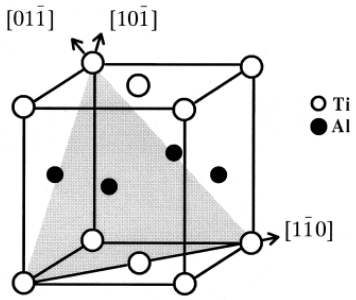

Figure 2-3: Tetragonal γ-TiAl phase (Strukturbericht designation $L1_0$) (Yamaguchi et al., 2000)

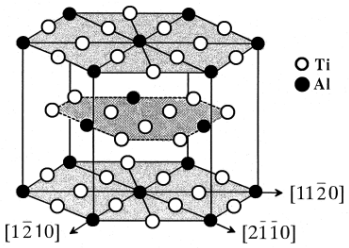

Figure 2-4: Hexagonal Ti_3Al phase (Strukturbericht designation $D0_{19}$) (Yamaguchi et al., 2000)

Depending on chemical composition and heat treatments, TiAl-based alloys with varying composition or heat treatment exist in four different microstructures namely near-gamma, duplex, near lamellar and fully lamellar microstructure.

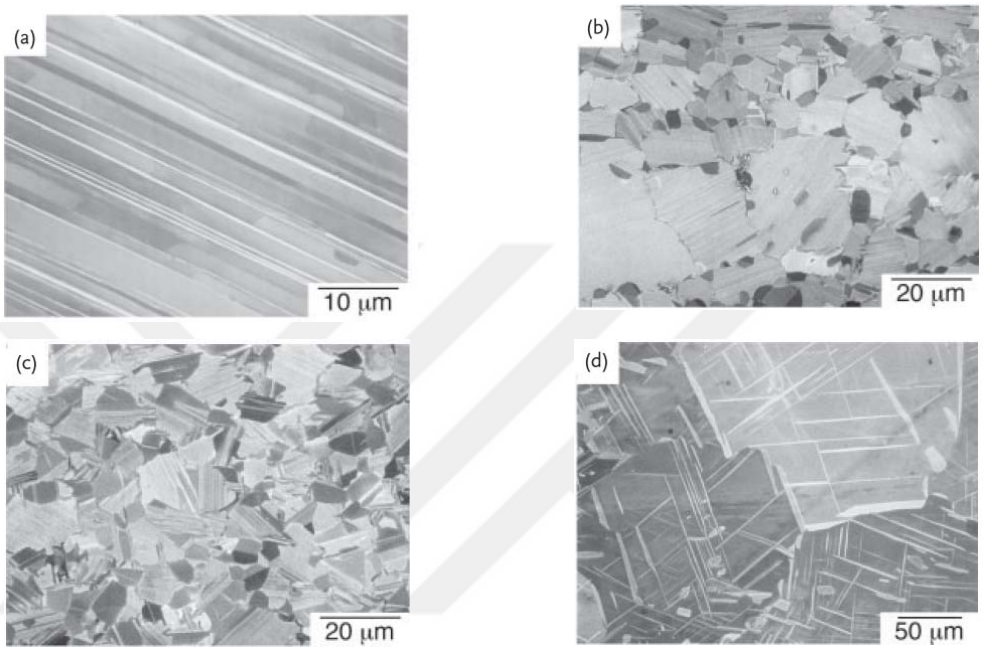

Figure 2-5: Scanning electron micrographs (using backscattered electrons) showing (a) a fully lamellar microstructure, (b) a nearly lamellar microstructure, (c) a duplex microstructure and (d) Widmannstätten γ plates.(Appel et al., 2011)

The fully lamellar or nearly lamellar microstructure consists of the TiAl (γ-phase) and a small volume fraction of Ti_3Al (α_2 -phase). These microstructures exhibit better creep resistance (apart from primary creep), higher fracture toughness and crack propagation resistance. Whereas the duplex microstructures demonstrate higher tensile strength, ductility and longer fatigue life than the former.

The outstanding thermo-physical properties of these alloys mainly result from strongly ordered structure, which involves: high melting point, low density of 3.9-4.2 g/cm^3, high

elastic modulus, low diffusion coefficient, good structural stability, good resistance against oxidation and corrosion and high ignition temperature when compared to conventional titanium alloys.

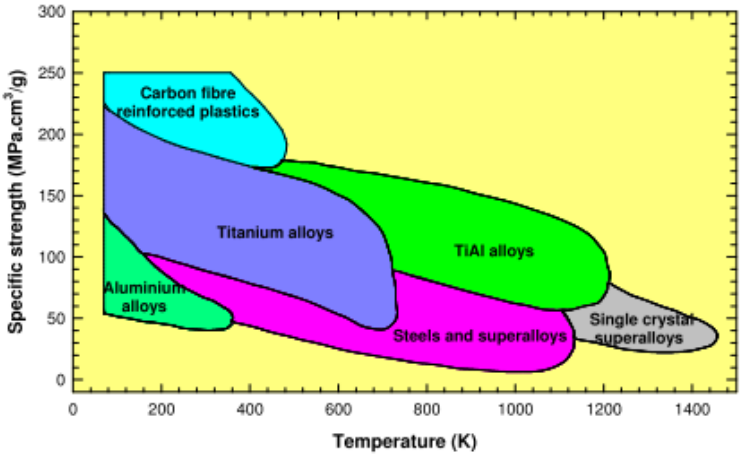

Figure 2-6: Temperature Dependence of specific strength of various groups of alloys (Lapin, 2009)

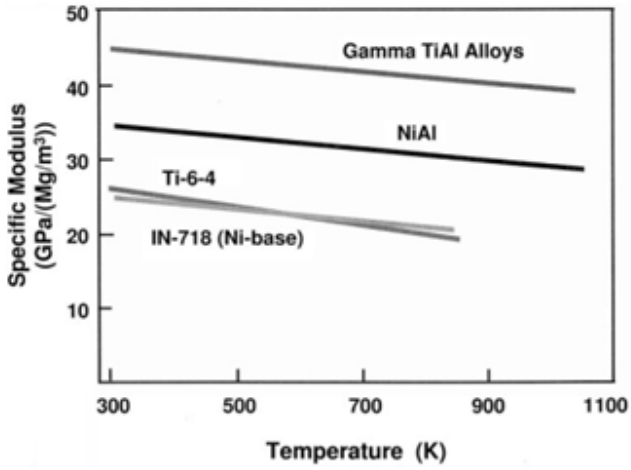

Figure 2-7: Specific modulus versus temperature for structural alloys and selected intermetallic (Dimiduk, 1999)

2.3.2 History

1st generation single phase materials were marred by poor tensile and creep properties later greatly improved with the introduction of fully lamellar 2nd generation Ti-48AI-2Nb-2Cr/Mn and its grain refined variant Ti-45AI-2Mn-2Nb-0.8TiB2XD (45-2-2-0.8) alloys. The 3rd generation alloys such as Ti-46AI-8Nb-1B improved in oxidation resistance. More recently, interest has shifted to thermos-mechanically processed duplex alloys such as Ti-45AI-8Nb-0.2C, having a tensile strength above 900MPa, where the presence of carbon or silicon has a beneficial effect on creep and high temperature performance, allowing operation up to 800°C, compared with around 600°C - 650°C with the earlier alloys(Aspinwall et al., 2005).

The mechanical properties at elevated temperature and low density of TiAl are not as good as for ceramics or Nickle based superalloys, added to that the toughness, cost and current manufacturability of it is inferior to other high-temperature steels and Ni superalloys. Difficulty in manufacture of large size components leaves reduction in inertia the only advantage warranting change of material for current high temperature applications.

The Reduction of mass for components that oscillate or rotate directly impact power output and efficiency for reciprocating internal combustion engines and turbine engines whether used for aircrafts or power generation. Therefore, turbine blades, blisks, valves, connecting rods, etc. have been the first candidates for application investigation.

2.3.2.1 Turbo Chargers:

The most successful application has been to automotive turbochargers. Starting with a manufacture and installation of 1000 turbo chargers in Japan for Lancer cars in 1998 (Wu, 2006) the manufacture and employment of TiAl turbochargers has expanded to included many automotive manufacturers specially in the high performance enthusiast and automotive sports market i.e. formula one.

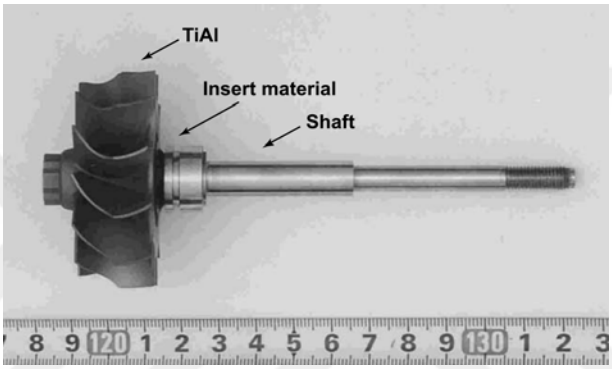

Figure 2-8: External appearance of TiAl turbine joined to shaft (Tetsui, 2002)

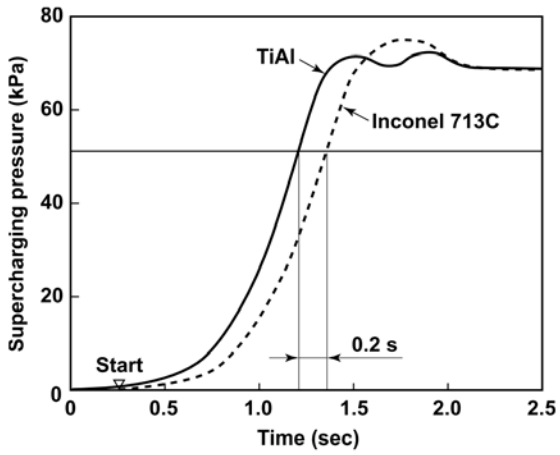

Figure 2-9: Comparison of response ability of a TiAl turbocharger and an Inconel 713C turbocharger (Tetsui, 2002)

2.3.2.2 Jet Engine

The development of gamma alloy technology has matured in the last two decades significantly such that γ-TiAl alloys have now been introduced for turbine blades in General Electric's GENx engine (Thomas, 2011). Within the all jet engine manufacturing industry programs exist for incorporation of the gamma titanium aluminide into the engine components. Some of them were reported technically as success with some requiring further adjustment to reach full maturity. To mention a few, a successful bench test for low pressure turbine blades for the CF6 engine was conducted by GE aircraft engines. Hot compressor blades and shrouds have investigated at the Rolls-Royce, Allison, General Electric and Pratt & Whitney. Pratt & Whitney has developed intermetallic compound blade retainers. Although the MTU is the business of manufacturing heavy diesel engines, nevertheless, they have been reported to have tested low pressure turbine blades as well. Volvo tested turbine dampers made from titanium aluminide.

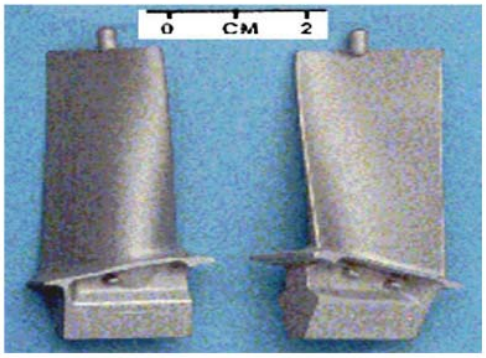

Figure 2-10:Small cast turbine blades used in the Turbomeca helicopter engines (Lasalmonie, 2006).

Figure 2-11: Cast Turbine vane for the Low pressure turbine sector of a civil engine (Lasalmonie, 2006).

Figure 2-12: High pressure compressor casing – produced by the powder metallurgy ISOPREC® process for a military engine (Lasalmonie, 2006).

2.3.2.3 Exhaust valves:

Heat resistant steels (superalloy 21-2N) are commonly used for IC engine valves where they are operating at temperatures closer to 700°C. The weight reduction brought by the intermetallic alloy valves shown in the Figure 2-13 and Figure 2-14, give a significant advantage as shown in Figure 2-15. The reduced weight of gamma TiAl, observed in the properties Table 2-2, valves contribute toward improved fuel economy and noise reduction. General Motors, Volvo, Ford Motor company and Nissan motor Company have all reported successful engine tests of gamma TiAl components (Keller et al., 1997).

Table 2-2: The comparison of properties for gamma TiAl and 21-2N (Chandley et al., 2000).

Property	γ −TiAl	Superalloy 21-2N
Density (gm/cm^3)	3.9	7.7
Tensile Strength (MPa) Room Temperature 760°C	 560 600	 1090 400
Thermal Conductivity (W/m-K)	28	25
Fatigue Strength, 10^8 cycles, smooth 440°C MPa 816°C MPa	 326 220	 -- 165
Hardness, BHN Room Temperature 760°C	 260 240	 300 140
Modulus (GPa)	170	200
Coefficient of thermal expansion (μm/m)	12.2	18.4

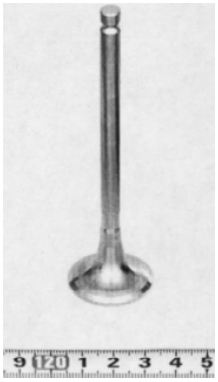

Figure 2-13: External appearance of an exhaust valve made of TiAl (Tetsui, 1999).

Figure 2-14: TRW car valves centrifugally cast at the Institute of Metal Research, China and surface engineered (courtesy K Gebauer) (Wu, 2006).

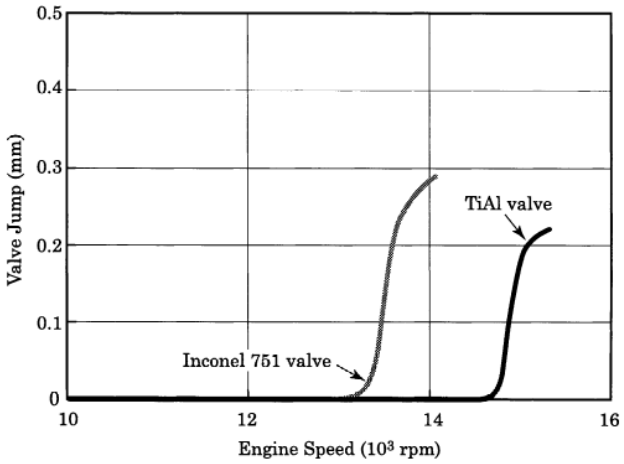

Figure 2-15: Relationship of valve jump and engine speed in a high performance sports car engine using Inconel 751 and TiAl valves (Tetsui, 1999).

(Maki et al., 1996) demonstrated as shown in Figure 2-15 that for an additional increment of over 1000 engine revs/min is achieved for equivalent of valve jump is for the gamma TiAl compound valves.

2.3.3 Machining of Titanium Aluminides:

A lot of effort has gone into developing the material Titanium Aluminides. The published research covers their thermo-mechanical properties, microstructure, alloying, manufacturing processes, etc. since 1984. However, literature for the last stage manufacturing of TiAl parts, namely machining is wanting.

After ingot processing the manufacture of parts with complex geometry are cast or forged to near net shape and finally machined to precise dimensions as is done with conventional heat resistant alloys. To have reliable engineering parts the various machining processes besides the other processing stages i.e. milling, drilling, tapping, etc. require to be well understood. This would require final part to be without detrimental effects after processing.

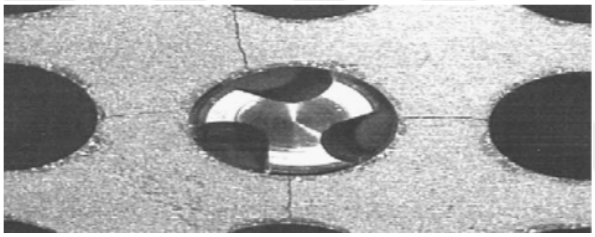

Figure 2-16: Cracks around holes in TiAl (Lasalmonie, 2006)

Titanium alloys are in general considered to be difficult-to-machine materials. Their elevated temperature strength, low conductivity and chemical reactivity have made them such. In addition to these difficulties the gamma TiAl are brittle and the machining of them have been reported to suffer from surface cracking or so called fracture/pullout, as shown in the Figure 2-17 and Figure 2-18, micro-hardness (Priarone et al., 2012) and residual stresses (Aspinwall et al., 2013) in machined surfaces besides the tool wear issues. The change in microhardness from surface to depth is shown in the Figure 2-19. Moreover, The fracture of work piece during clamping or machining have been reported as well as shown in Figure 2-16 (Aust and Niemann, 1999).

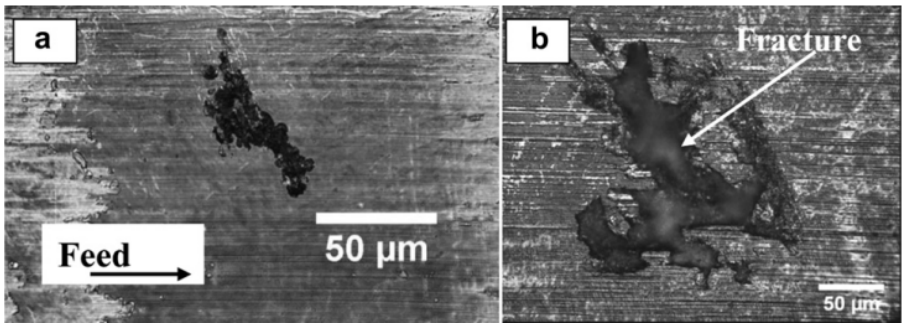

Figure 2-17: Images of machines surfaces with fracture/pullout (Hood et al., 2013a)

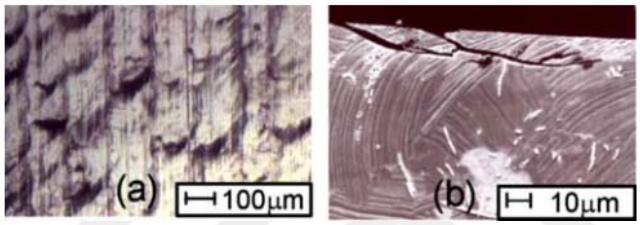

Figure 2-18: Workpiece (a) surface; and (b) subsurface crack (Aspinwall et al., 2005)

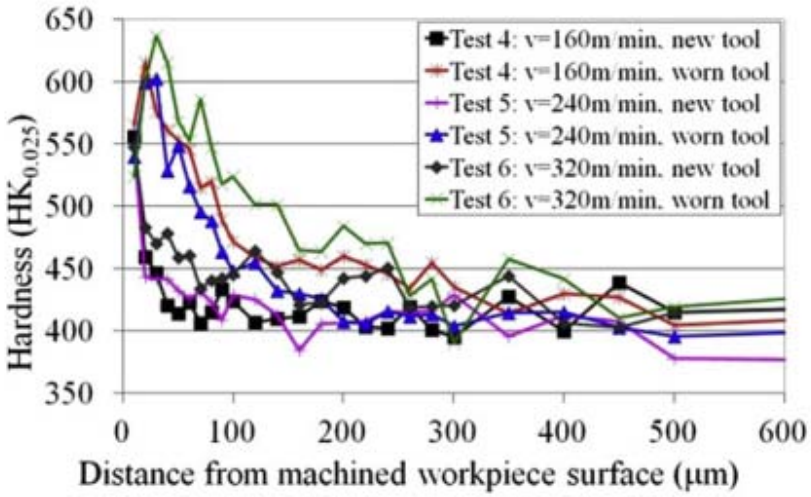

Figure 2-19: Microhardness depth profiles, Tests 1-3, Ti-45Al-8Nb-0.2C, Tests 4-6, Ti-45Al-2Mn-2Nb+0.8%vol. TiB_2 (Hood et al., 2013a)

2.3.4 Tool wear

Typical tool wear mechanism involves, flank wear, chipping and workpiece material adhesion. The family of titanium aluminide compounds investigated exists within a very narrow band of chemical composition variation. In terms of the weight percentage of aluminum content, it is 43% Al to 48% Al. The tool life ranges from less than 2 minutes to little above 30 minutes.

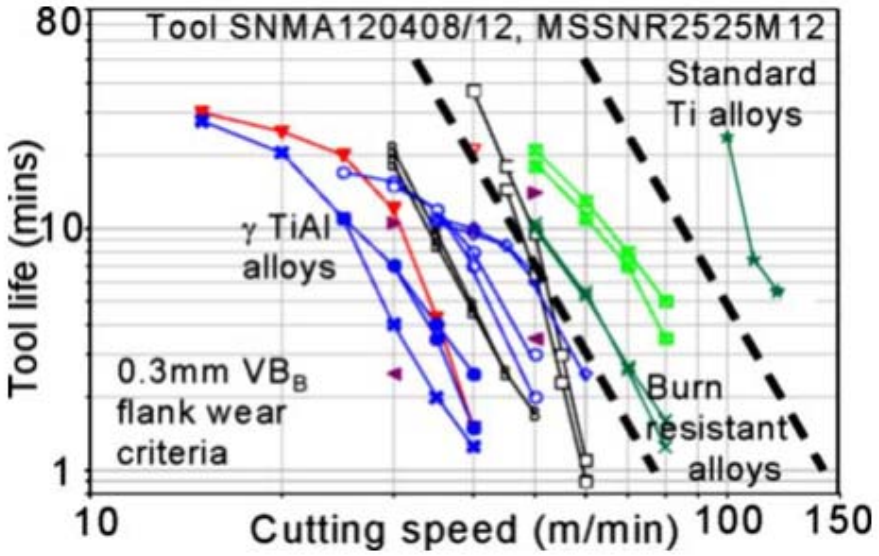

Figure 2-20: The comparison WC tools when machining Ti6Al4V and the gamma titanium aluminide for varying speeds (Hood et al., 2013b).

Besides the attempts at improving machinability of TiAl compounds through microstructure refinement, the manufacturing research community investigated the following for machining TiAl alloys.

1. Cutting Strategies are investigated for their viability with respect to the tool life and workpiece integrity.
    a. Although the tool life increases with reduction in cutting speeds and cut volume (Settineri et al., 2014) but it is counter intuitive from the

productivity stand point. Milling TiAl requires 2 to 3 times lower cutting speeds that can be used for Ti-based and Nickle based alloys (Aust and Niemann, 1999).

b. High speed machining; to benefit from ductile mode machining, where the cutting speeds are such that the localized temperature rise will produce thermal softening. Higher cutting speeds of around 300 m/min in high speed milling have been suggested and tested to produce crack free surfaces (Hood et al., 2013a).

2. Different combinations of tool material, surface coatings and coating techniques have been explored for the desired outcome.

a. (Hood et al., 2013a) used AlTiN PVD coated tungsten carbide tools WC for machining the gamma titanium aluminide parts in dry machining and with negative tooling geometry.

b. (Settineri et al., 2014) used 10 mm uncoated K10 grade carbide end-mills. The specification of the used end-mills is given in the

Table 2-3: The tested end-mill geometry as reported by this paper.

Mill diameter	10	mm
Length of cut	23	mm
Cutting tool angle	12	deg
Helix angle	30	deg
Axial primary relief angle	6	deg
Axial secondary clearance angle	16	deg
End cutting edge concavity angle	2	deg
Radial rake angle	12	deg

c. (Weinert et al., 2007) reported performance of a wide array of tool materials. Cubic Boron Nitride, polycrystalline diamond, and ceramics. This study reported to have achieved better wear results with the diamond based tools like PCD or CVD are used in turning operations.

d. (Tetsui et al., 2005) used K10 grade carbide turning inserts for the machining tests at 10 – 40 m/min cutting speeds and found that the machining is possible for gamma titanium aluminide compounds if cutting conditions similar to what are used for machining the nickel alloys.

e. (Aust and Niemann, 1999) reported an optimum cutting speed of 12-18 m/min for K10 and K20 grade carbides.

f. (Aspinwall et al., 2013) used TiAlN PVD coated solid carbide 8mm end-mills for three cutting speeds; 160 m/min, 250 m/min and 340 m/min. they reported surface defects for all test cases, where the higher cutting speeds higher magnitudes of damage. They suggested for acceptable workpiece integrity lower cutting speeds should be employed.

Chapter 3
Machining of Inconel 718

3.1 Tool Design

The nickel alloys are materials designed materials for the harshest operational environments in terms of temperature, stress and fatigue. Nickel alloys not only possess high mechanical properties at room temperature but maintain them for elevated temperatures as well, observed in Figure 3-1, besides demonstrating strong strain hardening. Such properties made them most suitable for the components in the high temperature compressor and turbine parts of jet engines. The properties that made them attractive render them the toughest materials to machine. The investigation and discovery for new machining strategies, tool materials, coatings and tool geometries is an ongoing effort.

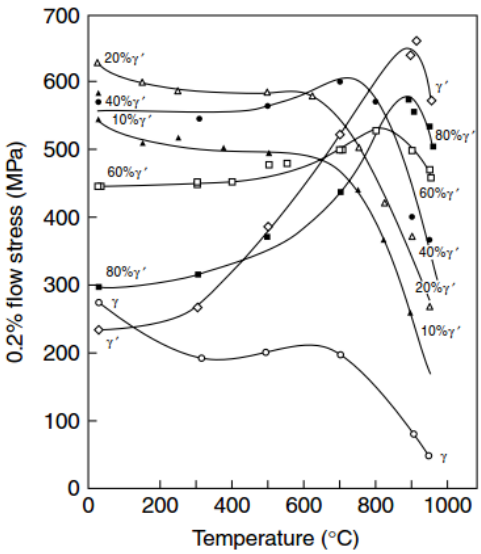

Figure 3-1: The variation of yield stress with temperature for the Ni-Cr-Al alloy (Reed, 2008).

The nickel alloys demonstrate a varied ductility behavior with the increase in temperature as shown in Figure 3-2 (Shapiro and Dieter, 1970). Three zones are distinguishable from the figure, a) a moderate ductility zone for temperatures between 400°C and 650°C, b) minimum ductility zone for temperatures between 700°C and 850°C and then c) a high ductility zone for temperatures above 900°C.

The availability of high speed machining allowed to produce sufficiently high cutting speeds to produce localized elevated temperatures and the material is cut when the it is in the very high ductility zone of the temperature stress curve given in Figure 3-2 for the nickel alloys. This strategy is also called the ductile mode machining.

The machining of nickel alloys at elevated temperatures is evident. Nevertheless, the question arises that what cutting tool materials can withstand such harsh cutting conditions. The ceramics have been employed for many different extreme temperature applications, and befittingly have been investigated for ductile mode machining of many different materials. The ceramic tools, where they have received appreciation for improved material removal rates are also vilified considered to be poor in absorbing mechanical and thermal shocks (Richards and Aspinwall, 1989). The ceramic materials are well known refractory material for their superior hot hardness, a necessity for cutting tool material when the challenge is to maintain the sharpness of the cutting edge at elevated temperatures.

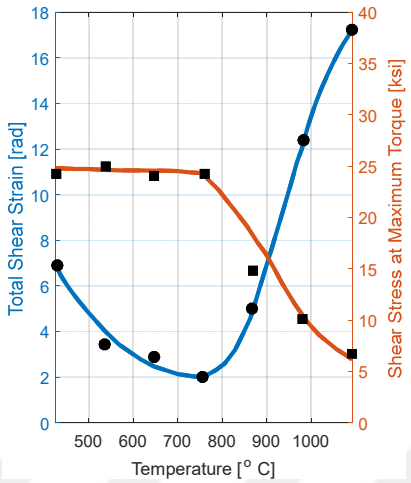

Figure 3-2: Total shear strain at separation, γ_s, and the shear stress at maximum torque, τ_s.

The drawback of the ceramic materials use in machining operations is the fact that they are brittle in nature, whereas the machining operations, specially milling, is an interrupted process in nature. The cutting forces fluctuate in a cyclic manner, which is consider the primary reason for the tool wear. The mode of wear for ceramic tools is mainly notching by the attrition wear mechanism.

Now if sufficient high cutting speed is employed to soften up the workpiece material, especially for nickel base alloys where the chips are 1000°C or above, and the fluctuations of the cutting forces is reduced, the viability of ceramic tools for machining nickel based alloys will improve.

The very high temperatures and extreme speeds and loads make it very difficult to establish accurate and reliable temperature and deformation data for high-speed machining of nickel based alloys. Most of studies either depend on inverse techniques or finite element

modeling to indirectly estimate the temperature distribution and corresponding constitutive law.

3.1.1 Constitutive model

Number of models have been introduced to establish the constitutive law for select materials. The most famous is the Johnson-Cook flow stress model. The parameters required by the Johnson-Cook (JC) model are traditionally established using the split Hopkins pressure bar test (SHPB) (Shapiro and Dieter, 1970) or uniaxial compression (Hastings et al., 1974) or shear tests with controlled environment elevated temperatures for varying strain rates. Although these tests are employed for commonly used materials, the testing conditions, namely, the effective strain, effective strain rate and temperatures are much less than what are encountered in a typical machining process. In a typical SHPB test the strain rates could be up to 10^4 s^{-1}, whereas the machining process could produce strain rates in excess of 10^6 s^{-1}. As a result, the application of such data to machining processes require large extrapolations.

The mechanical properties reported by some of the researchers using material testing apparatus are produced in Table 3-1.

Table 3-1: Research reporting Inconel 718 constitutive law.

	Test	Temperature	Strain Rate
(Yuan and Liu, 2005)	Uniaxial quasi static compression test	900°C – 1080°C	10^{-3} – 10^{o} s^{-1}
(Si et al., 2015)	Hot compression test	900°C – 1060°C	10^{-3} – 0.5 s^{-1}
(Wang et al., 2008)	Hot compression test	950°C – 1100°C	10^{-3} – 10^{o} s^{-1}
(Soo et al., 2004)	Hot compression test	20°C – 850°C	10^{o} – 10^{2} s^{-1}
(Wang et al., 2013)	SHPB	500°C – 800°C	10^{3} – 10^{4} s^{-1}
(Lee et al., 2011)	SHPB	-150°C – 550°C	10^{3} – 5 x10^{3} s^{-1}

Table 3-2: The comparison of the strain and strain-rates for material tests and machining (Iturbe et al., 2017).

	SHPB	Machining
$\bar{\varepsilon}$	<1	1 – 7
$\dot{\bar{\varepsilon}}$	< 10^{4} s^{-1}	0 – 10^{6} s^{-1}
$\dot{Q}$		10^{6} s^{-1}

Some researchers used the machining data to deduce the required parameters, the pioneer being Oxley (Hastings et al., 1974; Stevenson and Oxley, 1970, 1969) (Lin, 1978), then from recent year (Stevenson and Stephenson, 1995), (Li and Wang, 2013), (Vogtel et al., 2014) and (Lei et al., 1999) are selected for mention. (Serge Jaspers, 1999), (Pawade et al., 2009)

and (Lorentzon et al., 2009) reported parameters required for the material constitutive law for Inconel 718.

The Johnson-Cook model is essentially an empirical formulation for the flow stress, where the effects from the magnitudes of strain, strain rate and temperature are decoupled, namely strain hardening, strain rate hardening and thermal softening respectively. The first term provides the adjustment for the strain hardening. The second term provides the correction for the strain rate and finally the third term accounts for the thermal softening of the material for rise in temperature. The traditional model given by equation 1 does not allow for including the effects of temperature on the individual terms.

$$\sigma_{JC} = (A + B\epsilon^{n})\left[1 + C\ln\left(\frac{\dot{\epsilon}}{\dot{\epsilon}_0}\right)\right]\left[1 - \left(\frac{T - T_0}{T_m - T_0}\right)^{m}\right] \quad (1)$$

Some researcher have introduced modified models to account for the influence of the elevated temperatures. (Iturbe et al., 2017) combined reported modification in research literature for different components of the JC model. They found the correctional model proposed by (Lurdos et al., 2008) to capture the strain hardening-softening behavior of Inconel 718 closely. The model was built on five parameters; the saturation stress σ_s, The yield stress σ_0 and an index r to account for the softening after the peak stress value.

$$\sigma_\varepsilon = \sigma_s + (\sigma_0 - \sigma_s + A\varepsilon^{n})e^{(-r\varepsilon)} \quad (2)$$

Table 3-3: The coefficients to account for the strain hardening used for the modified Johnson-Cook Model.

	σ_0	σ_s	A	n	r
Terms for σ_ε	1388	1565	1600	0.6767	3

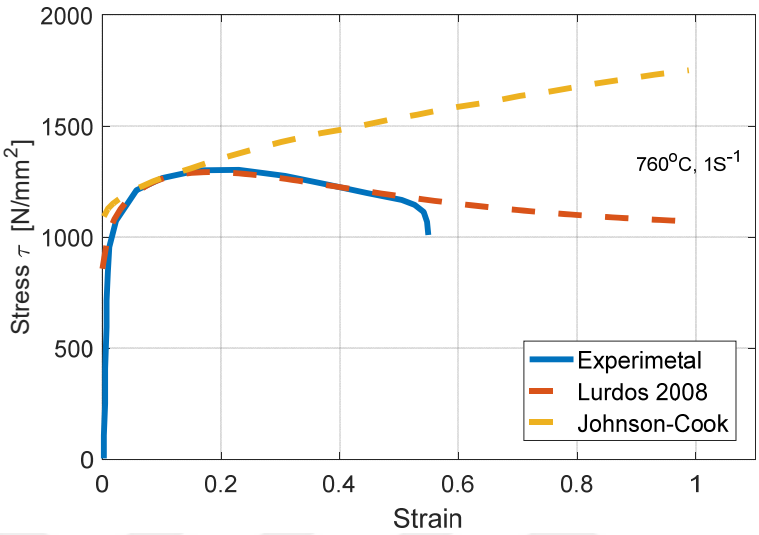

Figure 3-3: Modified model for strain hardening that captures softening after the peak stress values. (Iturbe et al., 2017)

The second term in the Johnson-Cook model accounts for the strain-rate hardening. The conventional coefficient was changed with a modified temperature dependent function given by equation 3, which is capable of capturing the thermal softening for elevated temperatures.

$$\sigma_{\dot{\varepsilon}}(\dot{\varepsilon}, T) = 1 + \left(C + De^{-\frac{T}{x}}\right) \ln\left(\frac{\dot{\varepsilon}}{\dot{\varepsilon}_0}\right) \tag{3}$$

	C	D	x
Terms for $\sigma_{\dot{\varepsilon}}$	0.003	0.00285	232

And the final term in the Johnson-Cook model provides the correction for the thermal softening. the conventional model has an index value independent of temperature. The improved model introduced temperature dependent thermal softening index given by equation 4.

$$\sigma_T = \frac{1}{1 + e^{-m(T-B)}} \tag{4}$$

Table 3-4: The index constants for the thermal softening term.

	m	B
Terms for $\sigma_{\dot{\varepsilon}}$	0.00663	832.27

The final form of the modified Johnson-Cook model is then given by equation 5.

$$\sigma_{JC_m} = \left(\sigma_s + (\sigma_0 - \sigma_s + A\varepsilon^n)e^{(-r\varepsilon)}\right) \cdot \left(1 + \left(C + De^{-\frac{T}{x}}\right)\ln\left(\frac{\dot{\varepsilon}}{\dot{\varepsilon}_0}\right)\right) \cdot \left(\frac{1}{1 + e^{-m(T-B)}}\right) \quad (5)$$

Several Johnson-Cook models, modified and original were used to simulate for flow stress magnitudes. The parameters are reproduced in table

Table 3-5: The Inconel 718 constitutive law parameters reported in research literature.

		A	B	C	n	m	D
1	(S Jaspers, 1999)	1029	1477	0	0.326	1.9	
2	(Lorentzon et al., 2009)	1241	622	0.0134	0.652	1.3	
3	(Klocke et al., 2013)	1485	904	0.015	0.777	1.689	
4	(E. Uhlmann et al., 2007)	450	1700	0.017	0.65	1.3	0.8
5	(Wang et al., 2013)	963	937	C (T)	0.33	1.3	
6	(Iturbe et al., 2017)	$\sigma(\varepsilon)$		C (T)		m (T)	
7	(Li and Wang, 2013)	980	1370	0.02	0.164	1.03	

3.1.2 Machining Parameters for Johnson-Cook Model

The Johnson-Cook model requires the strain, strain rate and temperature as input. The machining cutting condition are used to derive the constitutive model inputs.

3.1.2.1 Strain

The shear strain for oblique cutting operation is given by the equation 6.

$$\gamma = \frac{\cos \alpha_n}{\sin \phi_n \cos(\phi_n - \alpha_n) \cos \eta} \tag{6}$$

Where α_n is the normal rake angle also called the effective rake angle, η is the chip flow angle and ϕ_n is the normal shear angle. Stabler's rule is employed for the chip flow angle η and the normal shear angle is approximated to be equivalent to the average shear angle obtained from an orthogonal machining test. (Pawade and Joshi, 2011) reported the chip ratio for turning Inconel 718 for different cutting speeds using PCBN inserts. The plot is reproduced here in Figure 3-4.

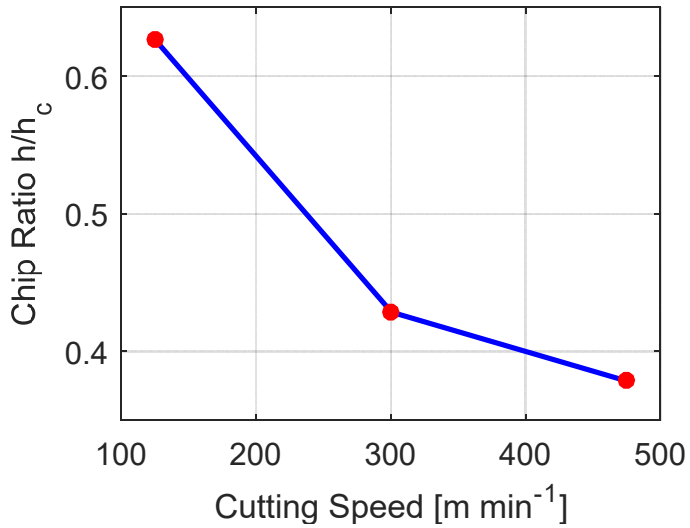

Figure 3-4: The chip ratio for increasing cutting speeds (Pawade and Joshi, 2011).

In the absence of direct and reliable experimental information for high-performance machining with SiAlON ceramics tools, it is found using the fundamental principles of mechanics. The shear angle is found using the minimum energy principle as is reported in the works of (Rowe and Spick, 1967).

$$\beta \sin^2 \phi = \frac{1}{\chi} \cos \alpha_r \cos(2\phi - \alpha) \quad (1)$$

Where β is a coefficient to the shear stress along the rake face, and describes the sticking or sliding of the chip along the rake face. And, χ is the multiple to the projected length of the uncut chip thickness on the tool rake face approximating the chip contact length along the tool rake face. The equation 1 is solved numerically for the scanning electron microscopy measured chip contact length along the rake face of the end-mill.

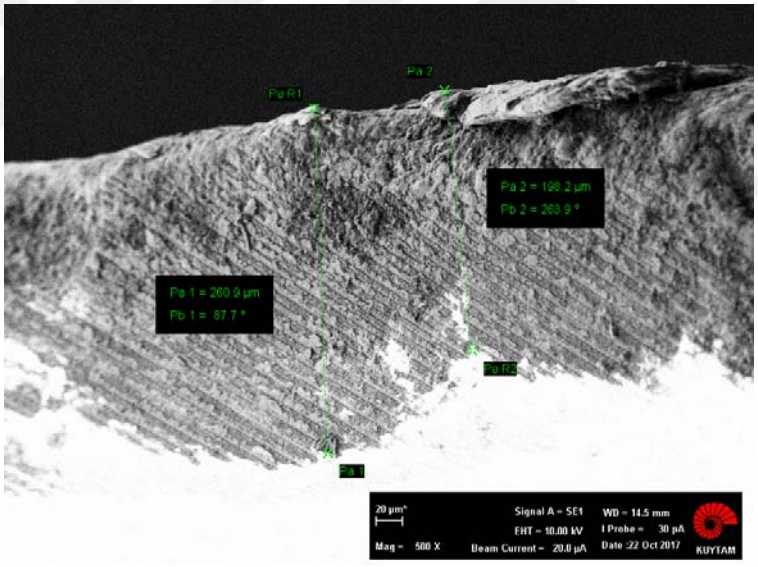

Figure 3-5: SEM image for SiAlON ceramic end-mill after machining Inconel 718.

Recognizing the fact that the SiAlONs are pure conductors of electricity and were found to be suffering from the charging phenomenon in SEM, the chip contact length was estimating from the region not showing the charging effect, on the assumption that the other

region has significant Inconel adhering to it. Considering the chip flow angle equal to the obliquity angle, the shear angle is found using the expression given in equation 7

$$\phi_c = \frac{r_c \sin \alpha_n}{1 - r_c \cos \alpha_n} \tag{7}$$

If α_r is the nominal rake angle and i is the obliquity angle then the normal rake angle is found using equation 8.

$$\tan \alpha_n = \frac{\tan \alpha_r}{\cos i} \tag{8}$$

The uniaxial flow stress is related to the plane strain shear flow stress through the following relationship

$$\sigma = \sqrt{3}\tau \tag{7}$$

Correspondingly the axial strain is related to the shear strain

$$\varepsilon = \frac{\gamma}{\sqrt{3}} = \frac{\cos \alpha_n}{\sqrt{3} \sin \phi_n \cos(\phi_n - \alpha_n) \cos \eta} \tag{8}$$

Also the strain rate in terms of shear strain rate is

$$\dot{\varepsilon} = \frac{\dot{\gamma}}{\sqrt{3}} \tag{9}$$

3.1.2.2 Shear Strain Rate

The shear rate in machining is calculated using the expression given in equation 8.

$$\dot{\gamma} = \frac{V_s}{\Delta d} \tag{10}$$

V_s is the velocity of the sheared material parallel to the shear plane and Δd is the thickness of the shear deformation zone and is approximated as 15% to 20% of the shear plane length l_t (Altintas, 2012).

$$l_t = \frac{h}{\sin \phi_c} \tag{11}$$

Then the shear deformation zone thickness Δd is approximated to be

$$\Delta d = 0.175 l_t \tag{12}$$

The shear plane velocity for an oblique cutting operation is given by the expression

$$V_s = \frac{V \sin i \cos \alpha_n}{\sin \phi_i \cos \alpha_n + \cos \phi_i \times \sin \phi_n \times \tan \eta} \tag{13}$$

The axial strain $\dot{\varepsilon}$ as mentioned in equation 9

$$\dot{\varepsilon} = \frac{\dot{\gamma}}{\sqrt{3}} = \frac{V_s}{\sqrt{3}\Delta d} \tag{14}$$

3.1.2.3 Shear Stress

The flow stress is calculated using the original and modified Johnson-Cook constitutive law given in section 3.1.1 for a wide range of temperature and is shown in the Figure 3-6.

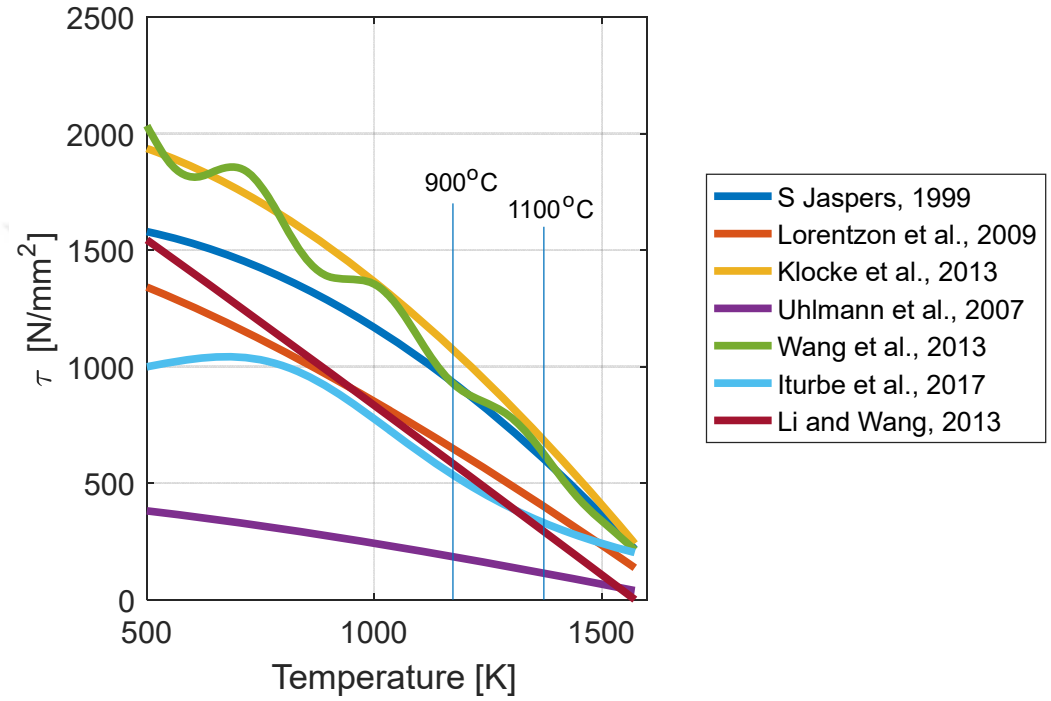

Figure 3-6: Comparison of the Johnson-Cook model parameters.

3.1.2.4 Temperature Estimation:

The next step to estimate the flow stress for the select machining condition is to establish the shear zone temperature. If F_s is the shear force parallel to the shear plane and the V_s is the velocity of the sheared material then the shear power per unit area expend in the shear zone is given by equation 6.

$$P_s = \frac{F_s(T) \times V_s}{db \times h_{ave} \times V} \tag{15}$$

Where h_{ave} is the average chip thickness, db is the width of cut and V is the cutting velocity. The shear force F_s for an oblique cutting process is calculated using the relationship in equation 16.

$$F_s = \frac{\tau(T) \times db \times h_{ave}}{\cos i \times \sin \phi_a} \tag{16}$$

Assuming that all of the shear power contributes to the heat generation and the process to be adiabatic then the temperature for the shear zone is given by

$$T = T_0 + \frac{P_s(T)}{\rho(T) C(T)} \tag{17}$$

The Inconel thermal properties are temperature dependent and are given by the plots in Figure 3-7, Figure 3-8 and Figure 3-9. Other mechanical Properties are given in the Table 3-6.

Table 3-6: Mechanical Properties of Inconel 718 (Kitagawa et al., 1997).

Youngs's Modulus	206	GPa
Tensile strength	1.73	GPa
Melting Temperature	1300	$°C$

The temperature dependent density $\rho[kg \cdot m^{-3}]$, constant pressure specific heat $C_p[J \cdot kg^{-1} \cdot K^{-1}]$ and thermal conductivity $k[W \cdot m^{-1} \cdot K^{-1}]$ of the nickel alloy Inconel 718 is given by the equations 18, 19 and 20. The units of temperature is Kelvin, K and the empirical relation are interpolated from the reported works of (Pottlacher et al., 2002), (Quested et al., 2009) and (Rice et al., 2003). The experimental data plots for the density, specific heat and the thermal conductivity are reproduced in the Figure 3-7, Figure 3-8and Figure 3-9.

$$\rho(T) = 8289 - 0.055T - 7.19 \times 10^{-4}T^2 + 7.97 \times 10^{-7}T^3 - 3.478 \times 10^{-10}T^4 \quad (18)$$

$$C_P = 361.34 + 0.24T^1 + 7.56 \times 10^{-6}T^2 \quad (19)$$

$$k = 3.45 + 0.027T^1 - 1.12 \times 10^{-5}T^2 + 3.61 \times 10^{-9}T^3 + 8.24 \times 10^{-14}T^4 \quad (20)$$

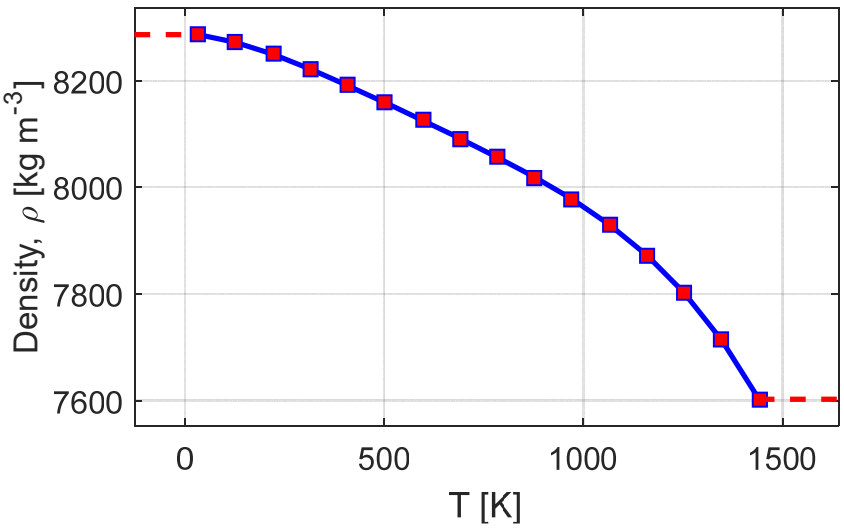

Figure 3-7: The density of Inconel 718 as a function of temperature

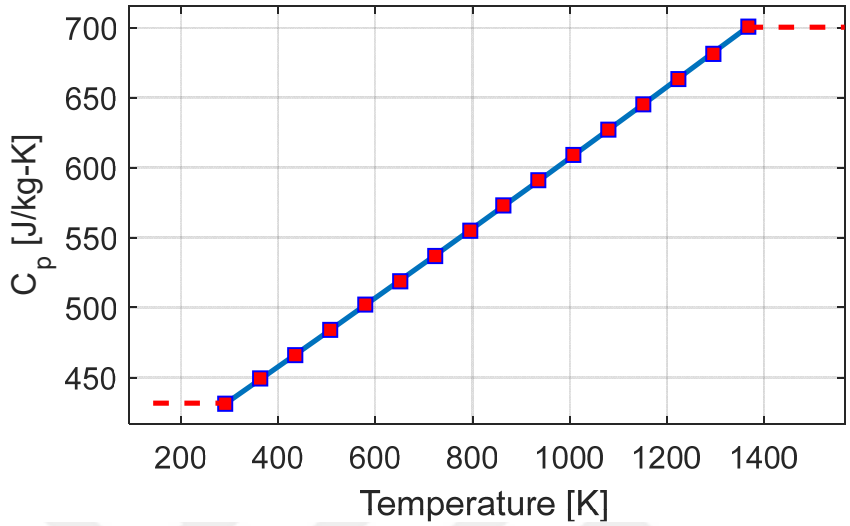

Figure 3-8: The heat capacity for Inconel 718 at constant pressure as a function of temperature.

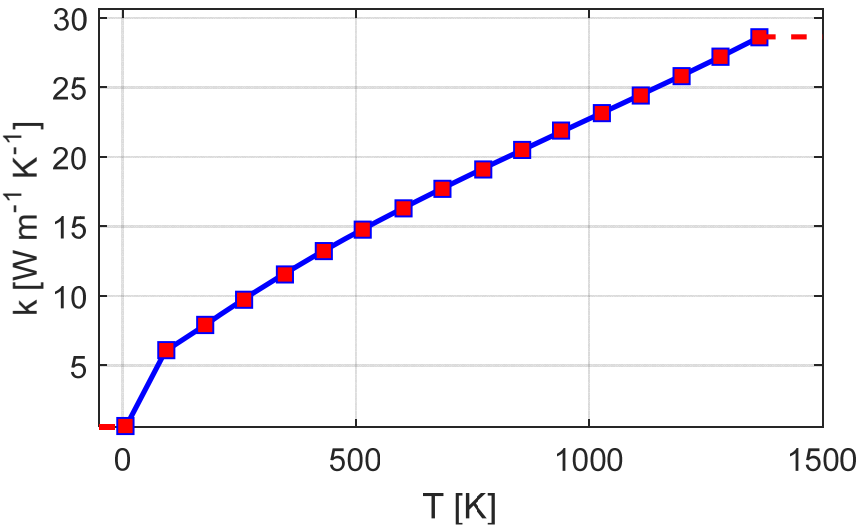

Figure 3-9: The temperature dependent thermal conductivity for Inconel 718.

The shear power responsible for the heat generation in the shear zone depend on parameters that are a function of local temperature. The shear zone temperature and corresponding flow stress then are calculated iteratively as shown in Figure 3-10 until the error is negligible.

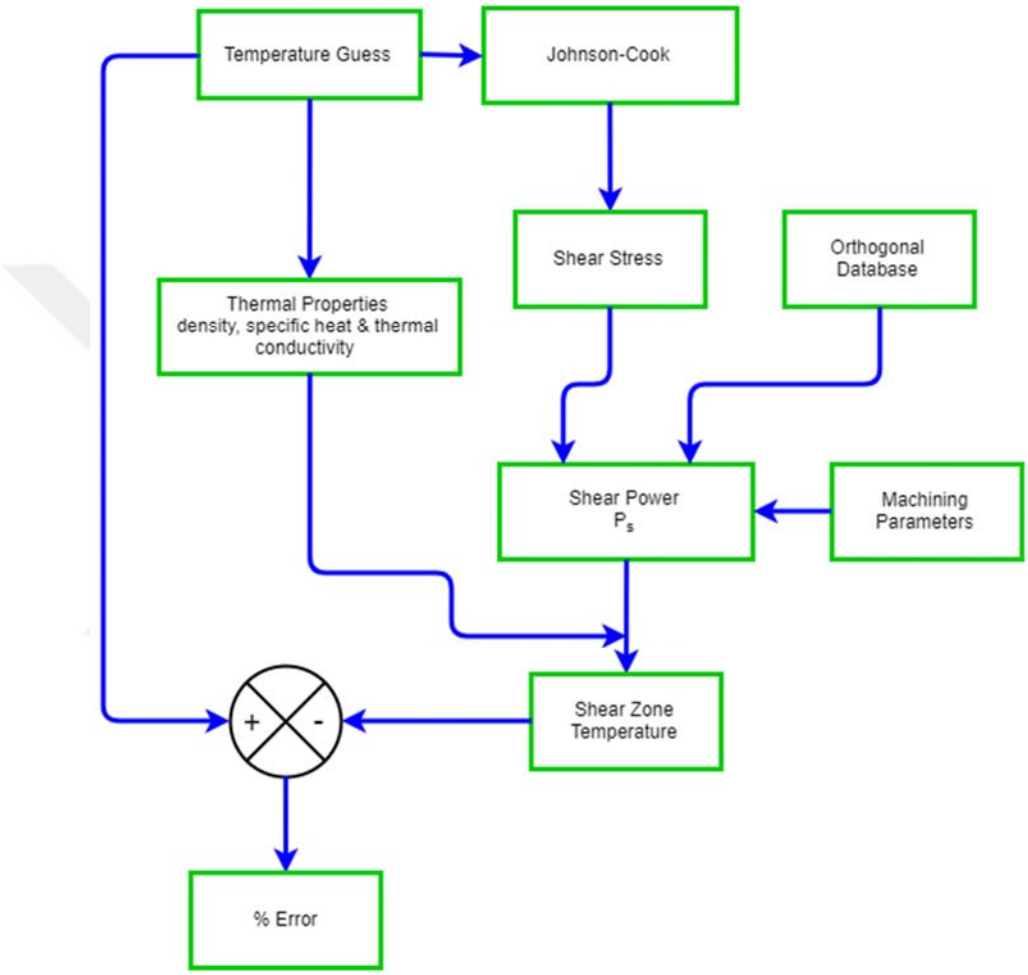

Figure 3-10: The iterative process to establish the shear zone temperature.

The parameters calculated for the shear zone when milling Inconel 718 are given in Table 3-7.

Table 3-7: Thermal properties of Inconel 718 for the given cutting conditions.

Thermal Conductivity, k	19.93	$W\ m^{-1}K^{-1}$
Heat Capacity, C_p	561.5	$J\ kg^{-1}K^{-1}$
Density, ρ	8042	$kg\ m^{-3}$
Flow stress τ	497	MPa
Shear Zone temperature	1215	K
Error	0.03%	
(S Jaspers, 1999)	868	MPa
(Lorentzon et al., 2009)	597	MPa
(Klocke et al., 2013)	995	MPa
(E. Uhlmann et al., 2007)	170	MPa
(Wang et al., 2013)	872	MPa
(Iturbe et al., 2017)	484	MPa
(Li and Wang, 2013)	522	MPa

There appears to be two distinct regions where the different models are converging for the select range of temperature.

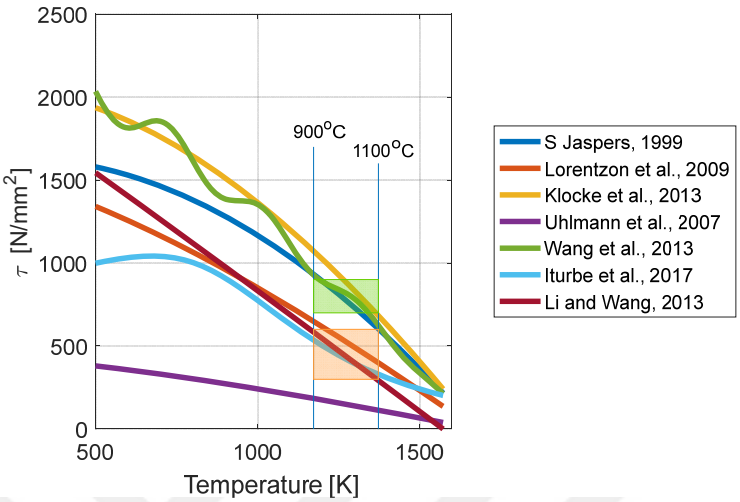

Figure 3-11: The converging regions for the flow stress from the different Johnson-Cook model parameters.

3.1.2.5 Cutting forces simulation

The cutting forces for the Inconel 718 workpiece were simulated following the steps given in the flow chart in the Figure 3-12 using the Armarego relationships for the orthogonal to oblique transformation.

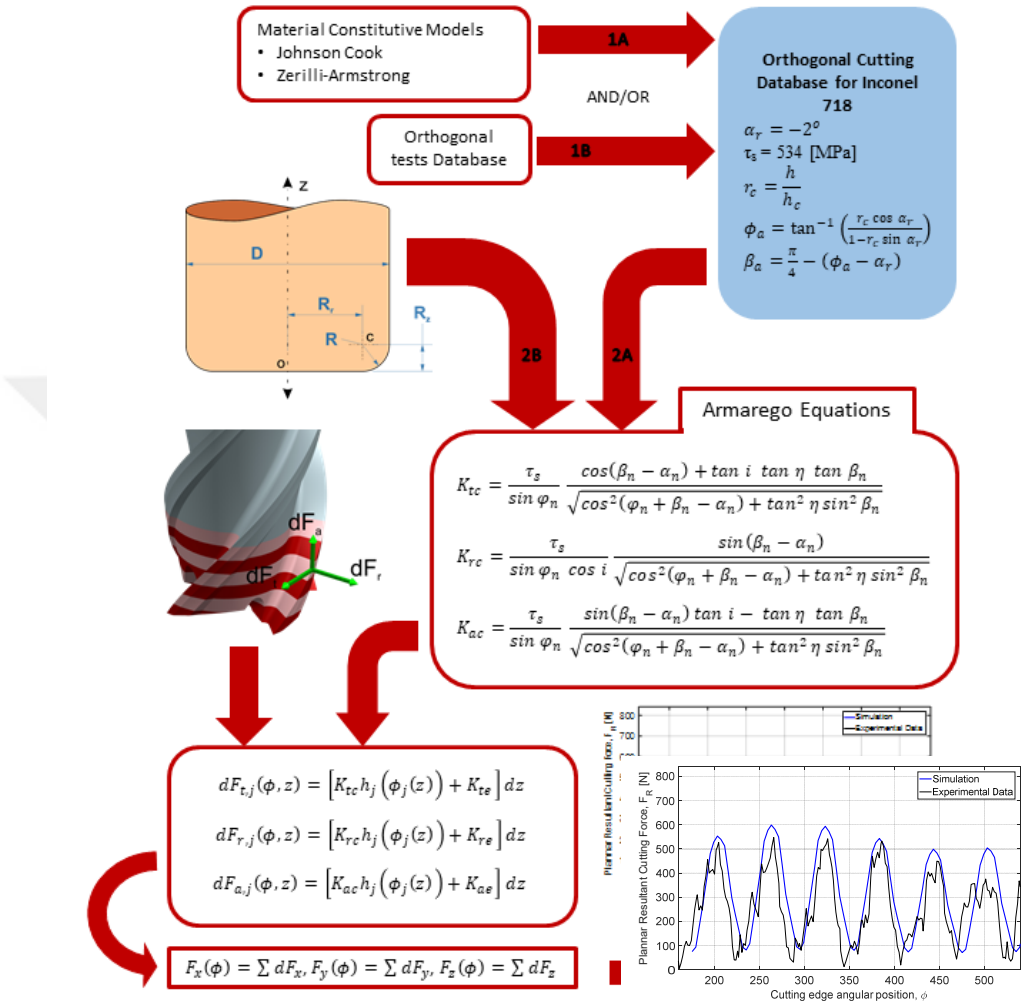

Figure 3-12: The steps for the simulation of cutting forces. (Gradišek et al., 2004) (Altintas, 2012).

Following the steps mentioned in the Figure 3-12, the cutting forces for end-milling of Inconel 718 is simulated for the cutting condition, which are kept confidential for the future scope of the work.

The cutting forces were measured using a Kistler table type dynamometer at 52 kHz sampling frequency. The tooth passing frequency was 1580 Hz. A low pass Butterworth filter with a cut off frequency of 3200 Hz was applied as 52 kHz sampling frequency was used against 2300 Hz natural frequency of the Kistler dynamometer. The comparison of the planar resultant of the cutting forces from the simulation with the experimentally measured forces is given in the Figure 3-13. The simulated forces were in good agreement with the experimental data. There were strong dynamic effects in the experimental data that the simulation did not account for. In general, the average of the simulation forces was over estimating by 7%.

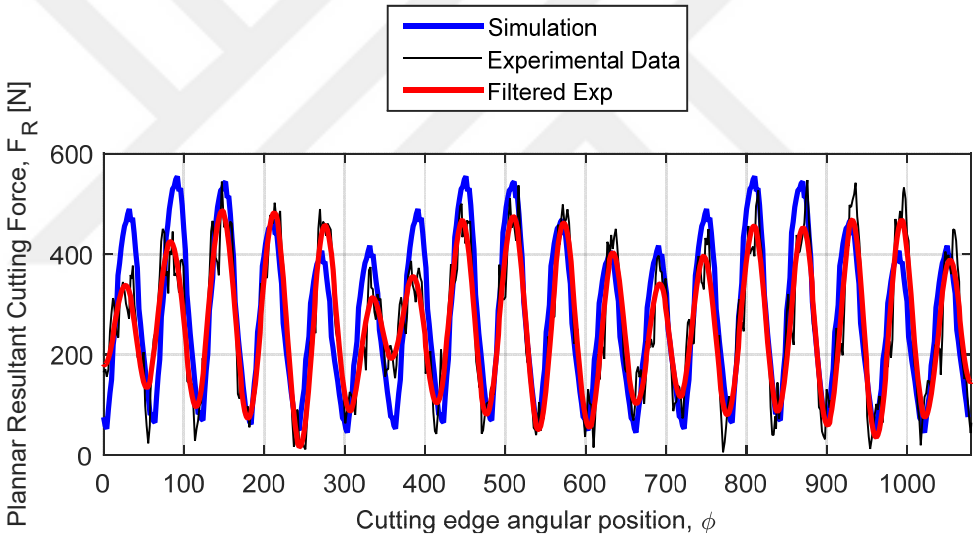

Figure 3-13: The comparison of simulation forces and the experimental cutting forces.

3.1.3 End-milling mechanics

The forces rising from cutting workpiece material in milling operations depend on three types of parameters. First set is related to the cutting conditions, namely the depth of cut a_p,

width of cut a_e and feedrate f as shown in the Figure 3-14. Full control exists over these parameters within the manufacturer set limits of the machine tool.

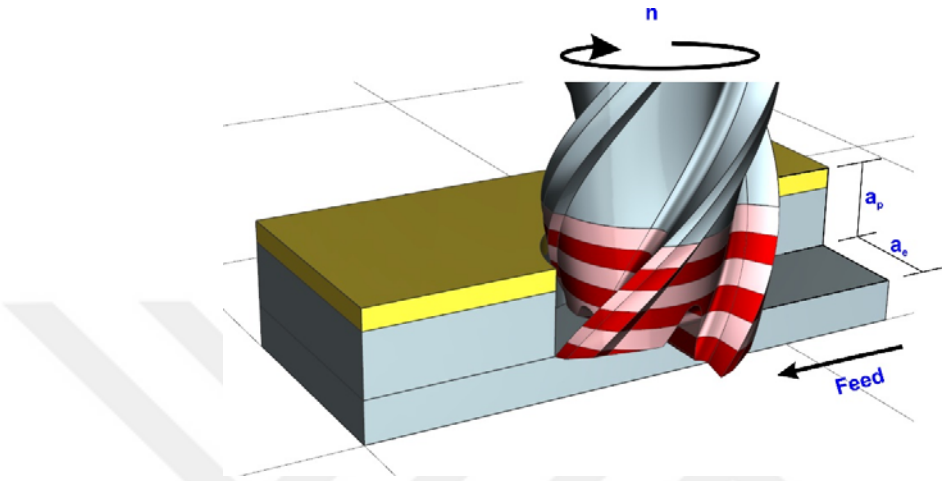

Figure 3-14: The cutting parameters during a milling operation.

To provide a common base for comparison, a single set of cutting conditions were selected. The cutting conditions for the comparison are kept confidential.

The second set of parameters are related to the geometry of the cutting tool. Once manufactured, the user does not have any liberty to change the design features of the end-mill tool. This second set of cutting tool geometry parameters are; the endmill diameter, number of flutes, the endmill helix angle β, the nominal radial rake angle α_r, the nominal axial rake angle, corner radius R_c, cutting edge radius R_e and the flank side clearance angle ψ as shown in the Figure 3-15.

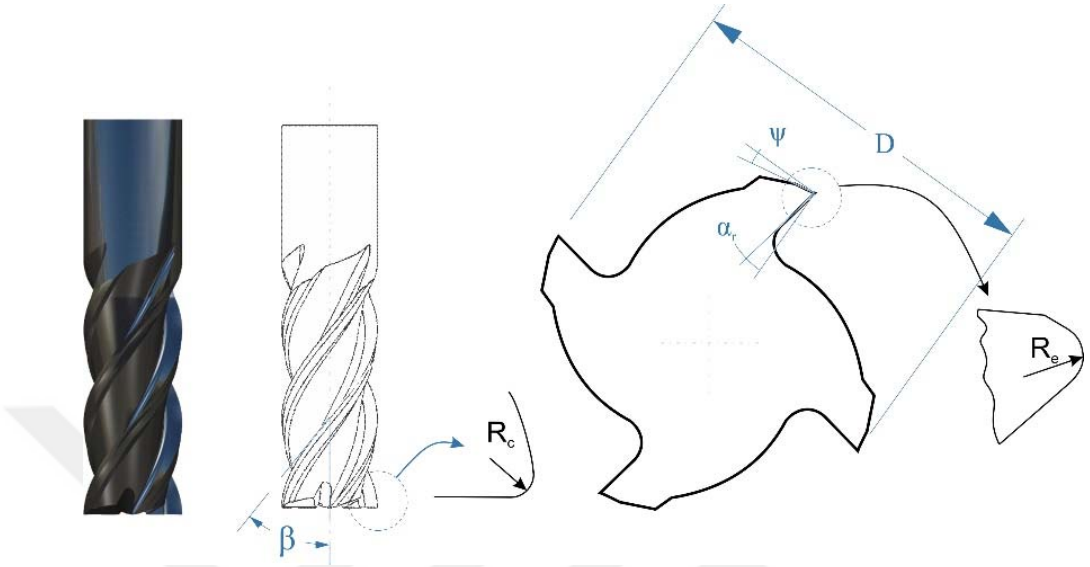

Figure 3-15: The endmill geometry parameters.

The third set of parameters relates to the cutting speeds and are responsible for the temperatures in the machining deformation zones. They are responsible for the strain hardening or softening, strain rate hardening and the thermal softening of the select material undergoing shearing from a sharp edge machining tool, as discussed in earlier sections in this chapter. Besides the cutting forces, the cutting temperature directly impact the tool and workpiece integrity as well. This research at this stage is entailing the cutting forces only and later work will expand to include the tool and workpiece integrity.

The ceramic tools employed for machining are reported to have shown wear from attritional wear mechanism. The ceramic endmill geometry features are investigated for the following issues.

1. Increased tool stiffness.
2. Reduced magnitude of force fluctuations.
3. Increased material removal rate.

With the bonus of improved material removal rate, any increase in tool stiffness will reduce tool chatter and the reduction in cutting force fluctuations will inhibit the attritional wear.

3.1.3.1 Endmill Stiffness

The endmill stiffness depends on the geometry of the tool and the modulus of elasticity. The mechanical and thermal properties of various tool materials currently in use are given in table. The ceramics have elasticity modulus 1/3rd of that for the carbides.

Table 3-8: The thermal and elastic properties of tool material at room temperature (Maekawa et al., 2013).

Tool material	Thermal Conductivity k $[W\ m^{-1}\ K^{-1}]$	Volumetric heat capacity ρC $[MJ\ m^{-3}]$	Coefficient of thermal expansion α_e $[10^{-6}K^{-1}]$	Modulus of elasticity E $[GPa]$	Thermal shock resistance $TRS/E\alpha_e$ $[\ ^{\circ}C\ ]$
Diamond	600-2000	2	3.1	960-990	-
PCD	100-550	2**	3.8-4.2	620-840	140-540
PCBN	≈100*	1.9-2.1	4.7-4.9	680-710	150-340
K-carbide	75-120	3.1-3.4	4.5-6.0	550-650	390-925
P-carbide	25-55	4.0-4.1	5.8-6.8	490-560	390-840
Cermet	11-35	2.4-2.7-	6.7-7.8	390-420	480-740
Al_2O_3	10-35	3.2-36.6	7.9-8.0	380-390	145-330
Al_2O_3/TiC	10-22	3.8-4.0	7.6-8.0	370-395	180-330
Al_2O_3/SiC	10-35	≈3.4*	7.0-7.5	345-425	300-500
Si_3N_4/SiAlON	15-30	2.1-2.3	3.2-3.6	280-320	650-1500
HSS	19-24	3.6-3.8	12-13	220-240	940-1740
*: information from limited data; **: assumed as for diamond.					

The geometrical stiffness is approximated as that of a cantilevered solid cylinder of an equivalent diameter. A typical geometry of the end-mill and the equivalent diameter is shown in the Figure 3-16.

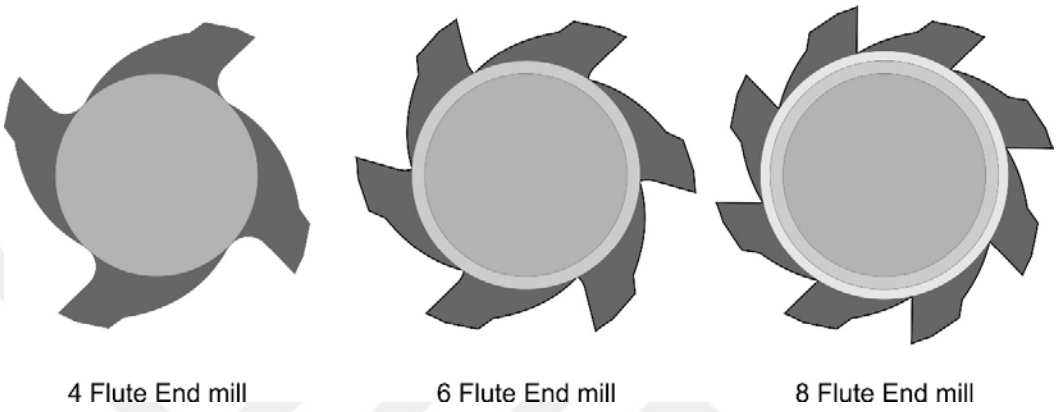

Figure 3-16: The solid webbing of end-mill for the 4, 6 and 8 toothed cases.

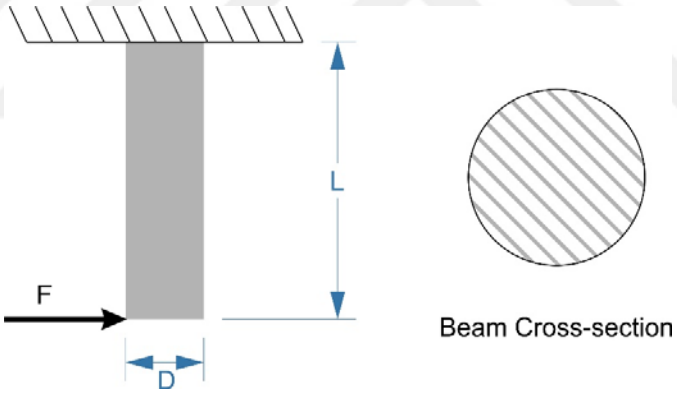

Figure 3-17: Cantilever beam with concentrated load.

The stiffness of a cantilever beam loaded by a concentrated load as shown in the Figure 3-17 and is given by equation 21.

$$k_{st} = \frac{EI}{3L^3} \tag{21}$$

Sacrificing flute depth to add to more flutes helped increase the geometrical stiffness of the tool. The decrease in flute depth is acceptable as the high-speed machining of Inconel produces dust like chips as shown in the Figure 3-18.

Figure 3-18: The Inconel 718 chips produced at the select cutting speed.

For equal length endmills the stiffness calculated for the solid webbing of the endmills is given in the Table 3-9.

Table 3-9: The percentage increase of stiffness for the modified end-mill.

Number of Flutes	End-mill Diameter [mm]	Solid Webbing Diameter [mm]	Cross-sectional area [mm^2]	Moment of inertia [mm^4]	% Increase in stiffness
6	12	8.1	51.8	213	-
8	12	8.8	61.2	298	39%
16	24	20.9	342.8	9349	4282%

3.1.3.2 Material Removal Rate

The addition of flutes and change in diameter of the tool produced improved stiffness for the solid ceramic end-mills. The increased number of flutes provided the additional bonus of increased material removal rate.

The analyses of the material removal rate for differently sized and fluted solid end-mills is provided in the Table 3-10.

Table 3-10: The material removal rate for differently sized solid ceramic end-mills.

	"D" Tool Diameter [mm]	"N_f" number of flutes	"Δs" arc length per flute [mm]	% change in flute gap	MRR [cm^3/min]
1	12	6	6.28		16.36
2	12	8	4.71	-25%	21.81
3	16	8	6.28	0%	16.36
4	16	12	4.19	-33%	24.53
5	20	10	6.28	0%	16.36
6	20	14	4.49	-29%	22.90
7	24	12	6.28	0%	16.36
8	24	16	4.71	-25%	21.81
9	24	18	4.19	-33%	24.53

Even though the added stiffness and improved material removal rate is evident, nevertheless the cutting force analyses is necessary for the viability of the proposed design change. The next section provides the approach for the end-mill parameter selection.

3.1.3.3 End-mill cutting edge geometry

The variation in individual endmill cutting edge geometry parameter is investigated to determine the most favorable combination. The parametric analysis is conducted with a starting set, given in the **Error! Reference source not found.**.

a. Rake angle

The influence of change in the radial rake angle is simulated for five magnitudes of the radial rake angle; -5°, -2°, 0°, 5° and 8° for three cases, while all other parameters are kept constant and equal to the values given in **Error! Reference source not found.**. The values for the maximums and the ranges for the planar resultant of the cutting forces are given in the

Table 3-11: The maximum and range for the planar resultant of the cutting forces when radial rake angle is changed.

Number of Flutes	6		8		16	
End-mill diameter	12 mm		12 mm		24 mm	
Radial rake angle	Max [N]	Range [N]	Max [N]	Range [N]	Max [N]	Range [N]
-5°	421	80	562	136	937	108
-2°	418	80	562	136	932	107
0°	415	79	558	134	929	106
5°	410	78	551	131	923	105
8°	408	78	547	130	919	104

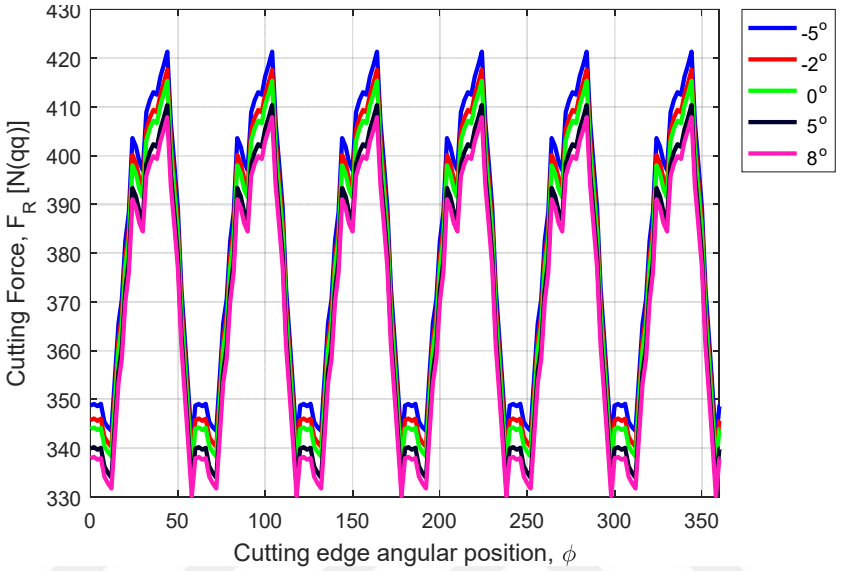

Figure 3-19: The cutting force simulation for a 6-flute end-mill for 5 different rake angles.

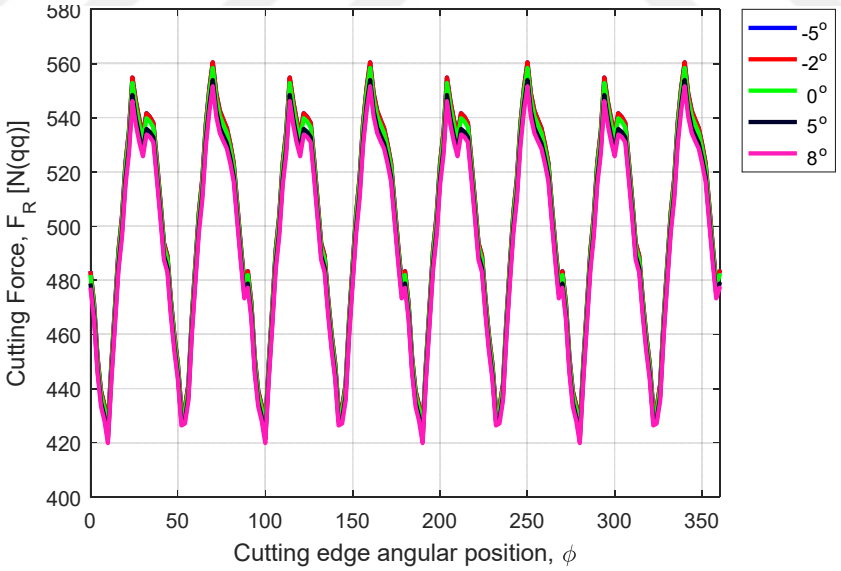

Figure 3-20: The cutting force simulation for a 8-flute end-mill for 5 different rake angles.

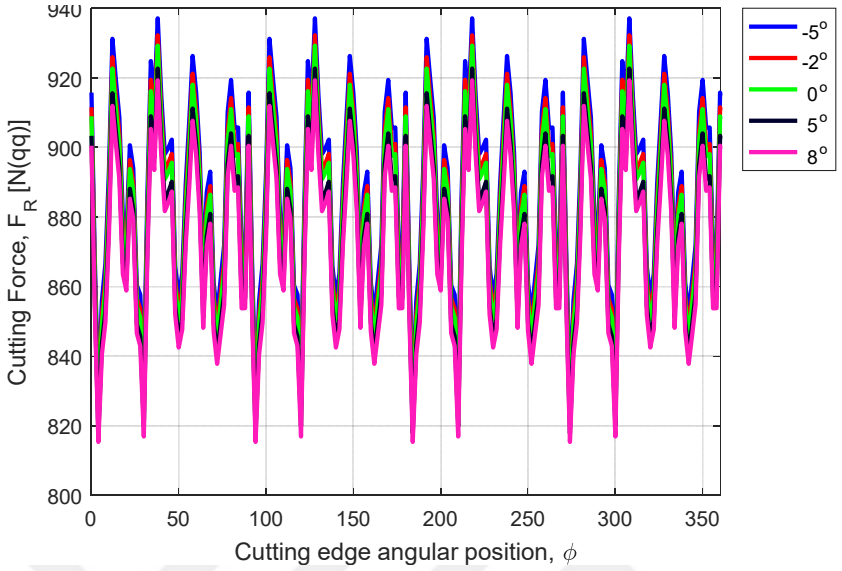

Figure 3-21: The cutting force simulation for a 16-flute 24 mm diameter end-mill for 5 different rake angles.

The simulations for the planar resultant of the cutting forces are plotted in Figure 3-19, Figure 3-20 and Figure 3-21. The advantage given by the positive values for radial rake angle is negligible. Nevertheless, it is noteworthy to mention that the radial rake angle is the determining parameter for the localized stiffness of cutting teeth. The negative rake angles provide the necessary strength for the cutting tooth to machine materials with superior mechanical properties.

b. Helix Angle:

The change in helix angle was investigated for its influence on the magnitudes of the cutting forces. A wide range of values for the helix angle was selected and is given in the Table 3-12.

Table 3-12: The range of helix angle selected for simulation.

Case No	1	2	3	4	5	6	7
Helix angle	20°	25°	30°	35°	40°	45°	50°

The values for the maximum and range of the planar resultant of the cutting forces for the investigated helix angle are provided in the Table 3-13.

Table 3-13: The maximum and range for the planar resultant of the cutting forces when helix angle is changed.

End-mill diameter	12			12			24		
Number of flutes	6			8			16		
Radial rake angle	-2°			-2°			-2°		
Helix Angle	Max	Range	Rank	Max	Range	Rank	Max	Range	Rank
20	659	659	7	670	474	7	755	191	7
25	569	509	6	575	276	6	780	119	6
30	511	351	5	515	117	4	771	63	1
35	458	214	4	513	84	2	863	110	4
40	418	80	1	562	136	5	932	107	3
45	457	110	3	570	73	1	1015	117	5
50	490	109	2	610	94	3	1103	87	2

The simulation confirmed the 6-flute original design to best work with 40° helix angle. The same magnitude for helix angle was not the best case for the 8-flute or 16-flute design.

The 8-flute tool recorded minimum value for cutting force fluctuations for 45° helix angle. The 16-flute design simulation predicted minimum force fluctuation for 30° helix angle. A sharper helix angle will reduce the number of flutes engaged for the given depth of cut and immersion angle. In essence, increasing the force intensity along a flute cutting edge, whereas the next best solution of 50° helix angle would improve the cutting force distribution over a larger number of flutes, therefore reducing the cutting force intensity for a given flute cutting edge. With the diameter of the endmill twice as the original dimension, the increased force magnitude penalty is tolerable.

Following the parameter selection criteria described in the section **Error! Reference source not found.**, the helix angles highlighted in Table 3-13 were selected for the new proposed end-mills. The force plots for the select range of helix angles for the three cases are shown in Figure 3-22, Figure 3-23 and Figure 3-24.

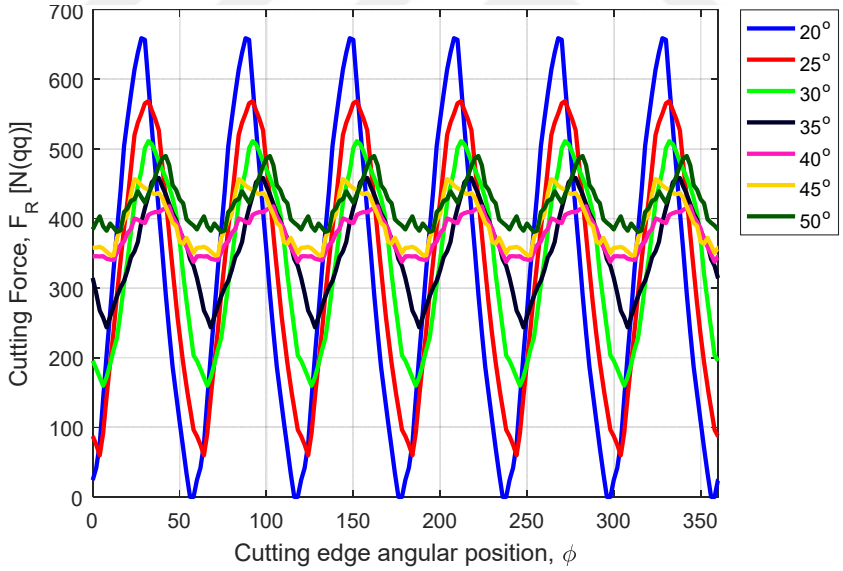

Figure 3-22: The cutting force simulation for a 6-flute end-mill for different helix angles.

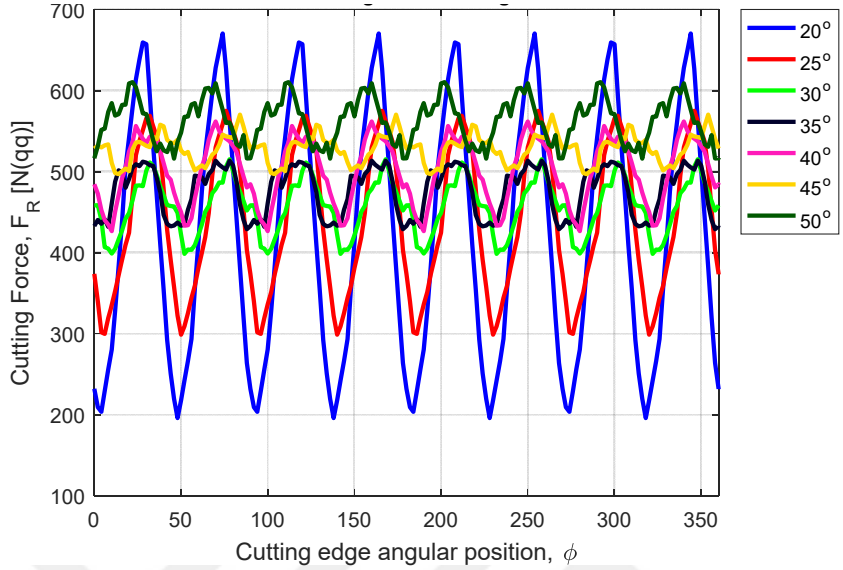

Figure 3-23: The cutting force simulation for a 8-flute end-mill for different helix angles.

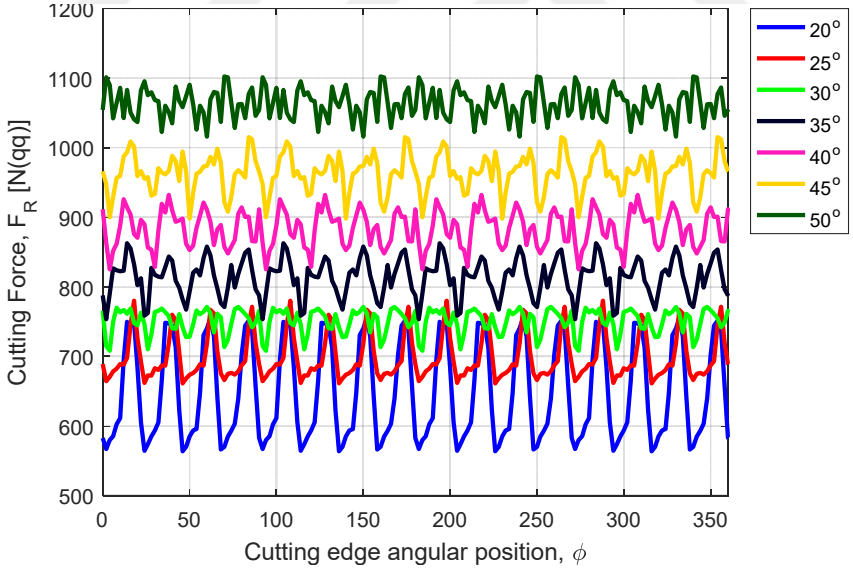

Figure 3-24: The cutting force simulation for a 16-flute 24 mm diameter end-mill for different helix angles.

c. Corner Radius:

The influence of the corner radius on the magnitudes of the cutting forces was investigated. The range of values for the corner radius selected is given in the Table 3-14.

Table 3-14: The range of corner radius selected for simulation.

Case No	1	2	3	4	5	6	7	8
Corner Radius mm]	0.5	1	1.5	2	2.5	3	3.5	4

The values for the maximum and range of the planar resultant of the cutting forces for the investigated corner radius are provided for the suitable helix angle in the Table 3-15.

Table 3-15: The maximum and range for the planar resultant of the cutting forces when corner radius is changed.

Endmill diameter	12 mm			12 mm			24 mm		
Number of flutes	6			8			16		
Radial rake angle	-2°			-2°			-2°		
Helix angle	40°			45°			50°		
Corner radius [mm]	Max [N]	Range [N]	Rank [N]	Max [N]	Range [N]	Rank [N]	Max [N]	Range [N]	Rank [N]
0.5	458	128	8	603	85	3	1156	93	4
1	432	105	2	579	61	1	1118	74	1
1.5	418	80	1	570	73	2	1103	87	3
2	420	109	3	552	88	4	1093	109	6
2.5	427	124	6	558	105	5	1076	116	7
3	416	121	5	564	130	6	1044	106	5
3.5	399	118	4	556	133	7	1024	119	8
4	383	126	7	544	148	8	977	85	2

The simulation force plots are given in the Figure 3-25, Figure 3-26 and Figure 3-27.

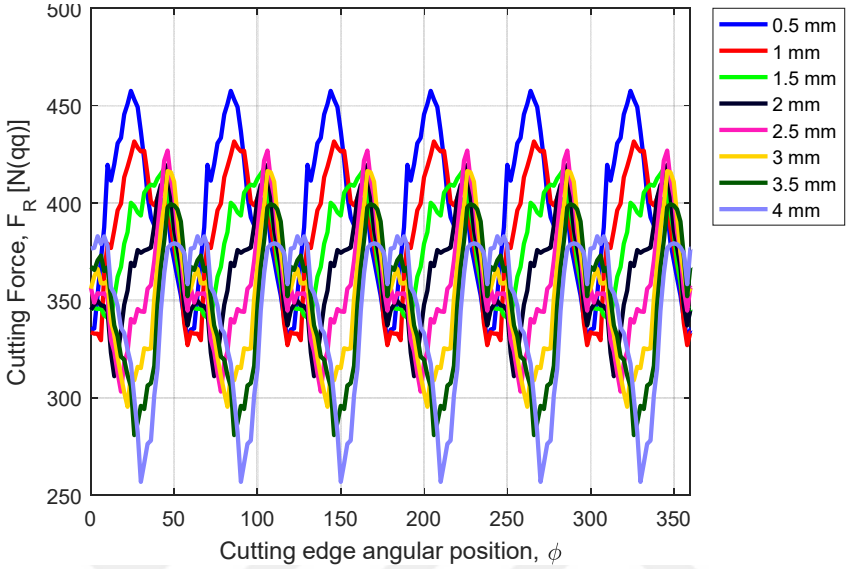

Figure 3-25: The cutting force simulation for a 6-flute end-mill for different corner radii.

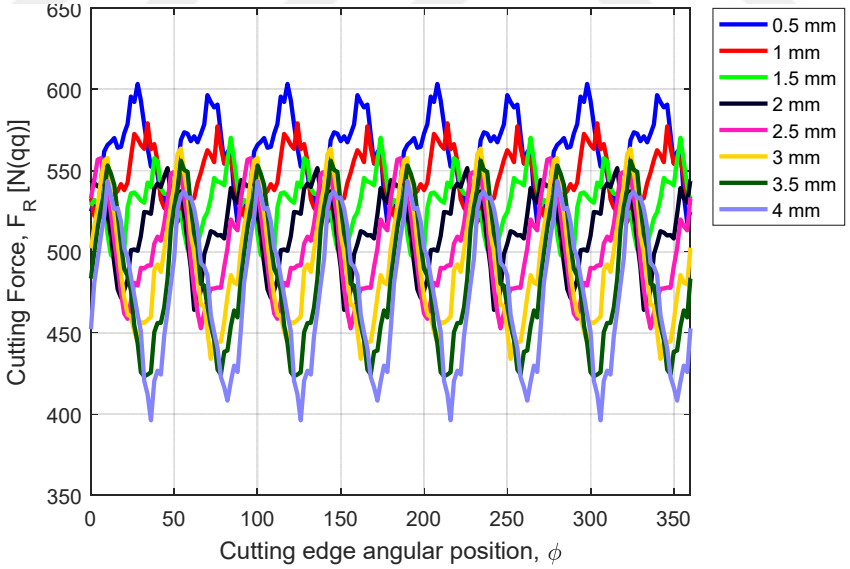

Figure 3-26: The cutting force simulation for a 8-flute end-mill for different corner radii.

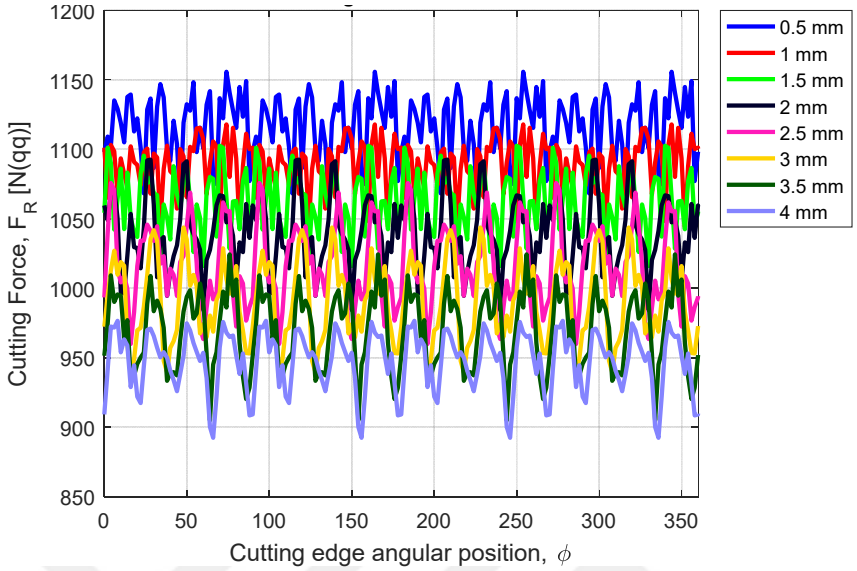

Figure 3-27: The cutting force simulation for a 16-flute 24 mm diameter end-mill for different corner radii.

d. Number of Flutes:

The influence of the number of cutting flutes is investigated. The number of flutes, not only do affect the stiffness of the end-mill and the flute depth but have a direct and proportional bearing on the material removal rate. The effect of the number of flutes on the 25 mm end-mill is evaluated for the cases given in the Table 3-16.

Table 3-16: The cases evaluated for effect of the number of flutes.

Case No	1	2	3	4
Number of Flutes	15	16	18	20

Table 3-17: The cutting force the cases with different flute numbers.

Diameter	25 mm	
Rake angle	-2°	
Corner Radius	1.5 mm	
Number of Flutes	Maximum	Range
15	1062	76
16	1118	74
18	1243	54
20	1394	67

Even though the fluctuations in the cutting forces for the cases with 18 and 20 flutes is less than the other cases as shown in the Figure 3-28, a conservative approach was decided and higher magnitude cutting forces were avoided. The 16-flute 25 mm end-mill design was selected for experimental validation.

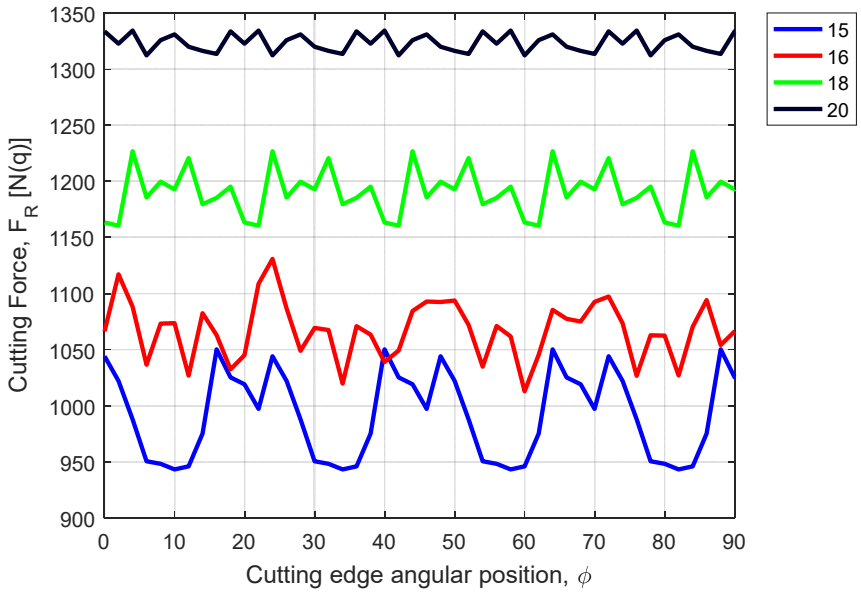

Figure 3-28: The cutting force simulation for a 16-flute 24 mm diameter end-mill for different numbers of flute.

3.1.4 Validation

The following the parameter selection from the previous section, the following solid SiAlON type ceramic end-mills were manufactured.

Table 3-18: The monolithic ceramic end-mill manufactured for validation.

Tool no.	Diameter [mm]	Number of Flutes	Measured Helix angle [deg]	Corner Radius [mm]	Runout [µm]
1	25	16	50.46	1.5	22.9
2.1	12	8	39.71	1.5	10
2.2	12	8	39.73	1.5	20.3
3.1	12	8	29.69	1.5	16
3.2	12	8	29.92	1.5	15.2
4.1	12	8	51.10	1.5	26.8
4.2	12	8	51.19	1.5	11.3
5.1	12	6	30.76	1.5	15.2
5.2	12	6	30.42	1.5	9.7
6.1	12	6	50.92	1.5	5.2
6.2	12	6	51.27	1.5	13.5
7.1	12	6	40.54	1.5	11.6
7.2	12	6	40.54	1.5	7.1

3.1.4.1 Setup:

The cutting tests for the solid ceramic end-mills were performed on Mori Seiki NMV5000 DCG 5-axis milling machine as is shown in Figure 3-29. The work piece is prepared for secure mounting on top of the table type dynamometer. The test setup is shown in Figure 3-30.

Figure 3-29: Experimental tests were performed on Mori Seiki NMV5000DCG 5-axis milling machine.

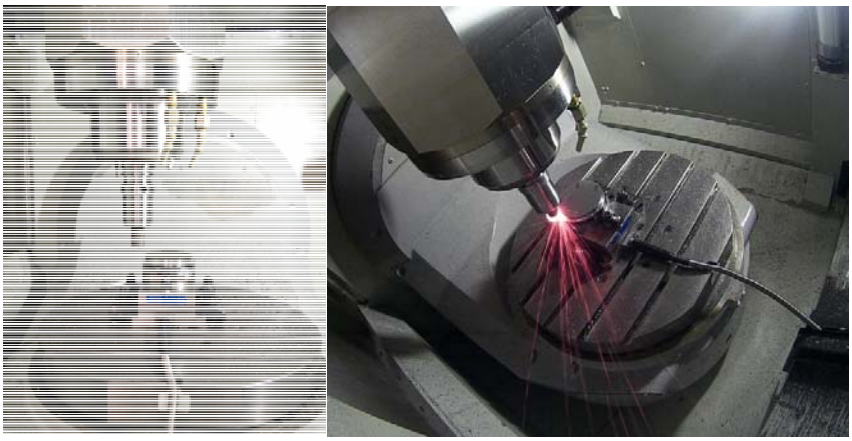

Figure 3-30: Inconel 718 workpiece machining with 25 mm diameter solid ceramic end-mill.

Force data was recorded for machining Inconel 718 with the differently designed solid end-mills for the select cutting conditions (confidential).

The cutting forces are compared for the maximum and range of there magnitudes as shown in the Figure 3-31.

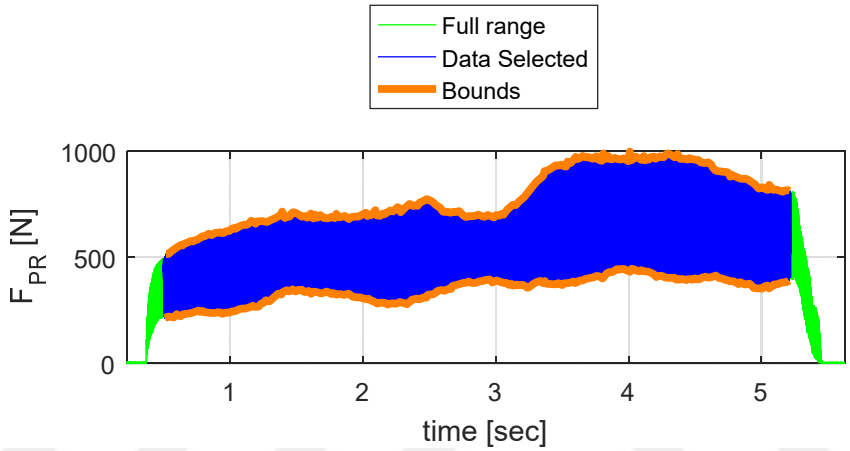

Figure 3-31: The outer bounds of the cutting forces for one of the investigated cases.

The experimental results confirm the advantage brought in by the design change, as was predicted in the simulations of the cutting forces for the manufactured solid ceramic end-mills.

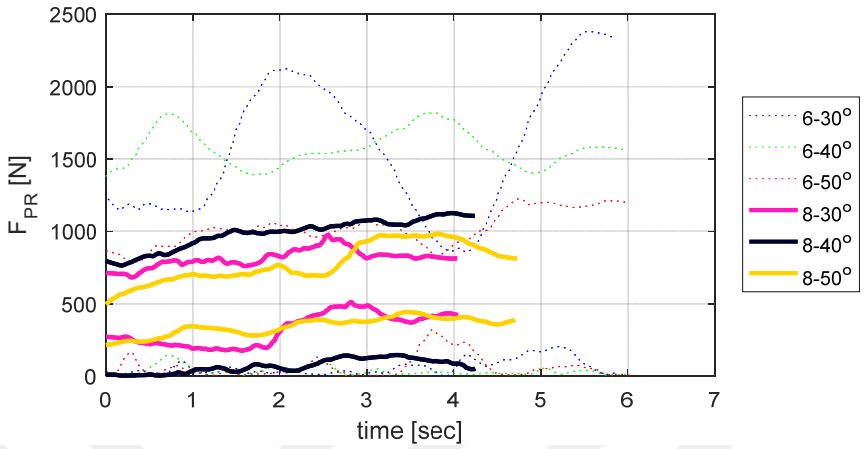

The 16-flute 25 mm diameter solid end-mill was tested for a harsher set of cutting conditions. The 80% larger width of cut resulted in 270% increased material removal rate. None of the leading manufacturers of ceramic end-mills market solid end-mill geometries of this size, as they have been reported to have failed at prototype stage. The cutting conditions for 16-flute end-mill are given in **Error! Reference source not found.**.

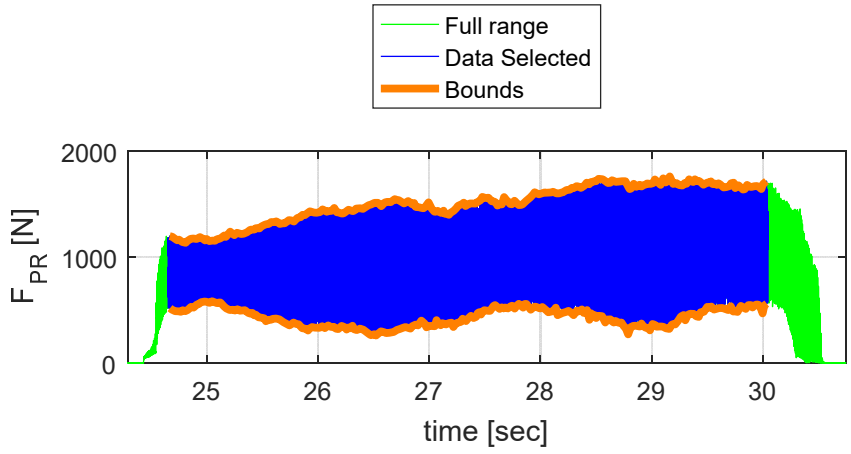

Figure 3-32: The planar resultant of the experimental forces for machining Inconel 718 with 25 mm solid end-mill.

The comparison of the designs amongst themselves and with the simulation are given in Table 3-19.

Table 3-19: The comparison of the solid ceramic end-mill designs.

Diameter [mm]	25		12											
No of flutes	16		8						6					
Helix Angle	50°		50°		40°		30°		50°		40°		30°	
Planar Resultant Forces	exp	sim	exp	sim	exp	sim	exp	sim	exp	sim	exp	sim	exp	sim
Overall average [N]	1000	1440	556	540	449	485	550	450	560	400	667	362	767	336
Maximum [N]	1760	1764	1000	720	1134	635	1027	590	1312	550	1840	439	2400	580
Material Removal Rate [cm^3/min]	45.5		21.8		21.8		21.8		16.35		16.35		16.35	

3.2 Competition evaluation

The performance of the locally manufactured ceramic end-mills were evaluated against leading brands in the market, namely Kennametal and Mitsubishi.

The performance and manufacture of the tested tools were compared on the following

1. Wear
2. Forces data

3.2.1 Wear

The improvement in tool life has direct dividends towards manufacturing costs. Accurate estimation of tool life guards against catastrophic failures. Such failures may damage the workpiece requiring further repair work if not all together a replacement. The proper

understanding of the wear and wear mechanisms will facilitate better tool design with improved life.

There are several mechanisms contributing towards tool wear. Tool wear may occur because of a single dominating mechanism or it may be a result of combination of the mechanisms. Commonly observed wear types in machining operations are the flank wear, crater wear, notch wear and chipping and tool breakage.

The wear performance of the solid ceramic end-mills was investigated for the high-speed milling operations. The ceramic tool wear was evaluated for leading cutting tool manufacturers and locally manufactured ceramic end-mill. The cutting forces were recorded during the tool wear test as well.

3.2.1.1 Setup:

The locally manufactured solid ceramic end-mill's tool life was evaluated against market leading brands, Kennametal and Mitsubishi when machining Inconel 718 at very high cutting speeds. The cutting tests were performed on Mori Seiki NMV5000 DCG 5-axis milling machine as is shown in Figure 3-29. The work piece is prepared for secure mounting on top of the table type dynamometer. The test setup is shown in Figure 3-33.

Figure 3-33: Inconel 718 Workpiece on Kistler table type dynamometer.

3.2.1.2 Cutting Parameters

The flank land wear was measured for ceramic end-mills from the Alp aviation and two from the leading brands in the ceramic tools market, namely, Mitsubishi and Kennametal.

The assessment was conducted for the select cutting conditions (confidential). The workpiece had a circular geometry. The toolpath was designed to cut around the periphery for the maximum utilization of the workpiece material. Each test cut, as shown in the Figure 3-34, reduced the diameter of the workpiece and consequently the machined length. The length of cut for each test for the Alp Aviation and Mitsubishi ceramic end mill is given in the Table 3-21. The machined lengths for the Kennametal ceramic end-mill are given the Table 3-22.

Table 3-20: Test setup parameters.

Cutting Parameters		
Material		
Inconel 718		
Tool		
Type	Solid endmill	
Diameter	12	mm
Number of Flutes	6	

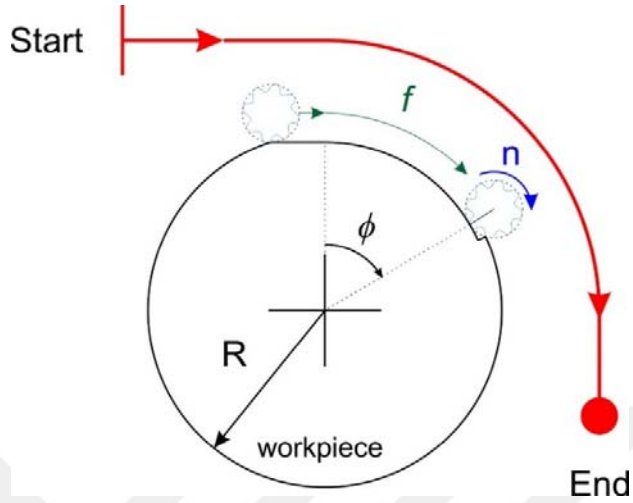

Figure 3-34: The schematic for geometry of toolpath defining the cut length.

The workpiece had a circular geometry. The toolpath was designed to cut around the periphery for the maximum utilization of the workpiece material. Each test cut, as shown in Figure 3-34, reduced the diameter of the workpiece.

Table 3-21: Lengths at which the tool flank wear was measured for the Mitsubishi and Alp Aviation ceramic end-mill.

Test Run	Radius, R [mm]	Arc Length [m]	Accumulated Cut length [m]
1	55.730	0.0875	0.0875
2	55.000	0.0864	0.1739
3	55.000	0.0864	0.2603
4	54.365	0.0854	0.3457
5	54.365	0.0854	0.4311

Table 3-22: The tool flank wear was measured after these cut lengths for the Kennametal ceramic end-mill.

Test Run	Radius, R [mm]	Arc Length [m]	Accumulated Cut length [m]
1	53.765	0.0845	0.0845
2	53.765	0.0845	0.1689
3	53.765	0.0845	0.2534
4	53.765	0.0845	0.3378
5	53.130	0.0835	0.4213
6	53.130	0.0835	0.5047

3.2.1.3 Result and discussion

The flank wear was measured for each of the six flutes on the three tested tools after each cut length using Nikon SMZ 645 stereoscopic zoom microscope shown in Figure 3-35. The progressive flank wear magnitudes are shown in the plots and given in the Table 3-24 and the Table 3-25.

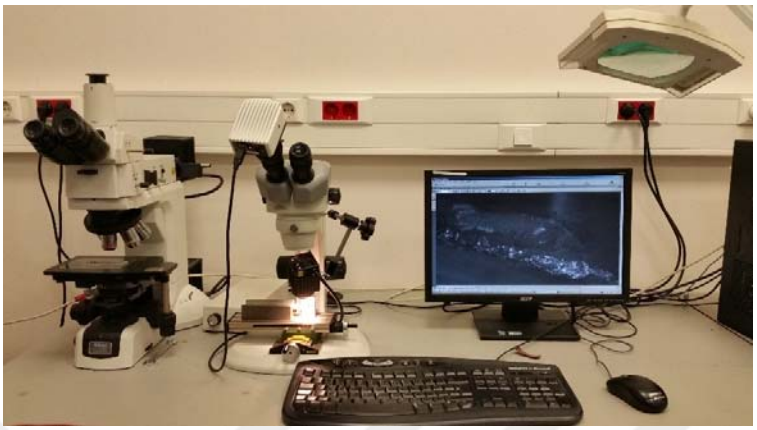

Figure 3-35: Nikon Stereoscopic Zoom Microscope was used for flank wear measurement.

Inconel alloys are known for welding to the cutting-edge when machined. A strategy was devised to measure the build-up edge separated from the wear of the tool flank land. The fresh flank land under the microscope was recognized to have two distinct edges. The width of the flank land for a fresh tool was measured using these two edges for each flute. The flutes were numbered for comparability and reference. The cutting edges on the end-mill flutes were observed to have considerable amount of workpiece material build-up as shown in Figure 3-36.

Mitsubishi Alp Aviation Kennametal

Figure 3-36: The Inconel workpiece material is welding to the tool cutting edge and creating the built-up edge.

A line (line 2) is drawn parallel to the flank land edge, which is not affected by machining test, and at a distance measured for a fresh tool as shown in Figure 3-37. All material below this line is built-up edge. This line is used to measure the flank land wear and to quantify the built-up edge also.

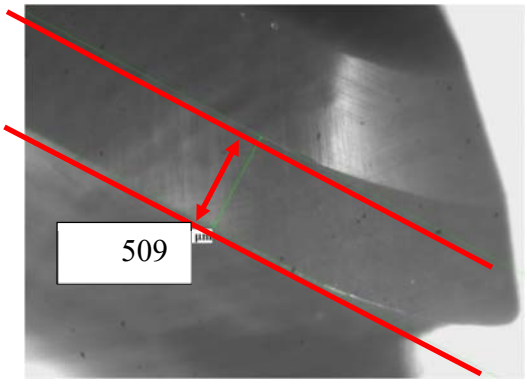

Figure 3-37: Optical microscope image of flank land for Fresh tool.

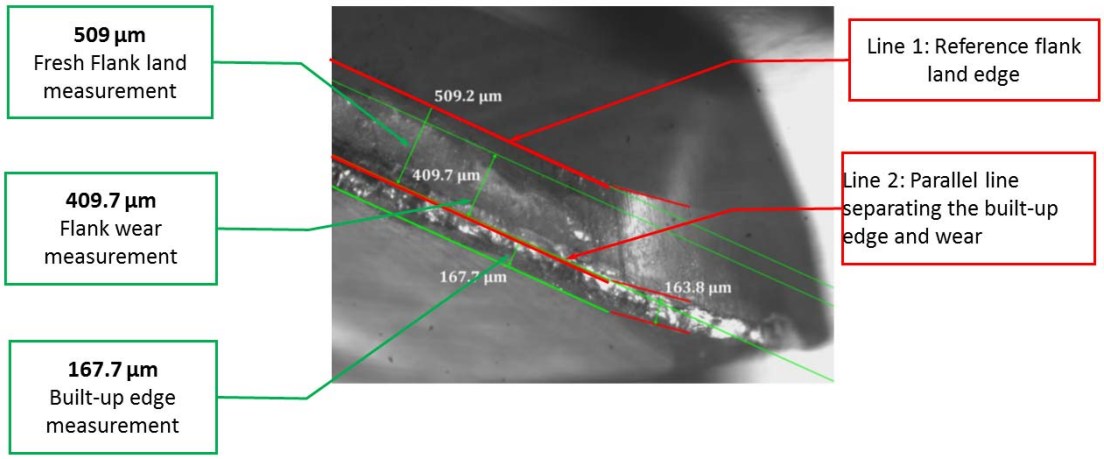

Figure 3-38: The method adopted for measuring the built-up edge and flank wear.

Table 3-23: The average wear on an end-mill for respective cut lengths.

Test Run	Accumulated cut length [m]	Volume removed [cm^3]	machining time [sec]	Flank land Wear [µm]		
				Mitsubishi	**Alp**	**Kennametal**
1	0.0875	0.500	1.84	0	153	105
2	0.1739	0.994	3.65	326	199	114
3	0.2603	1.488	5.46	413	261	138
4	0.3457	1.976	7.25	528	306	189
5	0.4311	2.464	9.04	**X**	349	250
6	0.5047	2.89	10.58	**X**	**X**	330

Table 3-24: The built-up edge on tested end-mills for respective cut lengths.

Test Run	Accumulated cut length [m]	Volume removed [cm^3]	machining time [sec]	Built-up Edge [µm]		
				Mitsubishi	**Alp**	**Kennametal**
1	0.0875	0.500	1.84	169	64	**X***
2	0.1739	0.994	3.65	159	61	**X**
3	0.2603	1.488	5.46	173	67	**X**
4	0.3457	1.976	7.25	157	107	**X**
5	0.4311	2.464	9.04	-	67	**X**
6	0.5047	2.890	10.58	-	-	**X**
* The size of built of edge on the Kennametal endmill for the selected wear analysis method was not enough to establish its size deterministically.						

Table 3-25: Flank land wear for individual flutes

Test Run	Accumulated cut length [m]	Flute number	Flank land Wear [µm]		
			Kennametal	Mitsubishi	Alp
1	0.0875	1	86	0	293
		2	126	0	168
		3	105	0	91
		4	104	0	67
		5	117	0	171
		6	91.5	0	127
2	0.1739	1	112	410	301
		2	128	398	271
		3	107	344	165
		4	113	389	82
		5	113	414	188
		6	113	0	188
3	0.2603	1	147	434	338
		2	164	409	233
		3	122	362	196
		4	118	426	87
		5	134	459	350
		6	140	388	364

4	0.3457	1	150	609	357
		2	164	534	425
		3	142	532	224
		4	204	458	103
		5	189	518	350
		6	283	518	375
5	0.4311	1	164	**X**	372
		2	164	**X**	404
		3	264	**X**	224
		4	306	**X**	368
		5	300	**X**	350
		6	300	**X**	375
6	0.5047	1	317	**X**	**X**
		2	317	**X**	**X**
		3	370	**X**	**X**
		4	312	**X**	**X**
		5	340	**X**	**X**
		6	321	**X**	**X**

a. Mitsubishi monolithic ceramic end-mill flank wear.

The wear measured on the flank side of the cutting flutes on the Mitsubishi monolithic ceramic end-mill was measured after select distance machined. The wear was measured on each flute individually and the progression of the wear is shown in the Figure 3-39. The solid line represents the average measure for the flank wear for the six flutes of the tested end-mill. The six circles mark the magnitude of flank wear for the six individual flutes for the test cut lengths. The difference in magnitude of wear between flutes is presented by the shaded region. The difference in magnitudes for the wear is due to the runout.

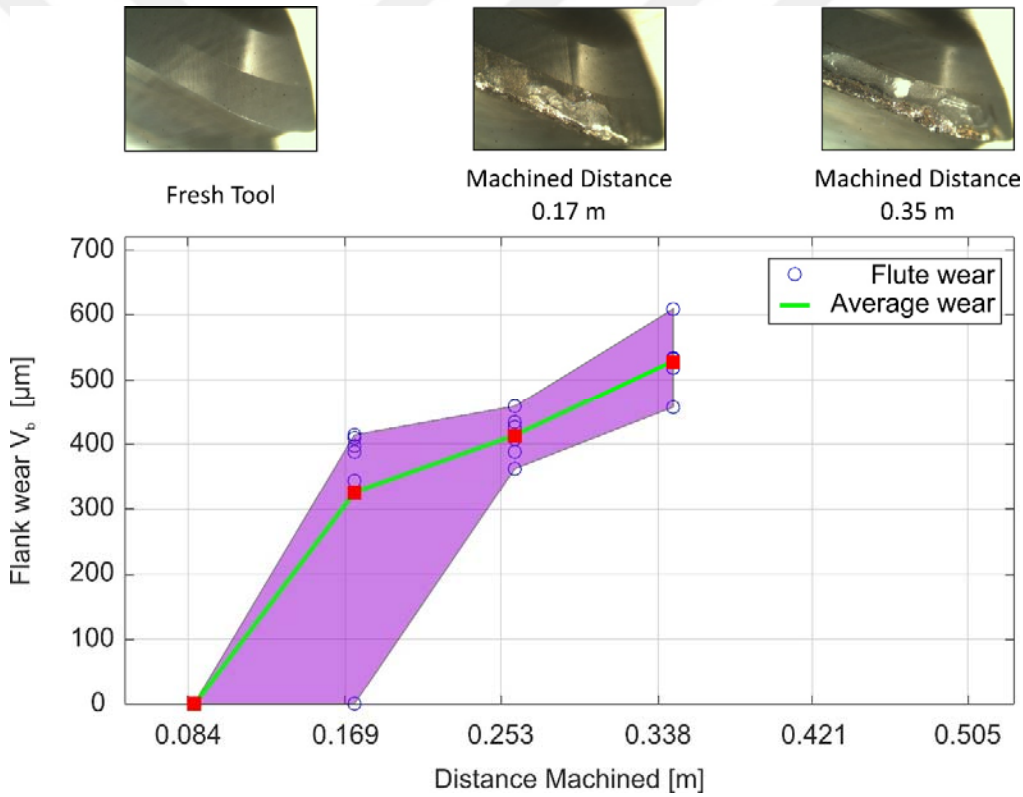

Figure 3-39: The flank land wear for the Mitsubishi ceramic end-mill.

The workpiece material was found to have strongly adhered to the cutting tool material, in process creating a sizable built-up-edge as shown in the Figure 3-40. An average built-up-edge of 165 μm was observed on the Mitsubishi monolithic ceramic end-mill from the start of the tests.

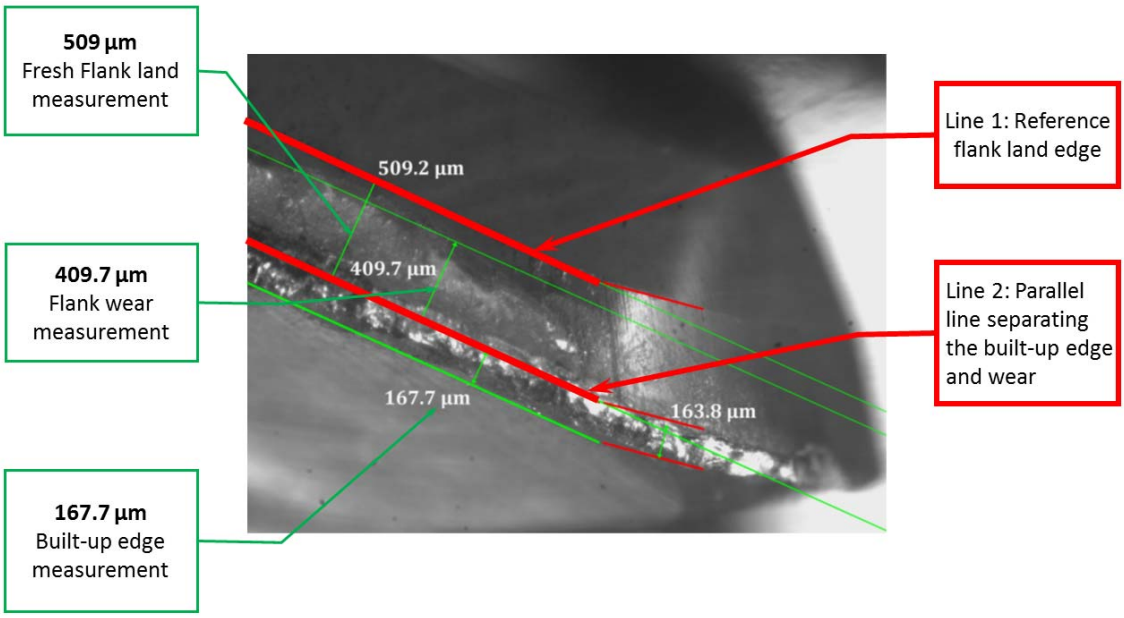

Figure 3-40: The wear and built-up-edge measurement for the Mitsubishi ceramic end-mill.

The end-mill cutting edges where examined by scanning electron microscopy and energy dispersive spectroscopy to confirm the built-up-edge and the wear mechanism.

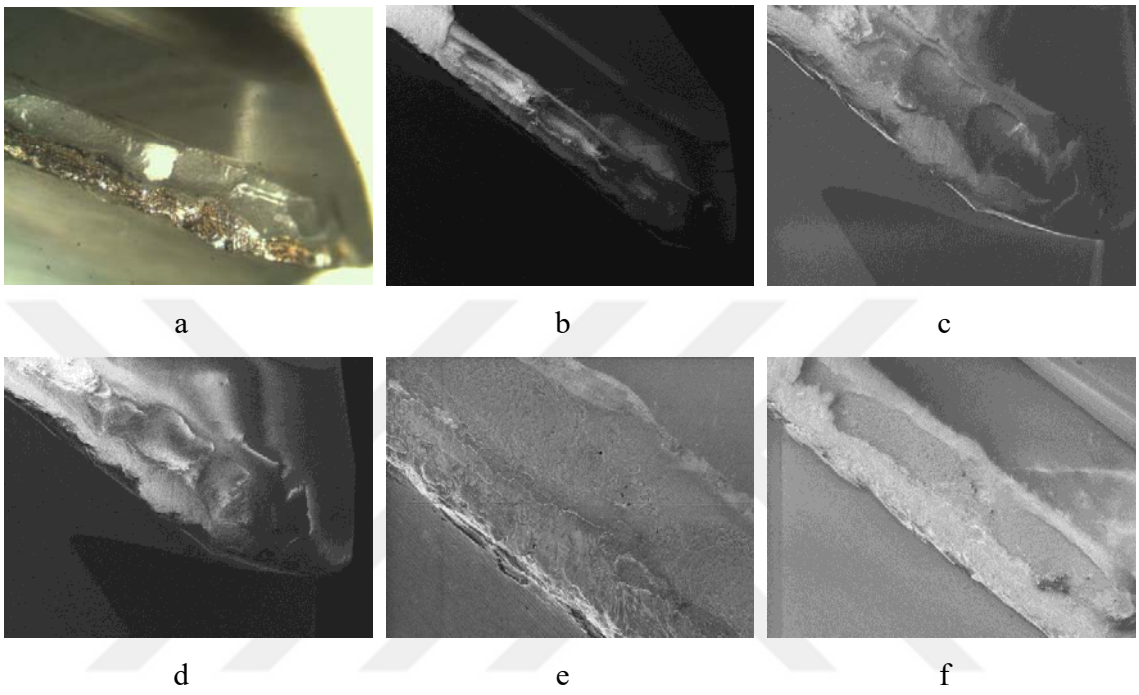

Figure 3-41: The flank side of the cutting edge for the Mitsubishi ceramic end-mill.

The Figure 3-41 (a) is showing the flank side of the cutting edge for the Mitsubishi ceramic end-mill from the optical microscope. The Figure 3-41 (b) to (f) are the scanning electron microscope images of the same region on the end-mill corner and the flank side.

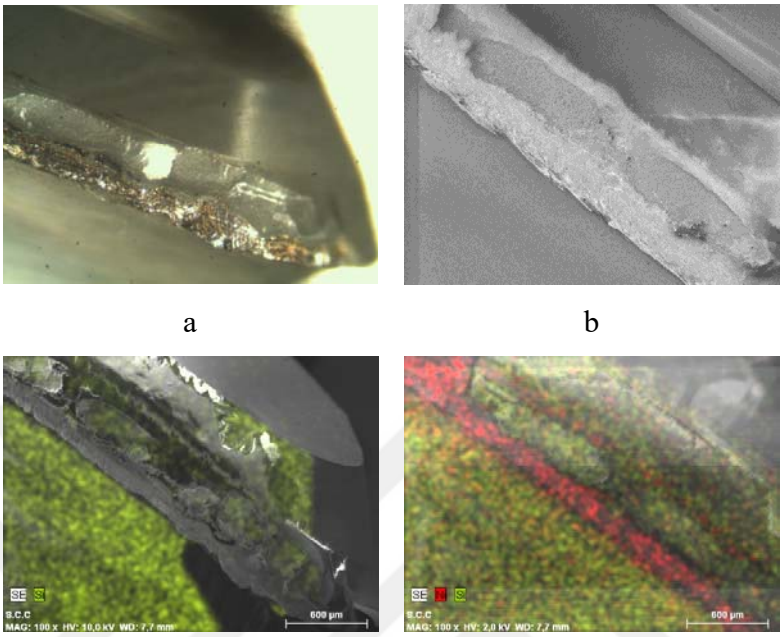

a b

c d

Figure 3-42: The EDS of the flank side of the cutting edge for the Mitsubishi ceramic end-mill.

The energy dispersive X-ray spectroscopy scans of the flank side of the cutting edge for the Mitsubishi ceramic end-mill confirmed presence of nickel on the cutting-edge flank side, a confirming the adhesion of the Inconel 718 workpiece material built-up-edge on the tool cutting edge. The from the optical and scanning electron microscopes. The Figure 3-42 (a) is the optical microscope image of the end-mill corner radius and the flank side. Image (b) is the scanning electron microscope image for the same region on the tool, whereas the image (c) is the EDS scan with Silicon element as pre-selection. and (d) is the EDS scan of the flute flank side with both nickel and silicon element as preselection. The silicon material is represented with green color points and the nickel element is represented by the red color detection points in the Figure 3-42.

The monolithic ceramic end-mill from Mitsubishi had larger flank side width of 500 μm than its counterparts' 350 μm. The machining test revealed a severe erosion of the cutting tool material on the flank side. The formed craters are visible in the all three versions of spectrum, namely, visible, scanning electron and X-ray in the Figure 3-42.

The ceramic elemental composition was performed and the EDS detection count plot is shown in Figure 3-43.

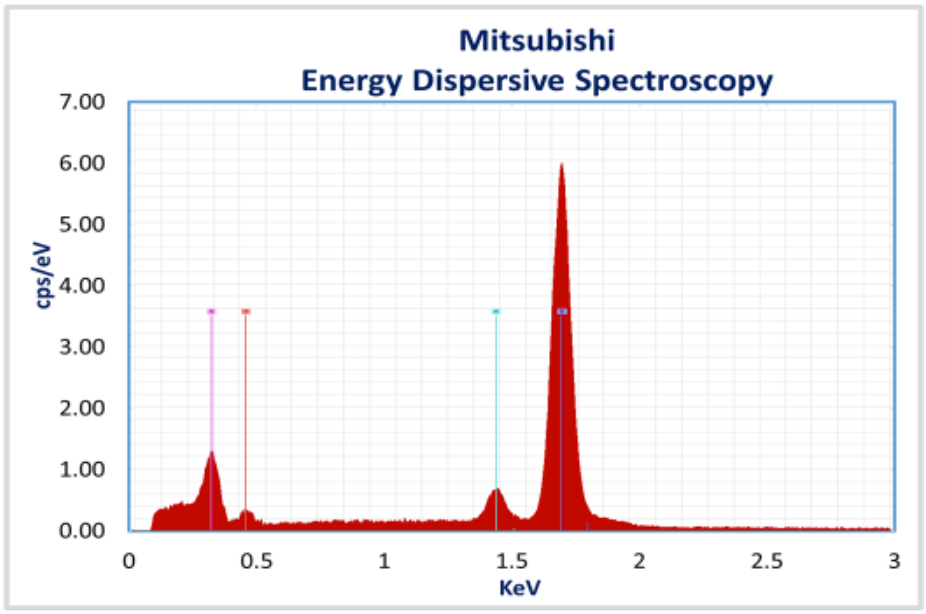

Figure 3-43: The elemental composition of the Mitsubishi end-mill ceramic.

The ceramics used for machining Inconel 718 are called SiAlON. It is a combination of silicon nitride and alumina or silicon alumina nitride. The percentile elemental composition is given in the Table 3-26.

Table 3-26: The elemental composition for the Alp aviation ceramic end-mill.

Element	Net count	Normalized with Carbon [wt.%]	Normalized with Carbon Atomic number [at.%]	Error (1 Sigma)
N (7)	7400	38.44	52.53	3.89
O (8)	2894	10.36	12.39	1.26
Al (13)	8078	6.06	4.31	0.22
Si (14)	43195	45.14	30.77	1.3
	Total:	**100%**	**100%**	

b. Alp aviation monolithic ceramic end-mill flank wear

The wear measured on the flank side of the cutting flutes on the Alp aviation monolithic ceramic end-mill was measured after select distance machined. The wear was measured on each flute individually and the progression of the wear is shown in the Figure 3-44. The solid line represents the average measure for the flank wear for the six flutes of the tested end-mill. The six circles mark the magnitude of flank wear for the six individual flutes for the test cut lengths. The difference in magnitude of wear between flutes is presented by the shaded region. The difference in magnitudes for the wear is due to the runout.

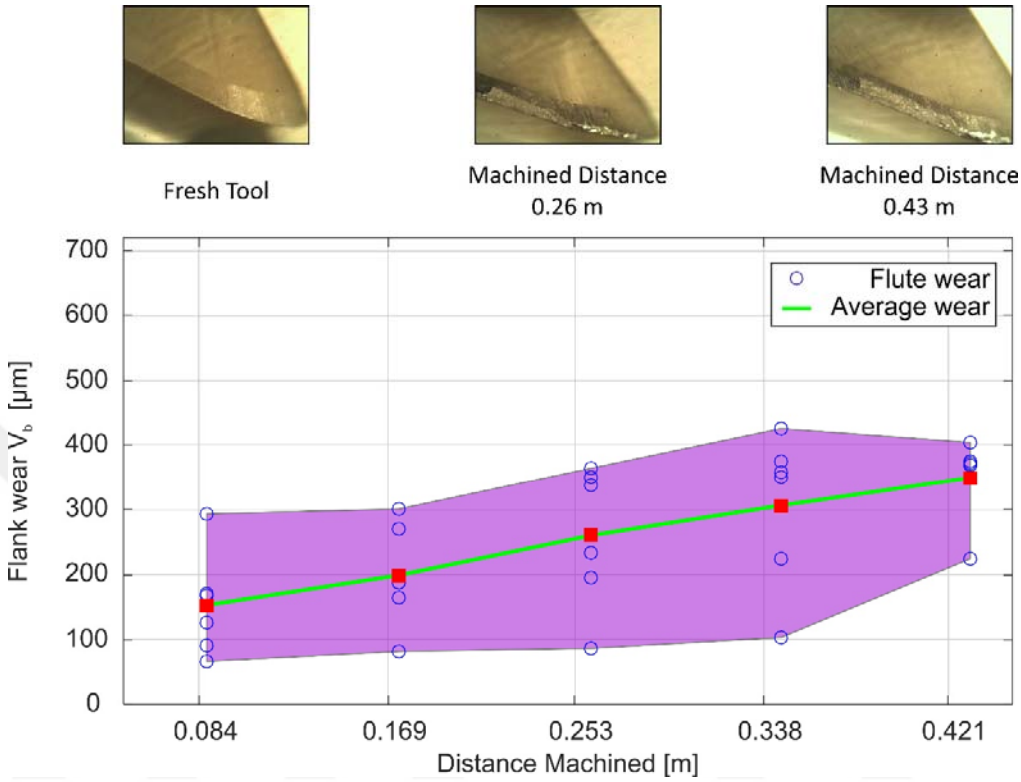

Figure 3-44: The flank land wear for the Alp Aviation ceramic end-mill.

The end-mill cutting edges where examined by scanning electron microscopy and energy dispersive spectroscopy to confirm the built-up-edge and the wear mechanism. The workpiece material adhesion to the alp aviation ceramic end-mill was not as severe as the Mitsubishi ceramic end-mill. The average size of the built-up-edge was 65 μm.

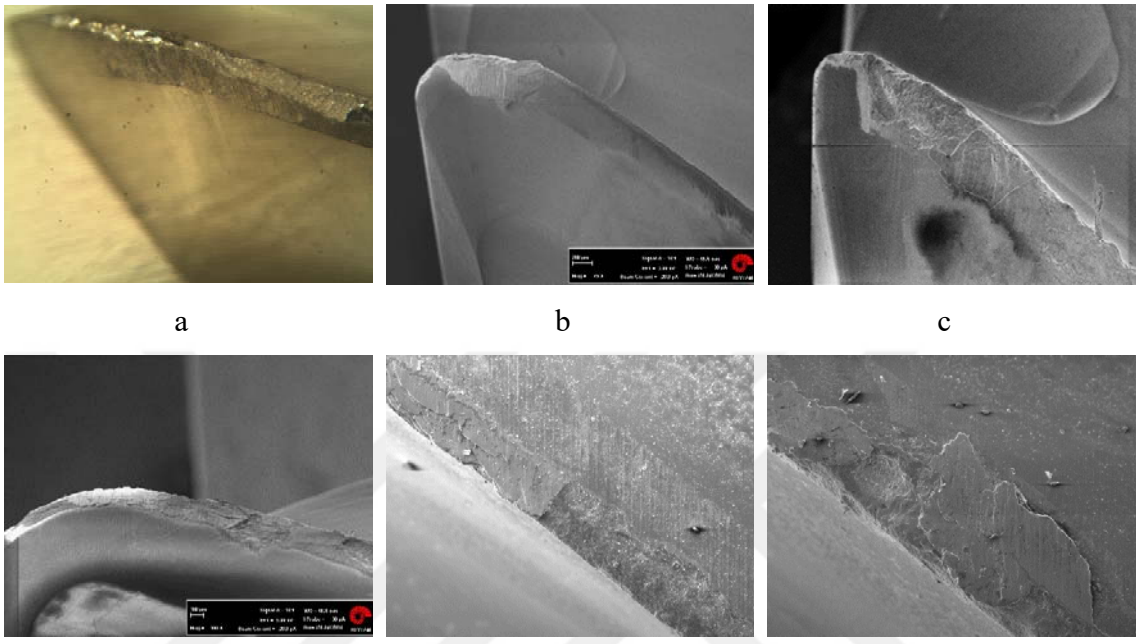

a b c

d e f

Figure 3-45: The flank land wear for the Alp Aviation ceramic end-mill.

The Figure 3-45 (a) is showing the flank side of the cutting edge for the Alp aviation ceramic end-mill from the optical microscope. The Figure 3-45 (b) to (f) are the scanning electron microscope images of the same region on the end-mill corner and the flank side. The cutting edge kept its integrity intact. Still strong adhesion of workpiece material to the tool cutting edge is observed.

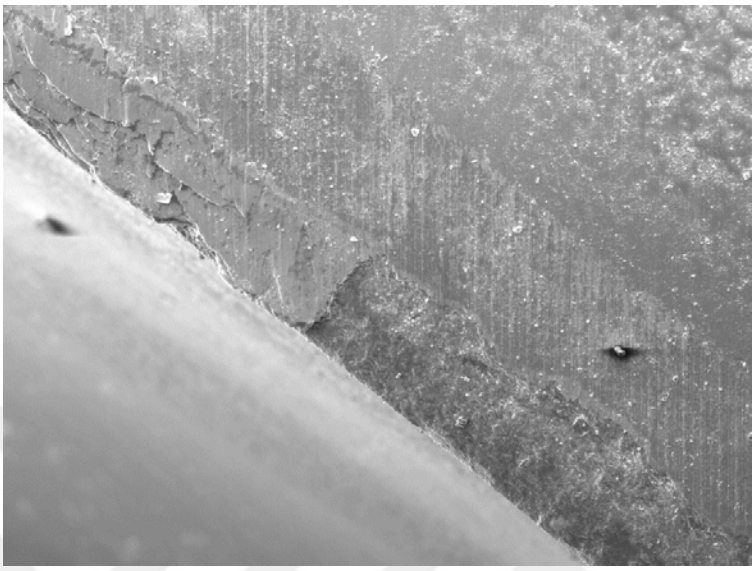

(a)

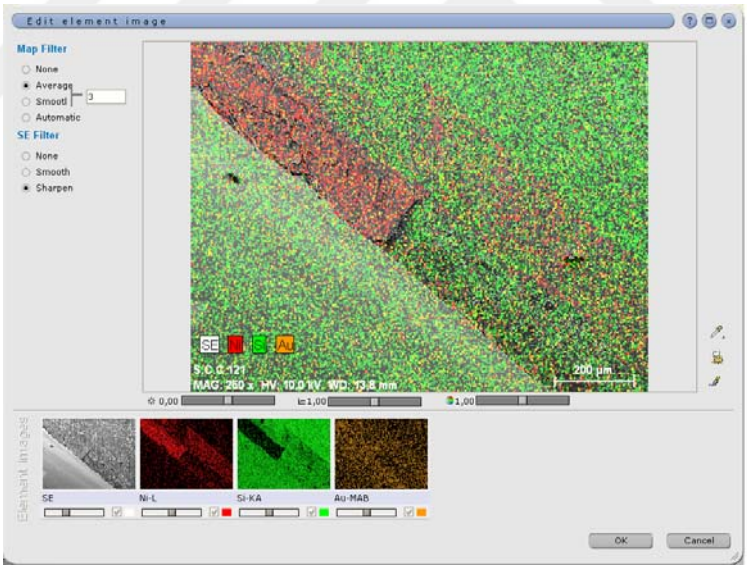

(b)

Figure 3-46: The EDS of the flank side of the cutting edge for the Alp aviation ceramic end-mill.

The energy dispersive X-ray spectroscopy scans of the flank side of the cutting edge for the Alp aviation ceramic end-mill confirmed presence of nickel on the cutting-edge flank side and confirmed the adhesion of the Inconel 718 workpiece material as built-up-edge on the tool cutting edge. The Figure 3-46 (a) is the scanning electron optical microscope image of the end-mill flank side. Image (b) is the EDS scan, where silicon and nickel element are pre-selections. The silicon material is represented with green color data points and the nickel element is represented by the red color detection points in the Figure 3-46.

The ceramic elemental composition was performed and the EDS detection count plot is shown in the Figure 3-47 and the percentage values are given in the Table 3-27.

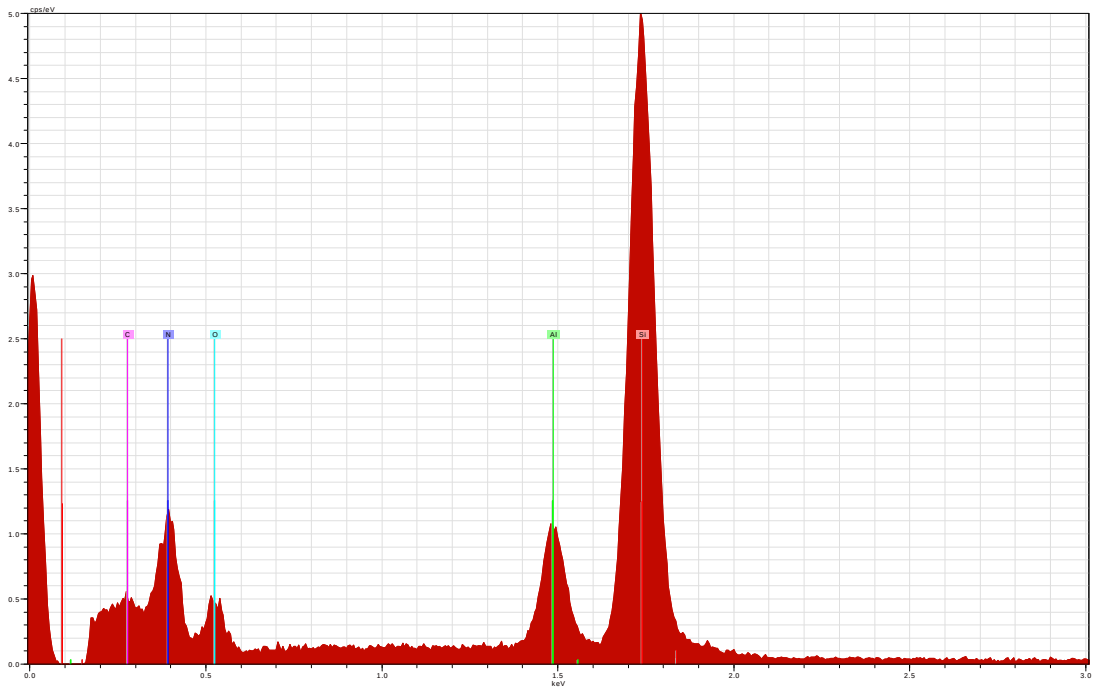

Figure 3-47: Detection count for respective elements for the Alp Aviation ceramic end-mill.

Table 3-27: The percentile elemental composition of the Alp Aviation SiAlON ceramic.

Element	Net count	Normalized with Carbon [wt.%]	Normalized with Carbon Atomic number [at.%]	Error (1 Sigma)
N (7)	7400	38.44	52.53	3.89
O (8)	2894	10.36	12.39	1.26
Al (13)	8078	6.06	4.31	0.22
Si (14)	43195	45.14	30.77	1.3
	Total:	**100%**	**100%**	

c. Kennametal monolithic ceramic end-mill flank wear

The wear measured on the flank side of the cutting flutes on the Kennametal monolithic ceramic end-mill was measured after select distance machined. The wear was measured on each flute individually and the progression of the wear is shown in the Figure 3-48. The solid line represents the average measure for the flank wear for the six flutes of the tested end-mill. The six circles mark the magnitude of flank wear for the six individual flutes for the test cut lengths. The difference in magnitude of wear between flutes is presented by the shaded region. The difference in magnitudes for the wear is due to the runout.

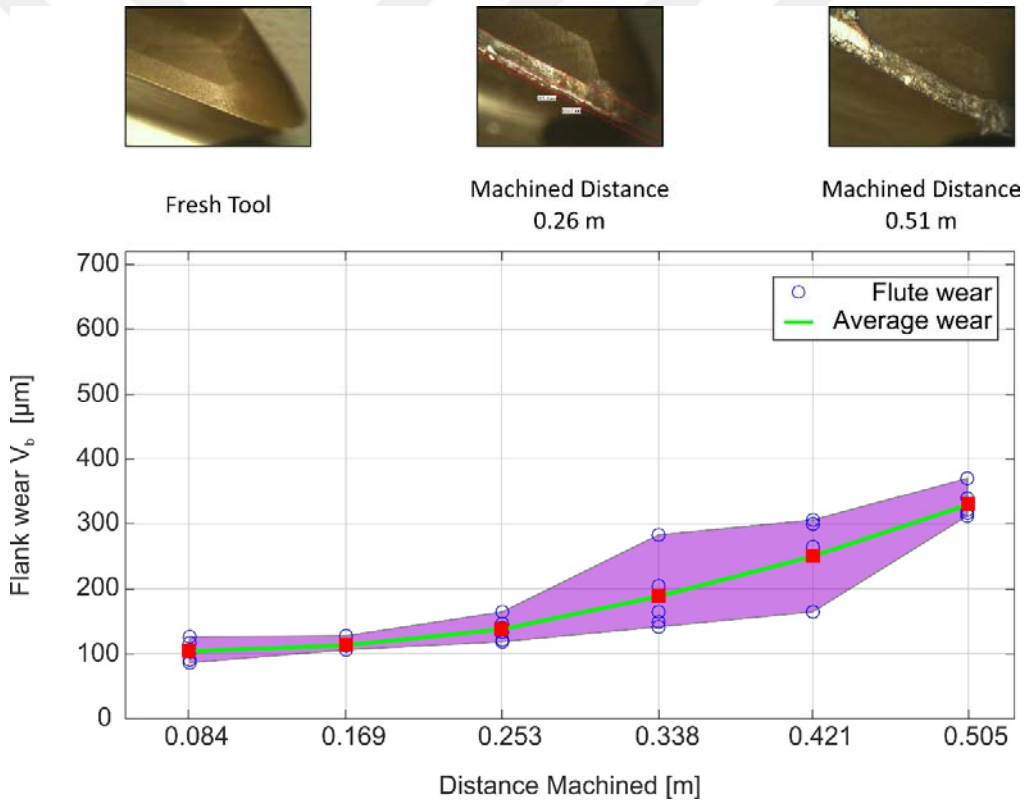

Figure 3-48: The flank land wear for the Alp Aviation ceramic end-mill.

The end-mill cutting edges where examined by scanning electron microscopy and energy dispersive spectroscopy to confirm the built-up-edge and the wear mechanism. The workpiece material adhesion to the Kennametal ceramic end-mill was the least of the three-tested monolithic ceramic end-mills.

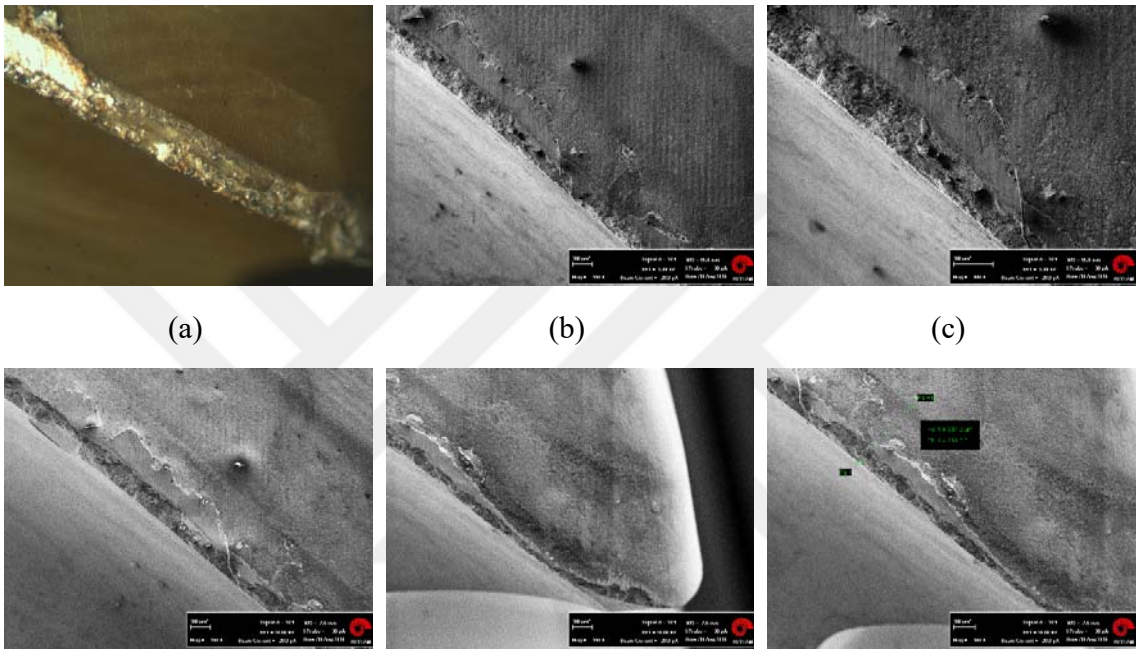

(a) (b) (c)

(d) (e) (f)

Figure 3-49: The flank side of the cutting edge for the Kennametal ceramic end-mill.

The Figure 3-49 (a) is showing the flank side of the cutting edge for the Kennametal ceramic end-mill from the optical microscope. The Figure 3-49 (b) to (f) are the scanning electron microscope images of the same region on the end-mill corner and the flank side.

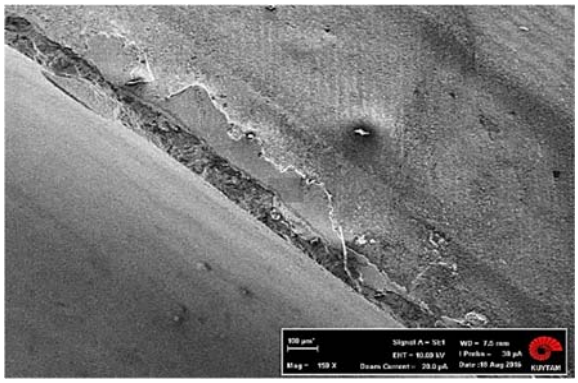

(a)

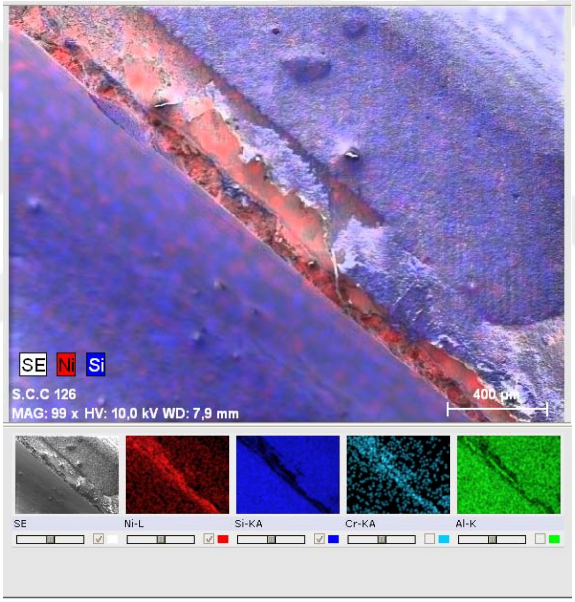

(b)

Figure 3-50: The EDS of the flank side of the cutting edge for the Alp aviation ceramic end-mill.

The energy dispersive X-ray spectroscopy scans of the flank side of the cutting edge for the Kennametal ceramic end-mill confirmed presence of nickel on the cutting-edge flank side, confirming the adhesion of the Inconel 718 workpiece. The Figure 3-50 (a) is the

scanning electron optical microscope image of the end-mill flank side. Image (b) is the EDS scan, where silicon and nickel element are pre-selections. The silicon material is represented with green color data points and the nickel element is represented by the red color detection points in the Figure 3-51.

The ceramic elemental composition was performed and the EDS detection count plot is shown in the Figure 3-51 and the percentage values are given in the Table 3-27.

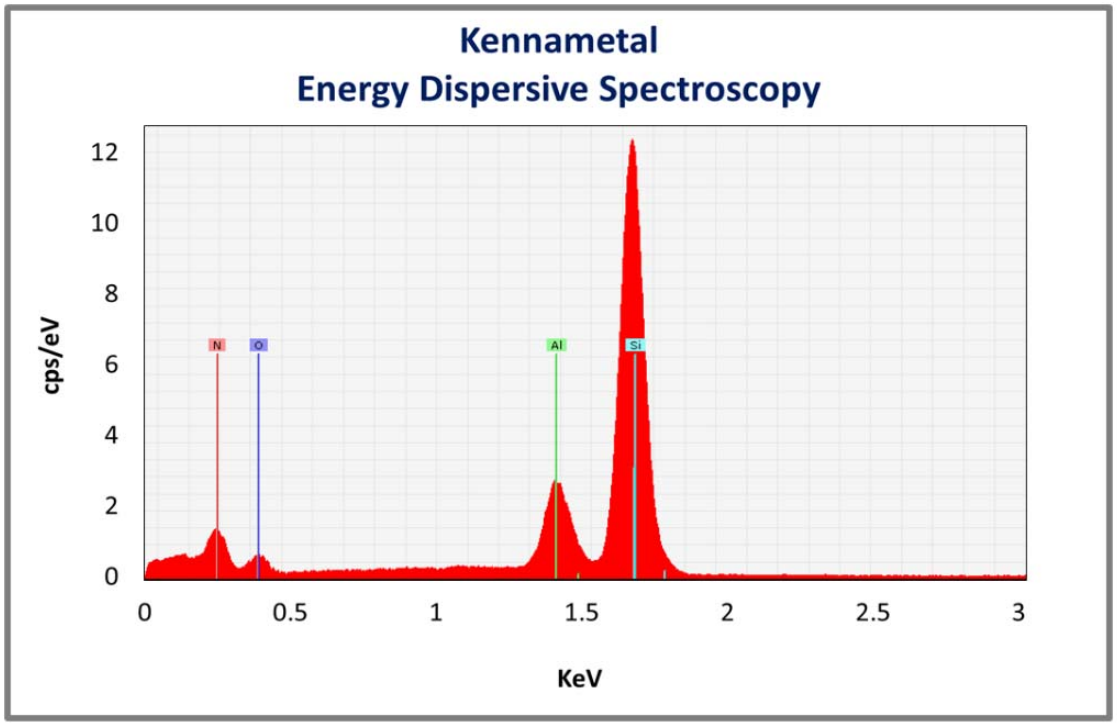

Figure 3-51: Detection count for respective elements for the Kennametal ceramic end-mill.

The ceramic elemental composition was performed and the EDS detection count plot is shown in Figure 3-51 and the percentage values are given in the Table 3-28.

Table 3-28: The elemental composition for the Kennametal ceramic end-mill.

Element	Net count	Normalized with Carbon [wt.%]	Normalized with Carbon Atomic number [at.%]	Error (1 Sigma)
N (7)	12074	24.90	38.33	2.52
O (8)	5010	6.47	8.72	0.76
Al (13)	29490	8.38	6.70	0.30
Si (14)	138039	60.23	46.23	1.83
	Total:	100%	100%	

3.2.1.4 Wear Conclusion

The Figure 3-52 combines the average wear for the tested three monolithic ceramic end-mills. The Mitsubishi ceramic end-mill showed the most accelerated wear of the three monolithic ceramic end-mills. The Mitsubishi ceramic end-mill wear rate was 816 $\mu m/m$. The Kennametal ceramic end transitioned to the accelerated wear rate approximately after 0.25 m of machined length to the wear rate of 800 $\mu m/m$. The Alp aviation monolithic ceramic end-mill maintained a steady wear rate of 580 $\mu m/m$ for the total length machined.

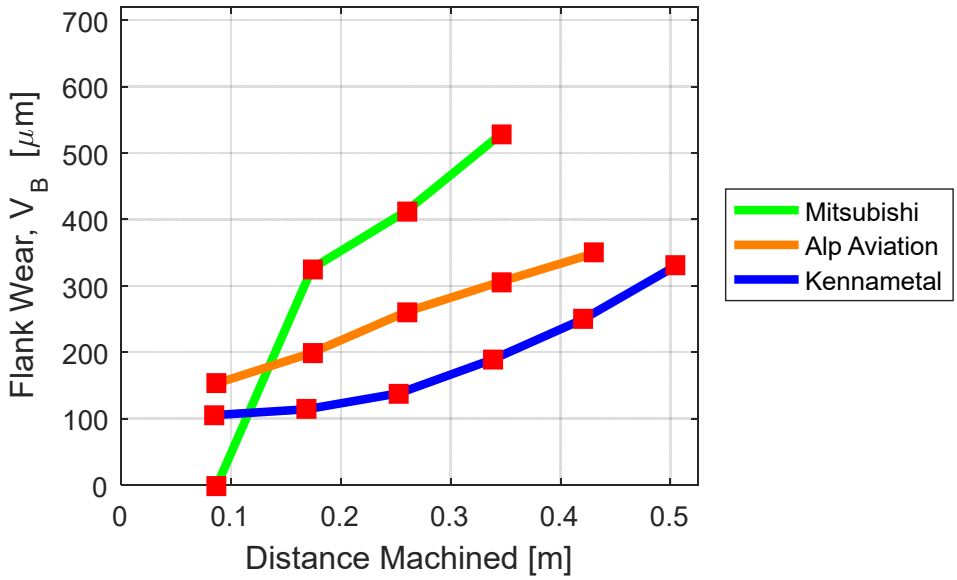

Figure 3-52: The comparison of the end-mill flank wear.

The average built-up-edge for the Mitsubishi ceramic end-mill was 165 μm. The size of the built-up-edge for the Mitsubishi end-mill was 2.5 times more than the Alp aviation ceramic end-mill. The size of the built-up-edge on the Kennametal ceramic end-mill was not recognized probably because the integrity of the cutting edge may have been compromised.

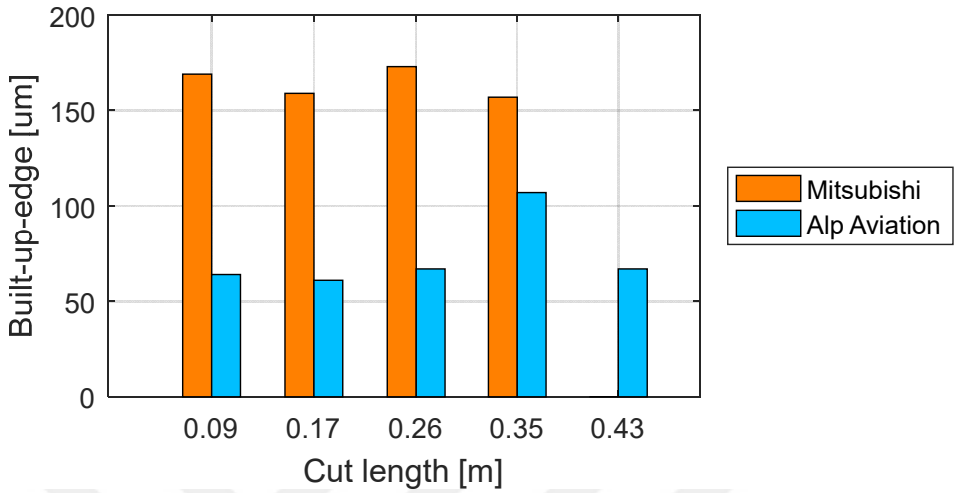

Figure 3-53: Comparison of Built-up edge for the ceramic end-mills when machining Inconel.

The percentile elemental composition of the three monolithic ceramic end-mills is given in the Table 3-29. The SiAlONs exist in two phases, namely, the α and the β phases. Some rare earth elements are added as sintering agent. Nevertheless, the Table 3-29 provides a comparison of the three tested ceramics.

Table 3-29: The elemental composition of the three monolithic ceramic end-mills.

Element	Kennametal	Mitsubishi	Alp Aviation
N (7)	38.33	52.47	52.53
O (8)	8.72	7.74	12.39
Al (13)	6.70	2.45	4.31
Si (14)	46.23	37.34	30.77

3.2.2 Cutting Forces

The cutting forces were recorded during the wear test of the end-mills with Kistler table type dynamometer as shown in the Figure 3-54. The magnitudes of cutting forces increased with the increase in wear on the end-mills.

Figure 3-54: Workpiece setup on table type dynamometer.

The average of the resultant planar of the cutting forces for each length for the three tested tools is shown in the Figure 3-52.

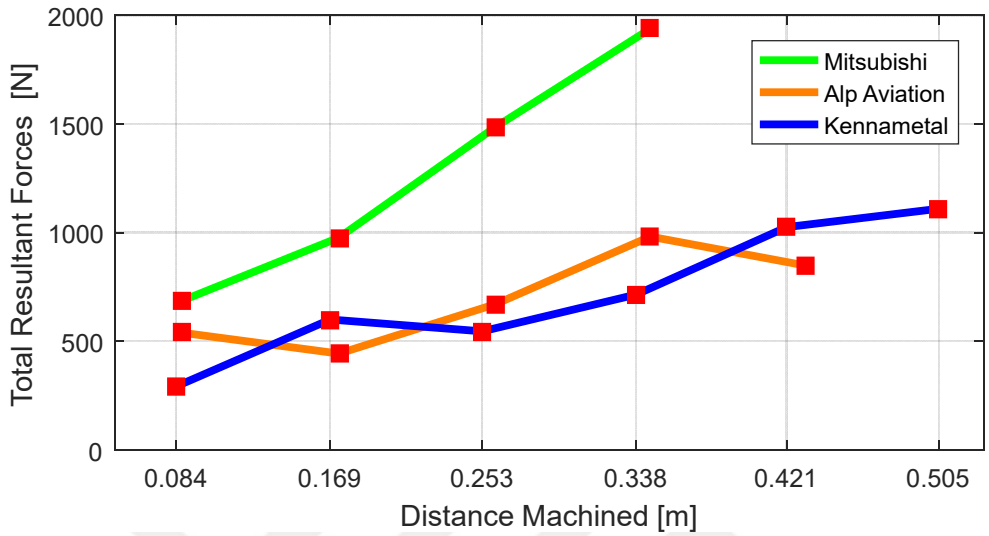

Figure 3-55: The progression of the cutting forces (planar resultant).

The cutting forces showed strong increasing trend for the Mitsubishi ceramic end-mill. The alp aviation and the Kennametal ceramic endmill also demonstrated an increasing trend in the cutting forces but much slower than the Mitsubishi ceramic end-mill. Also it is to be noted that strong dynamic behavior is observed in the recorded forces data as shown in the Figure 3-56.

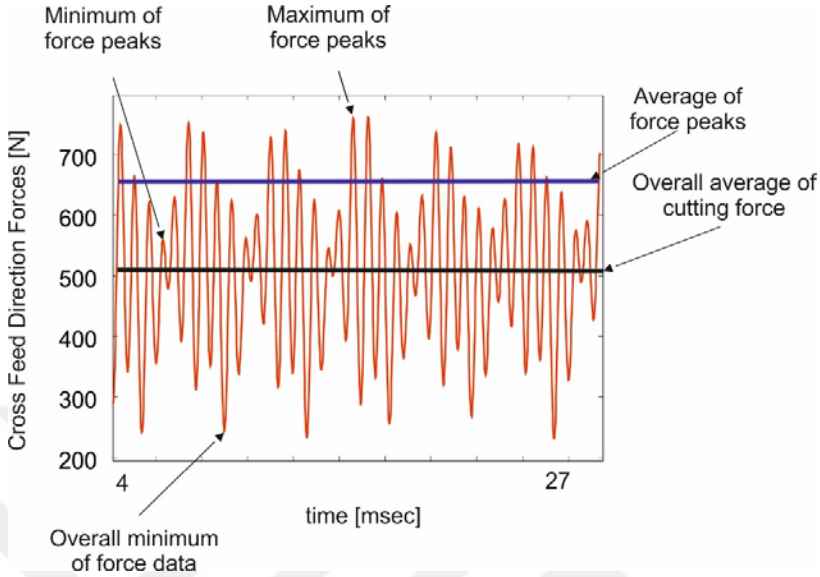

Figure 3-56: The planar resultant of the cutting forces for the Kennametal ceramic end-mill and the force nomenclature used for comparison.

The average and maximum of the peak of the planar resultant of the cutting forces data for the tested end-mills is compared in the Table 3-30 and the Table 3-31.

Table 3-30: The average of the peak forces for the planar resultant of the cutting forces when machining Inconel 718.

Planar Resultant of the Cutting force Average peak value [N]			
	Mitsubishi	Alp	Kennametal
Test 1	1232	839	455
Test 2	1827	574	1091
Test 3	2641	1015	705
Test 4	3232	1587	1150
Test 5	X	1398	1793
Test 6	X	X	1971

Table 3-31: The maximum of the peak forces for the planar resultant of the cutting forces when machining Inconel 718.

Planar Resultant of the Cutting force Maximum peak value [N]			
	Mitsubishi	Alp	Kennametal
Test 1	2020	1420	933
Test 2	2244	1101	1567
Test 3	3923	1370	1230
Test 4	4111	2022	1795
Test 5	X	1819	2164
Test 6	X	X	2480

Table 3-32: The average of the peak forces as the percentage of the maximum the peak forces for the planar resultant of the cutting forces when machining Inconel 718.

Planar Resultant of the Cutting force Maximum peak value [N]			
	Mitsubishi	Alp	Kennametal
Test 1	61%	59%	49%
Test 2	81%	52%	70%
Test 3	67%	74%	57%
Test 4	79%	78%	64%
Test 5	X	77%	83%
Test 6	X	X	79%

The Table 3-32 provides a measure for the dynamic behavior of the ceramic end-mill. Smaller the number in the Table 3-32, the stronger is the dynamic behavior of the particular end-mill. The vibrations of the Kennametal monolithic ceramic end-mill had the largest amplitudes followed by the Alp aviation ceramic end-mill and then the Mitsubishi ceramic end-mill.

3.3 Conclusion

The material removal rate for machining Inconel 718 was improved by 25%. The optimum geometry parameters were identified by the parametric analysis of the end-mill geometry for minimum cutting force concentration on the cutting edges of the end-mill. A conservative solution was selected for the number of flutes for the 24 mm end-mill. With the confirmation of the simulations, it warrants to evaluate the 18-flute design.

The primary mode of end-mill wear was chipping and fracture of the cutting edge for the high-speed milling of Inconel 718 superalloy.

Chapter 4
Machining of Titanium Alloy Ti6Al4V

4.1 Introduction:

The milling of titanium alloy Ti6Al4V using coated solid carbide end-mills is investigated. The performance of two coating materials, namely, aluminum titanium nitride and aluminum chromium nitride were evaluated. There are three end-mills for each coating type. These three end-mills have been produced using three different surface finishing techniques. The surface techniques are commonly employed in carbide tool manufacturing industry. The surface finish techniques explored for this thesis are the finish with magnetic powder, drag finish and the wet sandblast finish. The complete list of tools tested is given in the Table 4-1.

Table 4-1: The end-mills tested for machining Ti6Al4V.

	Coating material	Finishing technique
1	Aluminum Titanium Nitride, (AlTiN)	Finishing with magnetic powder (FPM)
2		Drag Finishing (DF)
3		Wet Sandblast Finishing (WSF)
4	Aluminum Chromium Nitride, (AlCrN)	Finishing with magnetic powder (FPM)
5		Drag Finishing (DF)
6		Wet Sandblast Finishing (WSF)
7	No Coating	Finishing with magnetic powder (FPM)

This study involves the evaluation of the surface finish technique and surface coating on the performance of solid carbide end-mill when machining the titanium alloy Ti6Al4V.

Figure 4-1: The 8 tools tested for best performance.

4.1.1 Coatings

The performance of two coating materials is investigated for this thesis, namely aluminum titanium nitride, AlTiN and aluminum chromium nitride, AlCrN. Coating materials with higher concentrations of aluminum are preferred for hard-to-machine materials as such coatings produce an oxidation inhibiting and wear resistant aluminum oxide layers on the tool's cutting surfaces. AlTiN typically have aluminum concentrations in access of 50%. The titanium based nitrides tend to have a limit to the amount of aluminum it can accommodate before the crystal structure changes. The crystal structure of the alloy changes from cubic centered to hexagonal lattice beyond a certain threshold value of aluminum concentration, resultantly effecting the mechanical properties of the coating (Kimura et al., 1999). The chromium as a replacement for titanium presents the possibilities of higher percentages of aluminum to be present in the coating compound. The increased aluminum holds the promise of better wear resistance and hot hardness.

4.1.2 Surface Finishing Techniques

The finishing with magnetic powder (FMP) techniques, sometimes called the magnetic abrasive polishing, uses magnetic abrasive grains or pins suspended in a loose media. And when the medium is agitated by either changing the magnetic field or moving the magnetic field all together (Gillespie, 2006), it slowly chips away workpiece material to produce a very fine finished surface. The low volume removal rates produce high luster and tight geometric conformity. The sharpness of the cutting-edge radius is essential feature of the solid carbide end-mill design and rightfully desired. The finishing with magnetic powder (FMP) technique is suited for high precision finishing of solid carbide end-mills.

The drag finishing (DF) technique has found increased application as an alternative to more conventional polishing methods for high quality and sensitive parts. Specially where the parts are restricted from coming in contact with each other during processing (Barletta et al., 2015). The magnitudes of the cutting-edge radius have direct impact on cutting forces and temperature. A polishing technique that would secure the geometric detail of the cutting edge is of utmost importance. drag finishing (DF) is capable of producing sub-micron level surface finish and fittingly selected as a candidate for producing the final finish on solid carbide end-mills.

The third and last surface finishing technique selected for this investigation is the sandblast finishing technique. The blasting techniques has been around and commonly employed and many varied industries.

The performance of the manufactured end-mills was evaluated. The performance and manufacture of the tested tools were compared on the following

1. Cutting Forces.
2. Wear.

4.2 Cutting forces

The performance of the differently coated and differently manufactured end-mills is evaluated for the cutting forces recorded during machining tests. The tests were conducted for different feedrates and repeated three times each for reliability.

4.2.1 Setup

The cutting tests were performed on Mori Seiki NMV5000 DCG 5-axis milling machine shown in the Figure 4-2. The work piece is prepared for secure mounting on top of the table type dynamometer. Whereas the cutting tool is held in tool-holder and Rotary type dynamometer assembly. The test setup is shown in Figure 4-3. The force data were acquired using Kistler Table type dynamometer whereas rotary type dynamometer provided the power consumption and torque. Kistler company signal conditioning modules were employed for accurate and reliable sensor signals. High speed Data Acquisition System from National Instruments is used to collect the signals at 5000 Hz sampling rate.

Figure 4-2: Experimental tests were performed on Mori Seiki NMV5000DCG 5-axis milling machine.

Figure 4-3: Ti-6Al-4V Workpiece setup with Rotary type and Table type dynamometers.

4.2.2 Cutting Parameters

The cutting forces and torques were measured twice for each of 5 feedrates selected for the investigation to improve data reliability. For the initial assessment the following cutting conditions were selected:

Table 4-2: Test setup parameters.

Cutting Parameters		
Material		
Ti 6Al 4V		
Tool		
Type	Flat	
Diameter	12	mm
Number of Flutes	4	
Helix angle	36.5	deg

Table continued…

Cutting Conditions		
Spindle Speed	1300	rpm
Cutting Speed	49	m/min
Depth of cut	1	mm
Width of cut	12	mm
Feedrates	a) 26 b) 52 c) 95 d) 112 e) 130	mm/min

4.2.3 Results and discussion

Forces and torque data were acquired from 124 test zones on the Ti6Al4V test specimen from the test setup shown in Figure 4-3. The Forces and torque data were then analyzed to select the best performance for the (a) surface finish technique, (b) coating material and (c) the cutting-edge geometry.

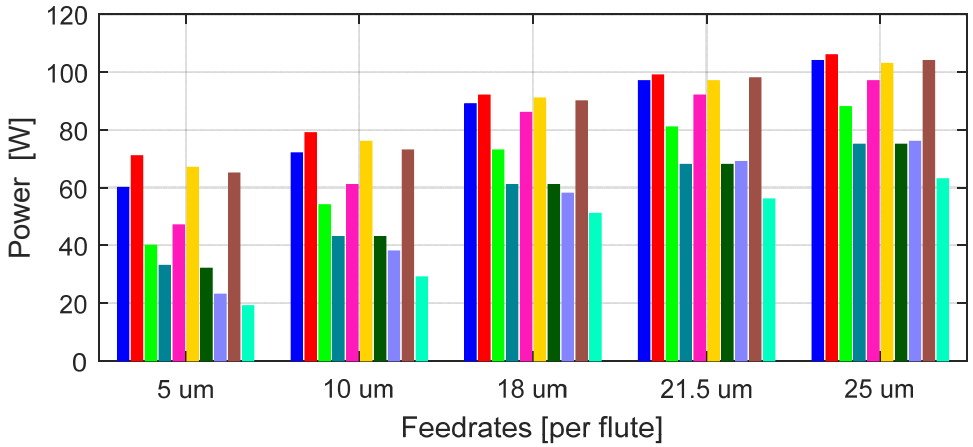

Figure 4-4: The power consumption for the tested end-mills.

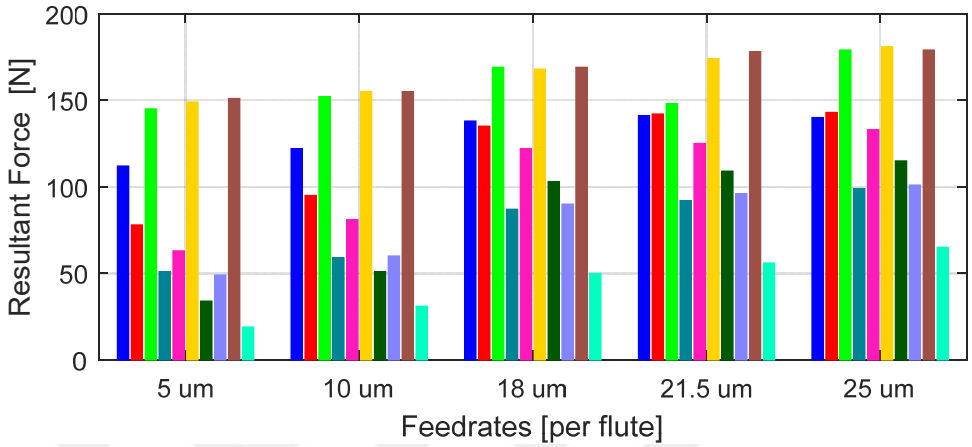

Figure 4-5: The resultant of the cutting forces for the tested end-mills.

Table 2 and Table 3 provide the overall ranking for the five selected feedrates in terms of power consumption and resultant force respectively.

Table 4-3: Tools sorted from best performance to worst with respect to the power consumption.

Resultant Force [N]								
			Feedrate [mm/min]	130	112	95	52	26
1	Karcan	No Coat	Preliminary clearance removed	63	43	37	16	5
2	Karcan	No Coat	Magnetic Finish	75	55	48	30	19
3	Karcan	AlTiN	Magnetic Finish	75	55	48	31	21
5	Karcan	AlTiN	Drag Finish	88	65	57	38	24
6	Karcan	AlCrN	Drag Finish	97	78	72	47	34
7	Karcan	AlTiN	Wet Sandblast	103	84	78	63	54
8	Karcan	AlCrN	Magnetic Finish	104	81	73	56	44
9	Karcan	No Coat	1 deg clearance	104	83	75	58	50
10	Karcan	AlCrN	Wet Sandblast	106	85	78	65	57

The removal of the preliminary clearance angle produced significant improvement in the performance of the end-mill for machining titanium alloy Ti6AlV4.

Table 4-4: Tools sorted from best performance to worst with respect to the resultant force.

Resultant Force [N]								
			Feedrate [mm/min]	130	112	95	52	26
1	Karcan	No Coat	Preliminary clearance removed	44	52	50	23	19
2	Karcan	No Coat	Magnetic Finish	90	82	76	59	46
3	Karcan	AlTiN	Magnetic Finish	98	89	68	63	42
5	Karcan	AlTiN	Drag Finish	118	110	106	78	56
6	Karcan	AlCrN	Drag Finish	143	142	135	95	78
7	Karcan	AlCrN	Magnetic Finish	137	135	127	114	101
8	Karcan	AlCrN	Wet Sandblast	172	166	160	145	134
9	Karcan	No Coat	Preliminary clearance	173	176	159	151	142
10	Karcan	AlTiN	Wet Sandblast	173	163	161	148	134

4.2.3.1 Comparison of Finish techniques:

Figure 4-6 and Figure 4-7 show the advantage magnetic finish has over the other finishing techniques. The Magnetic Finish based tools performed best consistently for all feedrates while the wet sandblast finished tools performed poorly, for all the end-mills having the same coating material.

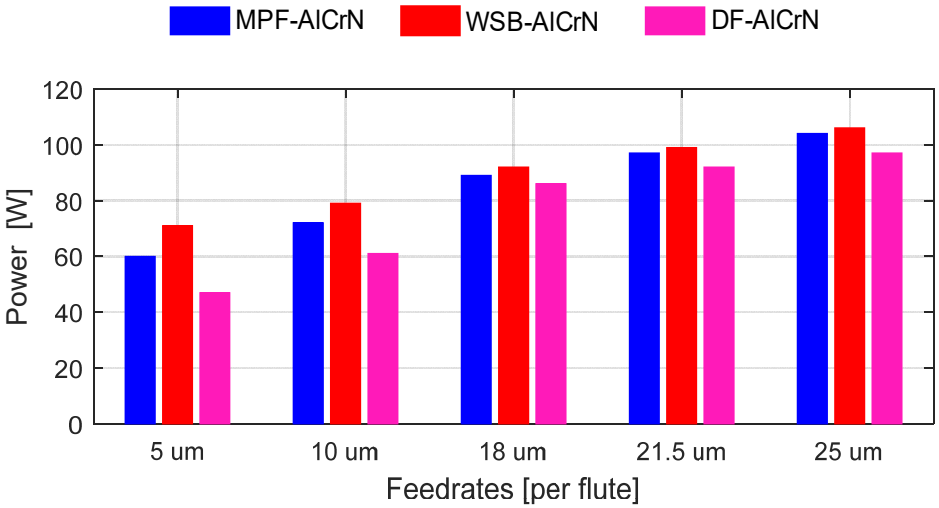

Figure 4-6: Comparison of power for end-mills with AlCrN type coating.

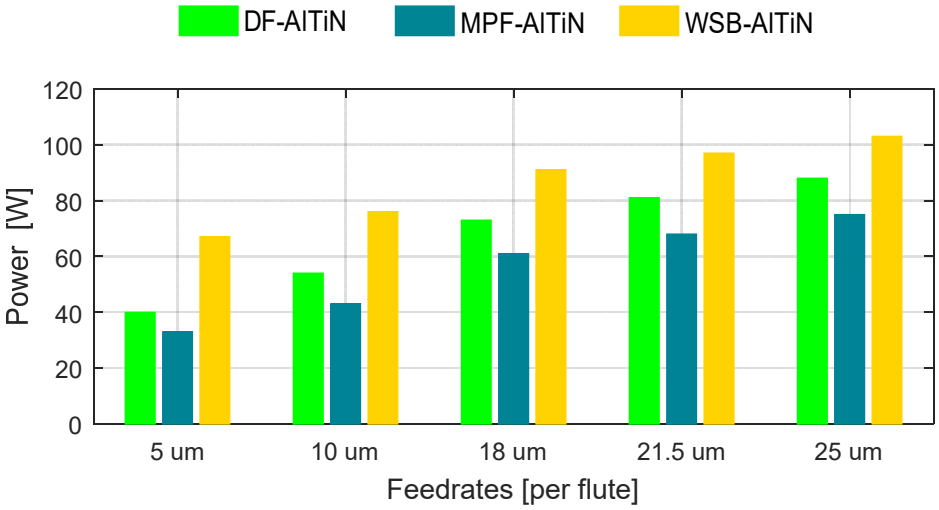

Figure 4-7: Comparison of power for end-mills with AlTiN type coating.

4.2.3.2 Comparison of Coatings:

The effect of the coating material shown in Figure 4-8, Figure 4-9 and Figure 4-10.

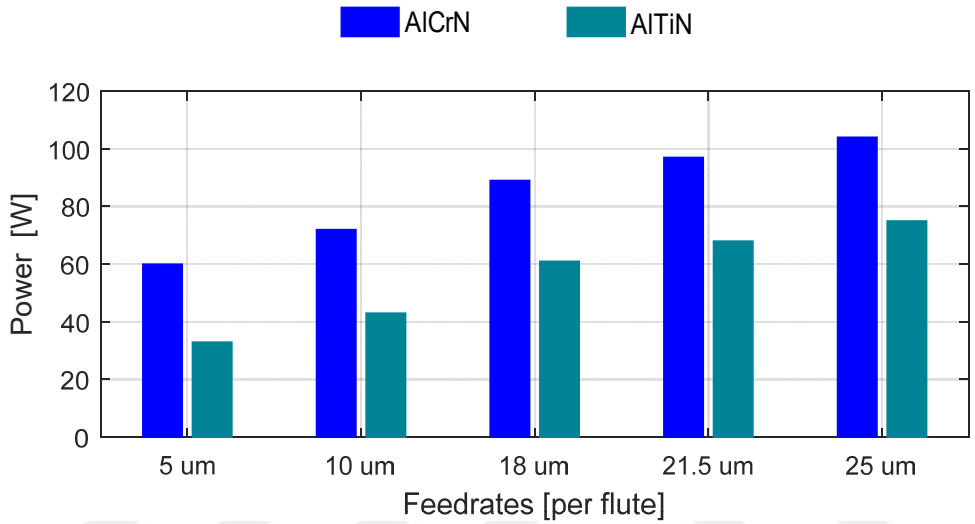

Figure 4-8: Performance of magnetic finish tool.

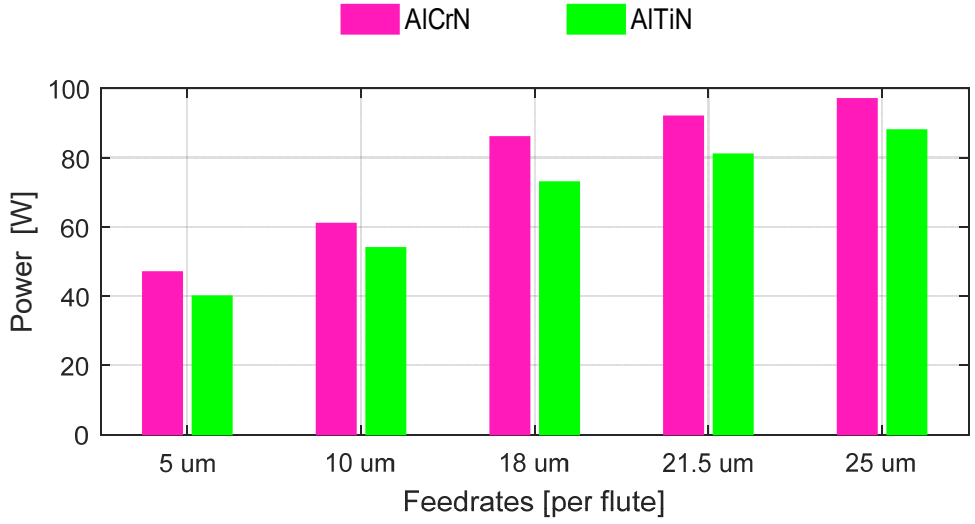

Figure 4-9: Performance of drag finish tools.

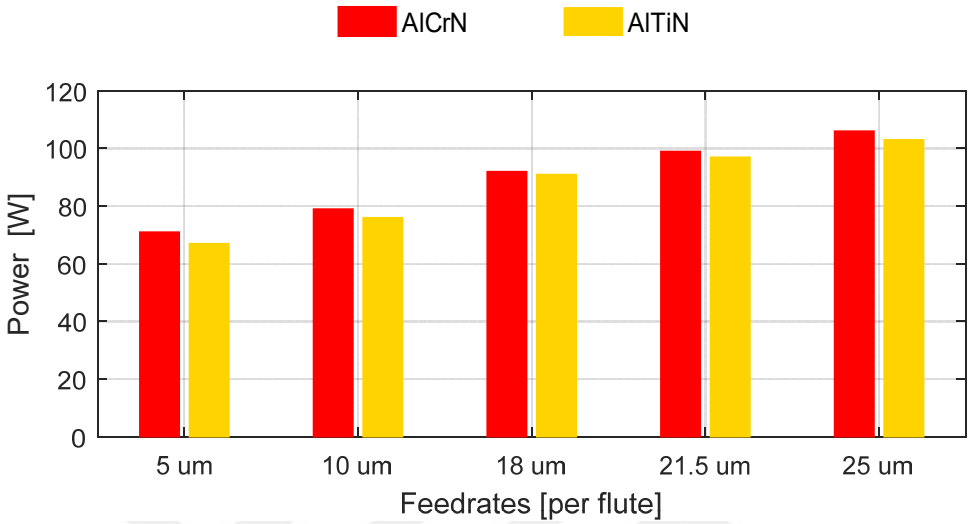

Figure 4-10: Performance of wet sandblast finish tools.

The test results shown in Figure 4-8, Figure 4-9 and Figure 4-10 show that the AlTiN based coating required lesser power than its counterpart, the AlCrN based coating for all tests consistently.

4.2.3.3 Burr Formation

The respective machined surface pictures for each tested tool are given in the Table 4-5. The rank column is providing the ranking of the tested tools with respect to power consumption.

Table 4-5: Burr formation results for all tested tools.

Rank	Coating	Finish	Batch	Machined regions
8	AlCrN	Magnetic Finish	B1	
10	AlCrN	Wet Sandblast	B2	
5	AlTiN	Drag Finish	B3	
3	AlTiN	Magnetic Finish	B4	
6	AlCrN	Drag Finish	B5	
7	AlTiN	Wet Sandblast	B6	
2	No Coat	Magnetic Finish	B7	
9	No Coat	1° clearance	B9	
1	No Coat	Preliminary clearance removed	B10	
Feedrate [mm/min]				130 | 112 | 95 | 52 | 52 | 26 | 26

4.2.3.4 Flank side Clearance angle:

The influence of the flank land clearance angle on the cutting forces was evaluated. The two end-mill cutting edge geometries are given in Figure 4-11 and Figure 4-12. Tests were performed to investigate the effect of the geometry modification. Increasing the flank side clearance angle by removing the 1° preliminary clearance angle improved the end-mill performance significantly as shown in Table 4-6.

Table 4-6: Effect of geometry change.

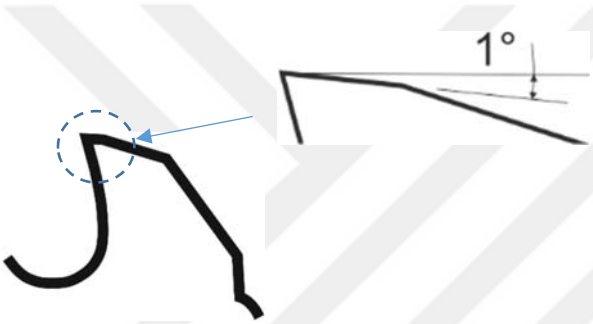

Figure 4-11: Cutting edge geometry with 1° preliminary clearance angle.

Figure 4-12: Cutting edge geometry with preliminary clearance angle removed.

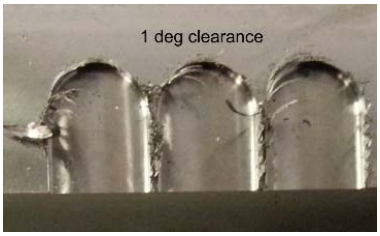

Figure 4-13: The machined surface from cutting edge with 1° preliminary clearance angle.

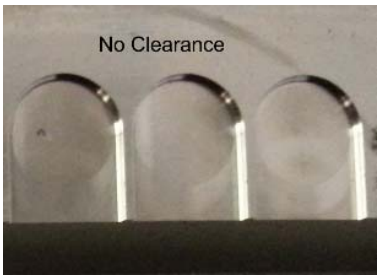

Figure 4-14: The machined surface from cutting edge with the preliminary clearance angle removed.

Table 4-7: The improvement shown by increasing the flank side clearance.

	mm/min	26	52	95	112	130
Power [W]	1° clearance angel	50	58	75	83	104
	7° clearance angel	5	16	37	43	63
Resultant Force [N]	1° clearance angel	142	151	159	176	173
	7° clearance angel	19	23	50	52	44

4.2.4 Conclusion

The investigation of machining Titanium alloy with Karcan cutting tools consisted of 124 tests. The following conclusions are deduced from the study and analysis of the respective test datasets.

1. The uncoated tool with the increased radial clearance angle on cutting edge geometry recorded the least power consumption and resultant force among all the tested tools.
2. The removal of the preliminary clearance angle produced significant improvement in the performance of the end-mill for machining titanium alloy Ti6AlV4
3. The magnetic finish based tools consistently performed best in all the cases for both types of coatings in the tested tools.
4. The wet sandblast finished tools performed poorly for both types of coatings in all the tested feedrates.

5. The AlTiN based coating required lesser torque than AlCrN based coating consistently for all tested feedrates.

6. The wet sandblast finish had the highest value for power consumption and appears to have the worst case of chip adhesion.

7. The AlCrN based coating performed poorer than in terms of chip adhesion.

4.3 Wear

The tool life is the main contributor towards manufacturing costs, any improvement in it has a direct influence over the costs. Accurate estimation of tool life will also guard against catastrophic failures. Such failures may damage the workpiece requiring further repair work if not all together a replacement. The proper understanding of the wear and wear mechanisms will facilitate better tool design with improved life.

There are several mechanisms contributing towards tool wear. Tool wear may occur because of a single dominating mechanism or it may be a result of combination of mechanisms. The main types of wear mechanisms are abrasion wear, adhesion wear and diffusion wear.

4.3.1 Setup:

The cutting tests were performed on Mori Seiki NMV5000 DCG 5-axis milling machine. The setup is shown in Figure 4-15. The workpiece was prepared for secure mounting on top of the table type dynamometer. The force data were acquired using Kistler Table type dynamometer. Kistler company signal conditioning modules were employed for accurate and reliable sensor signals. High speed Data Acquisition System from National Instruments is used to collect the signals at 5000 Hz sampling rate.

Figure 4-15: Experimental tests were performed on Mori Seiki NMV5000DCG 5-axis milling machine.

4.3.2 Cutting Parameters

The flank wear for the tested tools was measured after every test cut length. The cutting forces were recorded for each test as well. The coating and finish technique are given in the Table 4-8

Table 4-8: The end-mills tested for wear when machining Ti6Al4V.

	Coating material	Finishing technique
1	Aluminum Titanium Nitride, (AlTiN)	Finishing with magnetic powder (FPM)
2		Drag Finishing (DF)
3		Wet Sandblast Finishing (WSF)
4	Aluminum Chromium Nitride, (AlCrN)	Finishing with magnetic powder (FPM)
5		Drag Finishing (DF)
6		Wet Sandblast Finishing (WSF)
7	No Coating	Finishing with magnetic powder (FPM)

Cutting conditions selected for wear analysis of the tested tools are given in Table 4-9. The test cut lengths are given in Table 4-10.

Table 4-9: Test setup parameters.

Material		
Ti 6Al 4V		
Tool		
Type	Flat	
Diameter	12	mm
Number of Flutes	4	
Helix angle	36.5°	
Cutting Conditions		
Spindle Speed	1300	rpm
Cutting Speed	49	m/min
Depth of cut	1	mm
Width of cut	6	mm
Feedrates	130	mm/min

Table 4-10: The tool flank wear was measured at these cut lengths.

	Accumulated length [m]	Machining time [min]	Volume removed [cm^3]
Cut Length 1	0.408	3.14	2.448
Cut Length 2	0.816	6.28	4.896
Cut Length 3	1.224	9.42	7.344
Cut Length 4	1.632	12.56	9.792
Cut Length 5	2.04	15.7	12.24
Cut Length 6	2.448	18.84	14.688
Cut Length 7	2.856	21.97	17.136
Cut Length 8	3.264	25.11	19.584
Cut Length 9	3.672	28.25	22.032
Cut Length 10	4.080	31.39	24.48
Cut Length 11	4.488	34.53	26.928
Cut Length 12	4.896	37.67	29.376
Cut Length 13	5.304	40.8	31.824

4.3.3 Test Data and Analysis

The flank wear was recorded for the four flutes of all tested tools after a cut length of 0.4m using Nikon SMZ 645 stereoscopic zoom microscope. The progressing flank wear magnitudes are shown in the plots and given in Table 4-11 and Table 4-12.

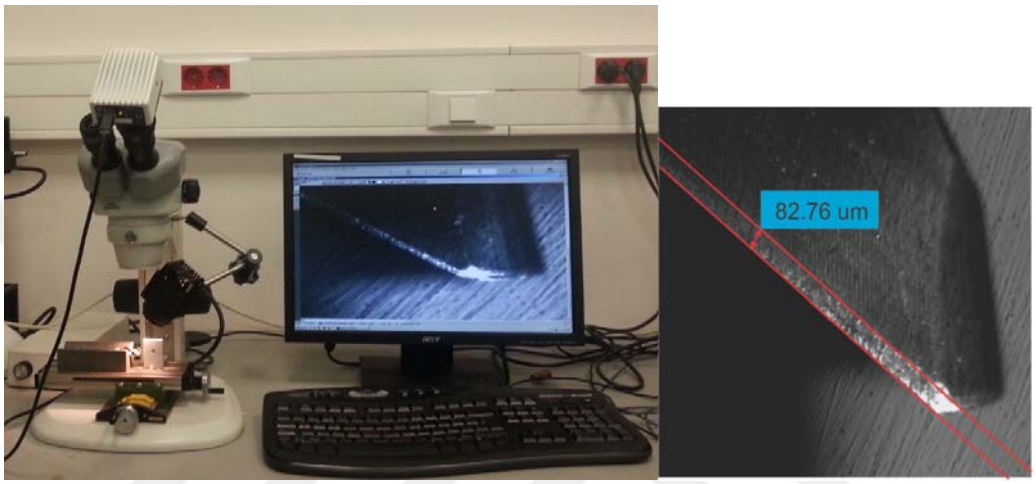

Figure 4-16: Stereoscopic zoom microscope was used for flank wear measurement.

Table 4-11: Average flank wear of all flutes of tested tools for each test cut length (all magnitudes are in microns).

Test cut length [m]	No Coating	AlTiN	AlCrN	AlCrN	AlTiN	AlCrN	AlTiN
	Magnetic Finish			Drag Finish		Wet Sandblast Finish	
0.4	34	67	74	38	69	69	100
0.8	36	69	78	44	72	76	108
1.2	36	70.9	80	52	75	78	110
1.6	37	71.4	82	54	76	79	111
2	38	71.9	83	57	77	80	117
2.45	39	74	86	59	78	81	Testing Stopped
2.9	39	75	87	60	78	82	
3.3	40	77	88	63	80	87	
3.7	41	77	89	64	81	88	
4.1	42	78	90	66	82	89	
4.5	42	79	94	67	82	90	
4.9	43	80	97	67	Testing Stopped	91	
5.3	43	81	97	68		93	

Table 4-12: Flank wear for each flute for the test cut lengths (all magnitudes are in microns).

Test cut length [m]	No Coating	AlTiN	AlCrN	AlCrN	AlTiN	AlCrN	AlTiN
	Magnetic Finish			Drag Finish		Wet Sandblast Finish	
0.4	28.32	65.8	84.03	31.64	62.51	76.98	101.0
	41.27	62.4	62.05	46.06	77.19	68.38	101.2
	33.46	61.75	78.72	31.64	63.77	70.7	94.4
	33.66	78.2	71.18	44.04	73.9	60.41	103.8
0.8	30.88	69.6	89.37	43.53	63.77	80.51	114.9
	41.53	64.11	66.56	48.59	80.98	79.76	102.5
	36.75	62.04	82.51	38.21	67.82	75.71	106.3
	35.92	79.22	72.89	45.06	75.67	66.33	107.3
1.2	30.9	72.45	90.35	46.82	66.58	82.51	115.4
	41.88	69.09	69.09	56.44	82.51	80.22	105.3
	37.25	62.7	87.83	51.43	72.43	79.9	108.9
	35.92	79.47	73.35	52.64	77.81	69.4	110.1

Continued…

Test cut length [m]	No Coating	AlTiN	AlCrN	AlCrN	AlTiN	AlCrN	AlTiN
	Magnetic Finish			**Drag Finish**		**Wet Sandblast Finish**	
1.6	31.5	72.98	91.12	48.85	66.75	83.2	117.4
	42.23	69.58	72.89	58.46	82.79	81.75	105.8
	37.25	63.08	88.33	52.14	74.4	80.75	109.6
	36.87	80.11	75.18	58.53	79.22	70.35	113.1
2	32.9	73.51	92.38	52.11	69.09	85.31	119.0
	42.5	70.07	74.93	61.24	83.01	82.02	115.1
	38.21	63.45	89.53	56.17	75.3	80.75	119.5
	40.27	80.74	76.93	58.64	79.47	71.38	113.4
2.45	33.01	73.68	92.38	52.91	69.75	86.57	Testing Stopped
	42.76	75.93	78.46	61.37	83.5	82.27	
	38.67	63.02	90.48	59.98	76.18	83.01	
	41.56	83.7	83.01	61.77	82.25	71.62	
2.9	33.64	75.67	92.56	53.53	69.75	87.83	Testing Stopped
	43.56	77.24	79.47	62.82	83.5	82.27	
	38.67	64.29	91.36	60.44	77.96	84.04	
	41.64	84.54	83.51	63.72	82.3	72.62	
3.3	34.75	75.67	93.41	59.65	70.35	87.83	
	44.5	78.46	80.22	63.38	85.04	82.39	
	38.78	67.62	92.85	60.65	80.22	89.09	
	41.8	84.75	84.03	66.67	82.51	88.83	

Continued…

Test cut length [m]	No Coating	AlTiN	AlCrN	AlCrN	AlTiN	AlCrN	AlTiN
	Magnetic Finish			**Drag Finish**		**Wet Sandblast Finish**	
3.7	38.07	75.8	94.91	60.28	71.11	88.83	
	44.5	79.54	82.51	65.42	87.83	82.76	
	40.07	67.62	93.14	60.89	81.53	89.59	
	42.5	85.04	85.64	67.92	83.01	90.85	
4.1	39.28	79.47	94.91	61.43	72.38	90.12	
	44.7	80.85	83.51	67.92	89.86	82.76	
	40.24	68.26	93.92	61.93	82.25	92.64	
	42.67	85.04	87.07	70.74	83.77	92.12	
4.5	39.67	80.01	95.17	61.68	72.77	91.62	
	44.89	81.75	84.54	70.74	89.86	82.9	
	40.53	68.33	95.67	62.28	82.25	94.14	
	42.9	85.04	98.65	71.56	83.77	92.63	
4.9	40.8	80.22	95.67	62.24	Testing Stopped	92.38	
	45.08	84.04	94.91	71.2		83.25	
	40.76	69.09	95.67	62.93		94.69	
	43.8	87.06	100.2	73.24		92.63	
5.3	42.1	80.22	95.67	63.72		92.59	
	45.56	84.53	95.18	72.77		83.51	
	40.95	70.09	96.43	63.38		98.47	
	44.2	87.4	100.2	74.02		95.92	

4.3.3.1 Flank wear plots

The following figures from the Figure 4-17 to the Figure 4-23 show the progressing trend in flank wear as the test progressed. The solid line represents the average measure for the flank wear for the four flutes of a tested tool. The four asterisks mark the magnitude of flank wear for each flute for the test cut lengths. The flank wear region as represented by the shaded area, accounts for the tool runout effect.

100 μm was set as a benchmark to compare the performance of the coating materials and finish techniques. A discussion of the results is given when the plots are compared in subsequent section.

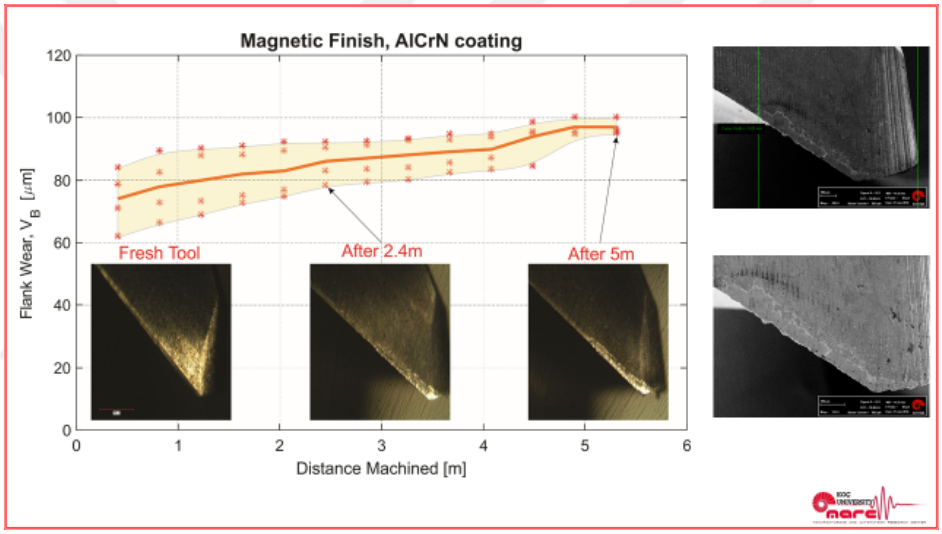

Figure 4-17: Flank wear for magnetic finish and AlCrN coating end-mill.

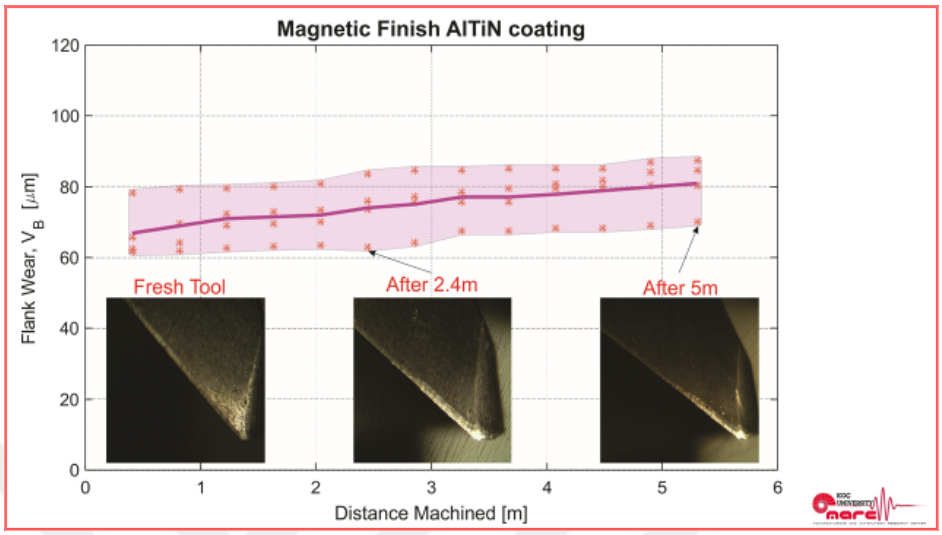

Figure 4-18: Flank wear for magnetic finish and AlTiN coating end-mill.

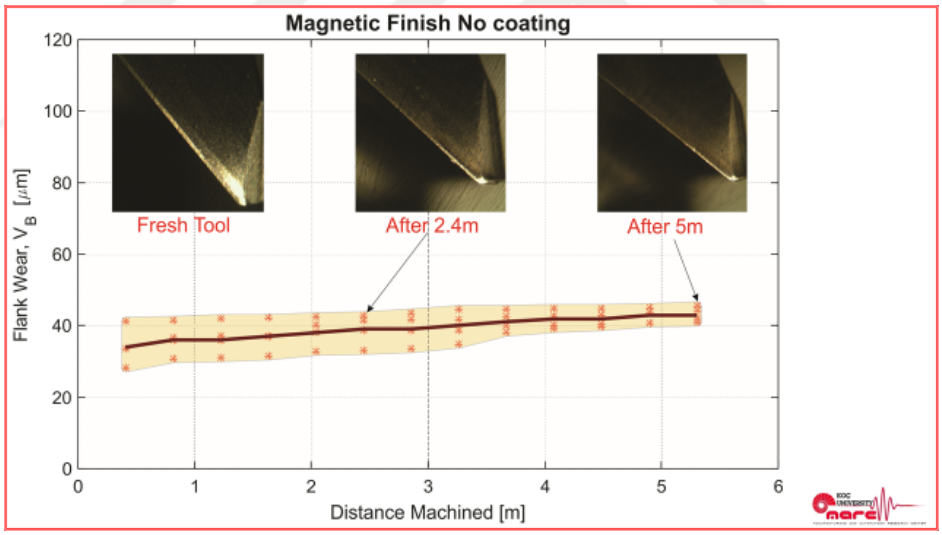

Figure 4-19: Flank wear for magnetic finish and no coating end-mill.

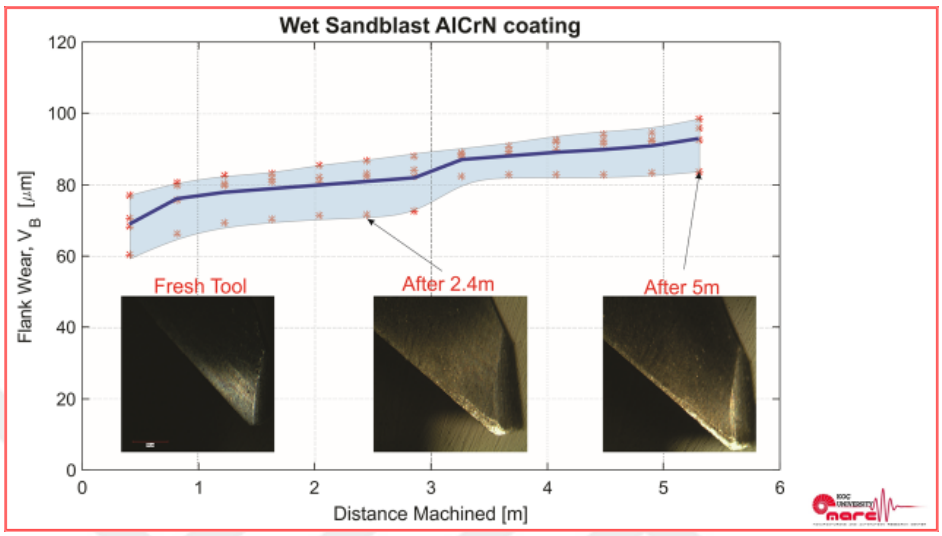

Figure 4-20: Flank wear for Wet sandblast finish and AlCrN coating end-mill.

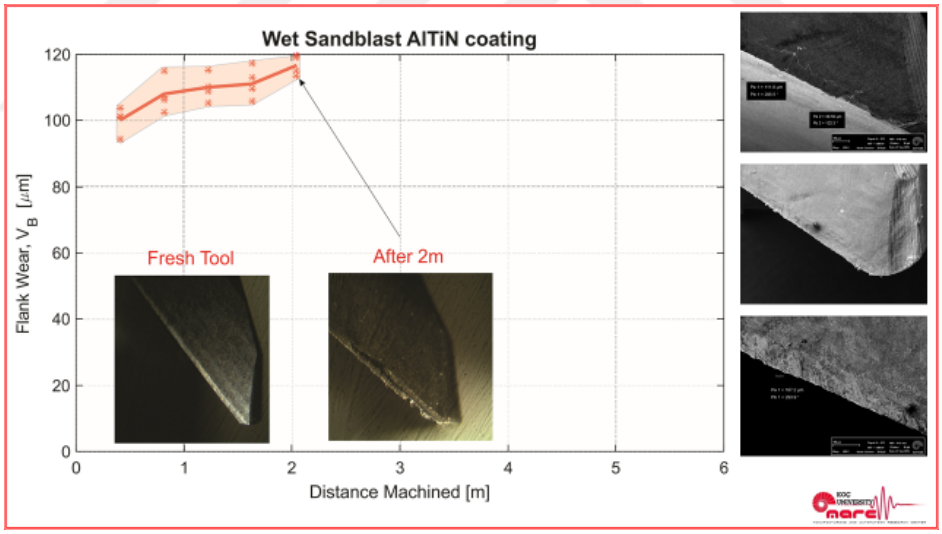

Figure 4-21: Flank wear for Wet sandblast finish and AlTiN coating end-mill.

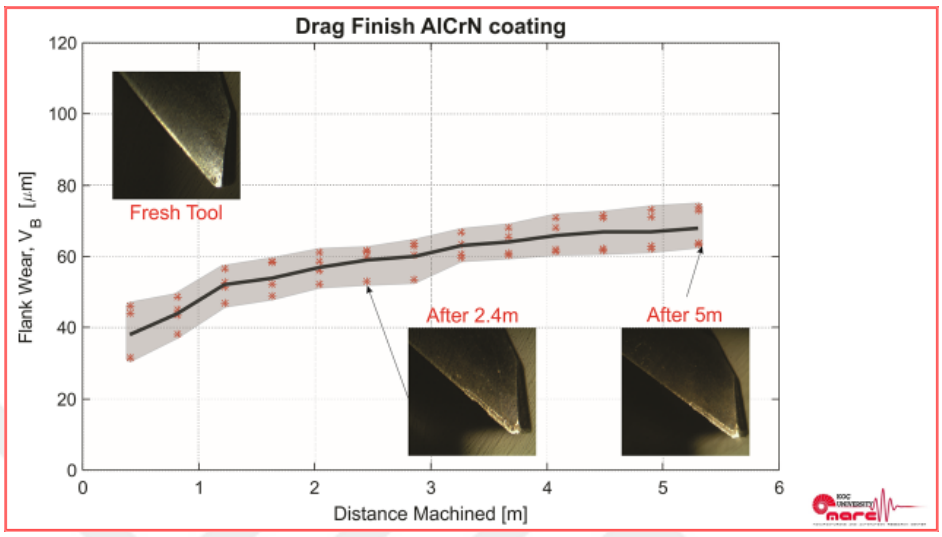

Figure 4-22: Flank wear for Drag finish and AlCrN coating end-mill.

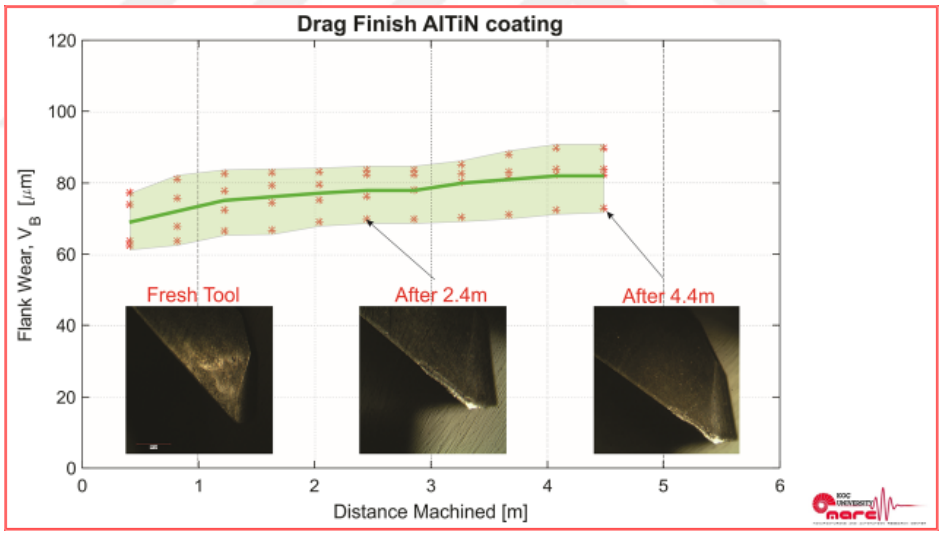

Figure 4-23: Flank wear for Drag finish and AlTiN coating end-mill.

The Figure 4-24 combines the average flank wear magnitudes. The shorter plots are for the end-mills that were removed from further testing because of excessive flute damage.

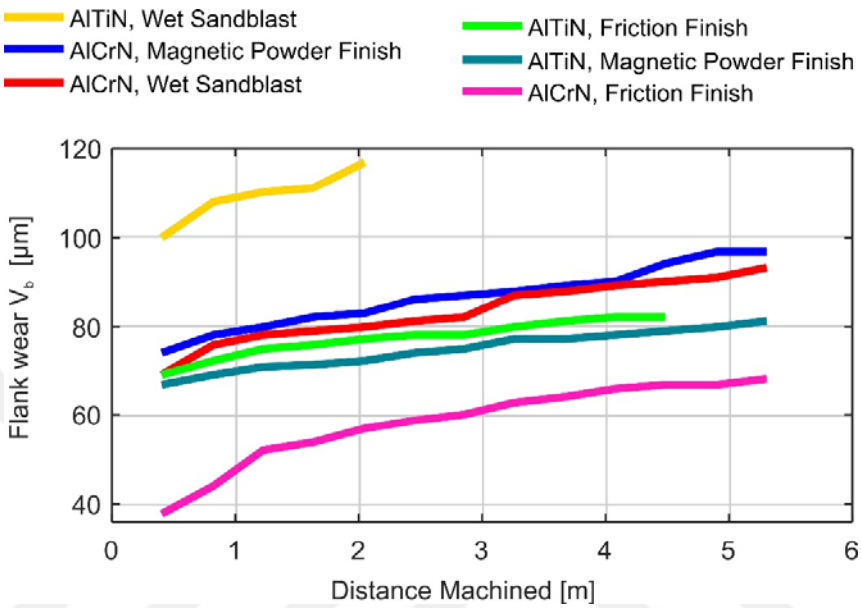

Figure 4-24: Average flank wear for all tested end-mills.

The position of the wear plot for a particular case depends on the initial flank land width on the tool and cannot be used as a measure of wear performance. The wear rate, i.e. $\mu m/m$ or the slope line fitted to the wear data is better measure of the wear performance of the different coatings and the surface finish techniques.

The end-mill manufacturer machined the end-mill flan land for a targeted width of $60 \pm 20\ \mu m$. The intercepts for the lines approximating the slop of the wear progression for the tested cases is a good measure of the flank land width for the tested end-mill. Two of the cases were observed to have out of tolerance flank land width, namely, the AlTiN coated end-mill with wet sandblast finish had 98 μm width and the un-coated end-mill with magnetic powder finish had 35 μm width.

Table 4-13: Flank wear after machining 5.3m.

Rank	Finish Technique	Coating Material	Average Flank wear [um]	Length machined [m]	Tool Condition
1	Magnetic	No Coating	43	5.3	
2	Drag	AlCrN	68	5.3	
4	Magnetic	AlTiN	81	5.3	
5	Drag	AlTiN	82	4.9	A flute was found out of shape after this length
6	Wet Sandblast	AlCrN	93	2	A flute was found chipped after this length
7	Magnetic	AlCrN	97	5.3	
8	Wet Sandblast	AlTiN	117	5.3	

a. Flank wear comparison for all Magnetic Finish tools

The comparison of the three end-mills produced with finish with magnetic powder showed that the wear rate on the aluminum chromium nitride coating was more aggressive than its counter parts. The final magnitudes of the wear are dependent on the starting value.

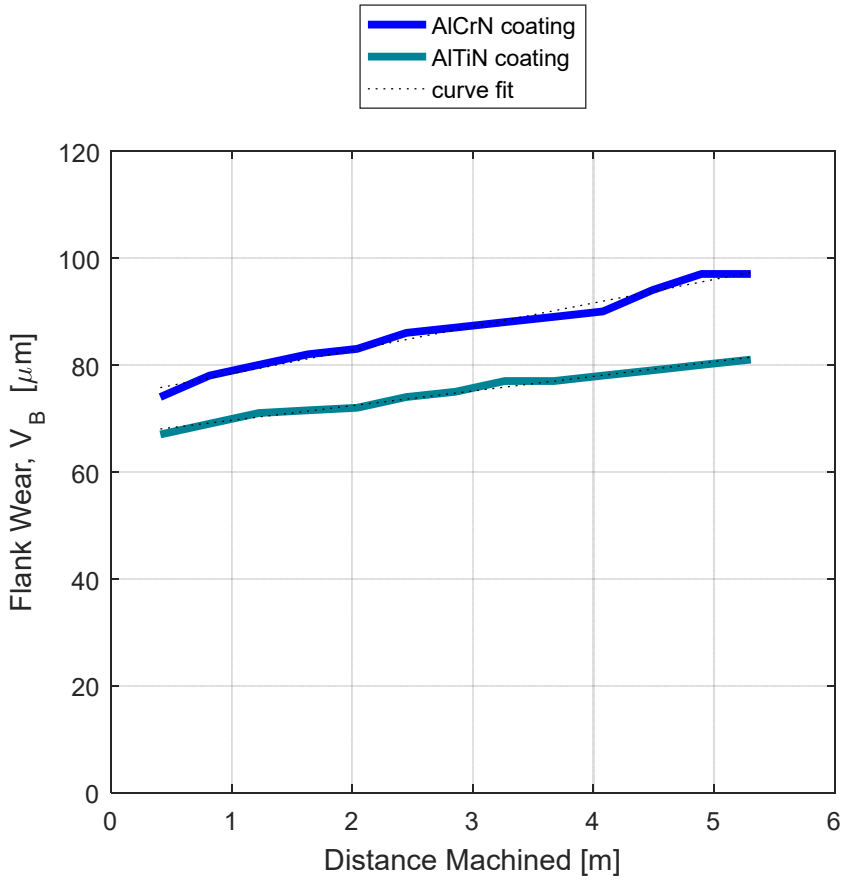

Figure 4-25: Flank wear comparison for all Magnetic Finish end-mills.

The wear rate is the criteria used to differentiate between the performances of the end-mills. The wear rate for the AlCrN coated and magnetic powder finish end-mill was 4.4 $\mu m/m$, whereas the wear-rate for the AlTiN coated and same finish technique end-mill is

2.74 $\mu m/m$. The AlCrN coating registered 60% higher wear-rate than its AlTiN coated counterpart.

b. Flank wear comparison for all Drag Finish tools:

The aluminum chromium nitride coating wear rate was higher than the aluminum titanium nitride coating material.

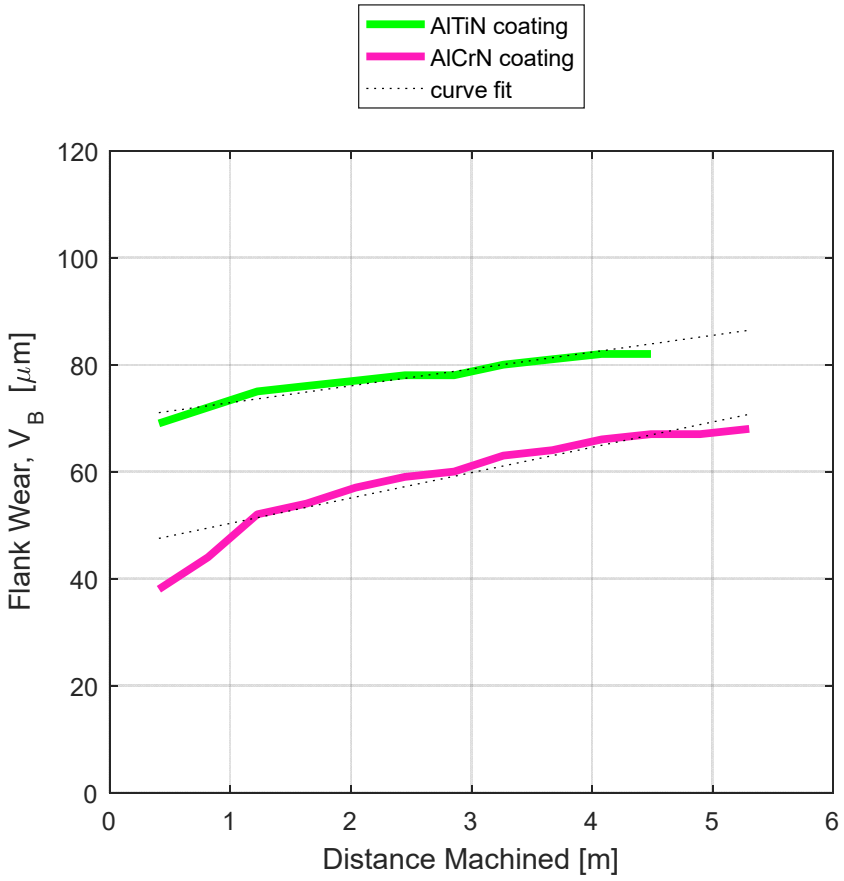

Figure 4-26: Flank wear comparison for all Drag Finish end-mills.

The wear rate for the AlCrN coated and magnetic powder finish end-mill was 4.74 $\mu m/m$, whereas the wear-rate for the AlTiN coated and same finish technique end-mill is

2.94 $\mu m/m$. Similar to the finish with magnetic powder, the AlCrN coating registered 60% higher wear-rate than its AlTiN coated counterpart.

c. Flank wear comparison for all Wet Sandblast Finish tools.

The end-mills with surface finish from the wet sandblast technique, the aluminum titanium nitride surface coating wear rate was higher than the aluminum chromium nitride coating material as shown in the Figure 4-27. This different behavior of the AlTiN coating from the other two surface finish techniques could be because of the much higher values of the flank side clearance surface width.

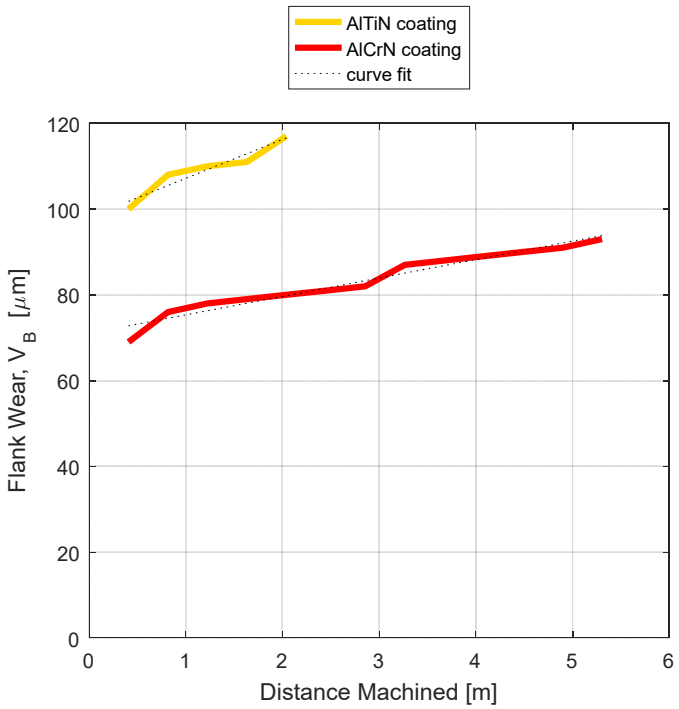

Figure 4-27: Flank wear comparison for all Wet Sandblast Finish tools.

d. Flank wear comparison for all AlCrN coated tools.

The wear rate for the three end-mill is comparable. The wear-rate for the magnetic powder finish was 4.4 $\mu m/m$, for drag finish 4.74 $\mu m/m$ and for the wet sandblast finish it was 4.3 $\mu m/m$. The average wear rate for the AlCrN coated end-mills is 4.48 $\mu m/m$.

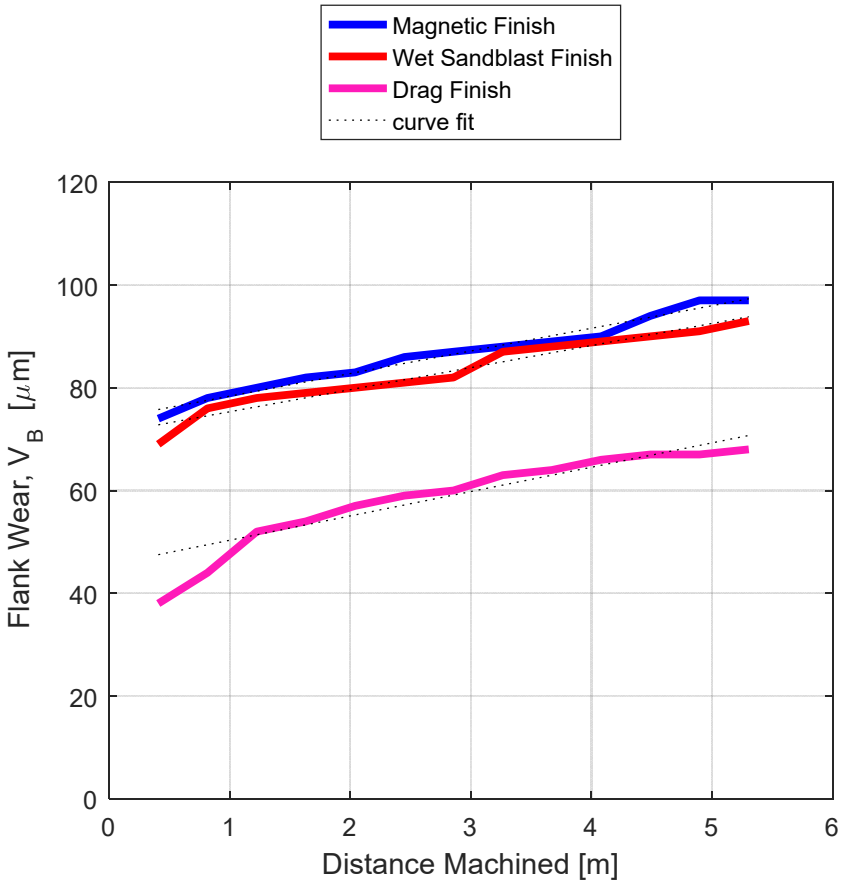

Figure 4-28: Flank wear comparison for all AlCrN coated tools.

e. Flank wear comparison for all AlTiN coated tools.

The wear rate for the AlTiN coated wet sandblast finished end-mill is different from its all other tested end-mills. This particular end-mill had a flank land width of 100 μm to begin with and the reason for the different from all the other tested end-mills.

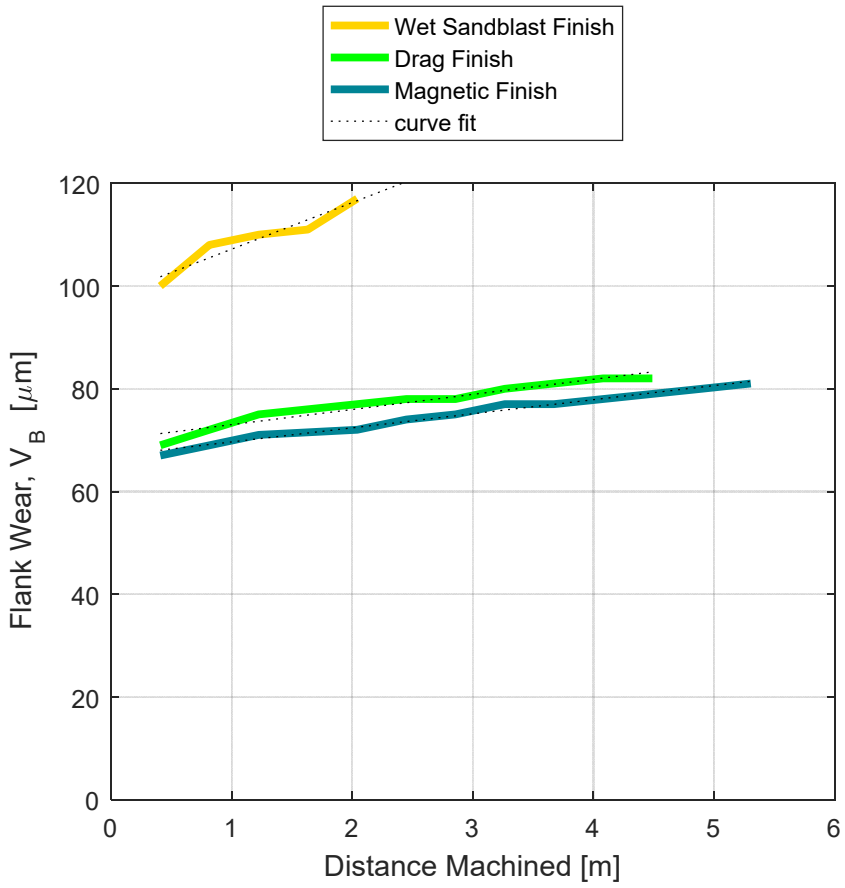

Figure 4-29: Flank wear comparison for all AlTiN coated tools.

The Figure 4-29 combines the wear plots for all the end-mills with AlTiN type coating. The end-mills with drag finish and magnetic powder finish had wear-rates of 2.94 $\mu m/m$

and 2.74 $\mu m/m$ respectively. The wear-rate for the wet sandblast end-mill was 9 $\mu m/m$, three times more than the end-mills with same coating material.

4.3.3.2 Chipped tool

Two tools were removed from testing before they completed their machined length quota. They were found to have accrued an excessive amount of chipping or flute geometry had changed significantly.

1. The "wet sandblast finish and AlTiN coated" end-mill was found chipped on inspection. The chipped section width was 39 um.

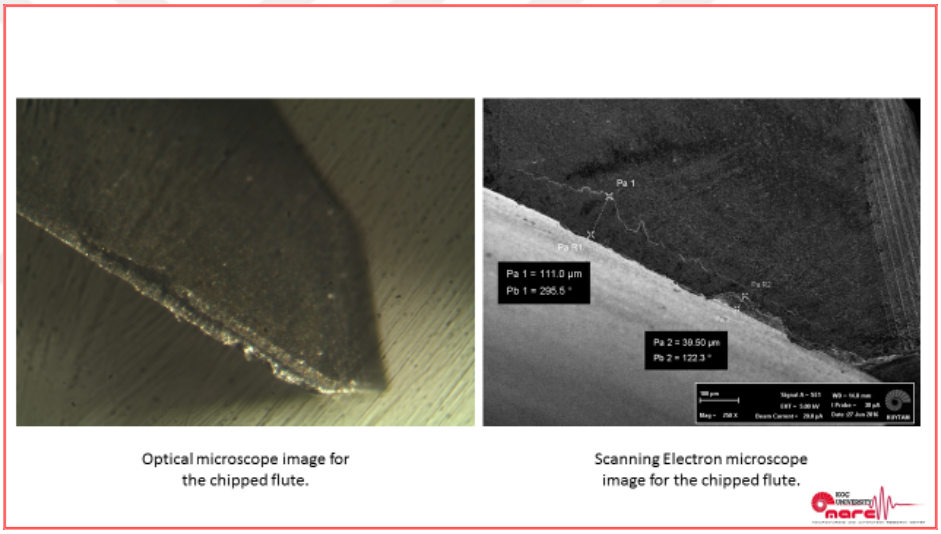

Figure 4-30: The chipped flute of the end-mill with wet sandblast finish and AlTiN coating.

2. One of the flutes on the end-mill with "drag finish and AlTiN coating" was found to have worn out of shape. Subsequently, this tool was also removed from further testing.

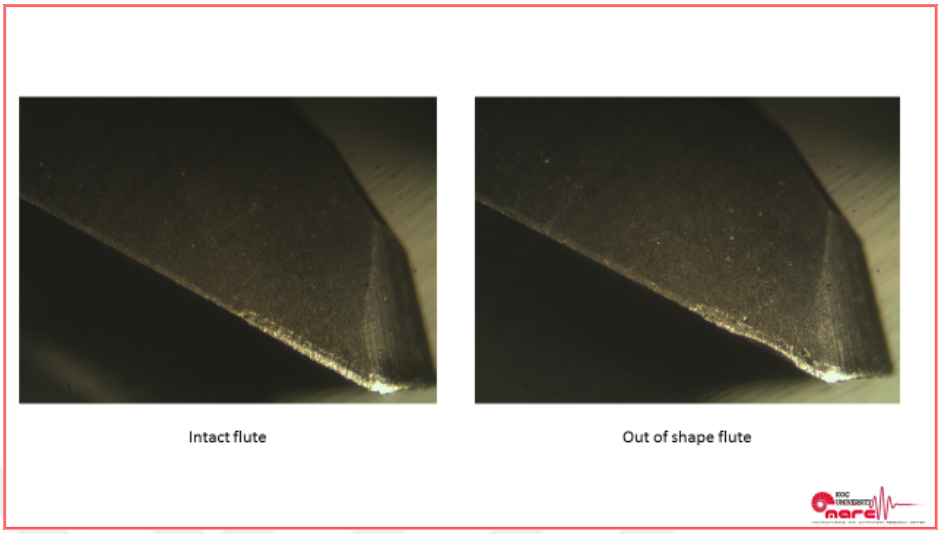

Figure 4-31: The out of shape flute for the drag finish and AlTiN coated end-mill.

4.3.3.3 Coating thickness

The coating thickness, its quality and uniformity was checked for the two coating materials. The sample end-mills were sectioned to expose the coated layers.

	Aluminum content in coating % by weight	Cobalt matrix in WC substrate % by weight	Average thickness [µm]
AlTiN-5	20.59	8.61	3.15
AlCrN-5	15.1	4.7	3.75

a. AlCrN coating

The SEM images and the EDS analysis of the coating and substrate are given in the Figure 4-32 and Figure 4-33. There was a single layer of coating and its thickness on average was 3.75 μm.

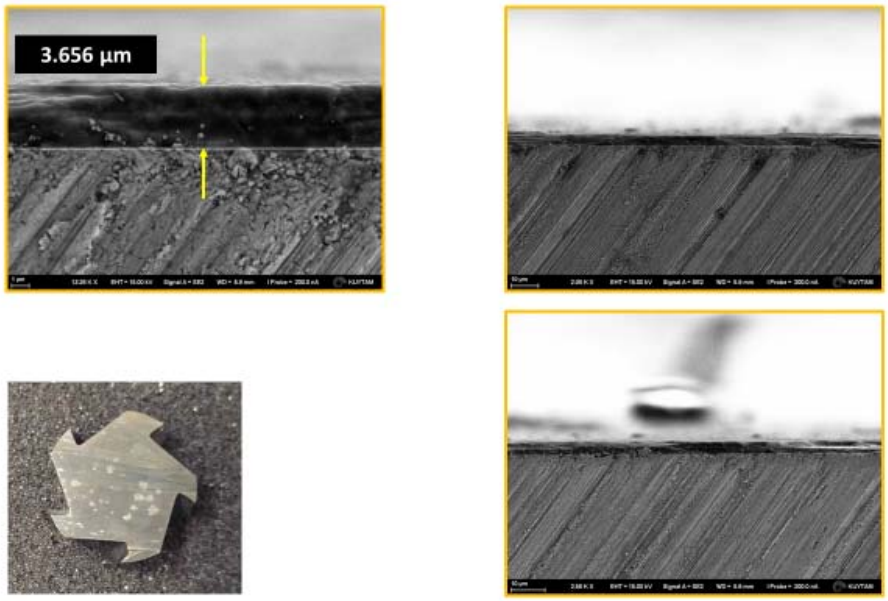

Figure 4-32: The sectioned sample and the AlCrN coating.

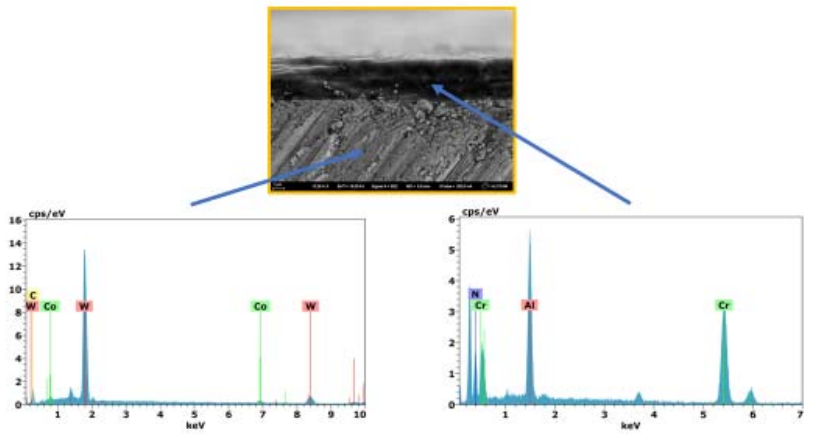

	Series	Unn. C [wt. %]	norm. C [wt. %]	Atom. C [at. %]	C error (1 sigma) [wt. %]
W	K-series	78.31	81.64	26.73	3.09
Co	K-series	4.51	4.7	4.8	0.24
C	K-series	13.11	13.66	68.47	2.58

	Series	Unn. C [wt. %]	norm. C [wt. %]	Atom. C [at. %]	C error (1 sigma) [wt. %]
Al	K-series	13.31	15.1	17.6	0.68
Cr	K-series	58.2	65.99	39.92	1.85
N	K-series	16.68	18.92	42.48	3.44

Figure 4-33: The elemental analysis by the EDS of the AlCrN coated sample.

The elemental composition of the coating and the WC substrate is given in the Figure 4-33. The WC substrate had approximately 5% cobalt binder, whereas the AlCrN coating had 15% aluminum.

b. AlTiN coating

The SEM images and the EDS analysis of the coating and substrate are given in Figure 4-34 and Figure 4-35. There was a single layer of coating and its thickness on average was 3.75 μm.

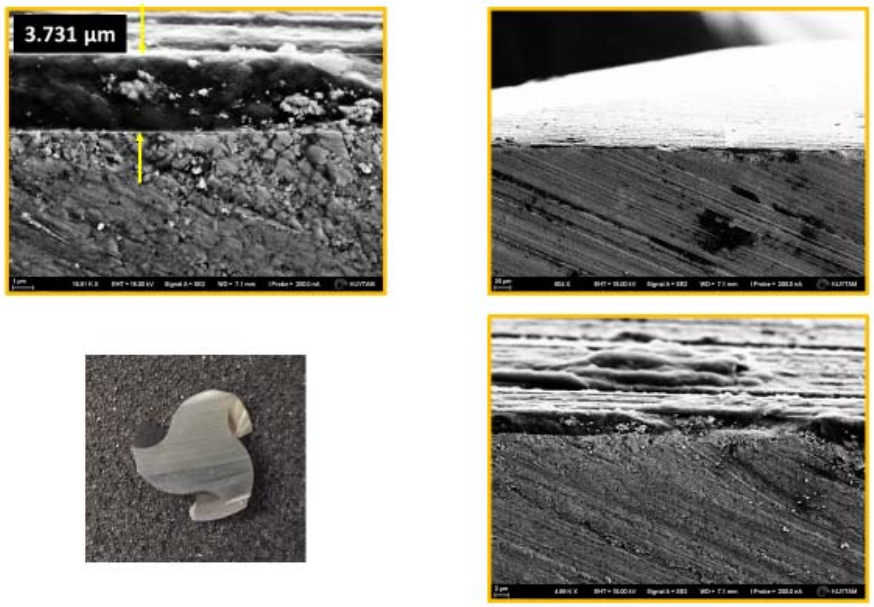

Figure 4-34: The sectioned sample with AlTiN coating.

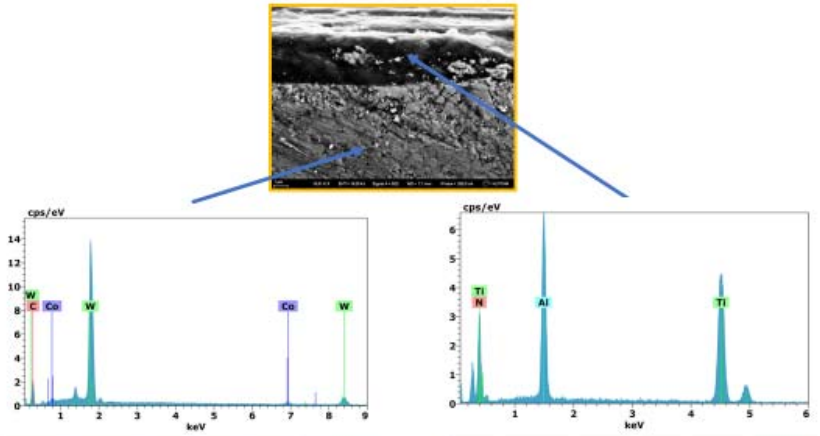

	Series	Unn. C [wt. %]	norm. C [wt. %]	Atom. C [at. %]	C error (1 sigma) [wt. %]
W	K-series	76.29	76.34	19.43	2.91
Co	K-series	3.75	3.75	2.98	0.2
C	K-series	19.9	19.91	77.59	3.23

	Series	Unn. C [wt. %]	norm. C [wt. %]	Atom. C [at. %]	C error (1 sigma) [wt. %]
Al	K-series	17.71	18.61	18.83	0.89
Ti	K-series	53.52	56.22	32.07	1.67
N	K-series	23.97	25.18	49.1	4.35

Figure 4-35: The elemental analysis by the EDS of the AlTiN coated sample.

The elemental composition of the coating and the WC substrate is given in the Figure 4-35. The WC substrate had approximately 5% cobalt binder, whereas the AlCrN coating had 15% aluminum.

4.3.4 Conclusion

The wear performance of the tested end-mills was analyzed based on the wear-rate. The following conclusions are drawn:

1. The differently coated and differently surface finished end-mills were tested for wear performance. The flank side wear of 100 μm was fixed as a bench mark to compare the performance of the end-mills.
2. The AlTiN material coating registered a wear-rate that was 60% lower than the AlCrN material coated end-mills.
3. In general, the wear-rate remained similar for the end-mills with same type of coating. The AlCrN coated end-mills had 4.4 $\mu m/m$, 4.74 $\mu m/m$ and 4.3 $\mu m/m$ of wear-rate for the finish with magnetic powder, wet sandblast finish and drag finish respectively. The wear-rates for tested machined length remained in the steady wear region when compared with conventional tool wear curve.
4. Similarly, the AlTiN coated end-mills had a wear-rate of 2.74 and 2.74 for the magnetic powder finish and the drag finish respectively. The AlTiN coated tool produced with wet sandblast finish recorded an accelerated wear-rate of 9 $\mu m/m$ when compared with the other tested end-mills. This was because of the out of tolerance feature on the end-mill cutting edge geometry.
5. The “Drag finish and AlCrN coated” end-mill recorded the least amount of flank wear for the same machined length from amongst the coated tools, including the competitor’s end-mill.
6. One of the flutes of the “wet sandblast finish and AlTiN coated” end-mill was found chipped on inspection after 2m machined length. Subsequently the tool was removed from further testing (Figure 4-30).

7. One of the flutes on the “magnetic finish and AlTiN coated” end-mill was found with significantly changed geometry. Subsequently the tool was removed from further testing also. (Figure 4-31)

8. The “wet sandblast finish and AlTiN coated” tool runout was highest and possibly may have contributed to the premature flute failure.

9. Two of three tools carrying the AlTiN coated had to be removed from further testing because of a significant change in cutting edge geometry (Figure 4-30 and Figure 4-31).

4.4 Friction Analysis

4.4.1 Coefficient of friction

The mechanics of cutting are governed by three deformation zones around the tool-workpiece interface, shown in Figure 4-36 The machined material is sheared in the primary deformation zone and is pushed to move over the rake face of the cutting tool in the secondary deformation zone. The cut chip slides over the rake face of the tool with the sliding friction coefficient.

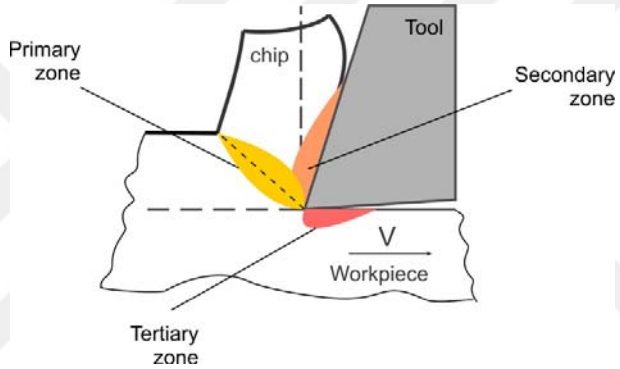

Figure 4-36: The three deformation zones in machining processes.

One of the early works describing the mechanics of machining, the Merchant model, establishes the relationships between the components of the cutting forces, tool geometry and physics of the process for the simplest of cutting modes, the orthogonal machining. The nominal rake angle α_r, average shear angle, ϕ_c and the average friction angle, β_a, illustrated in Figure 4-37, are the necessary angles for the synthesis of cutting forces as a function of tool geometry and workpiece material properties. The friction coefficient, μ is found using the ploughing force adjusted orthogonal machining force components by the equations 1 and 2.

$$\tan(\beta_a - \alpha_r) = \frac{F_{f_c}}{F_{t_c}} \quad (1)$$

$$\mu_a = \tan \beta_a = \frac{F_u}{F_v} \quad (2)$$

Where $\boldsymbol{F_{t_c}}$ and $\boldsymbol{F_{f_c}}$ are the tangential and feed direction cutting forces for an orthogonal machining process kinematics.

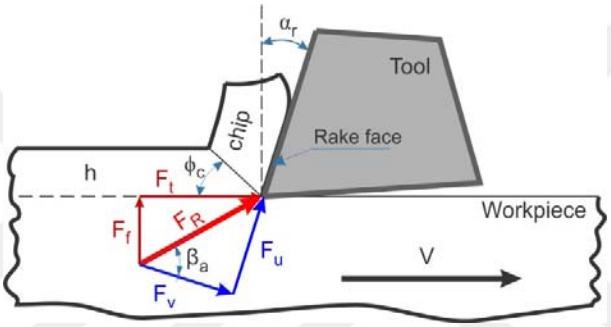

Figure 4-37: The cutting force components in an orthogonal machining process.

Two techniques are introduced to establish the friction coefficient for the tool – workpiece pair. The first is built on the specific cutting forces, whereas the other utilizes the cutting mechanics to deduce the friction coefficient.

4.4.1.1 Cutting coefficient method

The orthogonal model gives the relationship between the recorded cutting forces of an orthogonal test. If α_r is the nominal rake angle of the tool and β_a is the friction angle, as shown in Figure 4-37, then the friction coefficient μ is calculated using orthogonal machining identities given by the equations 1 and 2.

$$\tan(\beta_a - \alpha_r) = \frac{F_{fc}}{F_{tc}} \tag{1}$$

$$\mu_a = \tan \beta_a \tag{2}$$

where F_{tc} and F_{fc} are the tangential and feed direction forces for an orthogonal machining process kinematics.

The cutting coefficients for the tangential and radial directions in a milling operation are found by the average tangential (F_x) and feed force (F_y) equations (3) and (4) as reported in (Altintas, 2012).

$$\bar{F}_x = \left[\frac{N\Delta a_p f_z}{8\pi}\left[(K_{tc}\cos 2\varphi) - \left(K_{rc}(2\varphi - \sin 2\varphi)\right)\right] - \frac{Nf_z}{2\pi}[K_{te}\sin\varphi - K_{re}\cos\varphi]\right]_{\varphi_{st}}^{\varphi_{ex}} \tag{3}$$

$$\bar{F}_y = \left[\frac{N\Delta a_p f_z}{8\pi}[K_{tc}(2\varphi - \sin 2\varphi) + K_{rc}\cos 2\varphi] - \frac{Nf_z}{2\pi}[K_{te}\cos\varphi + K_{re}\sin\varphi]\right]_{\varphi_{st}}^{\varphi_{ex}} \tag{4}$$

where $\bar{F}_x$ and $\bar{F}_y$ are the average of the recorded forces in the experiment for a select number of revolutions in the fixed coordinate system. K_{tc}, K_{rc} and K_{te}, K_{re} are the cutting coefficients and edge coefficients. N is the number of flutes, Δa_p is the differential thickness, f_z is the feed per tooth and ϕ is the immersion angle for the test.

The machining cutting forces and ploughing forces for specified cutting conditions are recognized separately following equation (6), where the index q represents the tangential or feed directions. The tangential and radial force components for a discrete disk along the depth of cut, for any given immersion angle ϕ, are simulated using equation (7). The tangential F_t and the feed F_f directions in orthogonal cutting are shown in Figure 1. Noting that the axial forces contribution towards the resultant forces was less than 1%, direct mapping is

employed from the feed and tangential directions in orthogonal machining to tangential and radial directions in milling process.

$$F_f \rightarrow F_r \tag{5}$$

$$dF_q = df_{qc} + dF_{qe} \tag{6}$$

$$\left.\begin{aligned} dF_t(\phi) &= bh(\phi)K_{tc} + bK_{te} \\ dF_r(\phi) &= bh(\phi)K_{rc} + bK_{re} \end{aligned}\right\} \tag{7}$$

The friction coefficient μ for the workpiece material and tool coating pair is calculated using equation 2.

a. Experimental Setup

The machining tests were performed on 5-axis Mori Seiki NMV5000 DCG machining center. The workpiece material was titanium alloy of Ti6Al4V grade 5, commonly used for aerospace industry applications. The chemical composition and mechanical properties of the Ti6Al4V test workpiece are given in Table 1. The workpiece was carefully prepared for secure mounting on the table type dynamometer. The test setup is shown in Figure 2. The force data were acquired using a table type dynamometer and a high-speed data acquisition system.

Figure 4-38: Mori Seiki NMV5000 DCG 5-axis milling machine used for the investigation

Cutting force data was acquired for four tools during dry slot cutting process. The description of coating and surface finishing technique is provided in Table 2.

Table 4-14: Chemical composition and mechanical properties of Ti6Al4V.

Chemical Composition (%)						
C	V	N	Al	H	Fe	Ti
0.009	4.20	0.01	6.13	0.001	0.19	Rest

Mechanical Properties	
Yield Strength (0.2%)	855 N/mm^2
Ultimate Strength	895 N/mm^2
% elongation	17 %
% Area reduction	49 %

Table 4-15: The coating materials and surface finishing techniques selected for the study.

	Coating material	Finishing technique
1	Aluminum Titanium Nitride, (AlTiN)	Finishing with magnetic powder (FPM)
2		Drag Finishing (FF)
3		Wet Sandblast Finishing (WSF)
4	Aluminum Chromium Nitride, (AlCrN)	Finishing with magnetic powder (FPM)
5		Drag Finishing (FF)
6		Wet Sandblast Finishing (WSF)
7	No Coating	Finishing with magnetic powder (FPM)

The slot cutting operation is a relatively harsher machining strategy than other commonly employed strategies in the industry. Four-fluted 12 mm diameter solid carbide end-mills were used in the experiments. 1 mm and 1.5 mm depths of cut in dry cutting condition were

selected. The spindle speed was 1300 rpm corresponding to 49 m/min cutting speed. The feedrate and feed per tooth for the four test cases are given in Table 4-16.

Table 4-16: The feedrates used in the investigation.

Test case	Feedrate [mm.min^{-1}]	Feed per tooth [µm]
Test 1	52	10
Test 2	104	20
Test 3	156	30
Test 4	208	40

The effect of the bottom cutting edge was isolated by collecting force data for two depth of cuts as shown in Figure 4-39.

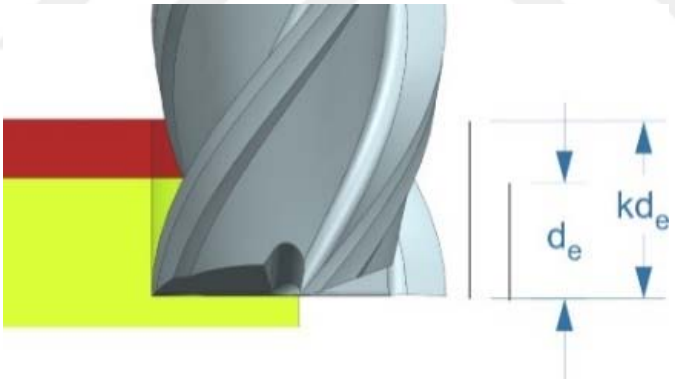

Figure 4-39: The two depths of cut to isolate the effect of bottom edge.

Subtracting one set of forces from the other, results in cutting forces such that the cutting forces are from the cutting edge only as shown in Figure 4-40.

Figure 4-40: The method adopted for cutting edge forces.

b. Results and Discussion

The resultant of the differential cutting forces calculated from the force data are shown in Figure 5.

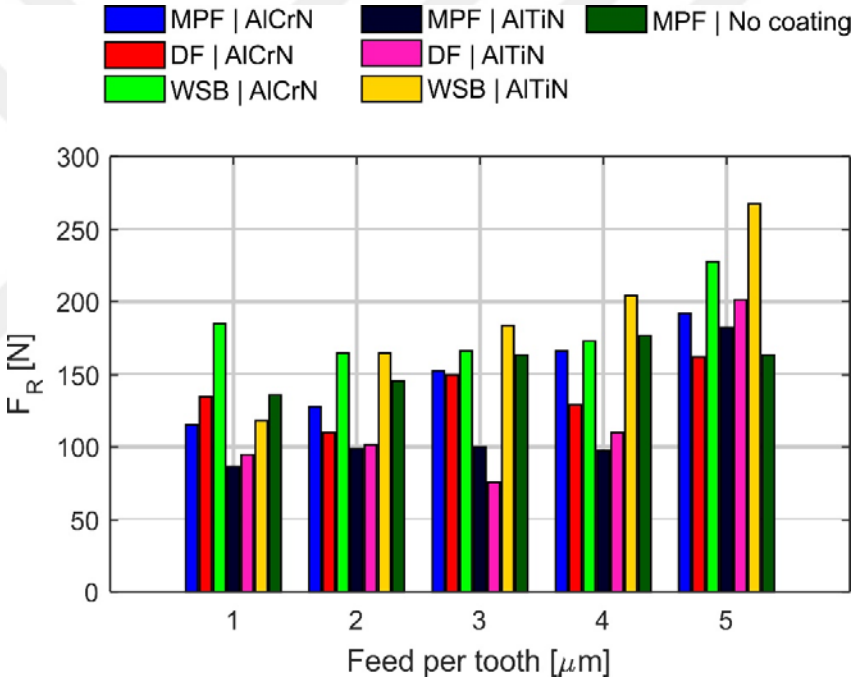

Figure 4-41: the resultant of the differential cutting forces for the test cases.

Subsequently, the cutting coefficients are determined using the x-axis and y-axis forces in equations 3 and 4. The cutting coefficients calculated for the four tools used for this study are given in Figure 6. The tangential cutting coefficient, K_{tc} and the radial cutting coefficient,

K_{rc} are then inputs in the friction analysis of the end-mills with different finishes by using equation 7 and equation 1. The relative difference in magnitude of the two cutting coefficients is a measure of the friction coefficient.

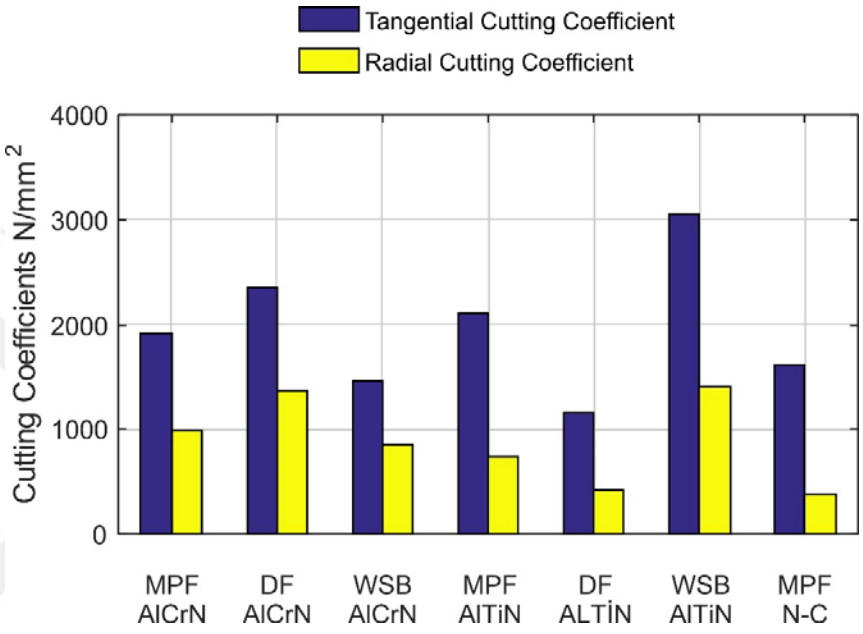

Figure 4-42: The cutting coefficients for the differently coated tools.

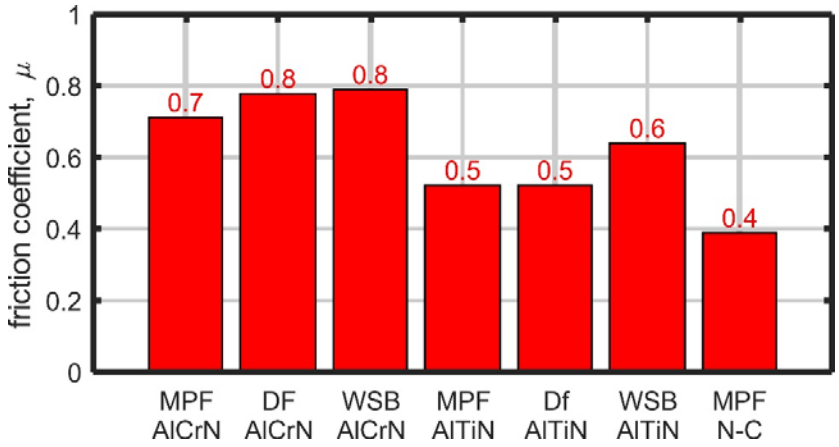

Figure 4-43: The friction coefficient for the seven test cases.

The friction coefficient is from the governing parameters for establishing the tool life and workpiece integrity. It is identified that the aluminum chromium nitride coating has the higher friction coefficient, of 0.8 among all the tools with different surface finish, and the lowest friction coefficients was determined as 0.5 in the AlTiN coated tools.

c. Conclusion

The friction coefficient is a measure for the heat generated at tool chip interface, which in turn is responsible for tool life and workpiece integrity.

A new and a direct method is introduced to establish the friction coefficient in a tool workpiece pair for a milling process. Friction coefficients on various finishing techniques were investigated in AlTiN and uncoated carbide tools in milling of Ti6Al4V.

4.4.1.2 End-mill mechanics based method

The oblique cutting processes, shown in Figure 4-44, as is the reality of the majority of machining processes, require many angles to completely define the cutting force components and the friction coefficient between the tool and the workpiece. They are the obliquity angle, $\boldsymbol{i}$: the angle between the cutting velocity and the normal to the cutting edge in the plane defined by the cut surface, the chip flow angle, $\boldsymbol{\eta}$: the angle between the normal to the cutting edge in a plane containing the rake face and the angle with which the cut chips slide over the rake face and the friction angle, $\boldsymbol{\beta_a}$: the angle between the resultant of the cutting forces and the unit vector normal to the rake face.

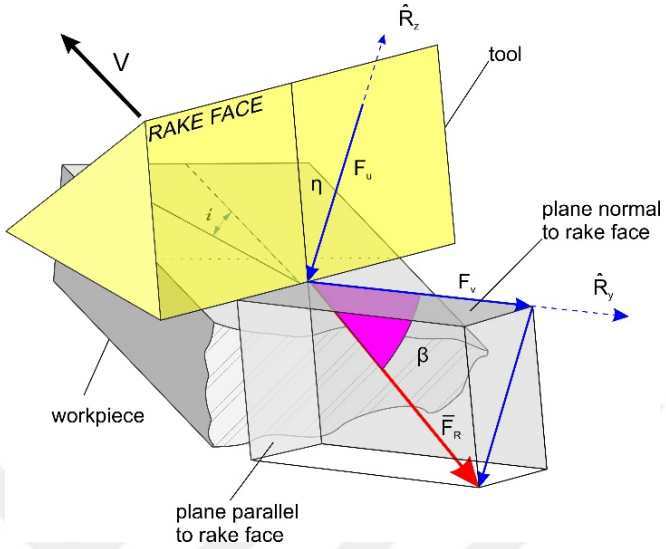

Figure 4-44: Kinematics of the oblique cutting process.

The nominal rake angle, $\boldsymbol{\alpha_r}$ is predefined and is manufactured as per demand, whereas the obliquity angle, $\boldsymbol{i}$ is a predetermined machining parameter, for the milling operations, it is equal to the helix angle of the cutting flutes. Lastly, the Stabler's rule gives a good estimation for the chip flow angle $\boldsymbol{\eta}$.

These angles are used to define three rotation matrices for coordinate transformation of the global coordinate system to a coordinate system where the resultant of the cutting forces is defined by two orthogonal components, such that one is collinear with the chip flow direction and the other to the normal to the rake face plane. The first of the three rotations is the obliquity angle, $\boldsymbol{i}$ rotation about the $\boldsymbol{z}$ axis. Then $\boldsymbol{\alpha_r}$ rotation about new $\boldsymbol{x}$ axis is followed and finally, $\boldsymbol{\eta}$ rotation about the new $\boldsymbol{y}$ axis. The three rotations are illustrated in Figure 4-45.

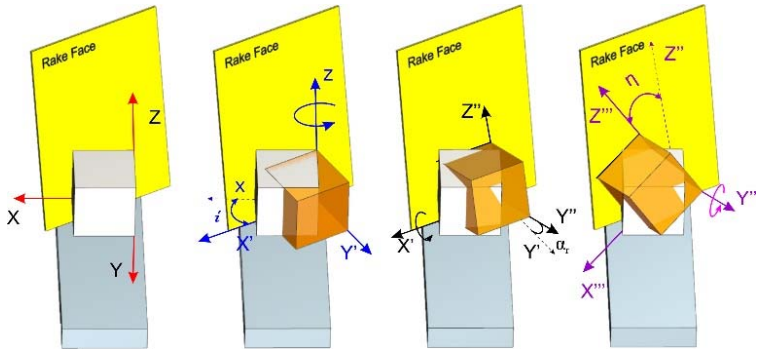

Figure 4-45: Coordinate transformation steps for the final transformation matrix.

The three transformation matrices are given by equations 3.

$$R_z = \begin{bmatrix} \cos i & \sin i & 0 \\ -\sin i & \cos i & 0 \\ 0 & 0 & 1 \end{bmatrix}$$

$$R_x = \begin{bmatrix} 1 & 0 & 0 \\ 0 & \cos \alpha_r & \sin \alpha_r \\ 0 & -\sin \alpha_r & \cos \alpha_r \end{bmatrix}$$

$$R_y = \begin{bmatrix} \cos \eta & 0 & -\sin \eta \\ 0 & 1 & 0 \\ \sin \eta & 0 & \cos \eta \end{bmatrix} \quad (3)$$

$$R = R_y \times R_x \times R_z$$

$$\begin{bmatrix} F_u \\ F_v \\ F_w \end{bmatrix} = R \times \begin{bmatrix} F_{x_c} \\ F_{y_c} \\ F_{z_c} \end{bmatrix}$$

The global directions ***x***, ***y*** and ***z*** are redefined in the new ***u***, ***v***, and ***w.*** The new coordinate system resolves the resultant of the cutting force vector into two components, one parallel to

the chip flow direction and the other normal to the rake face, the third being negligible in magnitude. Hence, the friction coefficient for the oblique cutting process is found using equation 2. The friction angle can also be found using the dot product of the unit vectors, where one is parallel to the resultant of the cutting forces and the other is normal to the rake face, as shown in Figure 4-44.

$$\beta_a = \cos^{-1}\left(\hat{F}_R \cdot \hat{F}_v\right) \tag{4}$$

Contrary to continuous machining processes e.g. turning, milling process is intermittent in nature, where the uncut chip thickness is continuously changing with the rotation of the milling cutter and is given by equation 1.

$$h(\phi) = f_z \cdot \sin\phi \tag{5}$$

Here f_z is the feed per tooth of the milling cutter and ϕ is the cutter immersion angle. The mechanics of the milling operation, shown in the Figure 4-46 (a) and Figure 4-46 (b), are defined by three force components, namely, tangential, radial and axial cutting force.

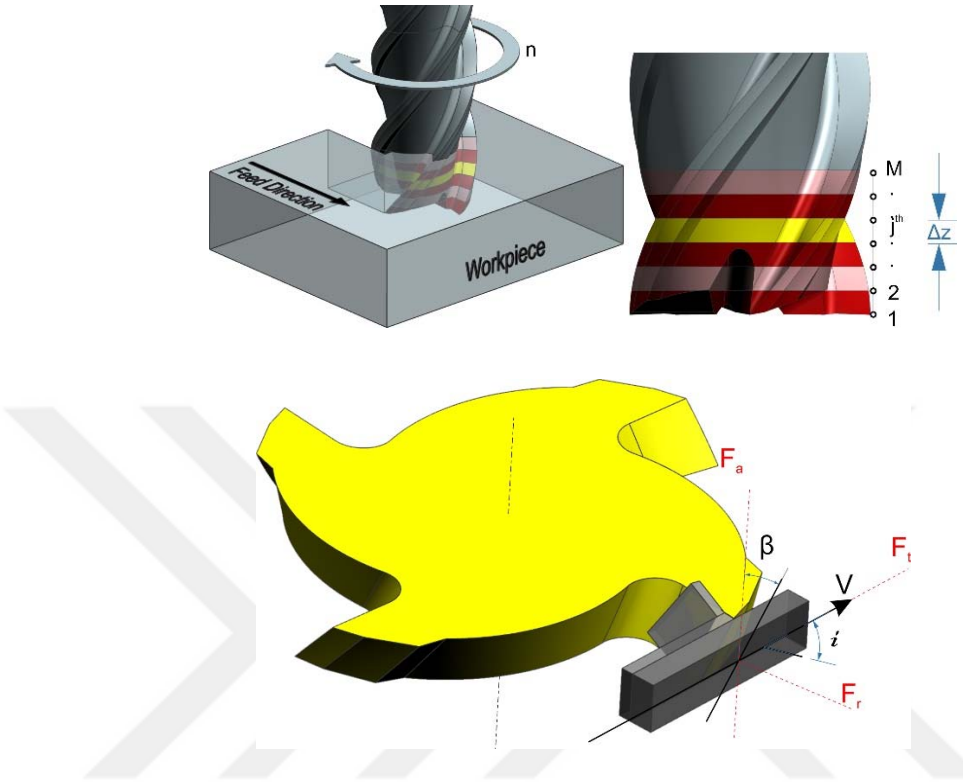

Figure 4-46: a) The discretization of the end-mill in to Δz thick disks. b) The cutting force components in the milling process for the selected discrete disk.

The endmill cutting edge approaches the workpiece material with an obliquity angle equal to the helix angle of the end-mill cutter. The components of the cutting forces, acting on the milling cutter, for $\boldsymbol{j^{th}}$ disk of infinitesimal thickness $\boldsymbol{\Delta z}$ are shown in Figure 4-46.

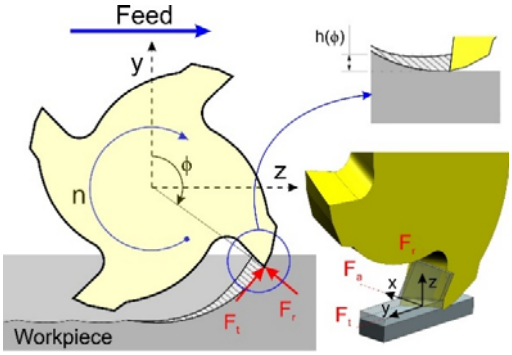

Figure 4-47: The mechanics of milling cutter.

The kinematics of the select disk of the end-mill shown in Figure 4-47, are approximated to be similar to a cutting tool with a straight edge. The curvature of the helical edge of a cylindrical body of the end-mill is minimized by the steep helix angle and differential thickness of the disk. The friction coefficient is calculated for the immersion angle, which gives the maximum chip thickness. At that particular instant, the tangential and the radial components of the cutting forces are parallel with ***y***-axis and ***x***-axis of the force measuring sensor's coordinate system.

The friction coefficient is found as the ratio $\boldsymbol{F_u/F_v}$ after the described coordinate transformation.

The geometry of the bottom cutting edge and respective mechanics involved in cutting is complex. Multiple sides of the bottom cutting edge on a flute, namely, the bottom, corner and side of it are cutting simultaneously. The effect of the bottom edge is eliminated by

machining for two depths of cut and subtracting one from the other as illustrated in the Figure 4-48, leaving away the differential forces from the side cutting edge only.

$$F_{\Delta \mathrm{d}} = F_{kd_e} - F_{d_e} \tag{6}$$

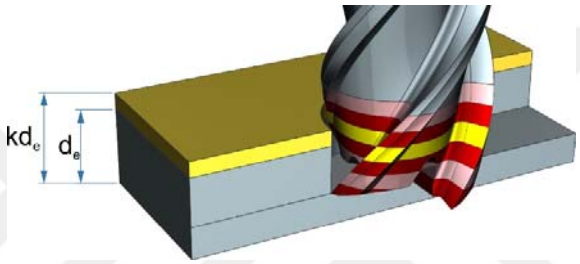

Figure 4-48: The two depths of cut isolate the effect of the bottom edge.

a. Experimental Setup

The machining tests were performed in 5-axis Mori Seiki NMV5000 DCG machining center. The material used for the investigation was the grade 5 titanium alloy Ti6Al4V, a commonly used material in the aerospace industry applications. The titanium alloy has further broader application in varied industries. The chemical composition found using the XRF technique is given in Table 4-17.

Figure 4-49: Mori Seiki NMV5000 DCG 5-axis milling machine used for tests.

The workpiece was carefully prepared for secure mounting on the table type dynamometer. The test setup is shown in Figure 4-49. The force data were acquired using a table type dynamometer and a high-speed data acquisition system.

Cutting force data were acquired for the test cases 1 to 7 for the titanium alloy Ti6Al4V workpiece material in a dry slot cutting process. The descriptions of the coating materials are provided in Table 4-18.

Table 4-17: Chemical composition and mechanical properties of Ti6Al4V.

Ti64Al4V Chemical Composition (%)							
C	V	N	Al	H	Fe	O_2	Ti
0.009	4.200	0.010	6.130	0.001	0.190	0.100	Rest

Table 4-18: The coating materials and surface finishing techniques selected for the study.

	Coating material	Surface finishing technique
1	Aluminum Titanium Nitride, (AlTiN)	Finishing with magnetic powder (FPM)
2		Drag Finishing (DF)
3		Wet Sandblast Finishing (WSB)
4	Aluminum Chromium Nitride, (AlCrN)	Finishing with magnetic powder (FPM)
5		Drag Finishing (DF)
6		Wet Sandblast Finishing (WSB)
7	No Coating	Finishing with magnetic powder (FPM)

Solid tungsten carbide end-mills with four-flutes, 12 mm diameter and 36.5° helix angle were used in the experiments. The machining test was performed for 1 mm and 1.5 mm depths of cut in dry cutting conditions with fresh tools. The spindle speed was 1300 rpm corresponding to 49 m/min cutting speed. The feedrate and feed per tooth for the test cases are given in Table 4-19.

Table 4-19: Experiment setup for the machining test of titanium alloy Ti6Al4V.

Ti6Al4V		
Test case	Feedrate [mm.min^{-1}]	Uncut chip thickness [µm]
Test 1	156	30
Test 2	204	40
Test 3	260	50
Test 4	312	60

b. Results and Discussion

The resultants of the differential cutting forces for the titanium alloy Ti6Al4V is calculated from the recorded force data and are shown in the Figure 4-50.

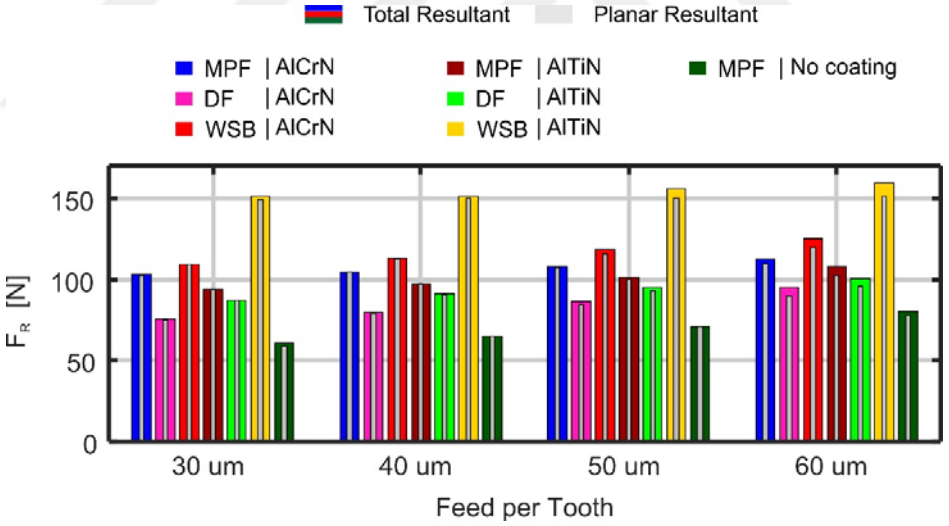

Figure 4-50: The resultants of the differential cutting forces for the differently coated solid carbide end-mills when machining Ti6Al4V.

The friction coefficient, given in the Figure 4-51, calculated using the two analytical methods differed by approximately 5% for Ti6Al4V, affirming Stabler's approximation for chip flow angle.

The friction coefficient values calculated for Ti6Al4V are for the combined regions of the rake face, hone radius and the flank side of the cutting edge on the end-mill.

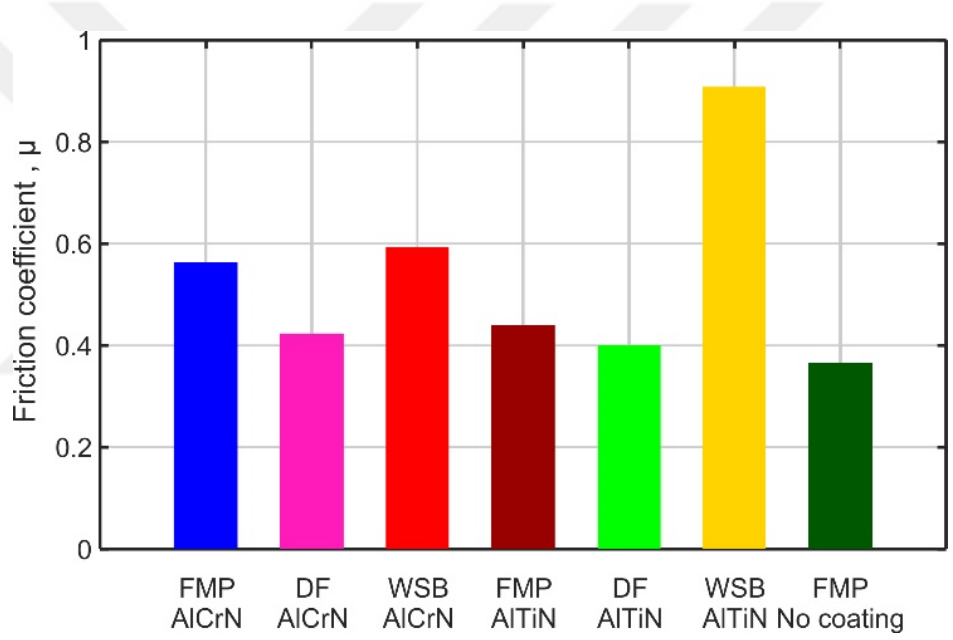

Figure 4-51: The friction coefficient for Ti6Al4V for different coating materials.

Furthermore, the Tools were evaluated for wear performance at one of the feedrate conditions. The flank wear was measured after every 400 mm of machining for 5 meters of total length machined. The test conditions are given in Table 4.

Table 4-20: Cutting condition for the wear test.

Wear Test Conditions		
Spindle Speed	1300	rpm
Cutting Speed	49	m/min
Depth of cut	1	mm
Width of cut	6	mm
Feedrates	130	mm/min

The flank wear progression was monitored up to 100 μm of flank wear. The testing was stopped for any tool showing an excess of 100 μm wear on the flank side. The flank side wear measurements and their respective wear rate and flank side width are shown in Figure 4-52, Figure 4-53and Figure 4-54.

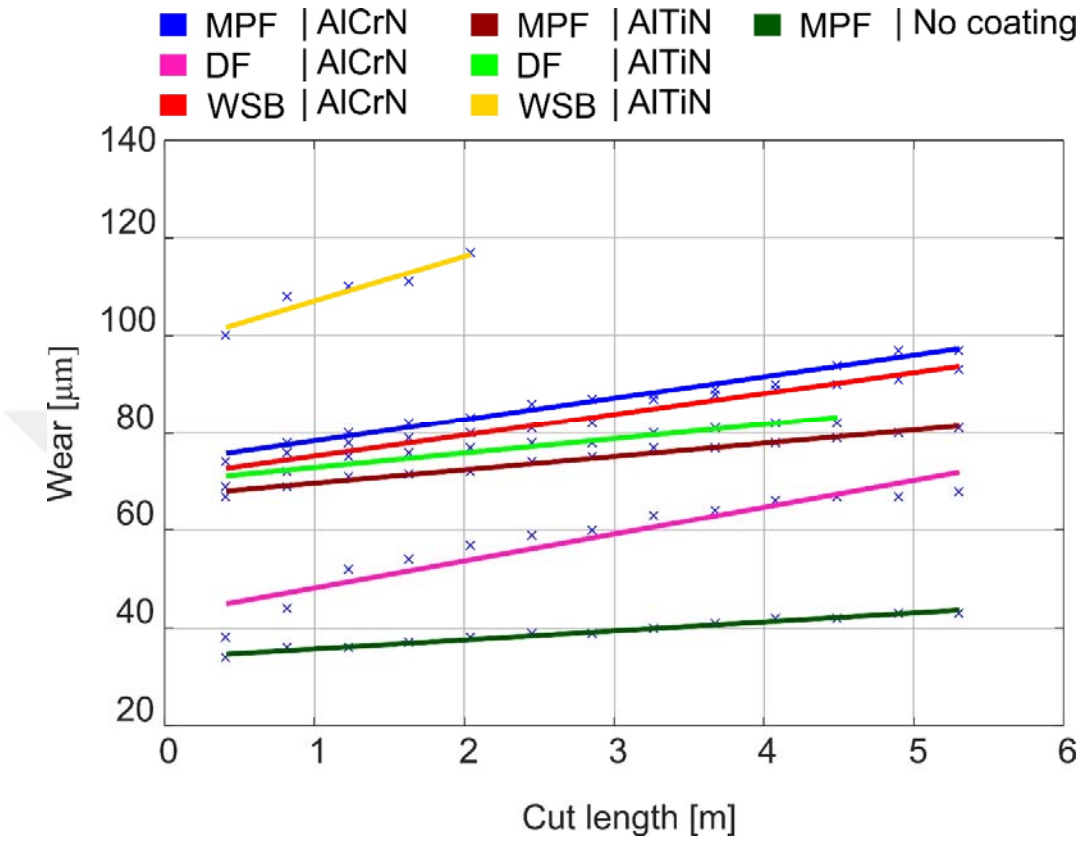

Figure 4-52: Tool flank wear for the test end-mills when machining Ti6Al4V.

The slopes in the Figure 4-52 represent the rate of wear, whereas the intercept of the line provides the flank land width for the tested tools. The rate of wear is shown in Figure 4-53 and the initial flank land width is given in Figure 4-54. The initial flank land width was further confirmed by optical and scanning electron microscopes, as shown in Figure 4-55.

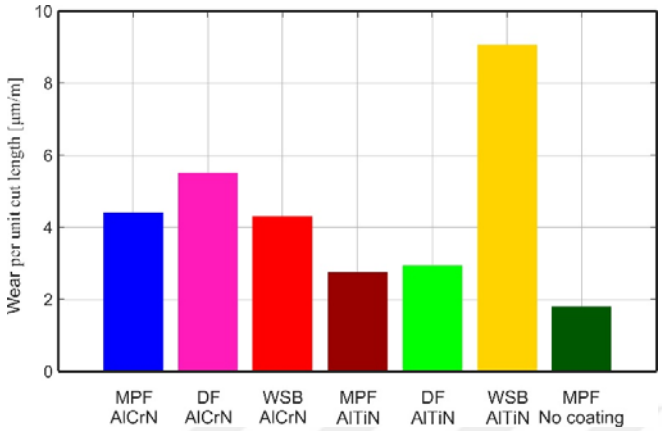

Figure 4-53: The rate of wear of the flank land when machining Ti6Al4V.

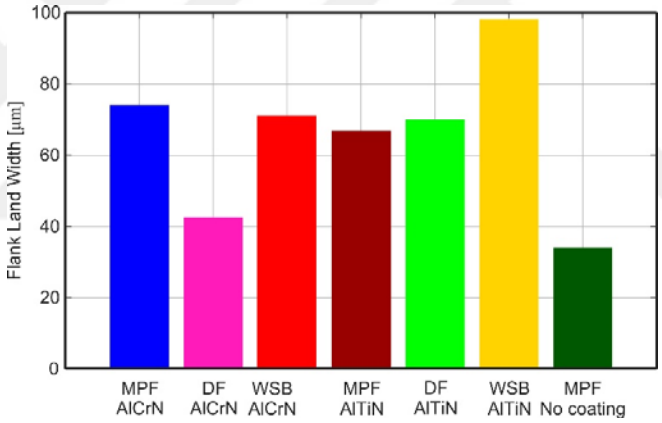

Figure 4-54: The initial width of the flank land for the tools used during wear analysis for machining Ti6Al4V.

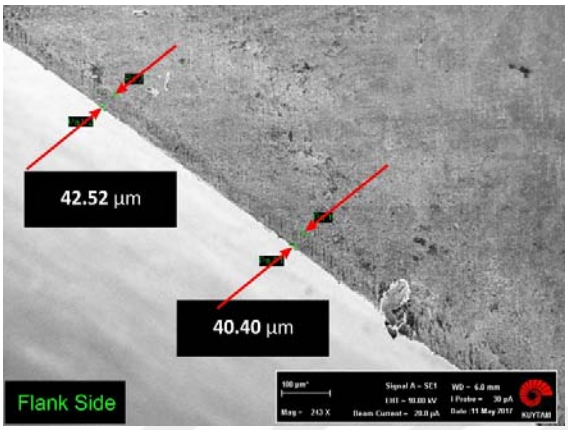

Figure 4-55: The scanning electron microscope image and flank side width measurement for the AlCrN coated and Drag finished end-mill.

The surface roughness of the end-mill finished surfaces was measured using white light interferometry technique on the flank side of the tool. The R_q and R_a values are given in Figure 4-56.

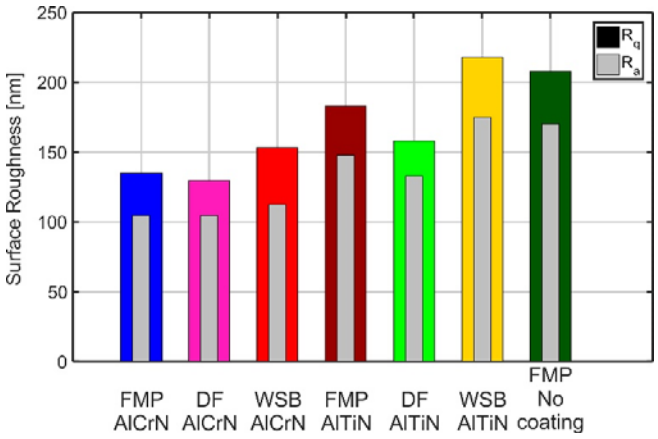

Figure 4-56: The surface roughness measured by WLI technique.

The investigated matters are put together and ranked to observe co-relationship between them. The tested tools are ranked, from least to maximum, with respect to the resultant of the cutting forces, the width of the primary flank side, the surface roughness of the primary flank side, the wear rate of primary flank side and the friction coefficient, lower the number being better.

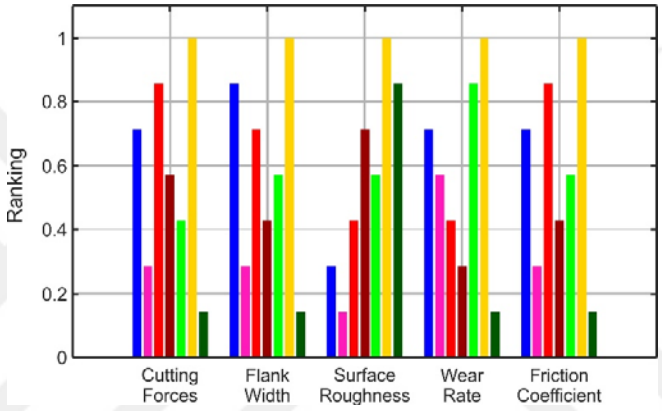

Figure 4-57: The tested tools ranked 1 to 7 for the respective category.

c. Conclusion

The tool surface preparation techniques and their coating materials were investigated for machining Ti6Al4V. The conclusions are summarized as follows

1. The tool performances were most sensitive to the flank side width. The end-mills with the highest magnitudes for the flank side width recorded the highest values for cutting forces. For comparison, the wet sandblast finished AlTiN coated tool had 98 µm flank side width and recorded 159 N for the resultant of the cutting forces on the side cutting

edge, whereas the resultant of the cutting forces on the side cutting edge was 95 N for the drag finished AlCrN coated end-mill with a flank side width of 43 μm when the feedrate per tooth was 60μm.

2. The performance and friction coefficient of the tested end-mills are not dependent on the given range of variation in surface roughness values.
3. The drag finished AlCrN coated end-mill registered the lowest magnitudes for cutting forces from the coated tools with a 0.5 friction coefficient for machining Ti6Al4V. For the same material, the friction coefficient was 0.7 for the end-mills with finished surfaces from the drag type and the wet sandblast type finishing techniques. The larger flank side width produced a significant detrimental effect on the friction coefficient.
4. The AlTiN coated tool and surface from finish with magnetic powder technique had the lowest wear rate with a friction coefficient of 0.6 when machining the titanium alloy Ti6Al4V material workpiece.
5. The friction coefficient for AlTiN coated end-mills with surfaces produced with finish from magnetic powder and drag type techniques was 0.6.
6. For the comparable flank side width, in general, the friction coefficient for the AlTiN type coating was less than the AlCrN coating. The exceptions were when either the flank side width is narrower or wider than the average of the lot. The AlTiN coated tool with wet sandblast finished surface had an unusually wide primary flank side width, which affected the friction coefficient values.

4.5 Drilling

Drilling is one of the common machining operations and is always necessary for parts requiring non or semi-permanent assembly. The titanium alloy Ti-6Al-4V is a widely used material, especially in aerospace and biomedical industries. This alloy is known as a difficult-to-cut material. Due to its poor thermal properties, the heat generated during machining processes traps near material deformation zones. This causes detrimental high temperatures for the cutting tools. This section combines the analytical and FEM modeling techniques to estimate the temperature evolution of carbide tools in Ti-6Al-4V drilling. A novel thermocouple based temperature measurement setup is also introduced in this section. Moreover, the simulated and measured temperatures under various cutting conditions for the drilling of Ti-6Al-4V are presented for the validation.

4.5.1 Rotary tool temperature device

This work was done in collaboration with Laboratoire Bourguignon des Matériaux et Procédés, Arts and Metiers ParisTech. The French team of researchers developed a novel device, shown in the Figure 4-58. It is named the Rotary Tool Temperature (RTT). It is capable of measuring the drilling temperature close to the cutting edge. This innovative device has the advantage to be easily associated with a rotating multi-component dynamometer for drilling and milling operations. The new measurement device is integrated to the rotary dynamometer and tool holder for simultaneous measurement of the temperature along with forces and torques during the drilling operations.

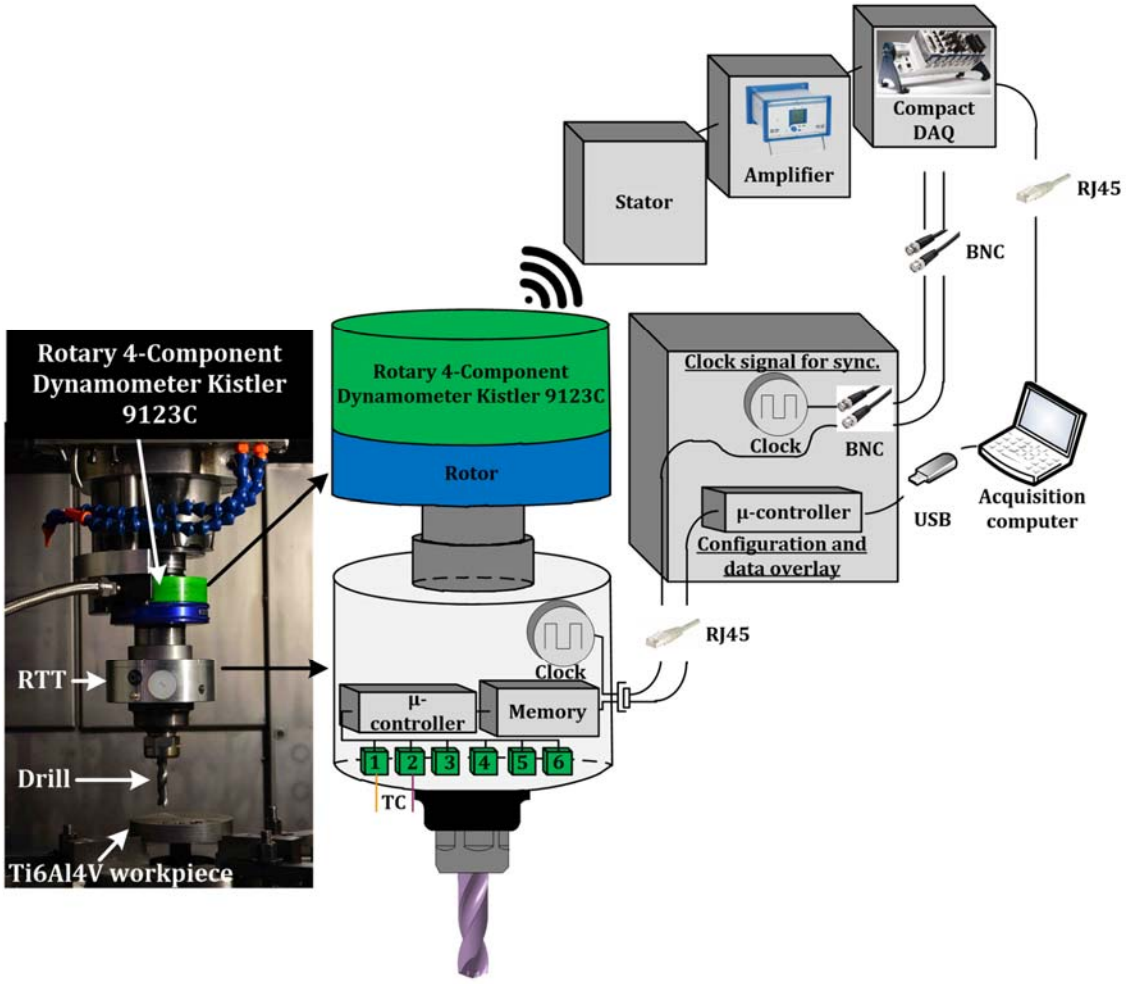

Figure 4-58: Experimental setup and scheme of the temperature acquisition.

This RTT device consists of following components:

- The connectors with cold junction compensations to acquire signal up to six thermocouples.
- An internal memory to store the signal as a function of time during machining.

- An on-board lithium battery (3.6 V, 3.6 Ah, and a maximum recommended continuous current of 130 mA).
- An internal clock to synchronize all the signals.

The RTT device is capable of being used with any standard tool holder and provide the temperature measurements for both drilling and milling operations. The system has two parts: the RTT itself assembled and spinning together with the drill, and an external module in charge of the data communication to the computer using an RJ45 connection. The external module includes an independent clock; this clock pulse is essential when a simultaneous measurement of cutting forces and temperature is necessary.

The RTT is prepared for temperature measurement using the following steps as shown in the Figure 4-59.

1 The two clocks are launched with the same pulse rate and triggered simultaneously. Once clock synchronization is complete, the two acquisition systems are unplugged.
2 Machining is performed. The temperature, clock and force data are collected by respective systems.
3 After the machining test, the temperature data are downloaded from the RTT on-board memory.
4 Post-synchronization of the collected signals is performed.

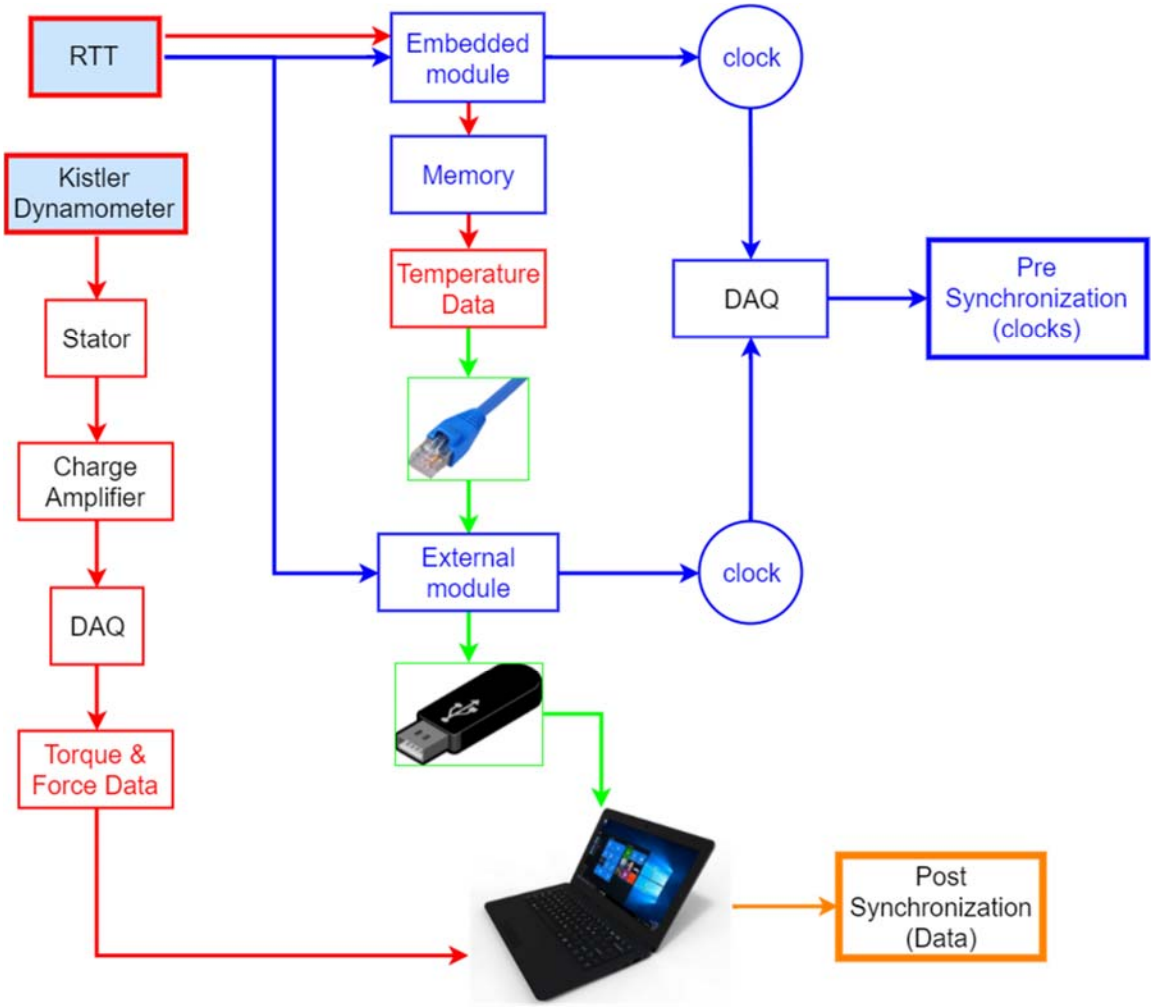

Figure 4-59: RTT prelaunch synchronization steps.

After the pre-launch sequence the machining is performed. The cutting forces and the external clock signal are recorded independently. The temperature data are downloaded from the RTT on-board memory and post-synchronized to the other signals using the two clock signals.

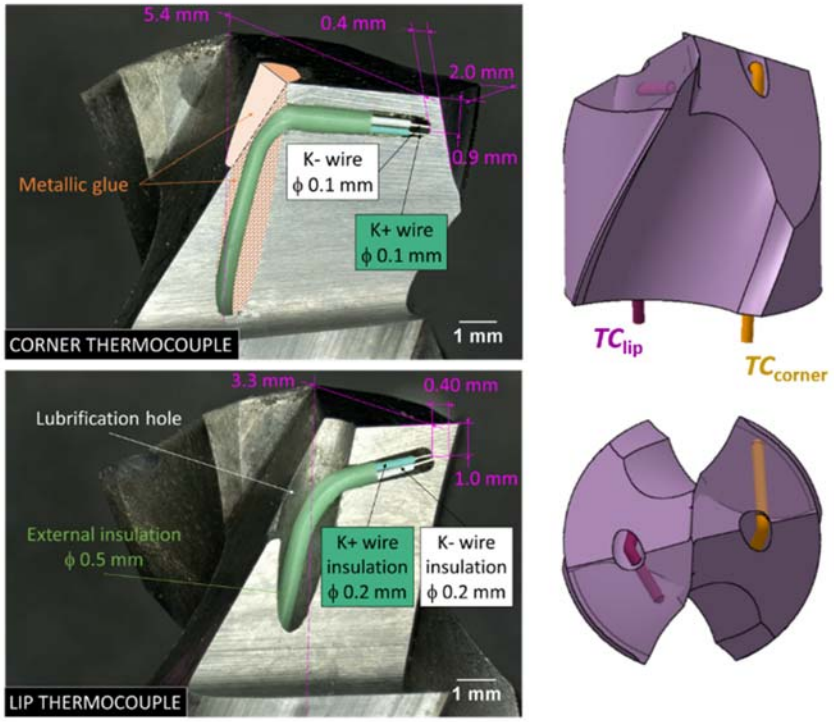

Figure 4-60: Illustration of the corner and lip thermocouple locations in the drill.

The RTT device is used to measure temperature using two thermocouples. Two holes are created by electrical discharge machining (EDM) in the drill. One of the hole allows the thermocouple location to be close to where the cutting edge and the flute side edge meet. Whereas the other hole allows the thermocouple to be located close to the junction of the drill chisel edge and the cutting lip. Those two temperature locations are labelled as TC_{corner} and TC_{lip} respectively. The wires connecting the two thermocouples with the RTT device are slipped through the lubricant conduits as shown on the Figure 4-60.

The two thermocouples are secured in the holes on the drill using a ceramic glue charged with silver particles. The silver particles improve the heat conductivity of the medium. The connecting wires are attached to the drill body using a ceramic adhesive to avoid any signal

distortion or disruption during the machining operation. The main characteristics of the RTT device presented and used in this work are summarized in the Table 4-21.

Table 4-21: RTT device specifications.

Memory capacity	64 Mb
Acquisition frequency	Up to 2.25 kHz
Accuracy	0.18 K
Tool-holder	body of 50 mm diameter

The thermocouples are used in a specific configuration to enable an instantaneous time response. The two thermocouple wires are in direct electrical contact with the bottom of the 0.5 mm holes in the tool as shown in the Figure 4-60. There are two hot junctions: K+/WCCo and WCCo/K-. As the tool material is part of the hot junction, the Seebeck's effect response is instantaneous. The only measurement time delay comes from the data acquisition frequency. The exact location of the measurement is at the K+/WCCo junction since the electromotive forces generated by the WCCo/K- is close to zero. The RTT calibration was conducted under the FD X07-029-2 standard, and the thermal drift checked and resulted as non-significant until 70 °C inside the RTT for both temperature measurement and for the clock generator.

4.5.2 Thermal modeling

The cutting forces are the input for the thermal modeling in the drilling operation. The cutting forces for the drilling process were estimated using the discretized orthogonal to oblique transformation model as described by Altintas (Armarego and Whitfield, 1985). The geometry of the helical drill used for the development of the oblique model is shown in the Figure 4-61.

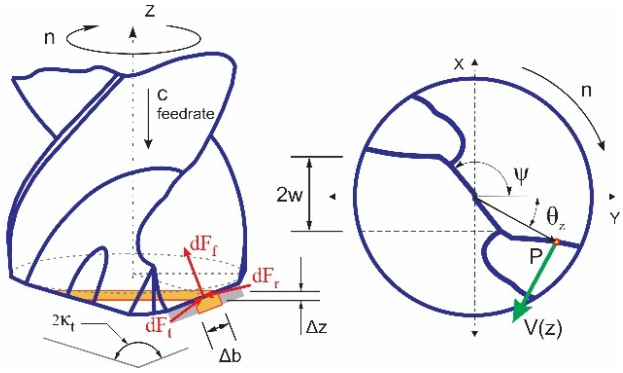

Figure 4-61: Discretization of cutting forces along the cutting lip.

$$\left.\begin{aligned} dF_{\mathrm{t}}(z) &= K_{\mathrm{tc}}(z)dA + \Delta b K_{\mathrm{te}} \\ dF_{\mathrm{f}}(z) &= K_{\mathrm{fc}}(z)dA + \Delta b K_{\mathrm{fe}} \\ dF_{\mathrm{r}}(z) &= K_{\mathrm{rc}}(z)dA + \Delta b K_{\mathrm{re}} \end{aligned}\right\} \qquad (1)$$

$$h = \frac{c}{2}\sin\kappa_t \,, \Delta b = \frac{\Delta z}{\cos\kappa_t}$$

Equation (1) determines the discrete force components along the tangential (dF_{t}), feed (dF_{f}) and radial (dF_{r}) direction for a selected disk with the differential chip load (dA) of ($\Delta b.\mathrm{h}$). Here, ($K_{\mathrm{tc}}, K_{\mathrm{fc}}, K_{\mathrm{rc}}$) and ($K_{\mathrm{te}}, K_{\mathrm{fe}}, K_{\mathrm{re}}$) are the cutting force and edge force coefficients for the tangential, feed and radial direction respectively. The cutting coefficients calculated and used to predict the cutting forces for these experiments are provided in the Table 4-22.

Table 4-22: Cutting coefficients calculated and used to predict the cutting forces during drilling; K_{te} and K_{fe} are 24 and 43 N.mm-1, respectively in all regions.

Cutting force coefficients [N.mm^{-2}]	Region 1	Region 2	Region 3	Region 4
K_{tc}	2445	2154	1953	1815
K_{fc}	1523	1042	774	606
K_{rc}	892	649	481	372

The mechanical properties of the workpiece material required by the transformation model for the cutting forces analytical modeling, and for a Δz thick discrete disk (as shown in Figure 4-61), were taken from the Ti-6Al-4V alloy material database reproduced in (Altintas, 2012). The analytical calculation of the transition torque required for the selected cutting conditions is in good agreement with the experimentally measured torque as shown in Figure 4-62.

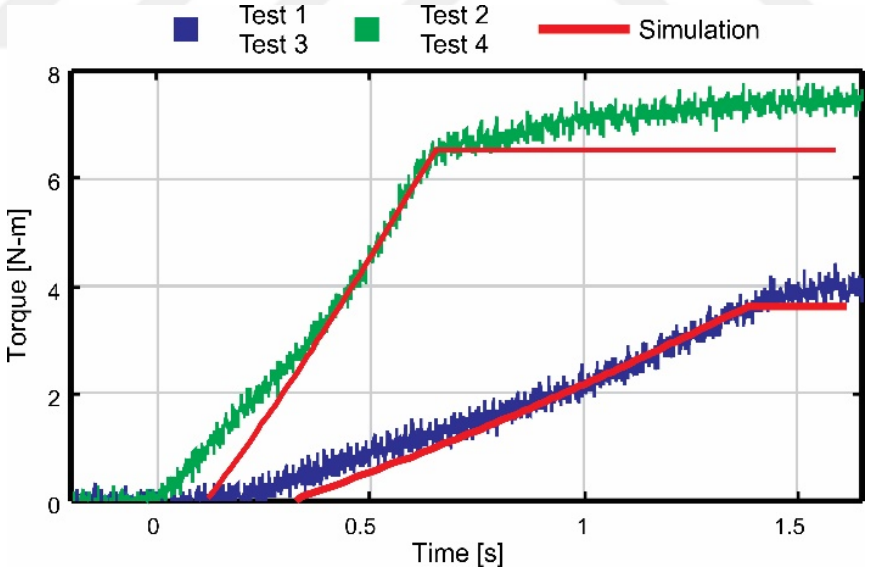

Figure 4-62: Torque prediction are compared with the experimental data for the two feedrates.

The experiment drill chisel edge width w and chisel edge angle ψ was 2 mm and 131° respectively. The drill geometry is complex and changes along the cutting lip. The critical parameters such as chip flow angle η, effective rake angle α_f, oblique shear angle ϕ_i, normal shear angle ϕ_n, local helix angle β_z vary and affect the differential cutting forces on the cutting lip. The variation of those angles are illustrated in the Figure 4-63.

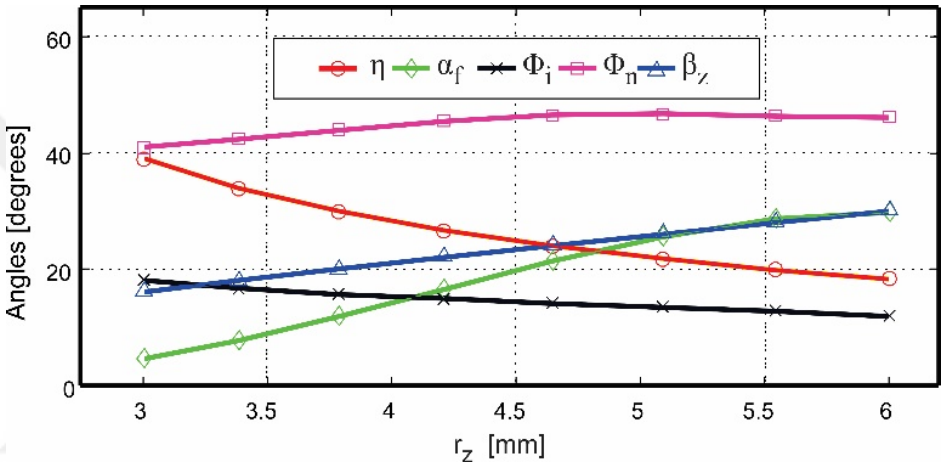

Figure 4-63: Variation of angles along the drill cutting lip.

The resultant cutting force (dF_R) on a differential chip load can be determined as the following:

$$dF_R(z) = \sqrt{dF_t^2(z) + dF_f^2(z) + dF_r^2(z)} \quad (2)$$

The resultant cutting forces were then dissolved into their friction (dF_u) and normal components (dF_v) using the friction angle (β_a) in equations (3) and (4) as follows:

$$dF_u(z) = dF_c(z)\sin(\beta_a) \quad (3)$$

$$dF_v(z) = dF_c(z)\cos(\beta_a) \quad (4)$$

Furthermore, the same parameters were used to establish the chip contact length l_c and chip velocity V_c as described in (Islam et al., 2012) using equations (5) and (6).

$$l_c = \frac{h \cdot \sec\eta \cdot sin(\phi_n + \theta_n)}{\sin\phi_n \cdot (\cos\alpha_n \cos\theta_n - \sin\alpha_n \sin\theta_n)} \quad (5)$$

$$V_c = \frac{V \cdot \sin i(z) \cdot \sin\phi_n(z) \cdot \sec\eta(z)}{\tan\phi_i(z) \cdot \cos\alpha_n(z) + \sin\phi_n(z) \cdot \tan\eta(z)} \quad (6)$$

The power lost to friction for the discrete section along the cutting edge of the drilling tool is the product of the differential friction force and the instantaneous chip velocity, given by equation (7).

$$dP_u(z) = dF_u \cdot V_c(z) \quad (7)$$

The second step used the information produced in the previous step to define the heating load and area which is active on the drilling tool. The heating load in this case for the tool is the heat partition coefficient corrected sum of all products of the differential friction force and the instantaneous chip velocity for a discrete element along the cutting edge of the drilling tool, calculated using the following equation:

$$P_u = \sum dP_u(z)\,;\; P_f = \lambda \cdot P_u \quad (8)$$

The heat partition coefficient for the tool (λ) was extrapolated to be 0.85 and 0.60 corresponding to the two cutting speeds as reported in (Rech et al., 2013) and (Egaña et al., 2012). The heat partition coefficient plots reported by the two are given in

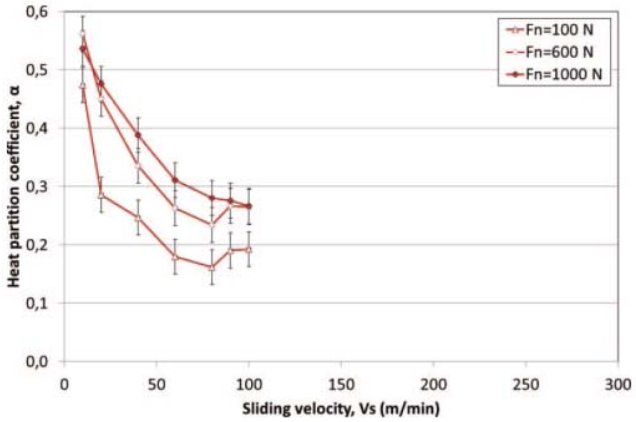

Figure 4-64: The evolution of the heat partition coefficient versus the cutting speed.(Egaña et al., 2012)

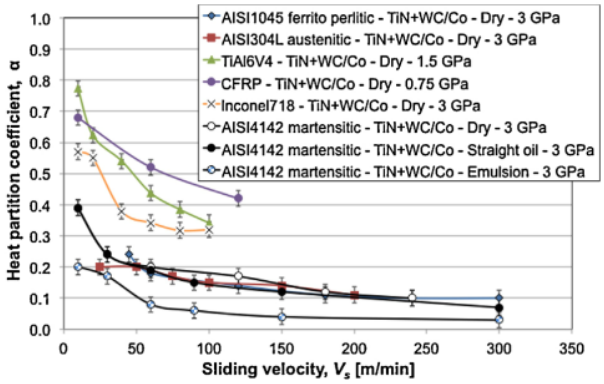

Figure 4-65: The heat partition coefficient for various tool workpiece material pairs. (Rech et al., 2013)

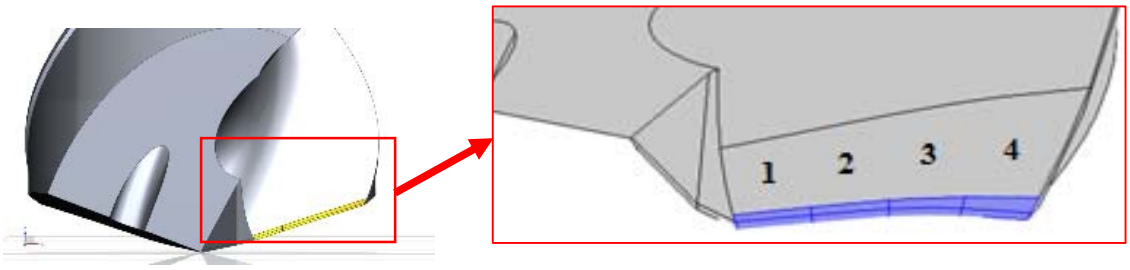

Figure 4-66:Chip contact zone divided into four discrete regions for the mechanical and thermal simulations.

Force, torque and temperature measurements were obtained in drilling of Ti-6Al-4V titanium alloy with a 12 mm diameter and 30° nominal helix angle, uncoated, two fluted carbide drill in dry cutting conditions as given in the Table 4-23. Drilling depth were kept at 20 mm in all tests.

Table 4-23: Cutting speed and feedrate values.

Test #	Rotational speed [rpm]	Cutting speed (V_c) [m.min^{-1}]	Feedrate (f) [mm.rev^{-1}]
1	266	10	0.1
2	266	10	0.2
3	796	30	0.1
4	796	30	0.2

The finite elements model (FEM) was developed for blind hole drilling. The tetrahedral type elements were selected to mesh the complex geometry of the tool. The mesh density was variable, but to capture the temperature distribution accurately it was made sure that the heat load areas had very fine mesh. The total number of tetrahedral element was 447267 with a minimum element size of 2 μm.

Thermo-dependent thermal properties were used for both the workpiece and the drill materials.

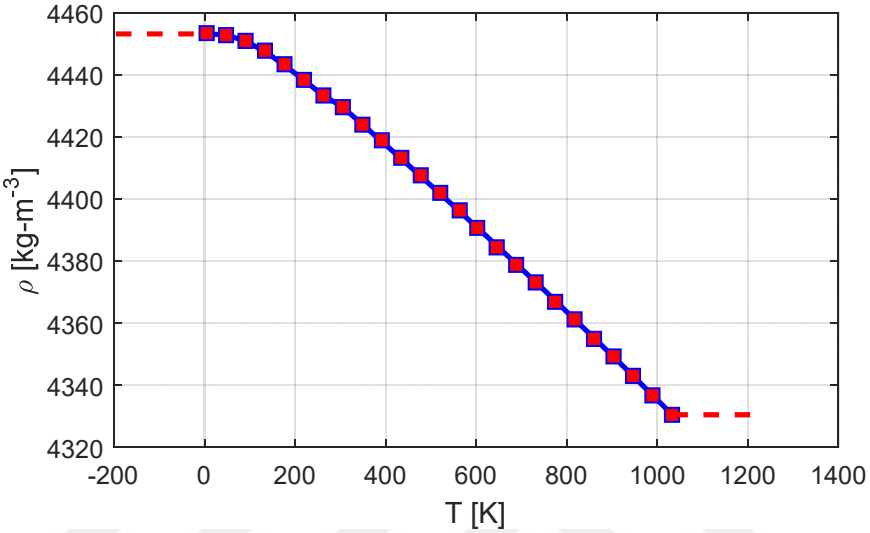

Figure 4-67: The Ti6Al4V temperature dependent density.

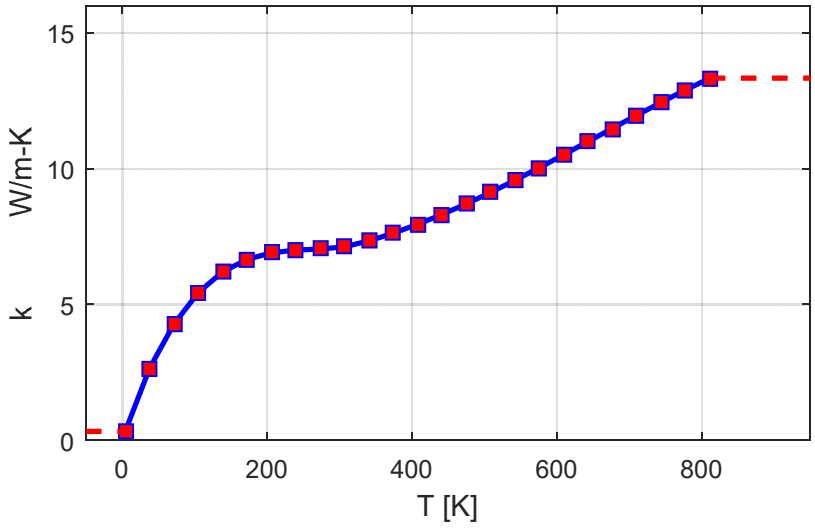

Figure 4-68: The Ti6Al4V temperature dependent thermal conductivity.

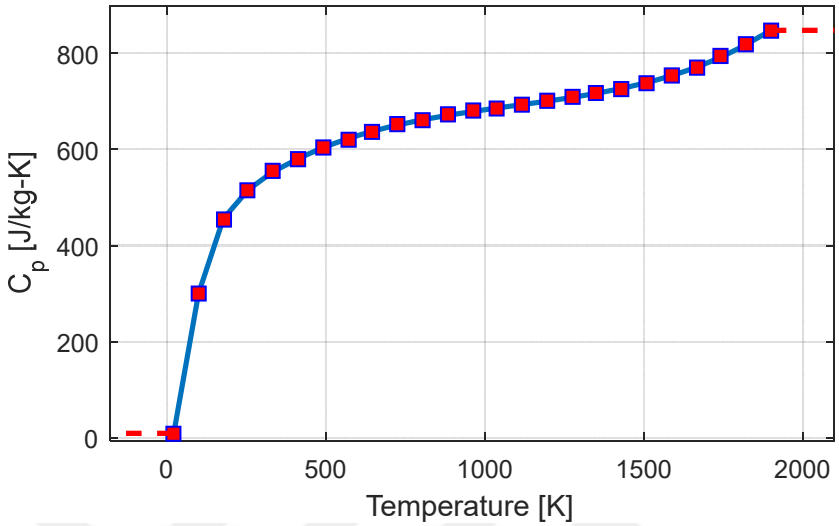

Figure 4-69: The Ti6Al4V temperature dependent constant pressure heat capacity.

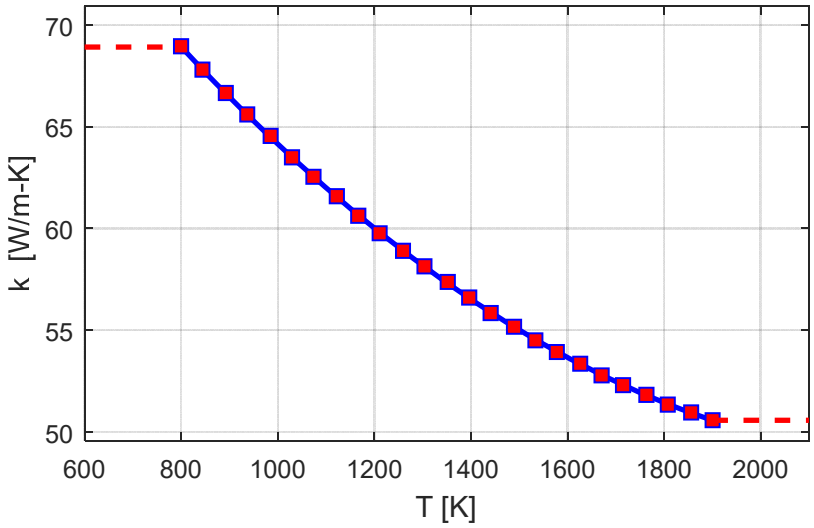

Figure 4-70: The tungsten carbide temperature dependent thermal conductivity.

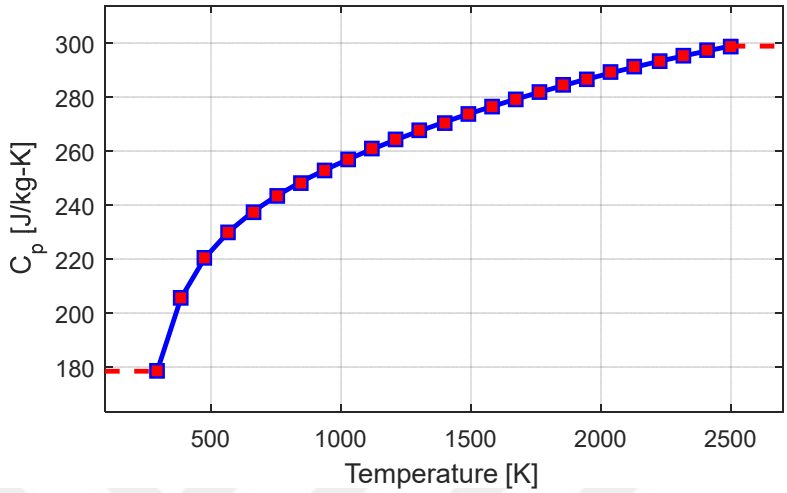

Figure 4-71: The tungsten carbide temperature dependent constant pressure heat capacity.

The boundary conditions on the tool and workpiece are selected to reflect the experimental conditions closely. The work piece bottom surface is given a constant temperature representing the much larger workpiece at constant temperature. The drill surface is given a boundary condition to reflect convective heat transfer for surface with moving medium. The magnitude for coefficient of convective heat transfer, h is taken equal to 10 $[W/m^2 \cdot K]$ (Holman J.P., 2010).

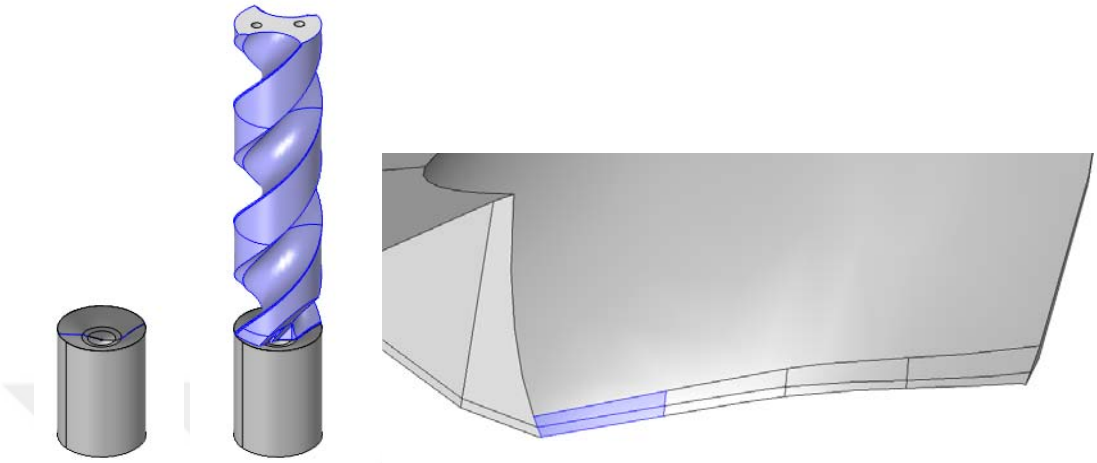

(a) (b) (c)

Figure 4-72: Boundary condition for the workpiece and the drill. (a) constant temperature boundary condition for workpiece base, (b) the convective cooling of the drill body and (c) the heat power surfaces on the cutting edge of the drill.

The cutting process is simulated as a time dependent heat transfer model, where the heat load will remain active for the duration of the cut as it was in the experiment. The heat load, as calculated earlier, is defined to be active only at the tool chip contact zone on the tool. Comsol Multiphysics software was used for the FEM analysis on an Intel Xeon CPU W5590 @ 3.33 GHz, 8 cores system for modeling the temperature distribution on the drill bit. Simulation time for each condition was less than 30 minutes.

4.5.3 Experimental validations

The drilling tests were performed on a DMC DMG 65 CNC machining center. Tests at each condition were performed three times to verify the repeatability. Only one drill had been used for the whole experimental campaign to avoid dispersion; a previous campaign ensured no tool wear can appear during the tests. Axial force F_z and torque M_z were also measured

by using a rotary type 9123C Kistler dynamometer (Figure 4-62). Force and temperature signals were sampled at the frequencies of 2 kHz and 256 Hz, respectively. During the drilling tests, the tool temperature at the two thermocouple locations specified previously were recorded. Simulated and measured tool temperatures at the specified tool corner and tool lip points are presented in Figure 4-73.

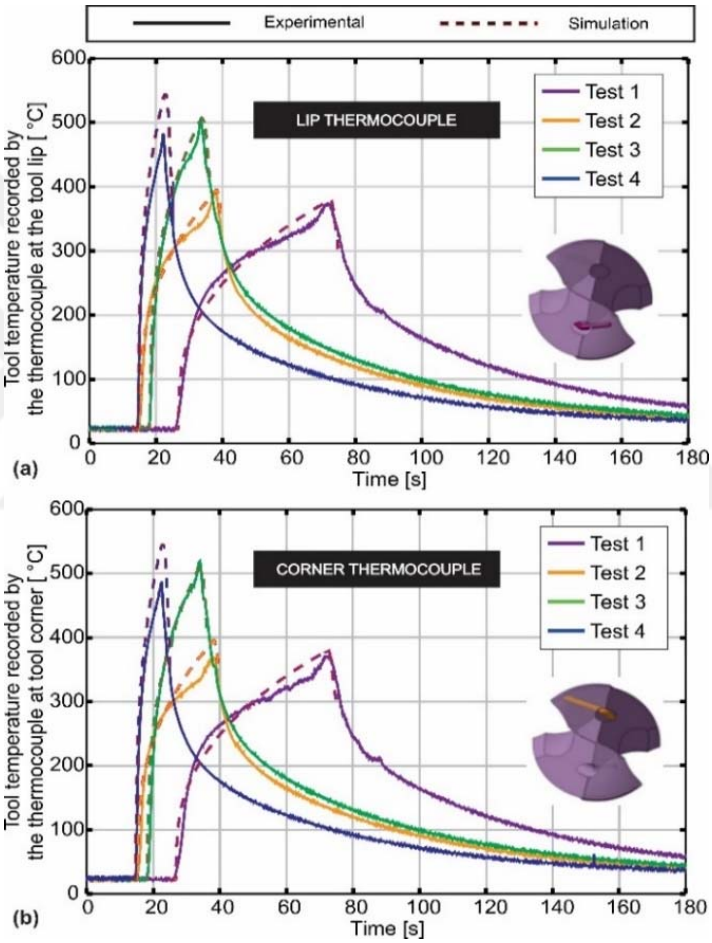

Figure 4-73: Simulated and measured tool temperatures: (a) for the thermocouple at the lip point (at TC_{lip}), (b) for the thermocouple at the corner point (at TC_{corner}) in the drilling of Ti-6Al-4V under the conditions given in Table 4-23.

4.5.3.1 Test 1

The test conditions are given in the Table 4-24. The Figure 4-74 gives the temperature distribution by the simulation for the test 1 cutting conditions. The subsequent plots in the Figure 4-75and Figure 4-76 give the comparison between the simulated and experimental values of the cutting temperature.

Table 4-24: Test 1 cutting conditions.

Cutting Speed	10	m/min
Feedrate	50	um/flute
Drilling Depth	20	mm
Drilling time	45.2	sec

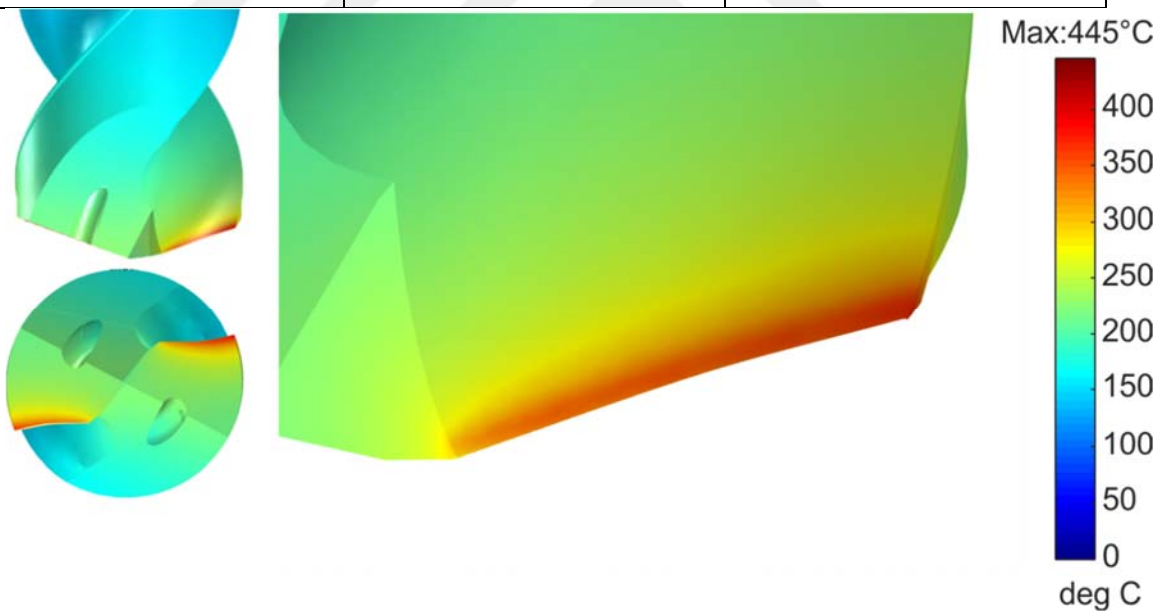

Figure 4-74: The temperature distribution simulation for the test 1 cutting conditions.

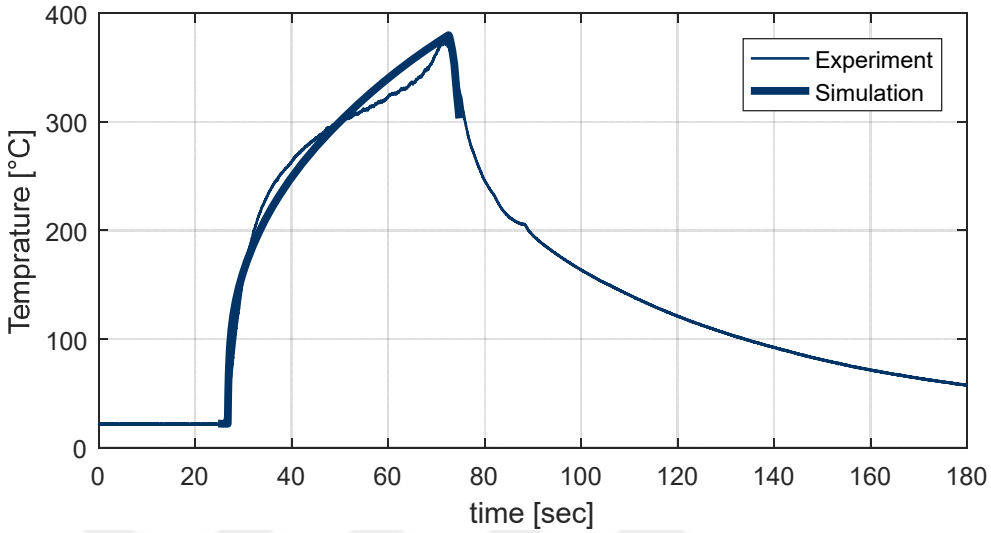

Figure 4-75: The change in drill cutting lip temperature as captured by the thermocouple at the inner corner for the test 1 cutting conditions.

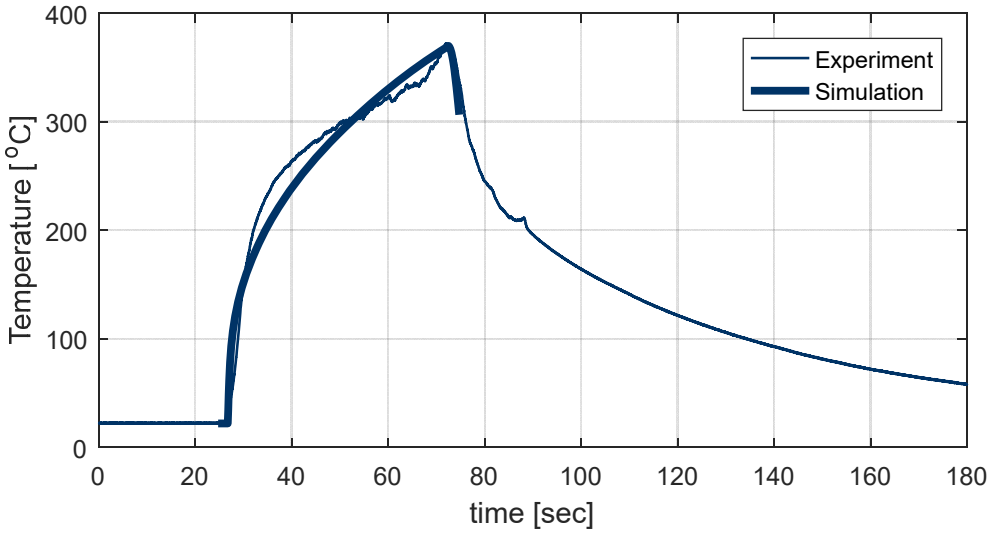

Figure 4-76: The change in drill cutting lip temperature as captured by the thermocouple at the outer corner for the test 1 cutting conditions.

4.5.3.2 Test 2

The test conditions are given in the Table 4-25. The Figure 4-77 gives the temperature distribution by the simulation for the test 1 cutting conditions. The subsequent plots in the Figure 4-78 and Figure 4-79 give the comparison between the simulated and experimental values of the cutting temperature.

Table 4-25: Test 2 cutting conditions.

Cutting Speed	10	m/min
Feedrate	100	um/flute
Drilling Depth	20	mm
Drilling time	22.6	sec

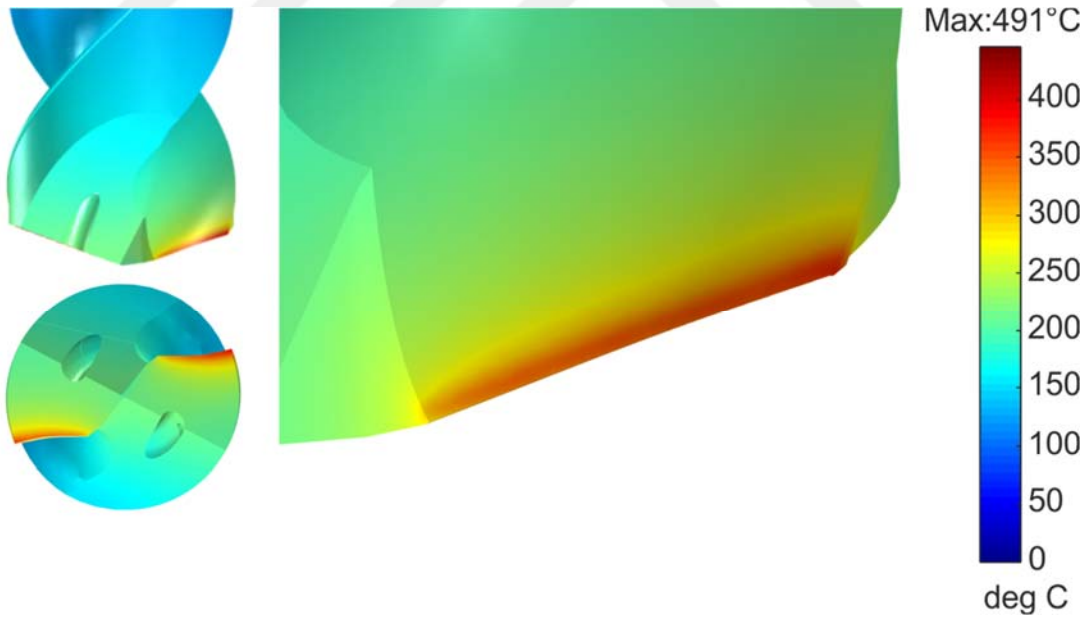

Figure 4-77: The temperature distribution simulation for the test 2 cutting conditions.

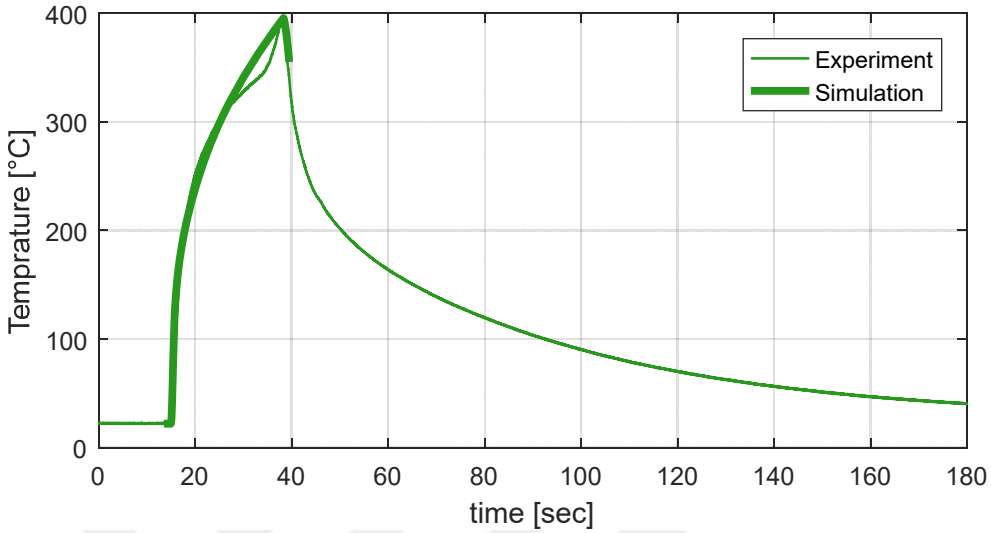

Figure 4-78: The change in drill cutting lip temperature as captured by the thermocouple at the inner corner for the test 2 cutting conditions.

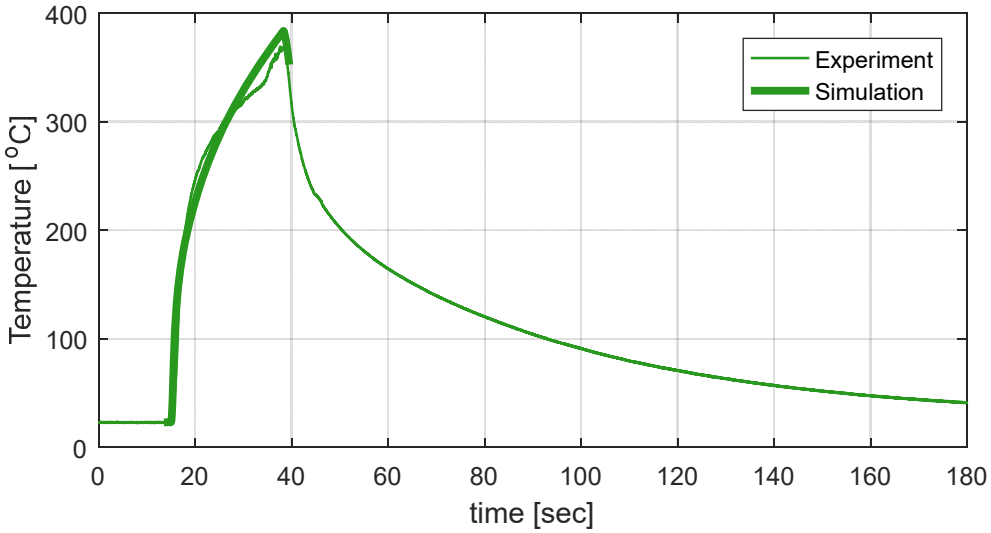

Figure 4-79: The change in drill cutting lip temperature as captured by the thermocouple at the outer corner for the test 2 cutting conditions.

4.5.3.3 Test 3

The test conditions are given in the Table 4-26. The Figure 4-80 gives the temperature distribution by the simulation for the test 1 cutting conditions. The subsequent plots in the Figure 4-75 and Figure 4-82 give the comparison between the simulated and experimental values of the cutting temperature.

Table 4-26: Test 3 cutting conditions.

Cutting Speed	30	m/min
Feedrate	50	um/flute
Drilling Depth	20	mm
Drilling time	15	sec

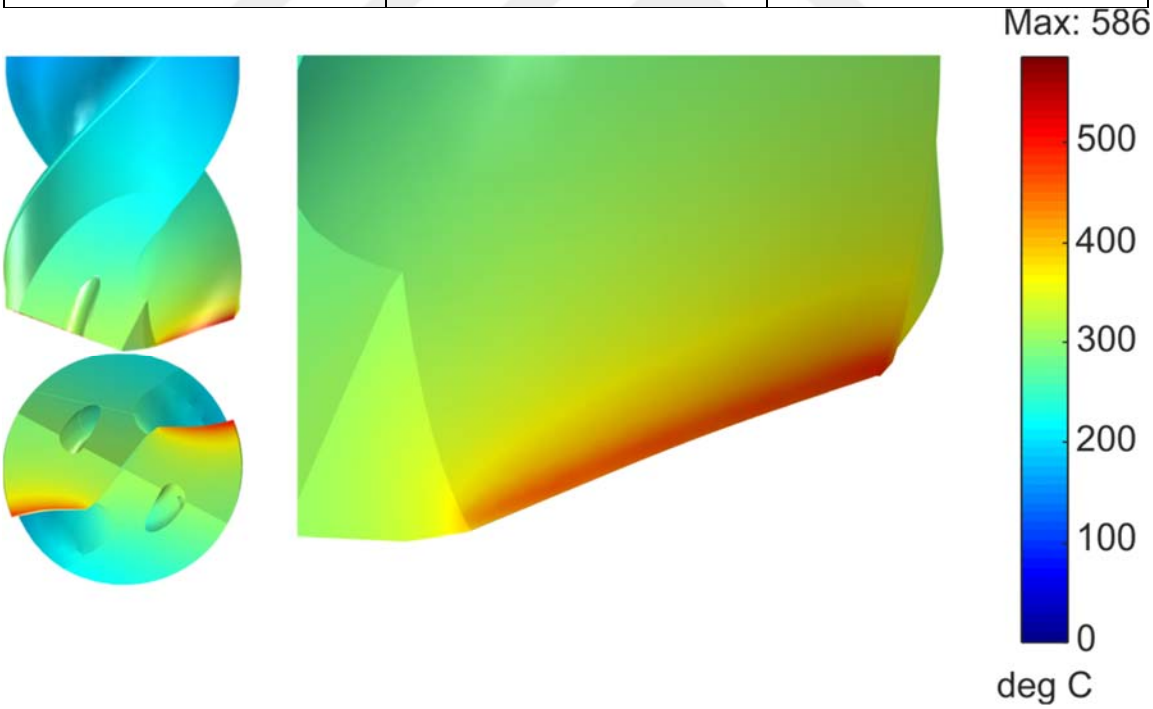

Figure 4-80: The temperature distribution simulation for the test 2 cutting conditions.

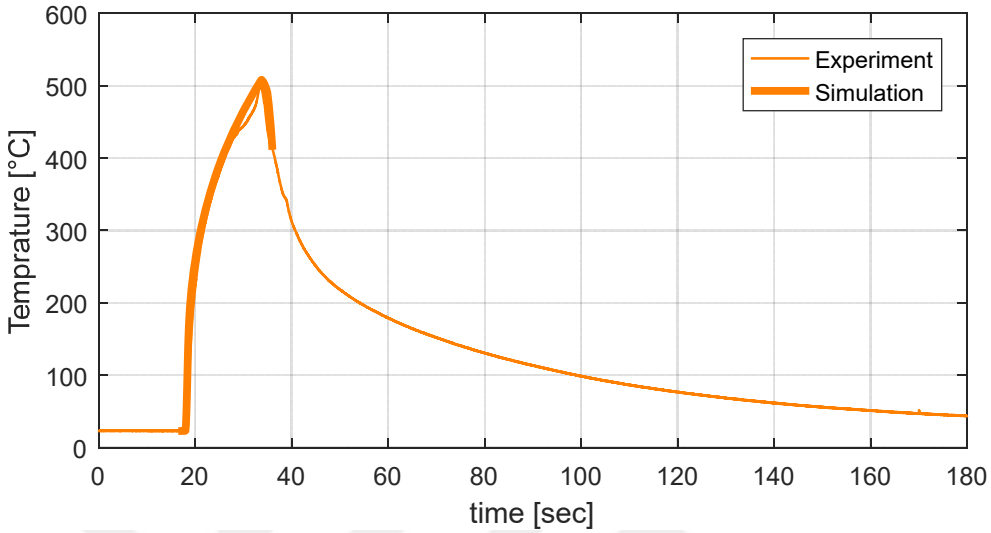

Figure 4-81: The change in drill cutting lip temperature as captured by the thermocouple at the inner corner for the test 3 cutting conditions.

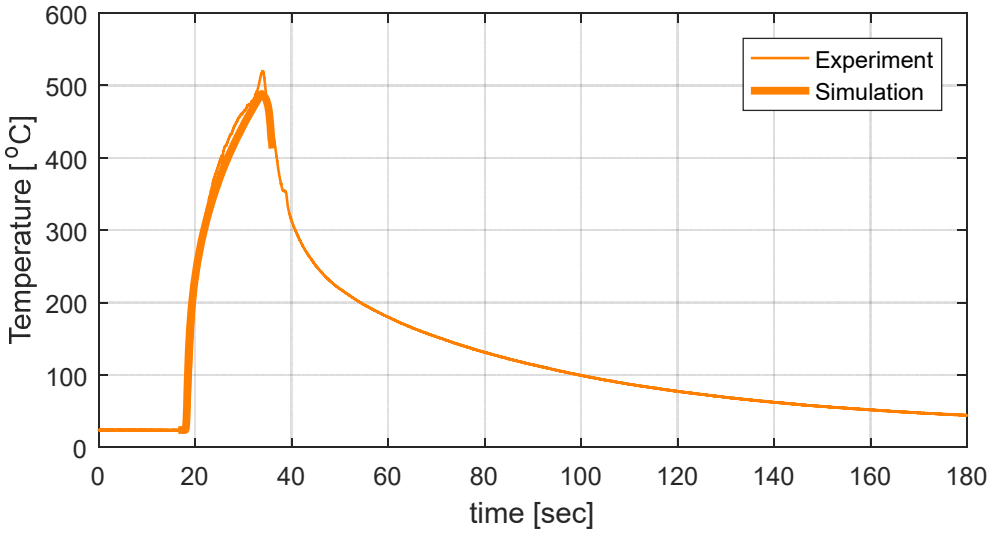

Figure 4-82: The change in drill cutting lip temperature as captured by the thermocouple at the outer corner for the test 3 cutting conditions.

4.5.3.4 Test 4

The test conditions are given in the Table 4-27. The Figure 4-83 gives the temperature distribution by the simulation for the test 1 cutting conditions. The subsequent plots in the Figure 4-84 and Figure 4-85 give the comparison between the simulated and experimental values of the cutting temperature.

Table 4-27: Test 4 cutting conditions.

Cutting Speed	30	m/min
Feedrate	100	um/flute
Drilling Depth	20	mm
Drilling time	7.5	sec

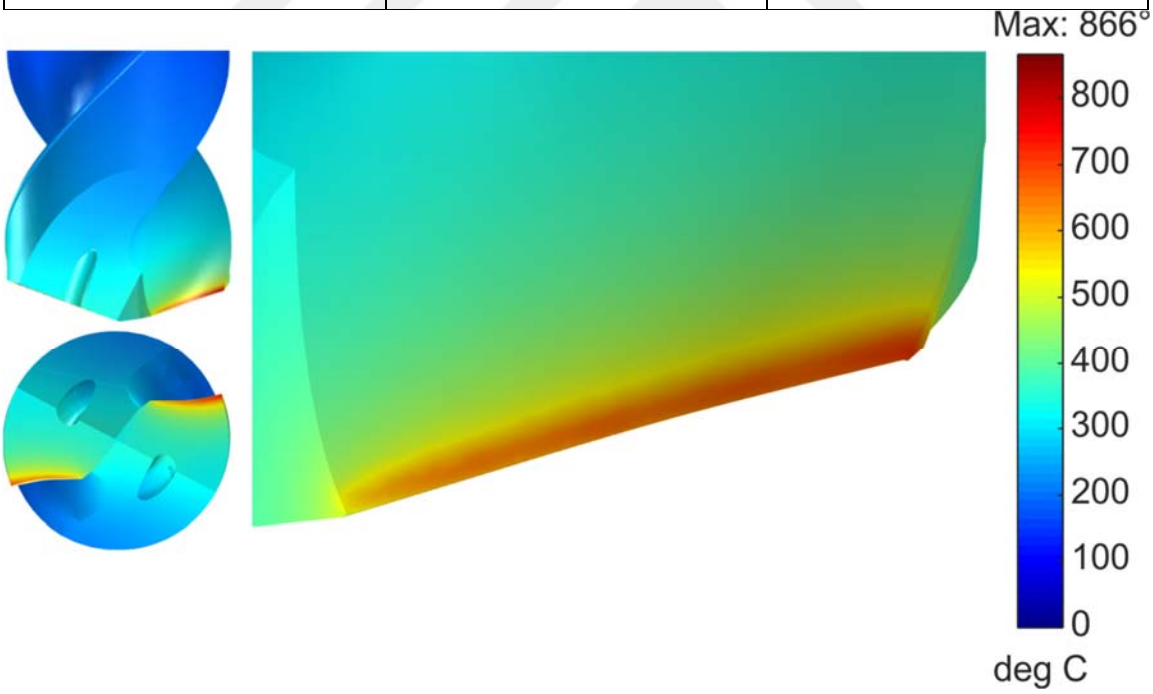

Figure 4-83: The temperature distribution simulation for the test 2 cutting conditions.

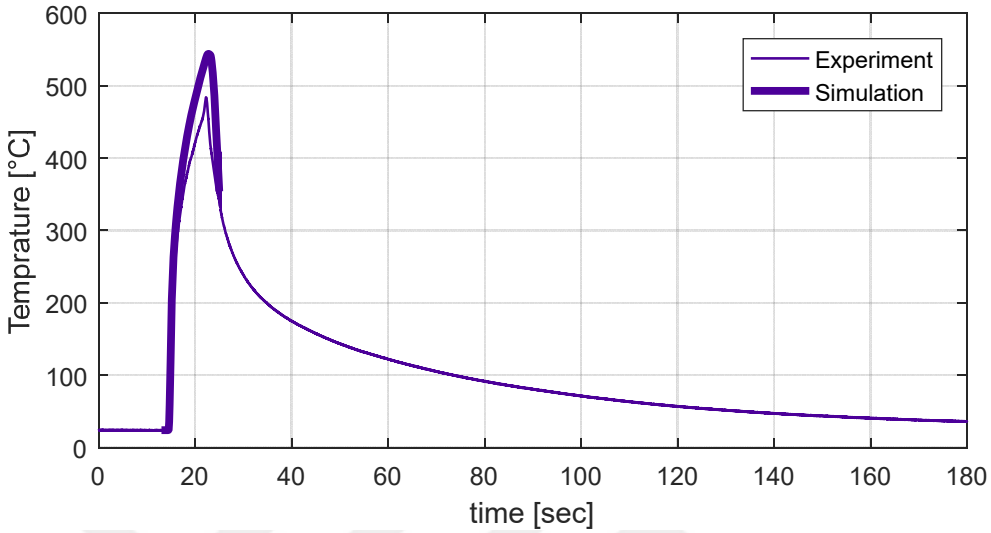

Figure 4-84: The change in drill cutting lip temperature as captured by the thermocouple at the inner corner for the test 4 cutting conditions.

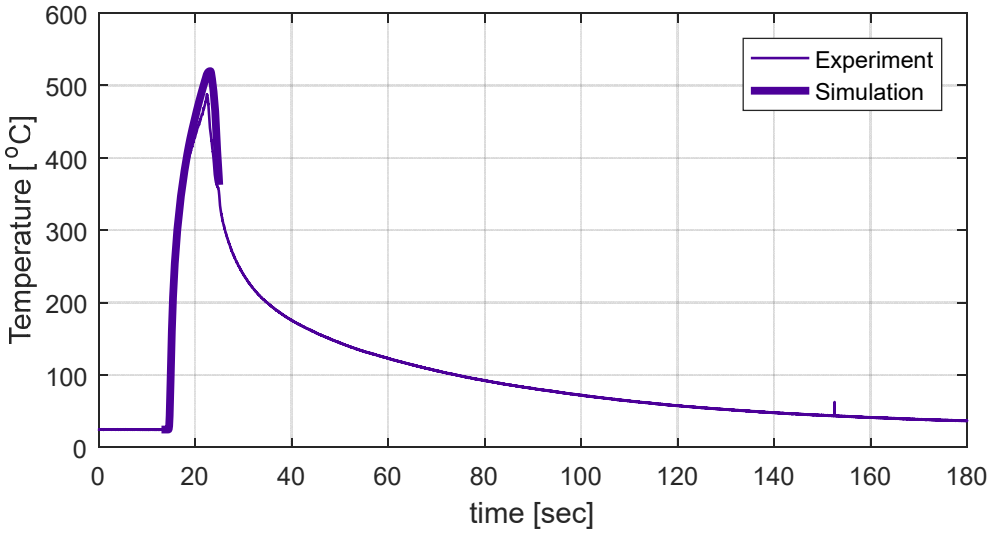

Figure 4-85: The change in drill cutting lip temperature as captured by the thermocouple at the outer corner for the test 4 cutting conditions.

Simulation results show that the local temperature near to the outer corner of the cutting lip, the tool temperature can be even higher as shown in the Figure 4-86.

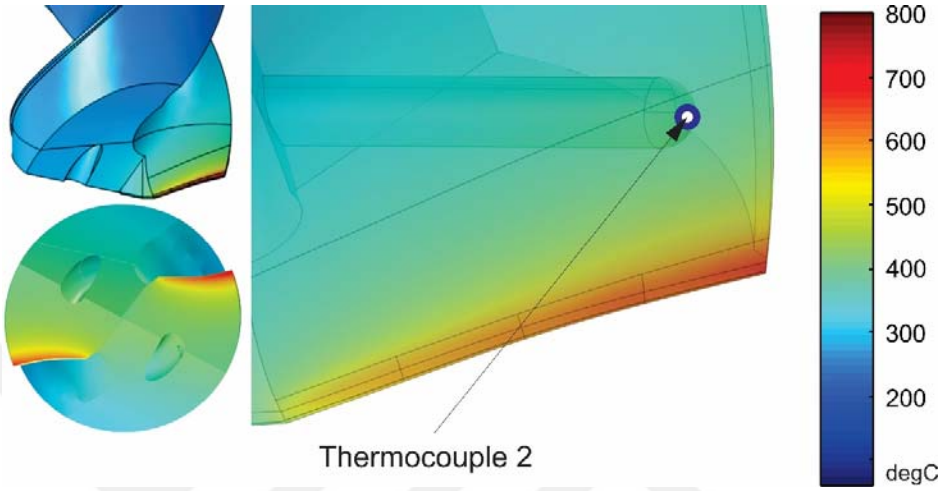

Figure 4-86: Temperature distribution on the drill cutting edge and tool body for V_c = 10 m.min^{-1} and f = 0.2 mm.rev^{-1}.

4.5.4 Conclusion

As seen in the simulation plots given in Figure 4-73 to Figure 4-85, the simulation results and experimental measurements with the lip and corner thermocouples are matching quite well in trends as well as amplitudes with less than 10% differences at the maximum temperature points. For the cutting speed of 10 $m.min^{-1}$ and feedrate of 0.1 $mm.rev^{-1}$, temperature is about 370 °C at the thermocouple locations. When the cutting speed is increased to 30 $m.min^{-1}$ and feedrate of 0.2 $mm.rev^{-1}$, tool temperature at the thermocouple points are increased to about 500 °C.

Temperature remains to be one of the major limiting factors towards improving productivity of advanced engineering materials like titanium alloys. Thermal analysis of drilling is critical for better understanding of the process. This article combined the analytical and FEM modeling techniques to estimate the temperature evolution of carbide tools in Ti-6Al-4V drilling. In the article, a new thermocouple based temperature measurement system, named as Rotary Tool Temperature (RTT) device, was introduced. Moreover, the simulated and measured temperatures under various cutting conditions for the drilling of Ti-6Al-4V were presented as validations for the thermal model.

Chapter 5
Machining of Intermetallic Alloy Gamma Titanium Aluminide

5.1 Introduction

The milling of gamma titanium aluminide intermetallic alloy with coated solid carbide end-mills is studied. The performance of two coating materials, aluminum titanium nitride and aluminum chromium nitride were evaluated. There were three end-mills with a particular coating, where each was produced with different surface finishing technique. The three surface finish techniques were the finish with magnetic powder, drag finish and the wet sandblast finish.

5.2 Setup

The cutting tests were performed on Mori Seiki NMV5000 DCG 5-axis milling machine shown in the Figure 4-2. The work piece is prepared for secure mounting on top of the table type dynamometer. Whereas the cutting tool is held in tool-holder and Rotary type dynamometer assembly. The test setup is shown in the Figure 5-1. The force data were acquired using Kistler Table type dynamometer whereas rotary type dynamometer provided the power consumption and torque. Kistler company signal conditioning modules were employed for accurate and reliable sensor signals. High speed Data Acquisition System from National Instruments is used to collect the signals at 2300 Hz sampling rate.

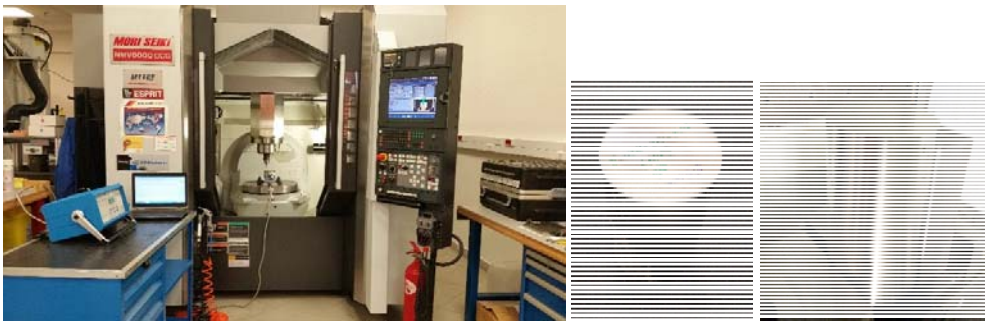

Figure 5-1: The Workpiece and its setup in the five axis Mori Seiki machine.

5.3 Cutting Parameters

The cutting forces were measured multiple times for selected feedrate in this investigation to improve data reliability. The list of tools selected is given in the Table 5-1. Three more test cases were included. The radial clearance angle on the cut edge of the case no 9 end-mill was changed to 7°. The earlier tests performed for machining of titanium alloy Ti6Al4V had showed the advantage of this design change. The number of flutes was increased from 4 to 5 for the case number 10 end-mill along with the radial clearance angle being changed to 7°.

Table 5-1: The end-mills tested for machining of γ −TiAl.

	Coating material	Finishing technique
1	Aluminum Titanium Nitride, (AlTiN)	Finishing with magnetic powder (FPM)
2		Drag Finishing (DF)
3		Wet Sandblast Finishing (WSF)
4	Aluminum Chromium Nitride, (AlCrN)	Finishing with magnetic powder (FPM)
5		Drag Finishing (DF)
6		Wet Sandblast Finishing (WSF)
7	No Coating	Finishing with magnetic powder (FPM)
8	Aluminum Chromium Nitride, (AlCrN)	Drag Finish (improved flute geometry)
9	Aluminum Chromium Nitride, (AlCrN)	Drag Finish (improved flute geometry)
10	Aluminum Chromium Nitride, (AlCrN)	Drag Finish (5 flutes)

For the initial assessment, the selected cutting conditions are given in the Table 5-2.

Table 5-2: Test setup parameters.

Cutting Parameters		
Material		
γ – TiAl		
Tool		
Type	Flat	
Diameter	12	mm
Number of Flutes	4 and 5	
Helix angle	36.5	deg
Pitch angle	84, 88, 94, 94	deg
Cutting Conditions		
Spindle Speed	400	rpm
Cutting Speed	15	m/min
Depth of cut	2	mm
Width of cut	0.5	mm
Max chip thickness	40	μm
Feedrates	64	mm/min

The workpiece was of cylindrical shape. The tool path was programmed to go a quarter of circle around the circular periphery for each test. The tool path trajectory is given in the

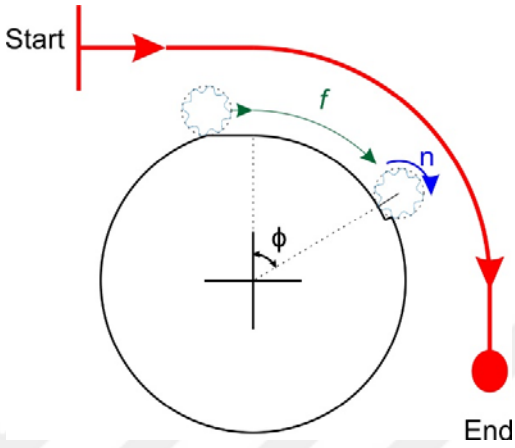

Figure 5-2: The tool path trajectory for the machining test of the gamma titanium aluminide compound.

The immersion angle was less than the lag angle of the end-mills, a nomenclature for the cutting forces is developed to compare between the test cases as shown in the Figure 5-3.

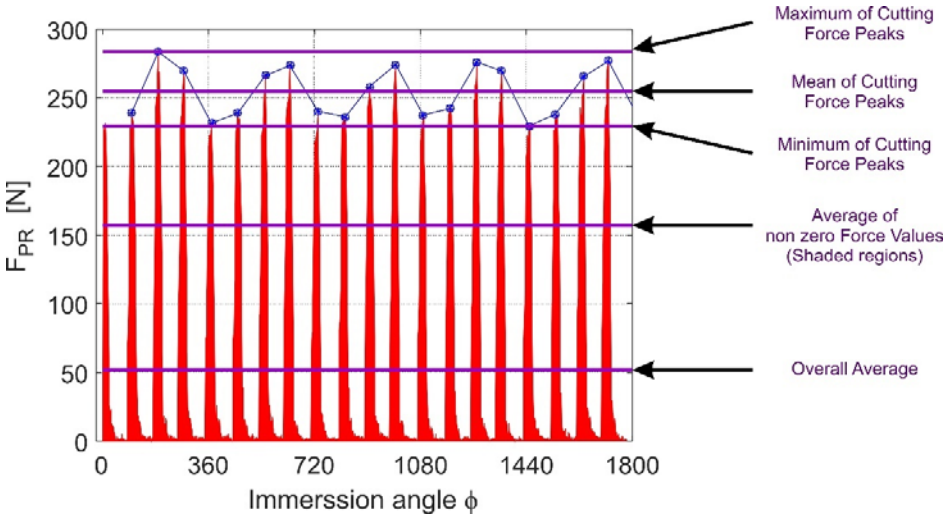

Figure 5-3:The nomenclature of forces for the machining test of gamma titanium aluminide.

The planar resultants of the recorded forces for the tested tools are given in the Table 5-3, Table 5-4 and Table 5-5. The performance of the end-mills is gauged on the force nomenclature shown in Figure 5-3.

Table 5-3: The planar resultant of the cutting forces for the test cases when machining gamma titanium aluminide for end-mills with aluminum titanium nitride coating.

Coating Material	Surface Finishing Technique		Maximum of peak cutting force [N]	Mean of peak cutting force [N]	Mean of non-zero Force values [N]
AlTiN	Magnetic	Test 1	313	256	167
		Test 2	329	288	159
		Test 3	371	296	168
		Ave	337	280	165
	Drag	Test 1	566	494	263
		Test 2	538	473	256
		Test 3	528	474	247
		Ave	544	480	255
	Sandblast	Test 1	334	267	167
		Test 2	358	303	165
		Test 3	368	320	180
		Ave	353	297	170

Table 5-4: The planar resultant of the cutting forces for the test cases when machining gamma titanium aluminide for end-mills with aluminum chromium nitride coating.

Coating Material	Surface Finishing Technique		Maximum of cutting force peaks [N]	Mean of cutting force peaks [N]	Mean of non-zero Force values [N]
AlCrN	Magnetic	Test 1	543	487	254
		Test 2	571	507	264
		Test 3	571	507	264
		Ave	562	500	260
AlCrN	Sandblast	Test 1	305	225	140
		Test 2	312	256	144
		Test 3	322	245	140
		Ave	313	242	142
AlCrN	Drag	Test 1	469	384	217
		Test 2	473	392	220
		Test 3	444	411	238
		Ave	462	396	225
No Coating	Magnetic	Test 1	413	344	219
		Test 2	413	376	204
		Test 3	423	379	216
		Ave	417	367	213

Table 5-5: The planar resultant of the cutting forces for the test cases when machining gamma titanium aluminide for end-mills with aluminum chromium nitride coating and modified cutting edges.

Coating Material	Surface Finishing Technique		Maximum of cutting force peaks [N]	Mean of cutting force peaks [N]	Mean of non-zero Force values [N]
AlCrN	Drag	Test 1	507	457	218
		Test 2	545	503	247
		Test 3	531	493	254
		Ave	528	485	240
	Drag	Test 1	216	140	81
		Test 2	217	141	89
		Test 3	239	156	93
		Ave	224	145	88
	Drag	Test 1	245	148	87
		Test 2	251	151	95
		Test 3	236	151	96
		Ave	244	150	93

The test cases are ranked from best to worst with respect to the average of the recorded forces in the three trials for each case. The cutting force data rank and summary are provided in the Table 5-6.

Table 5-6: The end-mill performance ranked and sorted.

	Coating Material	Surface Finishing Technique	Maximum of cutting force peaks	Mean of cutting force peaks	Mean of non-zero Force values	Rank
Test 9	AlCrN	Drag	224	145	88	**1**
Test 10	AlCrN	Drag	244	150	93	**2**
Test 2	AlCrN	Sandblast	317	251	142	**3**
Test 4	AlTiN	Magnetic	350	292	164	**4**
Test 6	AlTiN	Sandblast	363	311	172	**5**
Test 7	No Coating	Magnetic	418	378	210	**6**
Test 5	AlCrN	Drag	458	402	229	**7**
Test 8	AlCrN	Drag	528	485	240	**8**
Test 3	AlTiN	Drag	533	473	252	**9**
Test 1	AlCrN	Magnetic	571	507	264	**10**

5.4 Conclusion

Increasing the clearance angle improved the tool performance. Whereas the increase number of flutes increase the material removal rate.

Chapter 6
Aluminum Alloy Al7050

The machining of the aluminum alloy Al7050 is investigated to establish the cutting coefficients for the drilling operations and friction coefficient for differently coated end-mills in milling operation.

6.1 Drilling

6.1.1 Setup

The cutting tests were performed on Mori Seiki NMV5000 DCG 5-axis milling machine shown in the Figure 4-2. The work piece is prepared for secure mounting on top of the table type dynamometer. Whereas the cutting tool is held in tool-holder and Rotary type dynamometer assembly. The test setup is shown in figure 2. The force data were acquired using Kistler Table type dynamometer whereas rotary type dynamometer provided the power consumption and torque. Kistler company signal conditioning modules were employed for accurate and reliable sensor signals. High speed Data Acquisition System from National Instruments is used to collect the signals at 2300 Hz sampling rate.

Figure 6-1: The Al7050 workpiece setup for the drilling experiment

In a regular drill, the two flutes cut together. The cutting forces from the two flutes are equal in magnitudes but exactly opposite of each other. The net effect of the forces from the two is zero in the x and y direction of the dynamometer. The cutting forces in a drilling process are captured by grinding one of the flutes as shown in the Figure 6-2.

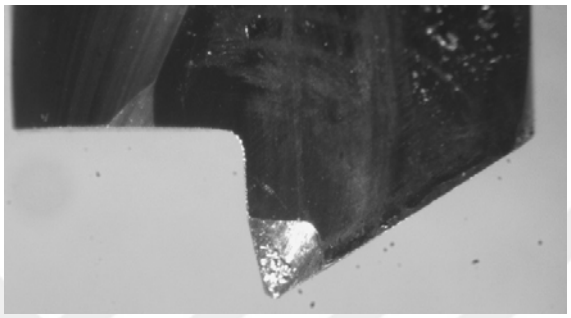

Figure 6-2: One of the flutes on the drill is grinded.

The drill geometry parameters and the test specifications are given in and the Table 6-1. Each test was repeated twice for reliability of the data.

Table 6-1: The drill geometry parameters and cutting conditions.

Cutting Parameters		
Material		
Al7050		
Tool		
Type	drill	
Diameter	7.7	mm
Number of Flutes	1	
Helix angle	30	deg

Table continued…

Tip angle	116	deg
Chisel angle	134.8	deg
Chisel width	1.752	mm
Cutting Conditions		
Spindle Speed	1000	rpm
Cutting Speed	24	m/min
Feedrates	a) 50 b) 75 c) 100 d) 150	mm/min

6.1.2 Force Model:

The drilling operation employs two different cutting modes. The drilling mechanics in the chisel edge engagement area is different from the cutting-edge engagement area. The forces from the two zones are added together to give the final force magnitudes. The experiment was designed to exclude the effect of the chisel edge.

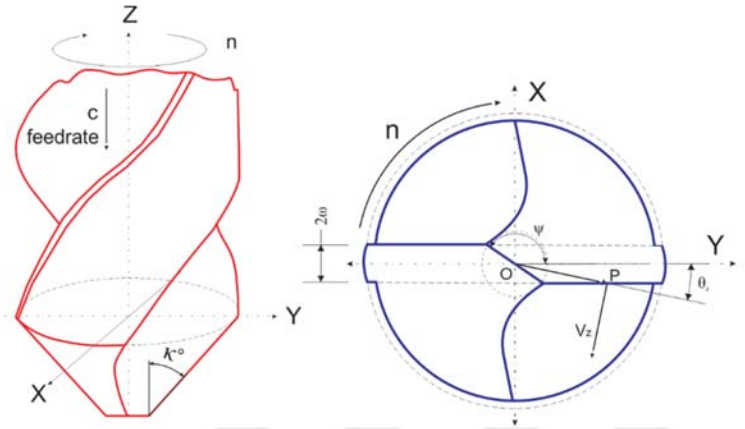

Figure 6-3: Mechanics of a Drill tip (Altintas, 2012)

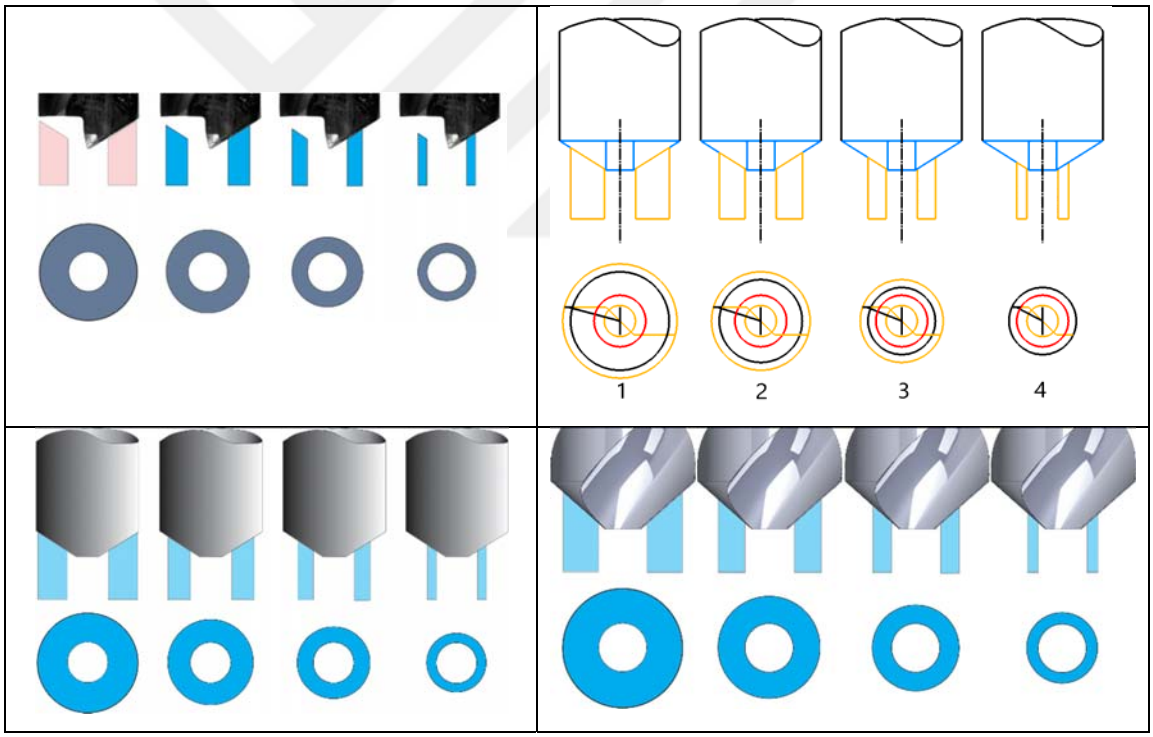

Figure 6-4: The section definition for drilling forces analysis

Figure 6-5: Workpiece before and after drilling.

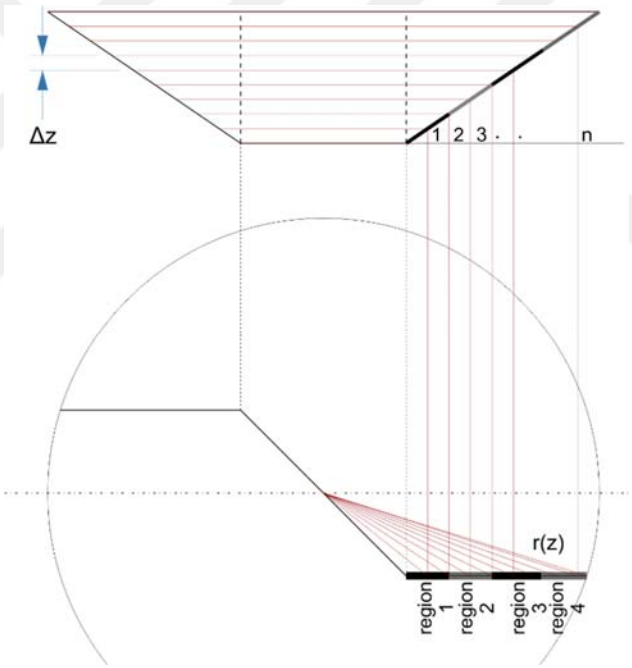

Figure 6-6: The discretization of the drill cutting edge.

The cutting forces were measured with a rotary type dynamometer. 3 mm pilot hole was drilled to exclude the contribution of forces produced by the chisel edge. This force data was used for section wise mechanistic calibration of the twist drill cutting edge. Mechanistic

calibration required transformation of measured forces in to the tangent/normal/psi coordinate system. The geometric relationship between the coordinate systems as given (Altintas, 2012) was used and reproduced here as equations 1 to 4.

The drill tip is discretized in to disks of height 'dz' as shown in the Figure 6-6. $\vec{r}_z$ is the vector defining the position of the point under consideration from the center in a plane normal to drill axis and at the corresponding heights.

$$\begin{bmatrix} dF_x \\ dF_y \\ dF_z \end{bmatrix} = \begin{bmatrix} -\cos\theta & \sin\gamma_d & \sin i \\ -\sin\theta & -\cos\gamma_d \cos\kappa_t & \sin i \cdot \sin\gamma_d \cdot \cos\kappa_t \\ 0 & \cos\gamma_d \cdot \sin\kappa_t & -(\sin i \cdot \sin\gamma_d \cdot \sin\kappa_t + \cos i \cdot \cos\kappa_t) \end{bmatrix} \begin{bmatrix} dF_t \\ dF_f \\ dF_\psi \end{bmatrix} \quad (1)$$

$$\begin{bmatrix} F_t \\ F_f \\ F_\psi \end{bmatrix} = \begin{bmatrix} -\cos\theta & \sin\gamma_d & \sin i \\ -\sin\theta & -\cos\gamma_d \cos\kappa_t & \sin i \cdot \sin\gamma_d \cdot \cos\kappa_t \\ 0 & \cos\gamma_d \cdot \sin\kappa_t & -(\sin i \cdot \sin\gamma_d \cdot \sin\kappa_t + \cos i \cdot \cos\kappa_t) \end{bmatrix}^{-1} \begin{bmatrix} \bar{F}_x \\ \bar{F}_y \\ \bar{F}_z \end{bmatrix} \quad (2)$$

$$\begin{aligned} F_t &= K_{tc}(z) \cdot db \cdot dh + K_{te}(z) db \\ F_f &= K_{fc}(z) \cdot db \cdot dh + K_{fe}(z) db \\ F_\psi &= K_{\psi c}(z) \cdot db \cdot dh + K_{\psi e}(z) db \end{aligned} \quad (3)$$

$$\begin{aligned} F_t &= \sum dF_t \\ F_z &= \sum dF_z \end{aligned} \quad (4)$$

The mechanistic calibration was obtained for individual sections as shown in Figure 6-4. The cutting coefficients were calculated for respective sections by subtracting sum of forces due to preceding sections. The cutting coefficients by mechanistic calibration for individual sections are given in the Table 6-2.

Table 6-2: Cutting coefficients for Aluminum 7050

Cutting coefficients		Section 1	Section 2	Section 3	Section 4
		1-1.65	1.65-2.15	2.15-2.65	2.65-3.13
K_{tc}	MPa/mm^2	553.32	604.25	742.89	922.05
K_{te}	MPa/mm	20.68	23.61	21.04	15.69
K_{fc}	MPa/mm^2	202.06	127.80	265.22	506.04
K_{fe}	MPa/mm	7.18	7.29	7.66	17.21
$K_{\psi c}$	MPa/mm^2	29.71	40.91	41.80	188.92
$K_{\psi e}$	MPa/mm	-2.6	-2.79	-3.28	-10.01

Armarego's classical oblique model represented by equations (5) and in combination with Al 7050 material database as reported in (Altintas, 2012) and given in Table 6-3 is used to predict cutting constants.

Table 6-3: Orthogonal Cutting Database for Aluminum Alloy Al 7050.

Aluminum Alloy Al 7050	
τ_s	250 MPa
β_a	19.25°
ϕ_a	23°

$$K_{tc} = \left[\frac{\tau_s}{\sin\varphi_n}\ \frac{cos(\beta_n - \alpha_n) + tan\ i\ tan\ \eta\ tan\ \beta_n}{\sqrt{\cos^2(\varphi_n + \beta_n - \alpha_n) + \tan^2\eta\sin^2\beta_n}}\right]$$

$$K_{fc} = \left[\frac{\tau_s}{\sin\varphi_n\ cos\ i}\ \frac{sin(\beta_n - \alpha_n)}{\sqrt{\cos^2(\varphi_n + \beta_n - \alpha_n) + \tan^2\eta\sin^2\beta_n}}\right] \quad (5)$$

$$K_{rc} = \left[\frac{\tau_s}{\sin\varphi_n} \frac{sin(\beta_n - \alpha_n)\, tan\, i - tan\, \eta\, tan\, \beta_n}{\sqrt{\cos^2(\varphi_n + \beta_n - \alpha_n) + \tan^2\eta \sin^2\beta_n}}\right]$$

Using both sets of cutting coefficients for aluminum 7050, one from mechanistic calibration and the other from orthogonal to oblique transformation, the predicted cutting forces are compared with the experimental data as shown in the Figure 6-7.

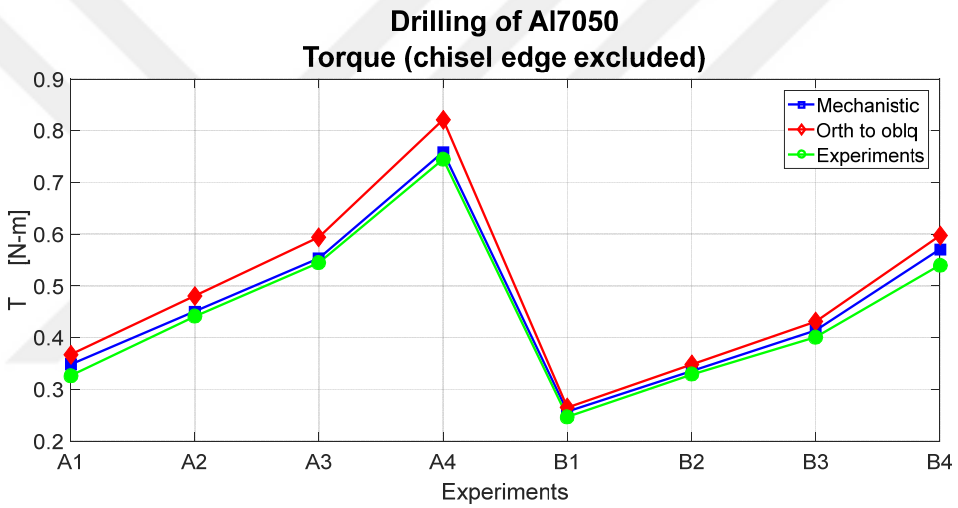

(a)

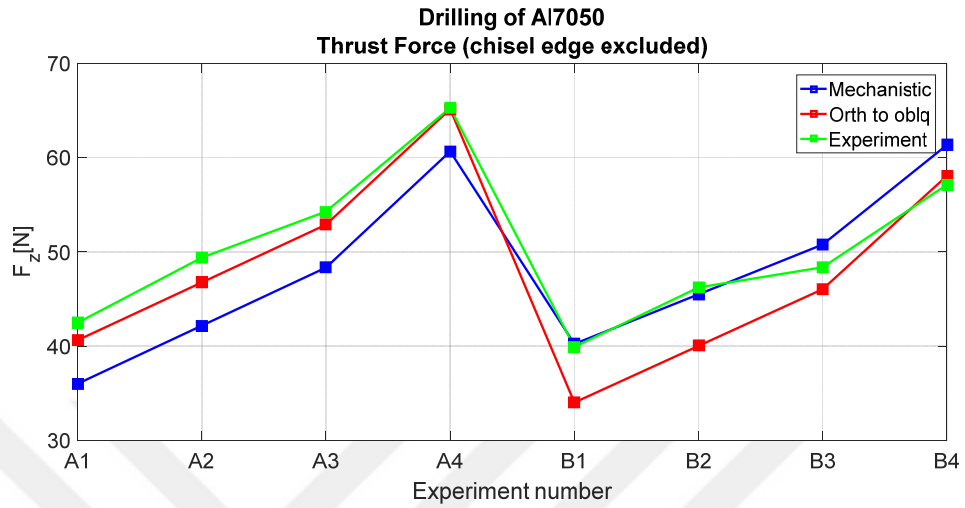

(b)

Figure 6-7: The comparison of mechanistic and orthogonal to oblique transformation model to the experimental data. (a) Torque (b) Thrust force.

6.1.3 Conclusion

The calculated cutting coefficients simulated the cutting torque in good agreement with the experimental data. The thrust force prediction was under estimating for some cases while matching closely in others.

6.2 Milling

6.2.1 Friction analysis

Specially designed friction analysis equipment is used for tribological tests. Nevertheless, the friction coefficient is deduced directly from the machining data is also reported in literature. Three methods have been reported.

6.2.1.1 Gradient method

(P. J. Arrazola and Meslin, 2002) reported the dependency of the ratio of the cutting and feed forces on the cutting-edge radius. They suggested to divide the force plot into distinct zones of constant friction coefficient and variable friction coefficient. The cutting forces are plotted against the feed forces. The slope of the line provides the friction coefficient for the workpiece and tool material pair. If the cutting force is given by f_c, the feed force by f_f and the rake angle of the cutting tool by α_r, then the friction coefficient for the tool-workpiece pair is given by the equation (1)

$$\mu = \tan\left(\alpha_r + \tan^{-1}\frac{f_f}{f_c}\right) \tag{1}$$

6.2.1.2 Mean friction coefficient

The friction coefficient is assumed to be quasi-static along the friction surface on the rake face. Then, the friction coefficient is calculated as the ratio of the mean cutting forces and the thrust forces (Ulutan and Özel, 2012). If the mean values for the thrust force is given by f_t and similarly the mean value for the cutting force by f_c, then the friction coefficient μ is given by the equation (2).

$$\mu = \frac{f_t}{f_c} \tag{2}$$

A similar approach is adopted where the cutting and thrust forces are adjusted by subtracting the ploughing force component from the mean value of the measured forces. the coefficient of friction calculated by this method is given by equation (3)

$$\mu = \frac{f_t - f_{t_0}}{f_c - f_{c_0}} \tag{3}$$

Where f_{t_0} is the edge force or the ploughing force in the thrust direction and f_{c_0} is the ploughing force in the cutting direction.

6.2.1.3 Two zone friction coefficient

Several works like (Bahi et al., 2011), (Ozlu et al., 2010), (Moufki et al., 1998), etc. have calculated the friction coefficient separately in two distinguished zones on the rake face of the tool, namely, the sticking zone and the sliding zone. Then the friction coefficient calculated from the total friction force and the normal force is called the apparent friction coefficient. The sliding friction coefficient is calculated from the friction force and normal force in the sliding region.

This work will report the friction coefficient for the milling process for solid carbide end-mill, calculated from two different methods. (a) using the cutting coefficients for the tool-workpiece pair, (b) using the mechanics of the end-milling process and (c) the mean friction coefficient method.

6.2.1.4 Friction coefficient calculation

a. Cutting coefficient method

The Merchant model of the orthogonal machining process is implemented for this study. The model establishes the relationships between the components of the cutting forces, tool geometry and physics of the process. The nominal rake angle α_r and the average friction

angle, β_a, illustrated in Figure 6-8, are related to the friction coefficient, μ through the orthogonal machining force components by the following equations.

$$\tan(\beta_a - \alpha_r) = \frac{F_{fc}}{F_{tc}} \tag{4}$$

$$\mu_a = \tan \beta_a \tag{5}$$

Where F_{tc} and F_{fc} are the tangential and feed direction forces for an orthogonal machining process kinematics.

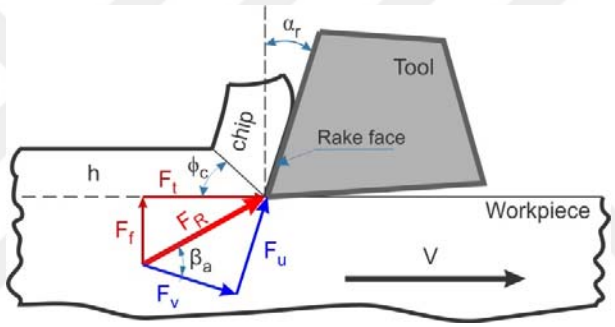

Figure 6-8: The cutting force components in an orthogonal machining process.

Contrary to continuous machining processes e.g. turning, milling process is intermittent in nature, where the uncut chip thickness is continuously changing with the rotation of the milling cutter and is given by equation 1.

$$h(\phi) = f_z \cdot \sin \phi \tag{6}$$

Here f_z is the feed per tooth of the milling cutter and ϕ is the cutter immersion angle. The mechanics of the milling operation, shown in Figure 6-9, are defined by three force components, namely, tangential, radial and axial cutting force.

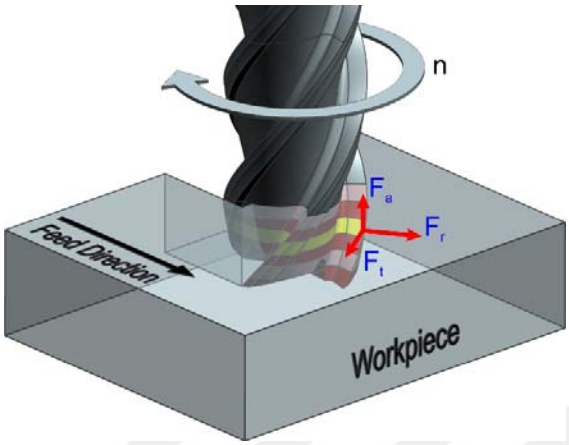

Figure 6-9: The cutting force components in the milling machining process.

The components of the cutting forces, acting on the milling cutter, for a disk of infinitesimal thickness Δz are shown in Figure 6-10.

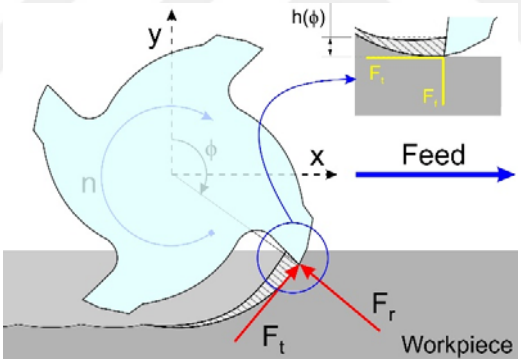

Figure 6-10: The mechanics of milling cutter.

The milling cutter has N flutes. If the cutting depth is divided into a discrete number of disks, M, then the cutting force components for the j^{th} disk on the i^{th} flute are a function of the uncut chip thickness, h, disk thickness, Δz and the respective cutting coefficients following the mechanics of milling cutters (Altintas, 2012).

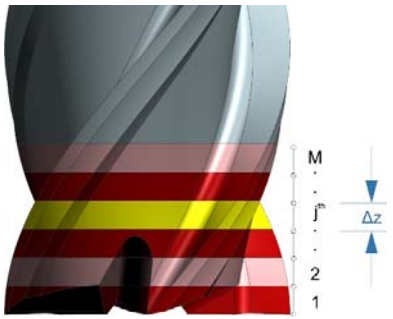

Figure 6-11: Discretization of the cutting depth for a milling cutter.

$$dF_t(\phi_{ij}, z) = \Delta z \cdot h(\phi_{ij}) \cdot K_{tc} + \Delta z \cdot K_{te}$$
$$dF_r(\phi_{ij}, z) = \Delta z \cdot h(\phi_{ij}) \cdot K_{rc} + \Delta z \cdot K_{re} \quad (7)$$
$$dF_a(\phi_{ij}, z) = \Delta z \cdot h(\phi_{ij}) \cdot K_{ac} + \Delta z \cdot K_{ae}$$

Or in general, the equations 4 are represented by having the cutting force components represented with ‘q’ then:

$$dF_q = df_{qc} + dF_{qe} \quad (8)$$

The relation of these force components with the global coordinate system is defined by the equations (2).

$$dF_{x,j}\left((\phi_{ij}), z\right) = -dF_{t_{ij}} \cos(\phi_{ij}) - dF_{r_{ij}} \sin(\phi_{ij})$$
$$dF_{y,j}\left((\phi_{ij}), z\right) = +dF_{t_{ij}} \sin(\phi_{ij}) - dF_{r_{ij}} \cos(\phi_{ij}) \quad (9)$$
$$dF_{z,j}\left((\phi_{ij}), z\right) = +dF_a$$

Combining the sets of equations given by Equations 4 and Equations 5 allows the direct relationship between the global coordinate system and the cutting parameters. After simplification, equations 6 gives the x and y components of the cutting forces:

$$
\begin{aligned}
dF_{x,j}\left(\phi_j(z)\right) &= \left[\frac{c}{2}\left(-K_{tc}\sin 2\varphi_j\,(z) - K_{rc}\left(1-\cos 2\varphi_j(z)\right)\right)\right. \\
&\quad \left. - K_{te}\cos\phi_j(z) - K_{re}\sin\phi_j(z)\right]\Delta z \\
dF_{y,j}\left(\phi_j(z)\right) &= \left[\frac{c}{2}\left(K_{tc}\left(1-cos\,2\varphi_j(z)\right) - K_{rc}\,sin\,2\varphi_j\,(z)\right)\right. \\
&\quad \left. + K_{te}\,sin\,\phi_j(z) - K_{re}\,cos\,\phi_j(z)\right]\Delta z \\
dF_{z,j}\left(\phi(z)\right) &= \left[cK_{ac}\sin\left(\,\phi_j(z)\right) + K_{ae}\right]\Delta z
\end{aligned}
\tag{10}
$$

The total cutting forces for an individual flute at a particular immersion angle are calculated by integrating along the cutting depth of the milling cutter.

$$
F_q\left(\phi_i(z)\right) = \int_{z_{i_1}}^{z_{i_2}} dF_q\left(\phi_i(z)\right)dz \tag{11}
$$

The integral will produce the average force along a particular axis for a flute, when the integration variable is changed from differential height dz to differential immersion angle $d\phi$. If ϕ_p is the pitch angle then the average force $\bar{F}_q$.

$$
\bar{F}_q = \frac{1}{\phi_p}\int_{\phi_{st}}^{\phi_{ex}} F_q(\phi)d\phi \tag{12}
$$

The cutting coefficients for the tangential and radial directions in a milling operation are found equations (9) (Altintas, 2012).

$$
\begin{aligned}
\bar{F}_x = \left[\frac{Nd_z f_z}{8\pi}\left[\left(K_{tc}\,cos\,2\varphi\right) - \left(K_{rc}(2\varphi - sin\,2\varphi)\right)\right]\right. \\
\left. + \frac{Nf_z}{2\pi}\left[-K_{te}\,sin\,\varphi + K_{re}\,cos\,\varphi\right]\right]_{\varphi_{st}}^{\varphi_{ex}}
\end{aligned}
\tag{13}
$$

$$\bar{F}_y = \left[\frac{N d_z f_z}{8\pi}[K_{tc}(2\varphi - sin\,2\varphi) + K_{rc}\,cos\,2\varphi] - \frac{N f_z}{2\pi}[K_{te}\,cos\,\varphi + K_{re}\,sin\,\varphi]\right]_{\varphi_{st}}^{\varphi_{ex}}$$

$\bar{F}_x$ and $\bar{F}_y$ are the average of the recorded forces in the experiment for a select number of revolutions in the fixed coordinate system. K_{tc}, K_{rc} and K_{te}, K_{re} are the cutting coefficients and edge coefficients in the tangential and feed directions respectively. *N* is the number of flutes, d_z is the differential thickness, f_z is the feed per tooth and ϕ is the immersion angle for the test.

The established cutting coefficients and equations set (4) can be used to simulate the tangential and radial force components for a discrete disk along the depth of cut, for any given immersion angle ϕ. The machining cutting forces and ploughing forces for specified cutting conditions are recognized separately following equation (5), where the index q represents the tangential or feed directions.

The comparison of Figure 6-8 for the orthogonal machining process and the Figure 6-10 for intermittent milling operation indicates similarity between the cutting forces components. The mechanics of the side cutting edge of a milling cutter is similar to a continuous machining operation, shown in Figure 6-10. Now if the contribution of the bottom edge of the milling cutter is removed from the force data, then the tangential and the feed direction forces in orthogonal cutting are analogous to the tangential and radial direction forces in the milling process.

The effect of the bottom cutting edge is isolated by collecting force data for two depths of cut as shown in Figure 6-12.

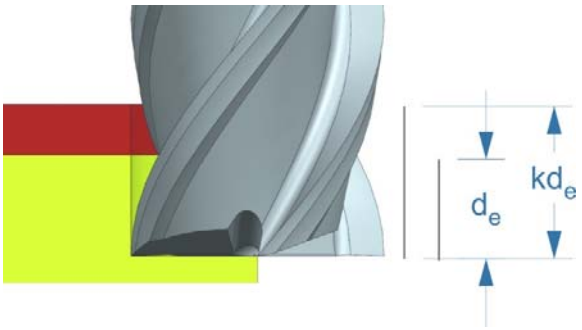

Figure 6-12: The two depths of cut to isolate the effect of the bottom edge.

Subtracting one set of forces from the other, hence produce a set of forces such that the obtained cutting forces are from the side edge only, as shown in Figure 6-13.

Figure 6-13: The method to isolate the cutting forces from the side edge of the milling cutter.

Additionally, the contribution of the axial cutting forces towards the overall resultant of the cutting forces, shown in Figure 6-14, was less than 1%.

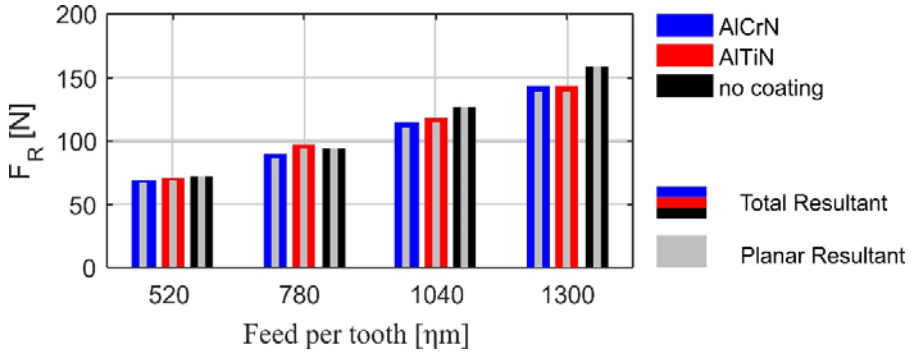

Figure 6-14: Comparison of the total resultant with the planar resultant of the cutting forces.

Accordingly, the radial direction component in the milling process is mapped to the feed direction component in orthogonal machining, $F_r \rightarrow F_f$.

With the force data being restricted to the side edge of the milling cutter and mapping allowed to utilize the identities defined for orthogonal machining to be implemented for the milling process mechanics. Therefore, for the pair of workpiece material and the tool coating, the friction coefficient, μ is calculated using relationship given by equation 2.

b. End-mill mechanics

The oblique cutting processes, shown in the Figure 6-15, as is the reality of the majority of machining processes, require many angles to completely define the cutting force components and the friction coefficient between the tool and the workpiece. They are the obliquity angle, $\boldsymbol{i}$: the angle between the cutting velocity and the normal to the cutting edge in the plane defined by the cut surface, the chip flow angle, $\boldsymbol{\eta}$: the angle between the normal to the cutting edge in a plane containing the rake face and the angle with which the cut chips slide over the rake face and the friction angle, $\boldsymbol{\beta_a}$: the angle between the resultant of the cutting forces and the unit vector normal to the rake face.

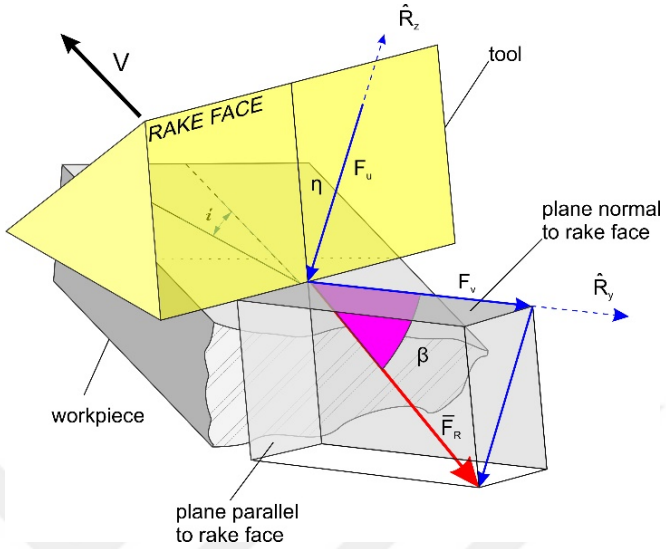

Figure 6-15: Kinematics of the oblique cutting process.

The nominal rake angle, $\boldsymbol{\alpha_r}$ is predefined and is manufactured as per demand, whereas the obliquity angle, $\boldsymbol{i}$ is a predetermined machining parameter, for the milling operations, it is equal to the helix angle of the cutting flutes. Lastly, the Stabler's rule gives a good estimation for the chip flow angle $\boldsymbol{\eta}$.

These angles are used to define three rotation matrices for coordinate transformation of the global coordinate system to a coordinate system where the resultant of the cutting forces is defined by two orthogonal components, such that one is collinear with the chip flow direction and the other to the normal to the rake face plane. The first of the three rotations is the obliquity angle, $\boldsymbol{i}$ rotation about the $\boldsymbol{z}$ axis. Then $\boldsymbol{\alpha_r}$ rotation about new $\boldsymbol{x}$ axis is followed and finally, $\boldsymbol{\eta}$ rotation about the new $\boldsymbol{y}$ axis. The three rotations are illustrated in Figure 6-16.

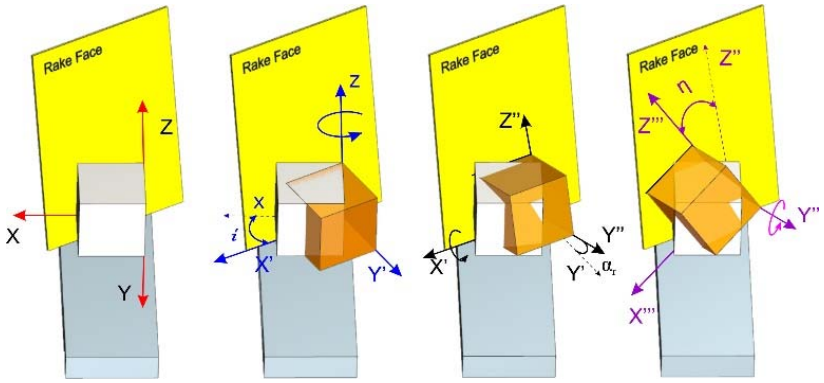

Figure 6-16: Coordinate transformation steps for the final transformation matrix.

The three transformation matrices are given by equations 3.

$$R_z = \begin{bmatrix} \cos i & \sin i & 0 \\ -\sin i & \cos i & 0 \\ 0 & 0 & 1 \end{bmatrix}$$

$$R_x = \begin{bmatrix} 1 & 0 & 0 \\ 0 & \cos \alpha_r & \sin \alpha_r \\ 0 & -\sin \alpha_r & \cos \alpha_r \end{bmatrix}$$

$$R_y = \begin{bmatrix} \cos \eta & 0 & -\sin \eta \\ 0 & 1 & 0 \\ \sin \eta & 0 & \cos \eta \end{bmatrix} \tag{14}$$

$$R = R_y \times R_x \times R_z$$

$$\begin{bmatrix} F_u \\ F_v \\ F_w \end{bmatrix} = R \times \begin{bmatrix} F_{x_c} \\ F_{y_c} \\ F_{z_c} \end{bmatrix}$$

The global directions ***x***, ***y*** and ***z*** are redefined in the new ***u***, ***v***, and ***w*.** The new coordinate system resolves the resultant of the cutting force vector into two components, one parallel to

the chip flow direction and the other normal to the rake face, the third being negligible in magnitude. Hence, the friction coefficient for the oblique cutting process is found using equation 2. The friction angle can also be found using the dot product of the unit vectors, where one is parallel to the resultant of the cutting forces and the other is normal to the rake face, as shown in the Figure 6-16.

$$\beta_a = \cos^{-1}\left(\hat{F}_R \cdot \hat{F}_v\right) \tag{15}$$

Contrary to continuous machining processes e.g. turning, milling process is intermittent in nature, where the uncut chip thickness is continuously changing with the rotation of the milling cutter and is given by equation 1.

$$h(\phi) = f_z \cdot \sin\phi \tag{16}$$

Here f_z is the feed per tooth of the milling cutter and ϕ is the cutter immersion angle. The mechanics of the milling operation, shown in the Figure 6-17 (a) and Figure 6-17 (b), are defined by three force components, namely, tangential, radial and axial cutting force.

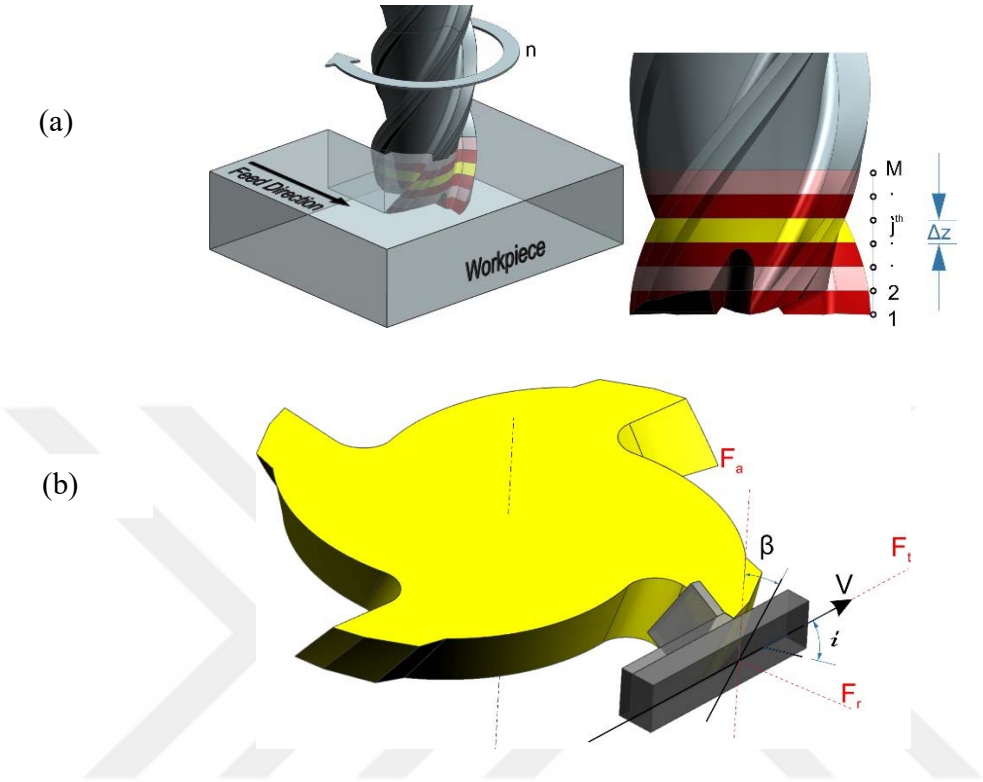

Figure 6-17: a) The discretization of the end-mill in to Δz thick disks. b) The cutting force components in the milling process for the selected discrete disk.

The endmill cutting edge approaches the workpiece material with an obliquity angle equal to the helix angle of the end-mill cutter. The components of the cutting forces, acting on the milling cutter, for $\boldsymbol{j^{th}}$ disk of infinitesimal thickness $\boldsymbol{\Delta z}$ are shown in Figure 6-17.

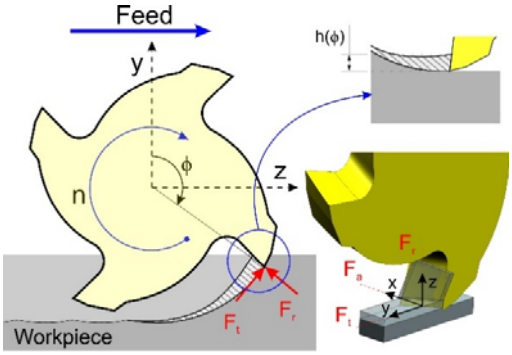

Figure 6-18: The mechanics of milling cutter.

The kinematics of the select disk of the end-mill shown in Figure 6-18, are approximated to be similar to a cutting tool with a straight edge. The curvature of the helical edge of a cylindrical body of the end-mill is minimized by the steep helix angle and differential thickness of the disk. The friction coefficient is calculated for the immersion angle, which gives the maximum chip thickness. At that particular instant, the tangential and the radial components of the cutting forces are parallel with ***y***-axis and ***x***-axis of the force measuring sensor's coordinate system.

The friction coefficient is found as the ratio $\boldsymbol{F_u/F_v}$ after the described coordinate transformation.

The geometry of the bottom cutting edge and respective mechanics involved in cutting is complex. Multiple sides of the bottom cutting edge on a flute, namely, the bottom, corner and side of it are cutting simultaneously. The effect of the bottom edge is eliminated by machining for two depths of cut and subtracting one from the other as illustrated in the Figure 6-19, leaving away the differential forces from the side cutting edge only.

$$F_{\Delta \mathrm{d}} = F_{kd_e} - F_{d_e} \tag{17}$$

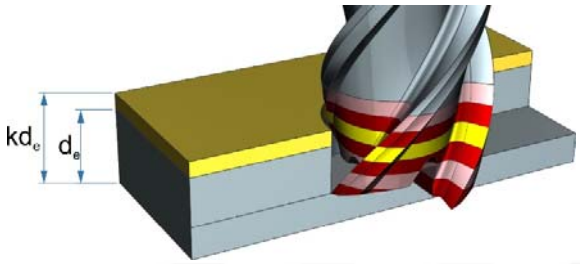

Figure 6-19: The two depths of cut isolate the effect of the bottom edge

c. Mean friction coefficient

The effect of the bottom cutting edge is removed from the cutting force data. Hence, the remaining force data is then for the cutting process with the side cutting edge of the end-mill. The tangential and the radial components of the forces are easily recognizable from the select disk engaged in cutting of the work piece material as shown in the Figure 6-18. The friction coefficient is defined as the ratio of the thrust force and the cutting force. In case of the end-mill section, it will be the ratio of the radial force and the tangential force. The cutting coefficient were calculated as described in section for the cutting coefficient method. The milling forces are simulated analytically using the obtained cutting coefficient for an individual disk of thickness Δz as shown in Figure 6-17(a) and the equations (7).

As the cutting forces are function of the immersion angle, initially the component representing the cutting forces has a smaller contribution in the total force then when the immersion angle is larger. The evolution of the friction coefficient as the immersion angle increases for the AlTiN coated, AlCrN coated and the un-coated end-mills are shown the Figure 6-20, Figure 6-21 and Figure 6-22.

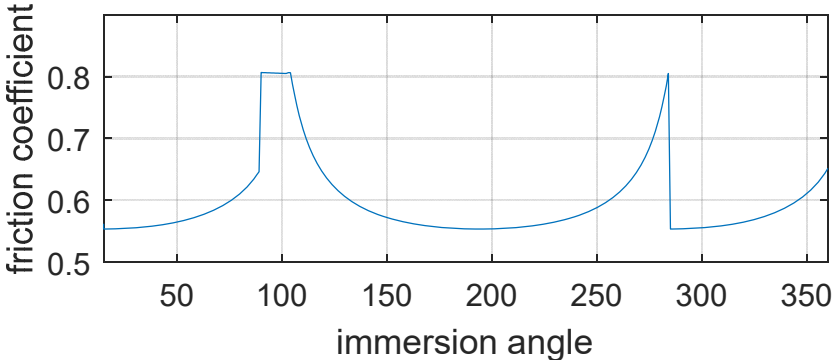

Figure 6-20: The change in Friction coefficient for the AlTiN coated endmill with the change in immersion angle.

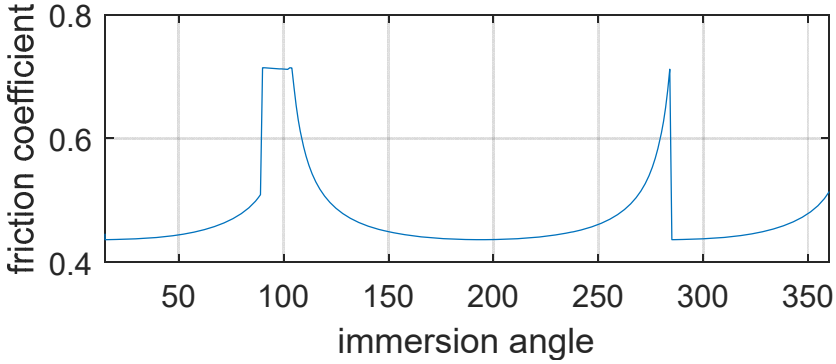

Figure 6-21: The change in friction coefficient for the AlCrN coated endmill with the change in immersion angle.

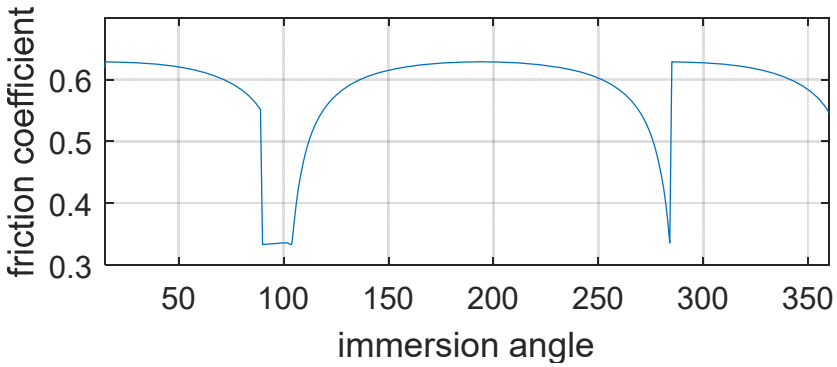

Figure 6-22: The change in friction coefficient for the un-coated endmill with the change in immersion angle.

The behavior of the friction coefficient for the un-coated carbide end-mill is different from the coated end-mills as the radial cutting coefficient was twice as much as it was for the cutting tools. The magnitudes for the cutting and edge coefficients is given in the Table 6-4.

Table 6-4: The cutting and edge coefficient for the end-milling of Al7050 for the differently coated tools

	Tangential cutting coefficient	Tangential edge coefficient	Feed cutting coefficient	Feed edge coefficient
	$N \cdot mm^{-2}$	$N \cdot mm^{-1}$	$N \cdot mm^{-2}$	$N \cdot mm^{-1}$
AlTiN coating	813	20	392	15
AlCrN coating	888	31	397	25
Un-coated	984	21	660	7

6.2.2 Experimental Setup

The machining tests were performed on 5-axis Mori Seiki NMV5000 DCG machining center. The workpiece material was 7000 series aluminum alloy Al7050, commonly used for aerospace industry applications. The chemical composition found using XRF technique are given in Table 6-5. The workpiece was carefully prepared for secure mounting on the table type dynamometer. The test setup is shown in Figure 6-23. The force data were acquired using a table type dynamometer and a high-speed data acquisition system. Cutting force data was acquired for three tools during dry slot cutting process. The description of the coating is provided in Table 6-6.

Figure 6-23: Mori Seiki NMV5000 DCG 5-axis milling machine used for tests.

Table 6-5: Chemical composition and mechanical properties of Al7050.

Chemical Composition (%)			
Al	Zn	Mg	Cu
Rest	4.20	0.01	6.13

Table 6-6: The coating materials and surface finishing techniques selected for the study.

	Coating material
Tool 1	Aluminum Titanium Nitride, (AlTiN)
Tool 2	Aluminum Chromium Nitride, (AlCrN)
Tool 3	No Coating

Table 6-7: The feedrates used in the investigation.

Test case	**Feedrate [mm.min^{-1}]**	**Uncut chip thickness [µm]**
Test 1	540	100
Test 2	780	150
Test 3	1040	200
Test 4	1300	250

The slot cutting operation is a relatively harsher machining strategy than other commonly employed strategies. Four-fluted 12 mm diameter solid carbide end-mills were used in the experiments. Machining was performed at 1 mm and 1.5 mm depths of cut in dry cutting conditions. The spindle speed was 1300 rpm corresponding to 49 m/min cutting speed. The feedrate and feed per tooth for the four test cases are given in Table 4-16.

6.2.3 Results and Discussion

The resultant of the differential cutting forces calculated from the force data are shown in Figure 6-24.

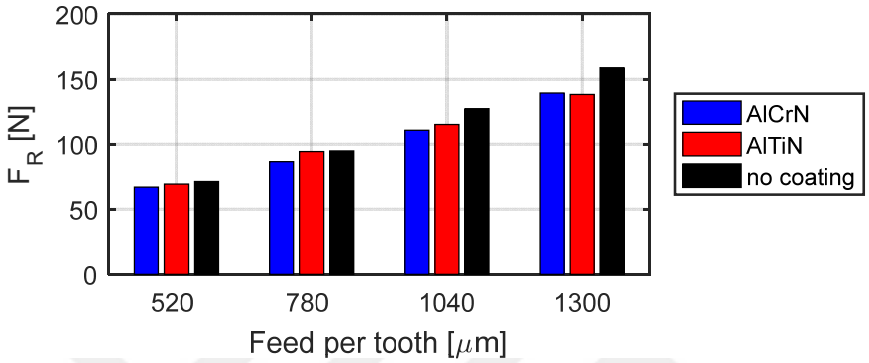

Figure 6-24: The resultant of the differential cutting forces for the differently coated solid carbide end-mills.

Subsequently, the cutting coefficients for the three differently coated carbide end-mills were found by applying the linear regression model on the cutting force data. The linear regression models for the force data are given in Figure 6-25

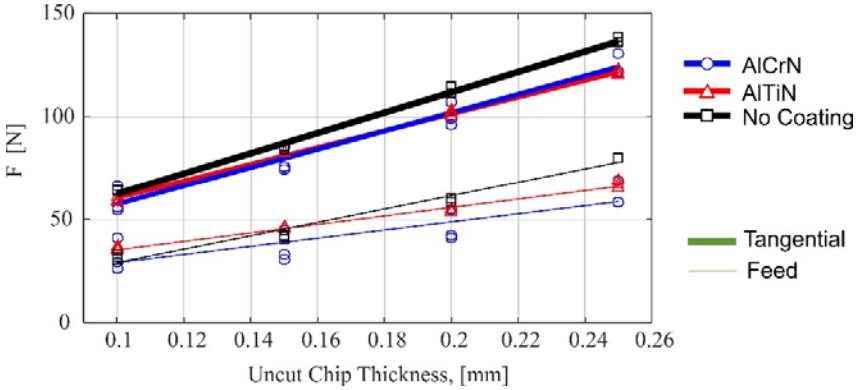

Figure 6-25: Linear regression model for cutting forces data of the differently coated end-mills.

Each test was repeated three times. The average R-square value for y axis and x axis forces data was 0.9926 and 0.9741, respectively. The cutting coefficients calculated for the three tools used for this study are given in Figure 6-26.

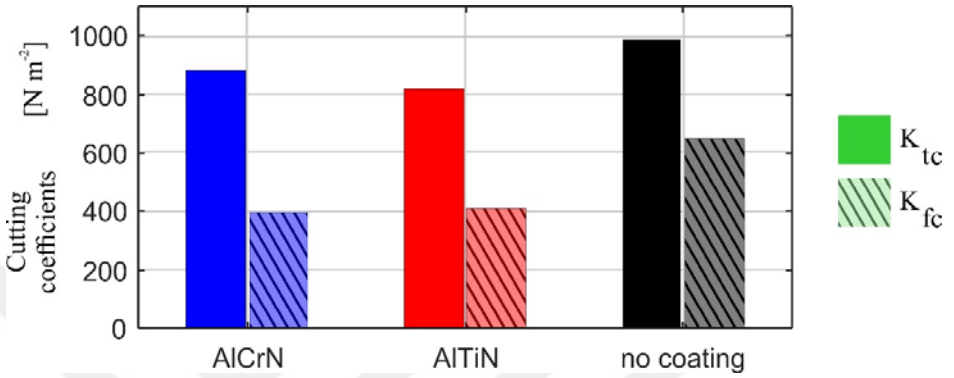

Figure 6-26: The tangential and feed cutting coefficients for the differently coated tools when machining Al7050.

The tangential cutting coefficient, K_{tc} and the radial cutting coefficient, K_{rc} are inputs for the friction analysis of the end-mills. The friction coefficient calculated from the cutting coefficients is given in Figure 6-27.

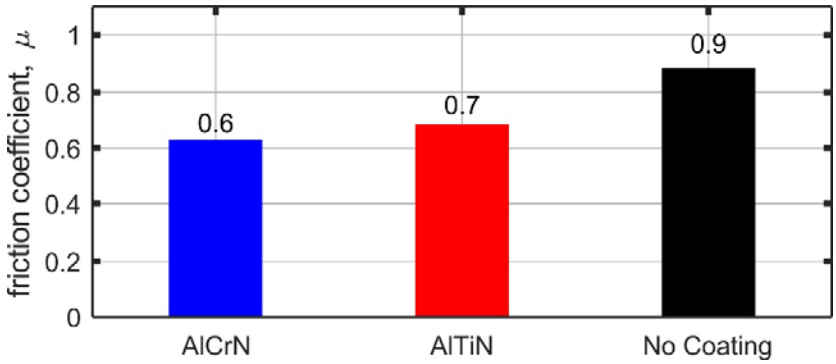

Figure 6-27: The friction coefficient values from the cutting coefficient method for the three differently coated carbide end-mills for machining Al7050 with coated solid carbide end-mills.

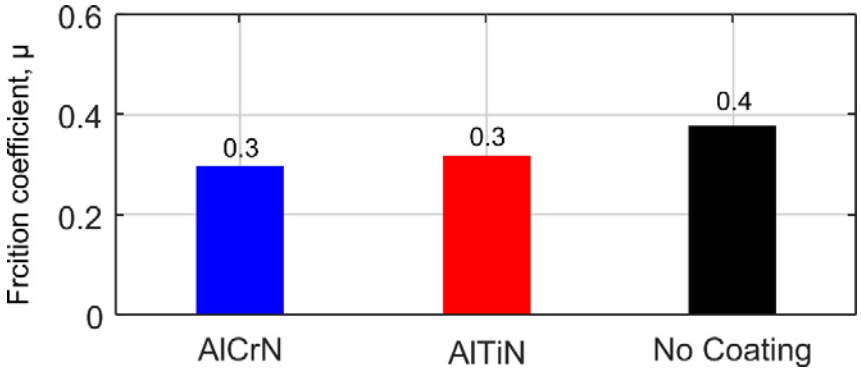

Figure 6-28: The friction coefficient values from the end-mill mechanics method for the three differently coated carbide end-mills for machining Al7050 with coated solid carbide end-mills.

The friction coefficient is from the governing parameters for establishing the tool life and workpiece integrity. The calculation of the friction coefficient is done using three methods. The friction coefficient values from one of the methods is much larger than the other two. The exact mechanics of the three methods require further evaluation to establish the full understanding of the friction phenomena. Further experimental evaluation of friction coefficient is warranted to quantify the accuracy of any method.

It is identified that the coated tool had lesser friction coefficient than the tool without coating. The carbide end-mill without any coating friction coefficient was 0.9. Whereas, the AlTiN coated end-mill friction coefficient was 07. The lowest value was 0.6 for the aluminum chromium nitride coating. The advantage of coating carbide end-mills is evident.

6.2.4 Conclusion

The temperatures produced during cutting processes affect the tool life and workpiece integrity. The friction coefficient has a direct impact on temperatures produced. In this investigation, the friction coefficients for differently coated carbide end-mills are found.

The friction coefficient for Al7050 and plain tungsten carbide end-mill is in agreement with published research of (Lazoglu and Bugdayci, 2014b). The friction coefficients for Al7050 are calculated after from ploughing forces adjusted cutting forces. Hence, these values are for the chip-tool interface on the rake face of the tool.

Chapter 7
Bibliography

Akmal, M., Layegh, K.S.E., Lazoglu, I., Akgün, A., Yavaş, Ç., 2017. Friction Coefficients on Surface Finish of AlTiN Coated Tools in the Milling of Ti6Al4V. Procedia CIRP 58, 596–600. doi:10.1016/j.procir.2017.03.231

Altintas, Y., 2012. Manufacturing Automation: Metal Cutting Mechanics, Machine Tool Vibrations, and CNC Design. Cambridge University Press.

AMG GfE, 2013. AMG Titanium Alloys & Coatings presentation [WWW Document].

Appel, F., Paul, D.H., Oehring, M., 2011. Gamma Titanium Aluminide Alloys. Wiley.

Armarego, E.J.A., Whitfield, R.C., 1985. Computer Based Modelling of Popular Machining Operations for Force and Power Prediction. CIRP Ann. - Manuf. Technol. 34, 65–69. doi:10.1016/S0007-8506(07)61725-9

Arrazola, P.J., Meslin, F., Maître, F.., Marya, S., 2004. Material Flow Stress Sensitivity Analysis in Numerical Cutting Modeling.: EBSCOhost. Mater. Process. Des. Model. Simul. Appl. 1408–1413.

Aspinwall, D.K., Dewes, R.C., Mantle, A.L., 2005. The Machining of γ-TiAI Intermetallic Alloys. CIRP Ann. - Manuf. Technol. doi:10.1016/S0007-8506(07)60059-6

Aspinwall, D.K., Mantle, A.L., Kok, W., Hood, R., Leung, S., 2013. Cutting temperatures when ball nose end-milling g -TiAl intermetallic alloys. CIRP Ann. - Manuf. Technol. 62, 75–78.

Aust, B.E., Niemann, H., 1999. Machining of g -TiAl. Adv. Eng. Mater. 53–57.

Bahi, S., Nouari, M., Moufki, A., El Mansori, M., Molinari, A., Mansori, M. El, Molinari, A., El Mansori, M., Molinari, A., 2011. A new friction law for sticking and sliding contacts in machining. Tribol. Int. 44, 764–771. doi:10.1016/j.triboint.2011.01.007

Bäker, M., 2015. A new method to determine material parameters from machining

simulations using inverse identification. Procedia CIRP 31, 399–404. doi:10.1016/j.procir.2015.04.090

Barletta, M., Pietrobono, F., Rubino, G., Tagliaferri, V., 2015. Drag finishing of sensitive workpieces with fluidized abrasives. J. Manuf. Process. 16, 494–502. doi:10.1016/j.jmapro.2014.06.003

Basturk, S., Senbabaoglu, F., Islam, C., Erten, M., Lazoglu, I., Gulmez, T., 2010. Titanium machining with new plasma boronized cutting tools. CIRP Ann. - Manuf. Technol. 59, 101–104. doi:10.1016/j.cirp.2010.03.095

Boeing, 2015. Major Investment in 747 Quality, Safety [WWW Document]. http://www.boeing.com/features/2015/02/bca-747-flextrak-02-10-15.page.

Brandt, G., Gerendas, A., Mikus, M., 1990. Wear Mechanisms of Ceramic Cutting Tools When Machining Ferrous and Non-ferrous Alloys. J. Eur. Ceram. Soc. 6, 273–290.

Budak, E., Armarego, E.J. a., Altintas, Y., 1996. Prediction of Milling Force Coefficients From Orthogonal Cutting Data. J. Manuf. Sci. Eng. 118, 216. doi:10.1115/1.2831014

Çelebi, C., Özlü, E., Budak, E., 2013. Modeling and experimental investigation of edge hone and flank contact effects in metal cutting. Procedia CIRP 8, 194–199. doi:10.1016/j.procir.2013.06.088

Chandley, D., Metal, P., Technology, C., 2000. Use of gamma titanium aluminide for automotive engine valves. Metall. Sci. Technol. 18, 8–11.

Christoph Leyens, Peters, M., 2003. Titanium and Titanium Alloys, Fundamentals and Applications. Wiley-VCH, Weinheim. doi:10.1002/3527602119

Davim, J.P., 2014. Machining of Titanium Alloys. Springer, Verlag Berlin Heidelberg.

Del Prete, A., Filice, L., Umbrello, D., 2013. Numerical simulation of machining nickel-based alloys. Procedia CIRP 8, 540–545. doi:10.1016/j.procir.2013.06.147

Denkena, B., Grove, T., Dittrich, M.A., Niederwestberg, D., Lahres, M., 2015. Inverse Determination of Constitutive Equations and Cutting Force Modelling for Complex

Tools Using Oxley's Predictive Machining Theory. Procedia CIRP 31, 405–410. doi:10.1016/j.procir.2015.03.012

Dimiduk, D.., 1999. Gamma titanium aluminide alloys—an assessment within the competition of aerospace structural materials. Mater. Sci. Eng. A 263, 281–288. doi:10.1016/S0921-5093(98)01158-7

Donachie, M.J., 2000. Titanium: A Technical Guide. ASM International, Materials Park, OH.

Egaña, A., Rech, J., Arrazola, P.J., P. J. Arrazola, 2012. Characterization of Friction and Heat Partition Coefficients during Machining of a TiAl6V4 Titanium Alloy and a Cemented Carbide. Tribol. Trans. 55, 665–676. doi:10.1080/10402004.2012.692007

Froes, F.H., 2015. Titanium Physical Metallurgy Processing and Applications. ASM International, Materials Park, OH. doi:10.1017/CBO9781107415324.004

Ghani, J.A., Hassan, C., Haron, C., Hamdan, S.H., Yasir, A., Said, M., Tomadi, S.H., 2013. Failure mode analysis of carbide cutting tools used for machining titanium alloy. Ceram. Int. 39, 4449–4456.

Gillespie, L., 2006. Mass finishing handbook. Industrial Press, New York.

Gradišek, J., Kalveram, M., Weinert, K., 2004. Mechanistic identification of specific force coefficients for a general end-mill. Int. J. Mach. Tools Manuf. 44, 401–414. doi:10.1016/j.ijmachtools.2003.10.001

Grzesik, W., 2000. Influence of thin hard coatings on frictional behaviour in the orthogonal cutting process. Tribol. Int. 33, 131–140. doi:10.1016/S0301-679X(00)00072-4

Hastings, W.F., Oxley, P.L.B., Stevenson, M.G., 1974. Predicting a material's machining characteristics using flow stress properties obtained from high-speed compression tests. Proc. Inst. Mech. Engrs 188, 245–252.

Holman J.P., 2010. Heat Transfer, 10th ed. McGraw Hill Higher Education.

Hood, R., Aspinwall, D.K., Sage, C., Voice, W., 2013a. High speed ball nose end-milling of

γ-TiAl alloys. Intermetallics 32, 284–291. doi:10.1016/j.intermet.2012.09.011

Hood, R., Aspinwall, D.K., Sage, C., Voice, W., 2013b. High speed ball nose end-milling of gamma-TiAl alloys. Intermetallics 32, 284–291. doi:10.1016/j.intermet.2012.09.011

Intermetallic Alloys [WWW Document], 2017. . Support. Eduction Across Eur. URL http://www.spaceflight.esa.int/impress/text/education/Solidification/Intermetallics_Immiscibles.html (accessed 9.12.17).

Islam, C., Lazoglu, I., Altintas, Y., 2015. A Three-Dimensional Transient Thermal Model for Machining. J. Manuf. Sci. Eng. 138, 21003. doi:10.1115/1.4030305

Islam, C., Lazoglu, I., Islam, C., 2012. Modeling of 3D temperature fields for oblique machining. CIRP Ann. - Manuf. Technol. 61, 127–130. doi:10.1016/j.cirp.2012.03.074

Iturbe, A., Giraud, E., Hormaetxe, E., Garay, A., Germain, G., Ostolaza, K., Arrazola, P.J., 2017. Mechanical characterization and modelling of Inconel 718 material behavior for machining process assessment. Mater. Sci. Eng. A 682, 441–453. doi:10.1016/j.msea.2016.11.054

Jafarian, F., Imaz Ciaran, M., Umbrello, D., Arrazola, P.J., Filice, L., Amirabadi, H., 2014. Finite element simulation of machining Inconel 718 alloy including microstructure changes. Int. J. Mech. Sci. 88, 110–121. doi:10.1016/j.ijmecsci.2014.08.007

Jaspers, S., 1999. Metal Cutting Mechanics and Material Behaviour. Textb.

Jaspers, S., 1999. Metal Cutting Mechanics and Material Behaviour. Eindhoven University.

Kaiser Aluminum, 2017. KaiserLiner Interactive Cutaway [WWW Document]. http://www.kaiseraluminum.com.

Karpat, Y., 2011. Temperature dependent flow softening of titanium alloy Ti6Al4V: An investigation using finite element simulation of machining. J. Mater. Process. Technol. 211, 737–749. doi:10.1016/j.jmatprotec.2010.12.008

Keller, M.M., Jones, P.E., III, W.J.P., Eylon, D., 1997. The Development of Low-Cost TiAl Automotive Valves. J. Met. 49, 4–6. doi:10.1007/BF02914683

Kim, Y.-W., 1989. Intermetallic alloys based on gamma titanium aluminide. Jom 41, 24–30. doi:10.1007/BF03220267

Kim, Y.W., 1994. Ordered intermetallic alloys, part III: Gamma titanium aluminides. Jom 46, 30–39. doi:10.1007/BF03220745

Kimura, A., Hasegawa, H., Yamada, K., Suzuki, T., 1999. Effects of Al content on hardness, lattice parameter and microstructure of Ti1−xAlxN films. Surf. Coatings Technol. 120–121, 438–441. doi:10.1016/S0257-8972(99)00491-0

Kitagawa, T., Kubo, a, Maekawa, K., 1997. Temperature and wear of cutting tools in high-speed machining of Incone1718 and Ti-6A1-6V-2Sn. Wear 202, 142–148. doi:10.1016/S0043-1648(96)07255-9

Klocke, F., Lung, D., Buchkremer, S., 2013. Inverse Identification of the Constitutive Equation of Inconel 718 and AISI 1045 from FE Machining Simulations. Procedia CIRP 8, 212–217. doi:10.1016/j.procir.2013.06.091

Lapin, J., 2009. TiAl-based alloys: Present status and future perspectives. 18th Int. Metall. Mater. Conf. Proc. 12.

Lasalmonie, A., 2006. Intermetallics: Why is it so difficult to introduce them in gas turbine engines? Intermetallics 14, 1123–1129. doi:10.1016/j.intermet.2006.01.064

Layegh K., S.E.E., Yigit, I.E.E., Lazoglu, I., 2015. Analysis of tool orientation for 5-axis ball-end-milling of flexible parts. CIRP Ann. - Manuf. Technol. 64, 97–100. doi:10.1016/j.cirp.2015.04.067

Lazoglu, I., Bugdayci, B., 2014a. Thermal modelling of end-milling. CIRP Ann. - Manuf. Technol. 63, 113–116. doi:10.1016/j.cirp.2014.03.072

Lazoglu, I., Bugdayci, B., 2014b. CIRP Annals - Manufacturing Technology. CIRP Ann. - Manuf. Technol. 63, 113–116. doi:10.1016/j.cirp.2014.03.072

Lazoglu, I., Poulachon, G., Ramirez, C., Akmal, M., Marcon, B., Rossi, F., Outeiro, J., Krebs, M., 2017. Thermal analysis in Ti-6Al-4V drilling. CIRP Ann. - Manuf. Technol. 66,

105–108. doi:10.1016/j.cirp.2017.04.020

Lee, W.S., Lin, C.F., Chen, T.H., Chen, H.W., 2011. Dynamic mechanical behaviour and dislocation substructure evolution of Inconel 718 over wide temperature range. Mater. Sci. Eng. A 528, 6279–6286. doi:10.1016/j.msea.2011.04.079

Lei, S., Shin, Y.C., Incropera, F.P., 1999. Material Constitutive Modeling Under High Strain Rates and Temperatures Through Orthogonal Machining Tests. J. Manuf. Sci. Eng. 121, 577–585. doi:doi:10.1115/1.2833062

Li, H.Z., Wang, J., 2013. A cutting forces model for milling Inconel 718 alloy based on a material constitutive law. Proc. Inst. Mech. Eng. Part C J. Mech. Eng. Sci. 227, 1761–1775. doi:10.1177/0954406212469167

Lin, G.C.I., 1978. Prediction of cutting forces and chip geometry in oblique machiing from flow stress properties and cutting conditions. Int. J. Mach. Tool Des. Res. 18, 117–130.

Lin, Y.C., Li, K.K., Li, H. Bin, Chen, J., Chen, X.M., Wen, D.X., 2015. New constitutive model for high-temperature deformation behavior of inconel 718 superalloy. Mater. Des. 74, 108–118. doi:10.1016/j.matdes.2015.03.001

Liu, C.T., 1995. Recent advances in ordered intermetallics. Mater. Chem. Phys. 42, 77–86. doi:10.1016/0254-0584(95)01546-9

Liu, C.T., Kumar, K.S., 1993. Ordered intermetallic alloys, part I: Nickel and iron aluminides. JOM 45, 38–44. doi:10.1007/BF03223218

Lorentzon, J., Järvstråt, N., Josefson, B.L., 2009. Modelling chip formation of alloy 718. J. Mater. Process. Technol. 209, 4645–4653. doi:10.1016/j.jmatprotec.2008.11.029

Lurdos, O., Montheillet, F., Damamme, G., 2008. Empirical and physically based flow rules relevant to high speed processing of 304L steel. Int. J. Mater. Form. 1, 1431–1434. doi:10.1007/s12289-008-0105-1

Maekawa, K., Obikawa, T., Yamane, Y., Childs, T.H.C., 2013. Metal Machining: Theory and Applications. Elsevier Science.

Maki, K., Ehira, A., Sayashi, M., Sasaki, T., Noda, T., Okabe, M., Isobe, S., 1996. Development of a High-Performance TiA1 Exhaust Valve, in: SAE Technical Paper. SAE International. doi:10.4271/960303

Mamedov, A., Lazoglu, I., 2016. Thermal analysis of micro milling titanium alloy Ti-6Al-4V. J. Mater. Process. Technol. 229, 659–667. doi:10.1016/j.jmatprotec.2015.10.019

Mattingly, J.D., 2006. Elements of Propulsion: Gas Turbines and Rockets, AIAA education series. American Institute of Aeronautics and Astronautics.

Merchant, M.E., 1945. Mechanics of the metal cutting process. I. Orthogonal cutting and a type 2 chip. J. Appl. Phys. 16, 267–275. doi:10.1063/1.1707586

Moufki, A., Molinari, A., Dudzinski, D., 1998. Modelling of orthogonal cutting with a temperature dependent friction law. J. Mech. Phys. Solids 46, 2103–2138. doi:10.1016/S0022-5096(98)00032-5

Naka, S., 1996. Advanced titanium-based alloys. Curr. Opin. Solid State Mater. Sci. 1, 333–339. doi:10.1016/S1359-0286(96)80022-2

Narutaki, N., Yamane, Y., Hayashi, K., Kitagawa, T., Uehara, K., 1993. High-speed Machining of Inconel 718 with Ceramic Tools. CIRP Ann. - Manuf. Technol. 42, 103–106. doi:10.1016/S0007-8506(07)62402-0

Ozlu, E., Molinari, A., Budak, E., 2010. Two-Zone Analytical Contact Model Applied To Orthogonal Cutting. Mach. Sci. Technol. 14, 323–343. doi:10.1080/10910344.2010.512794

P. J. Arrazola, Meslin, F., 2002. A technique for the identification of friction at toolchip interface during machining.pdf, in: Proceedings of The Second Asia International Conference on Tribology. pp. 319–320.

Pawade, R.S., Joshi, S.S., 2011. Mechanism of Chip Formation in High-Speed Turning of Inconel 718. Mach. Sci. Technol. 15, 132–152. doi:10.1080/10910344.2011.557974

Pawade, R.S.S., Sonawane, H.A., Joshi, S.S., 2009. An analytical model to predict specific

shear energy in high-speed turning of Inconel 718. Int. J. Mach. Tools Manuf. 49, 979–990. doi:10.1016/j.ijmachtools.2009.06.007

Pervaiz, S., Rashid, A., Deiab, I., Nicolescu, M., 2014. Influence of Tool Materials on Machinability of Titanium- and Nickel-Based Alloys: A Review. Mater. Manuf. Process. 29, 219–252. doi:10.1080/10426914.2014.880460

Pottlacher, G., Hosaeus, H., Kaschnitz, E., Seifter, a, 2002. Thermophysical properties of solid and liquid Inconel 718 Alloy. Scand. J. Metall. 31, 161–168. doi:10.1034/j.1600-0692.2002.310301.x

Prasad, N.E., Wanhill, R.J.H., 2017. Aerospace materials and material technologies. Volume 1, Aerospace materials /, 1st ed, Indian Institute of Metals series. Springer, Singapore. doi:10.1007/978-981-10-2134-3

Priarone, P.C., Rizzuti, S., Settineri, L., Vergnano, G., 2012. Effects of cutting angle, edge preparation, and nano-structured coating on milling performance of a gamma titanium aluminide. J. Mater. Process. Technol. 212, 2619–2628. doi:10.1016/j.jmatprotec.2012.07.021

Quested, P.N., Brooks, R.F., Chapman, L., Morrell, R., Youssef, Y., Mills, K.C., 2009. Measurement and estimation of thermophysical properties of nickel based superalloys. Mater. Sci. Technol. 25, 154–162. doi:10.1179/174328408X361454

Rech, J., 2006. Influence of cutting tool coatings on the tribological phenomena at the tool-chip interface in orthogonal dry turning. Surf. Coatings Technol. 200, 5132–5139. doi:10.1016/j.surfcoat.2005.05.032

Rech, J., Arrazola, P.J., Claudin, C., Courbon, C., Pusavec, F., Kopac, J., 2013. Characterisation of friction and heat partition coefficients at the tool-work material interface in cutting. CIRP Ann. - Manuf. Technol. 62, 79–82. doi:10.1016/j.cirp.2013.03.099

Reed, R.C., 2008. The Superalloys: Fundamentals and Applications. Cambridge University

Press.

Rice, R.C., Jackson, J.L., Bakuckas, J., Thompson, S., 2003. Metallic Materials Properties Development and Standardization. U.S. Department of Transportation, Federal Aviation Administration.

Richards, N., Aspinwall, D., 1989. Use of ceramic tools for machining nickel based alloys. Int. J. Mach. Tools Manuf. 29, 575–588. doi:10.1016/0890-6955(89)90072-2

Settineri, L., Priarone, P.C., Arft, M., Lung, D., Stoyanov, T., 2014. An evaluative approach to correlate machinability, microstructures, and material properties of gamma titanium aluminides. CIRP Ann. - Manuf. Technol. 63, 57–60. doi:10.1016/j.cirp.2014.03.068

Shapiro, E., Dieter, G.E., 1970. High Temperature-High Strain Rate Fracture of Inconel 600. Metall. Trans. 1, 1711–1719.

Si, J.Y., Liao, X.H., Xie, L.Q., Lin, K.R., 2015. Flow Behavior and Constitutive Modeling of Delta-processed Inconel 718 alloy. J. Iron Steel Res. Int. 22, 837–845. doi:10.1016/S1006-706X(15)30078-9

Song, J.H., Huh, H., 2007. The Effect of Strain Rate on the Material Characteristics of Nickel-Based Superalloy Inconel 718. Key Eng. Mater. 340–341, 283–288. doi:10.4028/www.scientific.net/KEM.340-341.283

Soo, S.L., Aspinwall, D.K., Dewes, R.C., 2004. 3D FE modelling of the cutting of Inconel 718. J. Mater. Process. Technol. 150, 116–123. doi:10.1016/j.jmatprotec.2004.01.046

Stevenson, M.G., Oxley, P.L.B., 1970. An experimental investigation of the influence of strain-rate and temperature on the flow stress properties of a low carbon steel using a machining test. Proc. Inst. Mech. Eng. 185, 741–754. doi:10.1243/PIME

Stevenson, M.G., Oxley, P.L.B., 1969. An experimental investigation of the influence of speed an scale on the strain-rate in a zone of intense plastic deformation. Proc. Inst. Mech. Eng. 184, 561–569. doi:10.1243/PIME

Stevenson, R., Stephenson, D.A., 1995. The Mechanical Behavior of Zinc During

Machining. J. Eng. Mater. Technol. 117, 172–178. doi:doi:10.1115/1.2804526

Tetsui, T., 2002. Development of a TiAl turbocharger for passenger vehicles. Mater. Sci. Eng. A 329–331, 582–588. doi:10.1016/S0921-5093(01)01584-2

Tetsui, T., 1999. Gamma Ti aluminides for non-aerospace applications. Curr. Opin. Solid State Mater. Sci. 4, 243–248. doi:10.1016/S1359-0286(99)00023-6

Tetsui, T., Shindo, K., Kaji, S., Kobayashi, S., Takeyama, M., 2005. Fabrication of TiAl components by means of hot forging and machining. Intermetallics 13, 971–978. doi:10.1016/j.intermet.2004.12.012

Thellaputta, G.R., Chandra, P.S., Rao, C.S.P., 2017. Machinability of Nickel Based Superalloys: A Review. Mater. Today Proc. 4, 3712–3721. doi:10.1016/j.matpr.2017.02.266

Thomas, M., 2011. Processing and Characterization of TiAl- based Alloys : Towards an Industrial Scale. Aaerospacelab 1–11.

Uhlmann, E., Schulenburg, M.G. Von Der, Zettier, R., 2007. Finite Element Modeling and Cutting Simulation of Inconel 718 56, 61–64. doi:10.1016/j.cirp.2007.05.017

Uhlmann, E., Von Der Schulenburg, M.G., Zettier, R., 2007. Finite element modeling and cutting simulation of inconel 718. CIRP Ann. - Manuf. Technol. 56, 61–64. doi:10.1016/j.cirp.2007.05.017

Ulutan, D., Lazoglu, I., Dinc, C., 2009. Three-dimensional temperature predictions in machining processes using finite difference method. J. Mater. Process. Technol. 209, 1111–1121. doi:10.1016/j.jmatprotec.2008.03.020

Ulutan, D., Özel, T., 2013. Determination of tool friction in presence of flank wear and stress distribution based validation using finite element simulations in machining of titanium and nickel based alloys. J. Mater. Process. Technol. 213, 2217–2237. doi:10.1016/j.jmatprotec.2013.05.019

Ulutan, D., Özel, T., 2012. Methodology To Determine Friction in Orthogonal Cutting With

Application to Machining Titanium and Nickel Based Alloys, in: The ASME 2012 International Manufacturing Science and Engineering Conference. pp. 1–8.

Valiorgue, F., Rech, J., Hamdi, H., Bonnet, C., Gilles, P., Bergheau, J.M., 2008. Modelling of friction phenomena in material removal processes. J. Mater. Process. Technol. 201, 450–453. doi:10.1016/j.jmatprotec.2007.11.266

Vogtel, P., Klocke, F., Lung, D., 2014. High Performance Machining of Profiled Slots in Nickel-Based-Superalloys. Procedia CIRP 14, 54–59. doi:10.1016/j.procir.2014.03.061

Wang, X., Huang, C., Zou, B., Liu, H., Zhu, H., Wang, J., 2013. Dynamic behavior and a modified Johnson-Cook constitutive model of Inconel 718 at high strain rate and elevated temperature. Mater. Sci. Eng. A 580, 385–290. doi:10.1016/j.msea.2013.05.062

Wang, Y., Shao, W.Z., Zhen, L., Yang, L., Zhang, X.M., 2008. Flow behavior and microstructures of superalloy 718 during high temperature deformation. Mater. Sci. Eng. A 497, 479–486. doi:10.1016/j.msea.2008.07.046

Wayne, S.F., Buljan, S.-T., 1990. Wear of Ceramic Cutting Tools in Ni-Based Superalloy Machining. Tribol. Trans. 33, 618–626. doi:10.1080/10402009008981997

Weinert, K., Biermann, D., Bergmann, S., 2007. Machining of high strength light weight alloys for engine applications. CIRP Ann. - Manuf. Technol. 56, 105–108. doi:10.1016/j.cirp.2007.05.027

Williams, J.C., Starke, E.A., 2003. Progress in structural materials for aerospace systems. Acta Mater. 51, 5775–5799. doi:10.1016/j.actamat.2003.08.023

Wright, P.K., Chow, J.G., 1982. Deformation Characteristics of Nickel Alloys During Machining. J. Eng. Mater. Technol. 104, 85–93.

Wu, X., 2006. Review of alloy and process development of TiAl alloys. Intermetallics 14, 1114–1122. doi:10.1016/j.intermet.2005.10.019

Wyen, C.F., Wegener, K., 2010. Influence of cutting edge radius on cutting forces in

machining titanium. CIRP Ann. - Manuf. Technol. 59, 93–96. doi:10.1016/j.cirp.2010.03.056

Yamaguchi, M., Inui, H., Ito, K., 2000. High-temperature structural intermetallics. Acta Mater. 48, 307–322. doi:10.1016/S1359-6454(99)00301-8

Yuan, H., Liu, W.C., 2005. Effect of the delta phase on the hot deformation behavior of Inconel 718. Mater. Sci. Eng. A 408, 281–289. doi:10.1016/j.msea.2005.08.126

Zitoune, R., Krishnaraj, V., Davim, J.P., 2013. Machining of Titanium Alloys and Composites for Aerospace Applications. Trans Tech Publications, Inc, Switzerland.